UNIVERSITY OF SOUTHAMPTON

FACULTY OF ENGINEERING AND THE ENVIRONMENT

Academic Unit of Mechanical Engineering

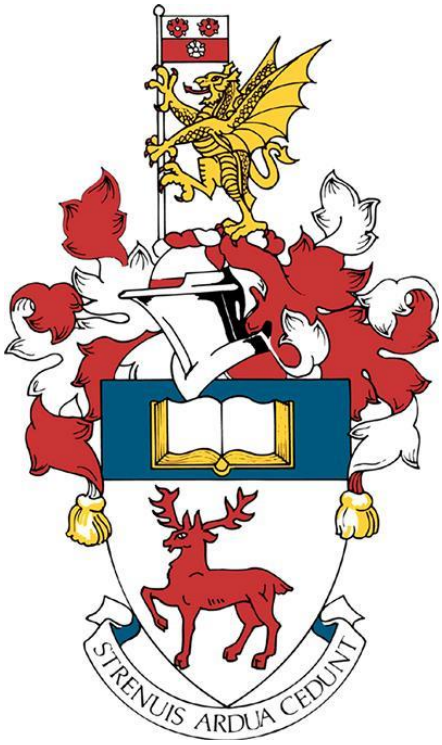

Novel 3D scaffolds for bone formation and cell printing

by

Gianluca Cidonio

Thesis for the degree of Doctor of Philosophy

September 2018

UNIVERSITY OF SOUTHAMPTON

ABSTRACT

FACULTY OF ENGINEERING AND THE ENVIRONMENT

Thesis for the degree of Doctor of Philosophy

NOVEL 3D SCAFFOLDS FOR BONE FORMATION AND CELL PRINTING

Gianluca Cidonio

Current approaches to treat bone fractures typically use: i) autologous bone graft harvested from the patient, which can be proved painful, and ii) non-degradable metal implants that provide the mechanical support needed, but can require numerous revisions and replacement. Biofabrication has come to the fore to target the unmet clinical needs in orthopaedic regenerative medicine aiming to produce degradable tissue-like structures in an automated fashion by the simultaneous extrusion of biomaterials (bioinks) and living cells. Such an approach contains a number of challenges including post-printing cell damage and limited functionality. The biofabrication paradigm involves the use of high polymeric content bioinks to ensure shape fidelity which often impacts on cell viability. Biopolymer-silicate nanocomposite hydrogels at low polymer fractions present remarkable shear-thinning and tuneable viscoelastic properties, ideal for bioprinting purposes.

This study has examined a library of clay-based bioinks for the fabrication of three-dimensional functional constructs for skeletal regeneration. This thesis investigates the hypothesis that a clay nanomaterial (Laponite, LAP) can be used to enhance printability and functionality of i) alginate-methylcellulose, ii) gellan gum and iii) gelatin methacryloyl bioinks.

Laponite-alginate-methylcellulose bioink (named 3-3-3 after the 3 % w/v concentration of each component) was fully characterised *in vitro* and the behaviour of printed cells investigated during 21 days of culture. Cells displayed evidence of proliferation ($p<0.0001$) after 7, 14 and 21 days in clay-based bioinks compared to silicate-free constructs. Skeletal stem cells (SSCs) were encapsulated and printed with the bioink to create viable and functional 3D scaffolds cultured *in vitro* for 21 days. Scaffolds implanted in a chick chorioallantoic membrane (CAM) model displayed excellent integration and vascular infiltration. SSCs-laden 3-3-3 printed scaffolds implanted subcutaneously in a mouse model induced significant ($p<0.0001$) new bone formation compared to acellular scaffolds and bulk controls.

Addition of Laponite to gellan gum (GG) significantly ($p<0.0001$) modulated the swelling kinetics. LAP-GG nanocomposite, printed in an agarose fluid gel, was found to sustain cell viability over 21 days *in vitro*, and support the functionality of printed cells evidenced by the significant ($p<0.0001$) alkaline phosphatase expression at 7 and 21 days compared to GG alone. LAP-GG scaffolds displayed functionality in a CAM model when absorbed in VEGF-agarose solution during printing evidenced by enhanced angiogenesis.

Laponite and GelMA (LAP-GelMA) bioink was observed to be printable with the application of a visible-light crosslinking technology during extrusion, producing scaffolds with significant ($p<0.0001$) shape fidelity. SSCs remained viable and functional in LAP-GelMA constructs. Drugs were demonstrated to be absorbable in cast discs which displayed enhanced ($p<0.0001$) angiogenesis and integration when implanted in CAM model following VEGF absorption.

Overall, the results presented in this thesis auger well for the generation of innovative approaches to deliver skeletal populations and bioactive agents for orthopaedic application using 3D printing technologies and clay-based bioinks.

Table of Contents

List of Tables

List of Figures

List of Figures

List of Figures

List of Supplementary Figures

Author's Declaration of Authorship

I, Gianluca Cidonio declare that this thesis entitled "*Novel 3D scaffolds for bone formation and cell printing*" and the work presented in it are my own and has been generated by me as the result of my own original research. I confirm that:

1. This work was done wholly or mainly while in candidature for a research degree at this University;
2. Where any part of this thesis has previously been submitted for a degree or any other qualification at this University or any other institution, this has been clearly stated;
3. Where I have consulted the published work of others, this is always clearly attributed;
4. Where I have quoted from the work of others, the source is always given. With the exception of such quotations, this thesis is entirely my own work;
5. I have acknowledged all main sources of help;
6. Where the thesis is based on work done by myself jointly with others, I have made clear exactly what was done by others and what I have contributed myself;
7. Parts of this work have been published-submitted as:
    I. Chapter 1 – Cidonio G, Glinka M, Dawson J I, Oreffo R O C The cell in the ink: improving biofabrication by printing stem cells for skeletal regenerative medicine - *Review - in submission (Sept 2018)*;
    II. Chapter 3 – Ahlfeld T and Cidonio G, Kilian D, Duin S, Akkineni A R, Dawson J I, Yang S, Lode A, Oreffo R O C and Gelinsky M 2017 Development of a clay based bioink for 3D cell printing for skeletal application *Biofabrication* **9** 034103;
    III. Chapter 7 – Cidonio G and Alcala-Orozco C R, Glinka M, Mutreja I, Kim Y-H, Dawson J I, Lim K S, Woodfield T B F, Oreffo R O C Novel nanocomposite light-curable bioink for 3D skeletal regeneration - *in submission (Sept 2018)*.

Signed:

Date:

Acknowledgements

I came to the UK three years ago to follow my interests for research. During these years, I have been working on a thriving field and in a great lab that have always made me feel welcome. I am first and foremost grateful to my supervisors Prof Shoufeng Yang, Dr Jon Dawson and Prof Richard Oreffo for their support during my studies at the University of Southampton. I especially take this opportunity to thank Dr Jon Dawson for his constant and precious guidance, and Prof Richard O.C. Oreffo for the volume of time he spent with me during this last period, the caring and mentoring he has been providing me, particularly during the last two years of my PhD.

I must thank collaborators from various universities institutes that have greatly contribute to this thesis. Prof Michael Gelinsky, who hosted me in Dresden for few months have been a real inspiration and mentor. Tilman Ahlfeld, collaborator and friend that have been always happy to share his knowledge and have taught me many printing tricks. Prof Tim Woodfield, who suggested forward thinking ideas on our projects, and Cesar Alcala Orozco, who it has been a pleasure to work with and a great companion and fellow in our research activities. Prof Liam Grover, who I am grateful to for hosting me in Birmingham and for useful discussions, and Megan Cooke for her patience in teaching me techniques for hydrogel preparations and osteoblasts culture. Without these collaborators, this thesis would not have been possible.

I am greatly thankful to all the people of the Bone & Joint Research Group that made the lab a fun place where to work. I must thank Dr Edoardo Scarpa and Dr Ines Moréno-Jiménez. Edo has been the one that convinced me to join the B&J lab in Southampton. He was the one that I could always count on during those first months in Southampton. Ines was so kind in spending hours with me answering my questions about working and living in Southampton during my first visit on July 2015.

I am particularly grateful to Antonio De Grazia, Catarina Moura and Miguel Queiroz de Almeida Xavier for their fellowship during these three years. Pillar and essential help in the lab has been Julia Wells. Most certainly, I would not be able to develop all the lab skills that I have now if it was not for her. I would like to thank Dr May de Andres Gonzalez for her friendship, precious help and invaluable support during difficult times through our shared passion (coffee). Above all, I had the privilege to work with two great researchers that have taught me more than I could ask. Dr Janos Kanczler has been a constant support in the *in vivo* and *ex vivo* work, being present and sharing crucial knowledge with me, he has made many experiments possible. Dr Stuart Lanham shared his precious expertise in CT and have always been available to help during all the *in vivo* studies (more than 12 weeks!). He

has been a good and fun company during long scans. Both Janos and Stuart have been essential to the writing of this thesis, proof-reading all and helping with English wording.

I am grateful to have met and co-supervised Vikash Dodhia for almost 6 months. Experiments and pints have always been fun with him. Last but not least, in the B&J group, I am truly grateful to two people: Dr Yanghee Kim and Michael Glinka. They have been, and still are, true companions in the lab and outside and I would not be writing this if it was not for them. Their help in the design of the studies with useful discussion, companionship during the experiments and unparalleled support in all aspects of my last couple of years of PhD in Southampton have been priceless.

In FEE I cannot thank more Sue Berger, for her invaluable help and Sebastian Rosini for his continuous friendship from the start of our PhD. Inestimable colleague and great friend is Dr Pedro Henrique Rodrigues Pereira, grateful to have been able to share with him the down and up sides of this journey.

Out of the lab, there are few people that have been essential for the work of my thesis. Carlo and Chiara Sabatini, Tecla and Giacomo Squicciarini have been great companions for my life in Southampton and I cannot thank them too much for their constant support. My true and inseparable friends, Guido and Valentina, have been and still are the best fellowship that I could ask for in my life. My parents, Paola and Lorenzo, my brother Emanuele and my grandmother Anna Maria, even if far away, have been a constant and caring presence in my life. Thank you for this. Finally, I owe my most sincere thanks to my wife, Chiara, which have always and undoubtedly be by my side every day. She encouraged my professional advancement and nourished my personal development. I am now happier than ever with our son Giovanni on our side.

This was and all will always be for her and for him.

Abbreviations

1α,25-OH_2-Vit D3 – Vitamin D

AA2P – Ascorbate-2-phosphate

ACS – Absorbable collagen sponges

Ad – Adamantane (Ad)

Al – Aluminium

ALP – Alkaline phosphatase

BDBM – Bovine demineralised bone matrix

BMMNC – Bone marrow mononuclear cell

BMP-2 – Bone morphogenetic protein 2

BMSCs – Bone marrow stromal stem cells

BSA – Bovine serum albumin

BV – Bone Volume

C – Carbon

Ca – Calcium

CAD – Computer-aided design

CAM – Chick chorioallantoic membrane

CaP – Calcium phosphate

CBB – Coomassie brilliant blue

CFU-F – Colony-forming unit fibroblast

Dex – Dexamethasone

DMA – Dynamic mechanical analysis

DMEM – Dulbecco's Modified Eagle Medium

DW – Deionised water

DiW – Direct writing

ECM – Extracellular matrix

EDTA – Ethylenediaminetetra-acetic acid

EDX – Energy-dispersive X-ray spectroscopy

FBS – Fetal bovine serum

FDA – Food and drug administration

FGF – Fibroblast growth factor

GAG – Glycosaminoglycan

GelMA – Gelatin methacryloyl (gelatin methacrylate)

GF – growth factor

GG – Gellan gum

GMSC – Goat mesenchymal stem cell

GUI – Graphical user interface

HA – Hyaluronic acid

HaCh – Human articular chondrocyte

HAFSC – Human amniotic fluid-derived stem cell

HAp – Hydroxyapatite

HB – Hyper-elastic bone

HBMSC – human bone marrow stromal cell

HBSS – Hank's balanced salt solution

HCEC – Human corneal epithelial cell

HCl – Hhydrochloric acid

HECM – Human bone extracellular matrix

HiPSC – Human induced pluripotent stem cell

HLC – Hepatocytes-like cells

HMSCs – Human mesenchymal stem cell

HNDF – Human neonatal dermal fibroblast

HTERT – Human telomerase reverse transcriptase

HTMSC – Human inferior turbinate-tissue derived mesenchymal stromal cell

HUVEC – Human umbilical vein endothelial cell

LAP – Laponite

LIFT – Laser-induced forward transfer

MAPK – Mitogen-activated protein kinase

MAPLE-DW – Matrix-assisted pulsed-laser

MESC – Mouse embryonic stem cell

Mg – Magnesium

MgGP – Magnesium glycerolphosphate

Micro-CT – Micro computed tomography

MSCs – Mesenchymal stem cells

Na – Sodium

NFC – Nanofibrillated cellulose

NIPAm – N-isopropylacrylamide

OCT – Optimum cutting temperature

PCL – Poly(ε-caprolactone)

PDMS – Polydimethylsiloxane

PEG – Poly(ethylene glycol)

HESC – Human embryonic stem cell

PEGDA – Poly(ethylene glycol) diacrylate

Pen/Strep – Penicillin/Streptomycin

PF127 – Pluronic (Lutrol) 127

PFA – Paraformaldehyde

PLA – Poly(lactic acid)

PLGA – Poly(lactic-co-glycolic acid)

PVP – Poly(N-vinylpyrrolidone)

ReCh – Rabbit ear chondrocyte

Ru – Ruthenium

RUNX-2 – Runt-related transcription factor-2

SCMM – Super cryomounting medium

SEM – Scanning electron microscope

Si – Silicon

SPS – Sodium persulfate

SSC – Skeletal stem cell

TE – Trypsin/EDTA

TGF-β – Transforming growth factor beta

VEGF – Vascular endothelial growth factor

W/V – weight/volume

α-MEM – Alpha modified eagle’s medium

β-CD – β-cyclodextrin

β-TCP – β-tri-calcium phosphate

Chapter 1 **Introduction**

1.1 Bone tissue and regeneration strategies

Bone is one of the most dynamic tissues in the human body, undergoing renewal and repair throughout life [1]. Skeletal tissue performs several physiological functions including structural support, as an aid for locomotion, mineral storage and a host for the marrow tissue [1–3]. Bones in the human skeleton can be distinguished between woven (disorganised) and lamellar (organised) bone deposited following primary and secondary processes, respectively [2]. Particularly, lamellar bone (Figure 1.1) can be distinguished as a dense layer (cortical) that can be found on the outer region of bone, and a less compact structure (cancellous or trabecular) mainly found in the distal portion of long bones.

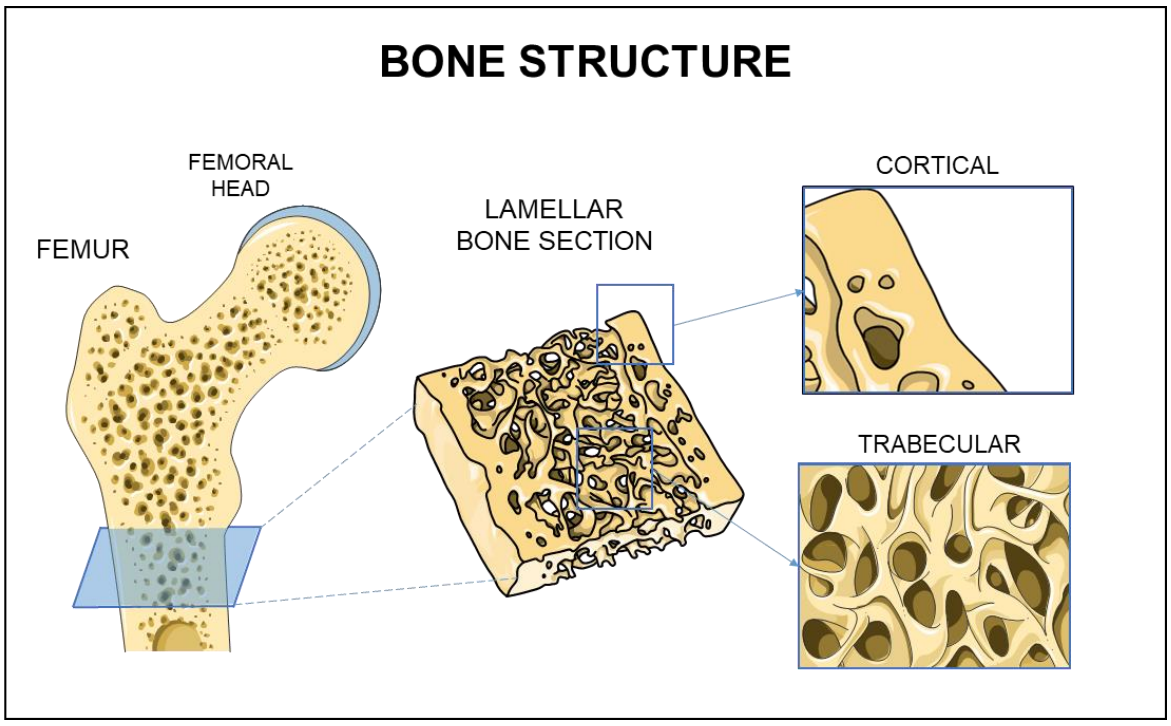

Figure 1.1. Bone structural morphology.

Schematic representation of bone architectural micro-arrangement. Femur distal portion is shown and a section is isolated to highlight cortical bone (outer portion) and trabecular bone (found in the inner core of the distal portion of the femur). Images modified and used with permission from Servier Medical Art – Creative Commons Attribution 3.0 Unported License.

1.1.1 Bone formation and remodelling, fracture and healing process

Two main ossification mechanisms are involved in bone tissue formation during embryonic skeletal development. Skeletal stem cells (SSCs) condensate in a high density structure, differentiating into i) osteoblasts to directly form bone (intramembranous ossification) or ii) chondrocytes generating a template for the future bone tissue (endochondral ossification) [4].

The fully developed adult skeleton is constantly renewed and remodelled during its life time, with approximatively 10 % of the bone undergoing turnover in one year [5]. Bone remodelling (Figure 1.2) is initiated by the attraction of osteoclast precursors, derived from osteoclast progenitors, to the remodelling site. Precursors start to condensate and differentiate into mature osteoclasts which resorb bone by acid and enzymatic degradation. Once resorption is complete, osteoclasts undergo apoptosis and osteoblast precursors are attracted to the bone site. During the reversal phase, fully differentiated osteoblasts deposit uncalcified collagenous matrix (osteoid) which will be subsequently converted into mature mineralised bone after about 10 days. In the formation process, osteoblasts entrapped in the mineralised matrix differentiate into osteocytes, which in the quiescence phase, compose the most abundant cell in the bone [1–5].

Following an initial trauma, the bone remodelling process is activated. Bone fractures (Figure 1.3 a) are repaired by a cascade of interventions that occur in the bone injury site that help the bone gap to heal without the formation of scar tissue [6]. Bone can heal via direct or indirect fracture healing [7]. Direct fracture healing is the consequence of the anatomically correct reduction in distance of the fracture ends by a stable fixation. This healing process aims to achieve direct lamellar bone remodelling, without the formation of a periosteal callus (haematoma coagulation between fracture ends). Indirect healing is a natural and common process, following both endochondral and intramembranous ossification. In contrast to the direct healing process, indirect repair is stimulated by micro-motion and weight-bearing. This process involves the formation of a callus, an inflammatory response, stimulation of angiogenesis, recruitment of SSCs, mineralisation and resorption of the callus. When the gap between the fracture ends is too large, a developed callus can undergo involution if the ends are not in contact [6]. Gap repair can be operated clinically where surgeons can fill the defect using established surgical intervention.

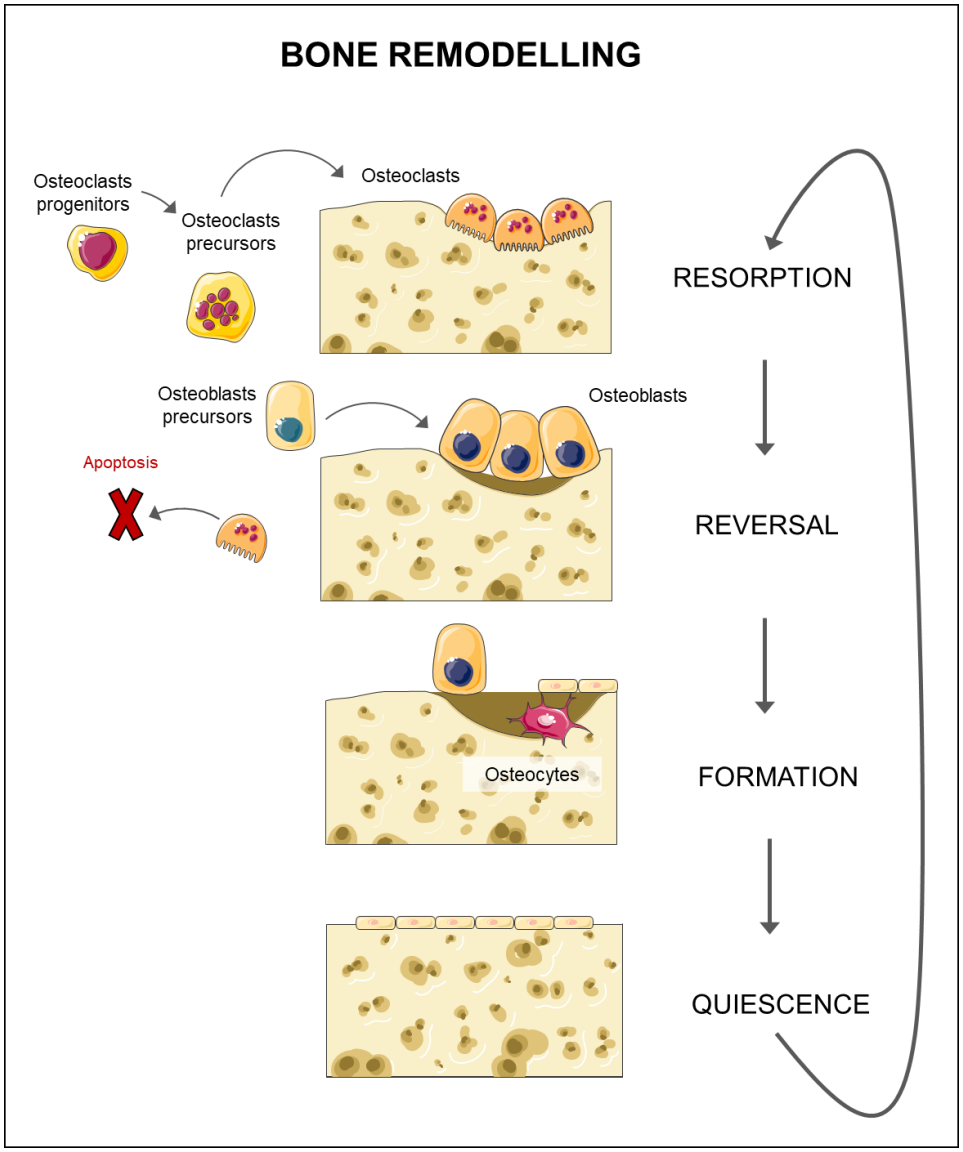

Figure 1.2. Bone remodelling cycle.

The schematic illustrates the remodelling process that is found in the bone tissue. Osteoclast progenitors attracted to the remodelling site, differentiate into precursors and the mature osteoclasts initiate tissue digestion. These cells become apoptotic once resorption is terminated. Reversal phase begins with osteoblast precursors attracted to the site and their differentiation into osteoblasts. Mature osteoblasts deposit uncalcified matrix. Cells entrapped in the matrix differentiate into osteocytes during the formation phase. The last phase is the quiescence phase when the remodelling cycle ends and the resorption phase is ready to start again when initiated. Images modified and used with permission from Servier Medical Art – Creative Commons Attribution 3.0 Unported License.

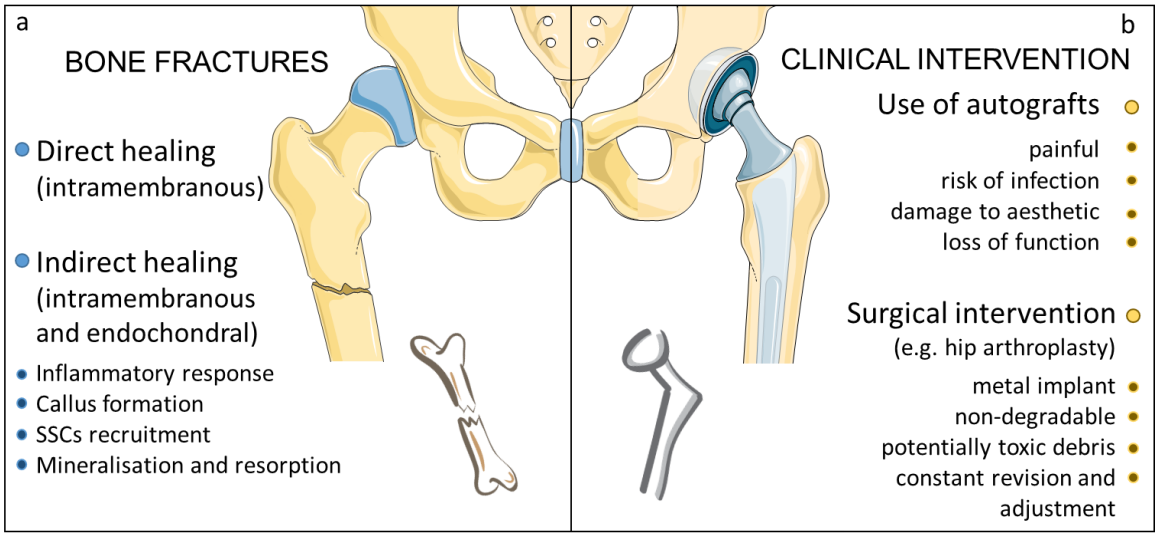

Figure 1.3. Bone fractures and current treatments.

The schematic lists (a) fracture healing processes (direct or indirect) and (b) clinical gold standards for treatment of large fractures such as hip arthroplasty. Images modified and used with permission from Servier Medical Art – Creative Commons Attribution 3.0 Unported License.

1.1.2 The clinical need for bone tissue and current treatments

There is an urgent unmet need for bone regeneration strategies as a consequence of tissue damage or failure, arising following bone fracture and loss from trauma, disease or as a consequence of aging. The cost of osteoporosis, including pharmacological intervention in the EU in 2010, was estimated at € 37 billion. In addition, the annual number of fractures in the EU will rise from 3.5 million in 2010 to 4.5 million in 2025, corresponding to an increase of 28 % [8]. Loss of skeletal tissue functionality due to injury or disease results in reduced quality of life and significant socio-economic costs worldwide. Each year osteoporosis will cost UK healthcare in excess of £ 2 billion [8]. Critical bone defects remain a significant challenge for orthopaedic repair and the gold-standard treatment remains the use of an autologous bone graft [9,10]. However, complications can be associated with the use of autografts such as painful collection, risk of infection, nerve damage and loss of function [11].

The current standard clinical approach to treat a fracture of the femoral head is hip replacement surgery (Figure 1.3 b). Thus, total hip arthroplasty is a common surgical procedure where failed bone is replaced with an implant to aid the hip-femur interplay and patient locomotion, improving the quality of life [12]. Implants are generally fabricated with hard metal or ceramic femoral heads, which are inclined to failure, rarely reaching over 25

years [13]. Subsequent revisions may require additive bone graft in order to further promote bone inclusion and reduce osteolysis. Acetabular cups, often manufactured with polyethylene may be subject to degradation, releasing 0.2-0.8 µm particles that can trigger macrophage activation with a consequent immune system reaction [14]. An increasing need for alternative solutions to autologous bone sources, non-biocompatible and non-biodegradable metal implants is thus needed [9].

1.1.3 Skeletal Tissue Engineering

Skeletal tissue engineering (Figure 1.4) seeks to target the unmet needs for new tissue for an aging population ensuring bone tissue regeneration and integration within the host, overcoming transplantation drawbacks such as rejections and donor shortage [15].

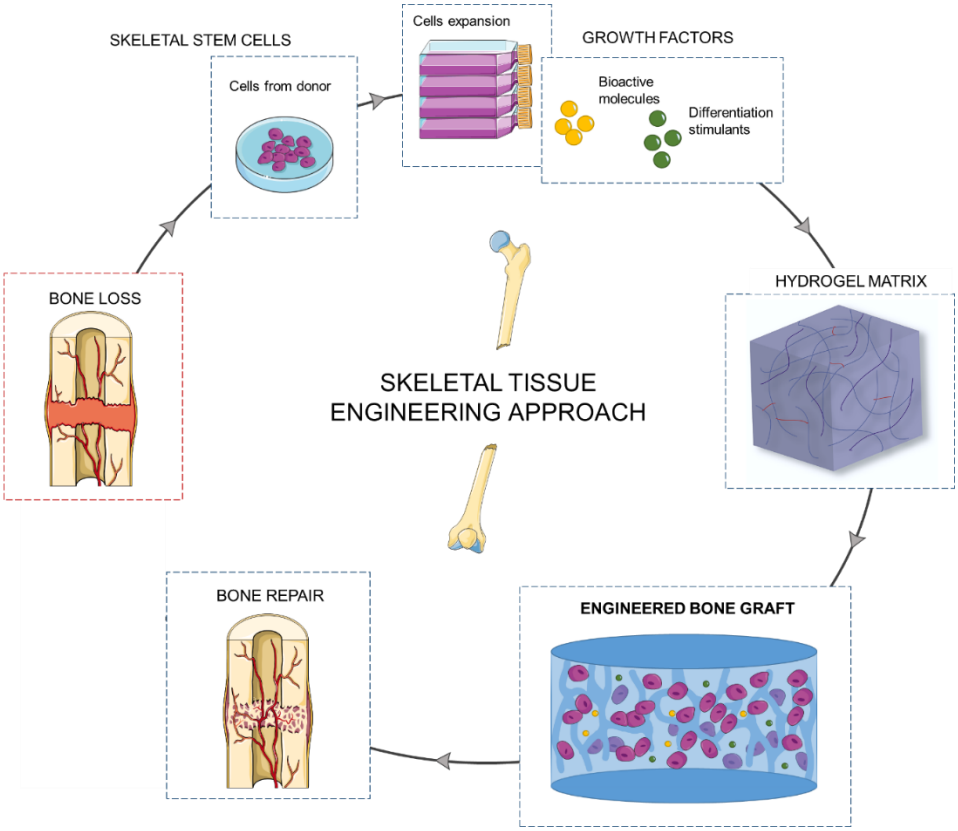

Figure 1.4. Skeletal tissue engineering paradigm.

Cells isolated from the patient are expanded and encapsulated in hydrogel matrix after inclusion of molecular signalling stimulants (growth factors). Constructs are then cultured *in vitro* or immediately implanted to aim for functional bone repair. Images modified and used with permission from Servier Medical Art – Creative Commons Attribution 3.0 Unported License.

Stem cells can be isolated from autologous sources and expanded. The inclusion of biomolecules that aid stem cell growth and differentiation (GFs, growth factors) can be combined with the cells and included in a supportive structure (hydrogel matrix) which can act as a scaffold implant. Engineered bone grafts can be implanted at the site of injury, ideally promoting osteoconduction, osteoinduction and osteogenesis [16]. In adopting such an approach, the hope is that skeletal tissue engineering constructs can overcome some of the major challenges in bone surgeries such as limited autologous bone graft and the use of non-degradable hard materials [15].

1.1.3.1 Skeletal stem cells

Stem cells are defined as those cell type which possess i) the intrinsic and unlimited capacity of self-renew in uncontrolled conditions, and ii) the potential to differentiate to form specialised cell types with a specific function [17]. In particular, skeletal stem cells are recognised as those bone marrow residing cells which can give rise to cartilage, fat and bone in defined *in vivo* assays [18–20]. This population of cells are also recognised as osteogenic stem cells, bone marrow stromal stem cells (BMSCs), mesenchymal stem cells (MSCs) and stromal precursor cells [21]. Nevertheless, the term MSC has gained popularity and is used interchangeably with the term SSCs. MSCs were firstly presented by Caplan [22] but the terminology MSC was also later extended to non-skeletal forming cells [23]. Therefore, the term SSC will be used in this work to indicate those stem cells exclusively isolated from bone marrow with the innate ability to generate all skeletal tissues. Alternatively, human BMSCs will identify the unselected population of SSCs used in the experimental section of this thesis.

A unique marker that may sort the SSCs has not, to date, been identified [24]. SSCs seeded onto tissue culture plastic are able to form independent colonies, referred to as colony-forming unit fibroblast (CFU-F) [25]. *In vitro*, SSCs have demonstrated the potential under appropriate culture conditions to differentiate into bone cartilage and adipose tissues [17]. *In vivo*, SSCs combined with bone grafts have shown to significantly enhance bone formation compared to acellular materials [26,27]. Indeed, in recent times, SSCs have been investigated in combination with scaffolds which are able to localise, retain and support SSCs *in vivo*, as an approach to aid the regeneration of large portions of missing bone tissue [28,29].

1.1.3.2 Skeletal biofabrication

Engineered bone grafts need to mimic, to some extent, the complexity of the skeletal tissue to fully support functional restoration of the structure and functionality of the organ [16]. Ideally, a scaffold for bone regeneration will be bioresorbable, highly porous, hierarchically organized in three dimensions allowing cell attachment or inclusion, proliferation and differentiation, bearing bone mechanical, chemical and physiological properties [15]. Recently, biofabrication has come to the fore in the regenerative process in providing the technology to generate such scaffolds.

The term “biofabrication” has been recently defined as *‘the automated generation of biologically functional products with structural organization from living cells, bioactive molecules, biomaterials cell aggregates such as micro-tissues, or hybrid cell-material constructs, through bioprinting or bioassembly and subsequent tissue maturation processes’* [30,31]. Skeletal biofabrication is aiming to manufacture personalised implants with highly complex architecture, shaping cells and biomaterials into constructs that closely resemble bone structures [32]. Within tissue engineering and regenerative medicine, biofabrication seeks to address unmet clinical needs such as fracture repair and the treatment of major skeletal injuries otherwise resulting in non-union, pain and a debilitating life [33]. Challenges in fabricating functional grafts of clinically relevant size include the incorporation of living cells that can survive the printing process and retain proliferative capacities and differentiation abilities in culture or when implanted [34].

In the following sections, the current technologies to produce viable cell-laden constructs will be presented, with specific emphasis on extrusion-based bioprinting technology, which is currently in use at the University of Southampton.

1.2 Cell printing: state-of-the-art

Cell printing is developing apace with input and innovation from a range of disciplines including engineering, physics, materials chemistry and biology, aiming to orchestrate tissue and organ regeneration as well as producing human-scale tissue formation [35]. Since the initial attempts to print cells [36], major advances have been achieved in the ability to deposit cells in a more accurate fashion resulting in a low percentage of cell loss. 3D printing of living cells uses computer-aided additive manufacturing approaches to position gel-like material inks loaded with cells in a layer-by-layer fashion through an automated dispensing system. Deposition is guided and controlled with an engineered program able to provide the printing system with precise pattern of movements based on the blueprint of a computer-aided design (CAD) [37].

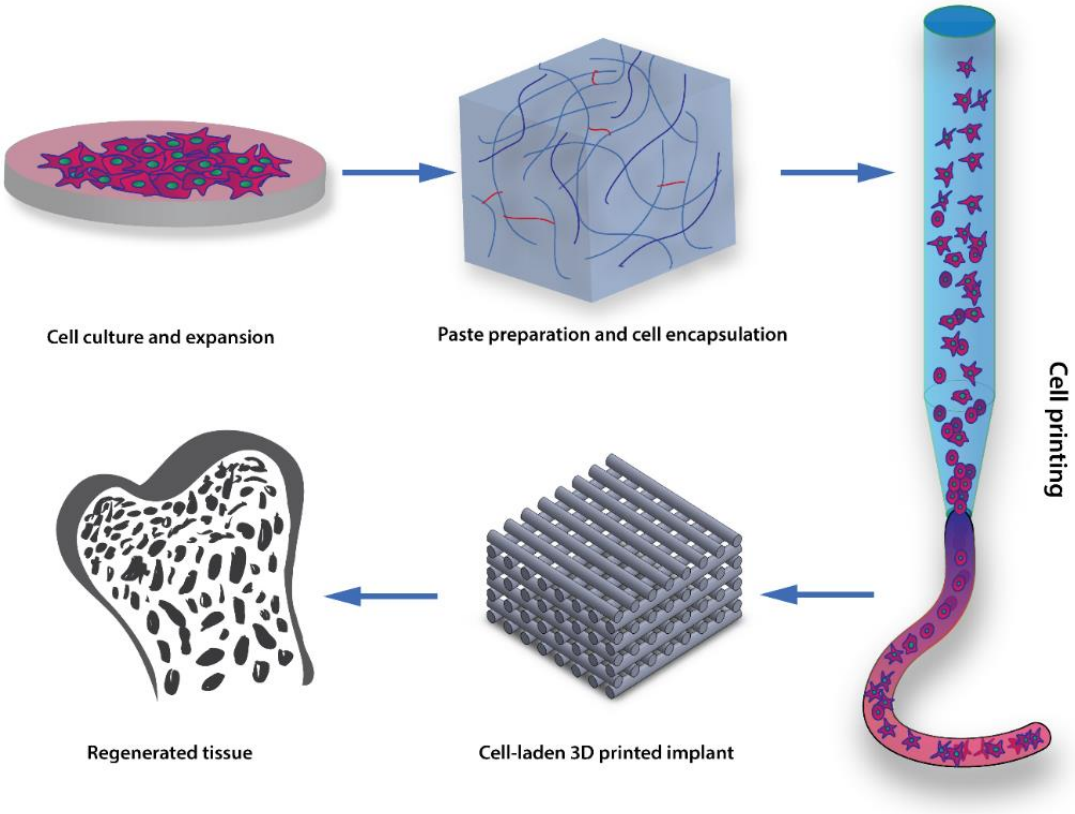

Figure 1.5. The cell printing paradigm.

Cell printing involves cell incorporation or encapsulation within biomaterials possessing viscoelastic properties that allow their use as a “bioink”. Upon printing, cell-laden 3D printed structures are fabricated with the aim, ultimately, of implantation into the patient to regenerate the specific tissue of interest.

Harnessing the biofabrication rationale (Figure 1.5), cells are isolated from donor tissue, encapsulated within polymeric matrices and printed at a resolution that matches the heterogenic components of natural skeletal tissue in the 10-100 µm range [38]. 3D printing systems have developed to try to address clinical demand, resulting in numerous techniques suitable for cell printing. The following sections describe the key cell printing technologies in current use, including inkjet [39], laser [40] and extrusion-based bioprinting [41,42].

1.2.1 Inkjet bioprinting

Inkjet-based bioprinting, first developed by Thomas Boland (Clemson University) in 2003 [43,44], is a widely employed, low cost, high speed 3D printing technology. 3D inkjet printing platforms (Figure 1.6) were firstly optimized for generating 3D constructs from a commercial 2D ink-based desktop printer in 2008 [43–46].

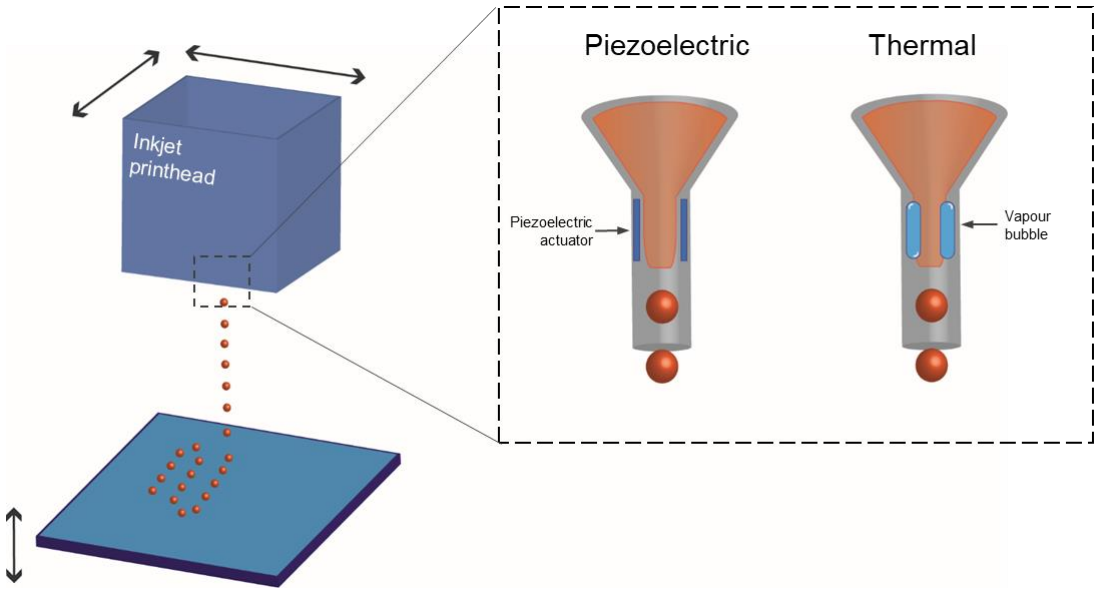

Figure 1.6. Inkjet bioprinting.

Based on desktop-printer technology, the inkjet bioprinter is able to eject drop-like cell-laden bioinks. The droplets can be deposited in three dimensions following a designed pattern. Print-head can move independently and droplets are ejected from a fine nozzle. Droplet forming mechanism using either piezoelectric actuators or thermally activate cavitation effects induced by a vapour bubble present in the nozzle.

Liquid state hydrogels can be deposited as a defined spot using electromagnetic- or thermal-induced physical displacement. The thermal or mechanical stresses employed for

extrusion purposes represent a considerable disadvantage for this type of printer. Cell density and cell death during printing represent two of the major limitations of this technology [47]. Droplets, low in cell density can be controlled with high efficiency and thus, to some extent, reduce shear stress and machine nozzle blockage. However, low cell density directly affects the tissue formation capability of the constructs. Modern inkjet printers are able to handle hydrogels in their liquid state with low viscosity given their physical droplet/jet formation. In a recent study, Gao *et al.* [48] printed human SSCs in a layer-by-layer fashion. Thus, poly(ethylene glycol) dimethacrylate - gelatin methacrylate (PEGDA-GelMA) mixed with SSCs were printed into a cylindrical construct and cultured for up to 21 days stimulating early differentiation into bone and cartilage tissues.

Although versatile and easy-to-use, inkjet cell printing technology is still, to date, not applicable to the development of human-size bio-constructs given issues with droplet non-uniformity, poor cell density, frequent nozzle blockage and physical stresses on cells (e.g. thermal and frequency shocks) [45,46].

1.2.2 Laser bioprinting

Laser bioprinting [49–53] is an effective process in preserving high cell viability following cell-deposition. This nozzle-free technique is based on laser-induced forward transfer (LIFT) physics through which cells seeded on a donor slide (covered in a radiation absorbing layer) can be safely propelled, encapsulated within droplets of biomaterial, toward a collector plate (Figure 1.7) [54]. The bio-construct droplet resolution is influenced by the biomaterial rheological properties, donor-collector system, laser energy and resolving power. Laser bioprinting approaches require specific biomaterials with defined viscoelastic properties to ensure that the biomaterial/cells constructs can rapidly gelate to ensure high-definition shape retention [52]. LIFT-based bioprinting has been reported to offer the most useful approach for two-dimensional patterning of cells, yet recent studies have shown the potential to produce complex three-dimensional constructs. Xiong *et al.* [50] applied matrix-assisted pulsed-laser evaporation direct-write (MAPLE DW) approaches to print 3D alginate-fibroblast hollow tubes. Despite the development of such a printing approach to enable a highly accurate and detailed 3D construct, the resultant printing process resulted relatively slow (6.5 mm high cellular tube printed in 45 min). In addition, cell viability, was found to be 63.8% immediately upon printing and 68.2% after 24 h. Low cell survival rate could be caused by both cell injury after printing (mechanical stress during droplet/jet formation and landing) and the requisite stationary conditions (45 min) to allow gel

crosslinking. Using a similar approach, Gruene *et al.* [49] successfully generated a SSCs graft using LIFT technology with evidence of chondrogenic and osteogenic differentiation. Hence, stem cells were able to survive the print process and retain their osteogenic differentiation capacity.

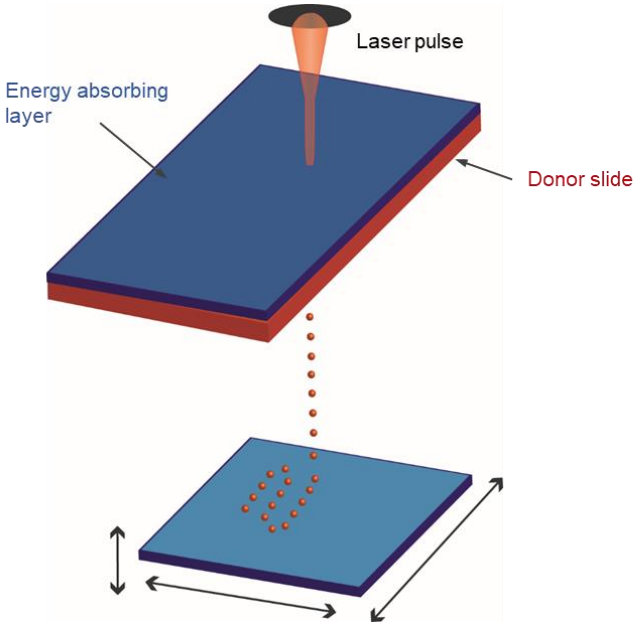

Figure 1.7. Laser bioprinting.

The printing system consists of an energy absorbing layer which is coated with a gel/resin material (donor slide). A laser pulse can be directed to a precise location on the absorbing layer which directly reflect the energy absorb to the donor slide to propel the bioink onto the depositing platform.

At present, laser-based techniques offer the possibility to print cells with low damage, although, critically, require i) specific bioink gelation properties for application, ii) expensive fabrication costs and, iii) a skilled workforce to operate the platform technology [51,52].

1.2.3 Extrusion-based bioprinting

Extrusion-based bioprinting is a widely used rapid prototyping approach able to precisely deposit hydrogels with shape retention depending on the physical and chemical properties of the biopolymer used (Figure 1.8) [55]. Extrusion-based bioprinting is currently one of the most widely employed platforms for cell printing given the advantages of ease of handling, ability to customise and versatility of the systems available [56]. This bioprinting technology typically uses post-processing curing methods or temperature-sensitive hydrogels for cell delivery. Fedorovich *et al.* [57] investigated the differentiation potential of

SSCs within organised cell-laden constructs. Cells were included within different types of hydrogels such as synthetic Lutrol F127 (PF127), matrigel, alginate and agarose. Lutrol and agarose extrusion resulted in precise deposition with a 150 µm nozzle tip, however with limited cell survival following printing in comparison to matrigel and alginate, emphasising the influence of material choice in the cell printing process. Cells can be encapsulated in modified-composite bioinks that enable shape fidelity post-printing even at low polymeric concentrations, preserving cell viability and sustaining proliferation [56].

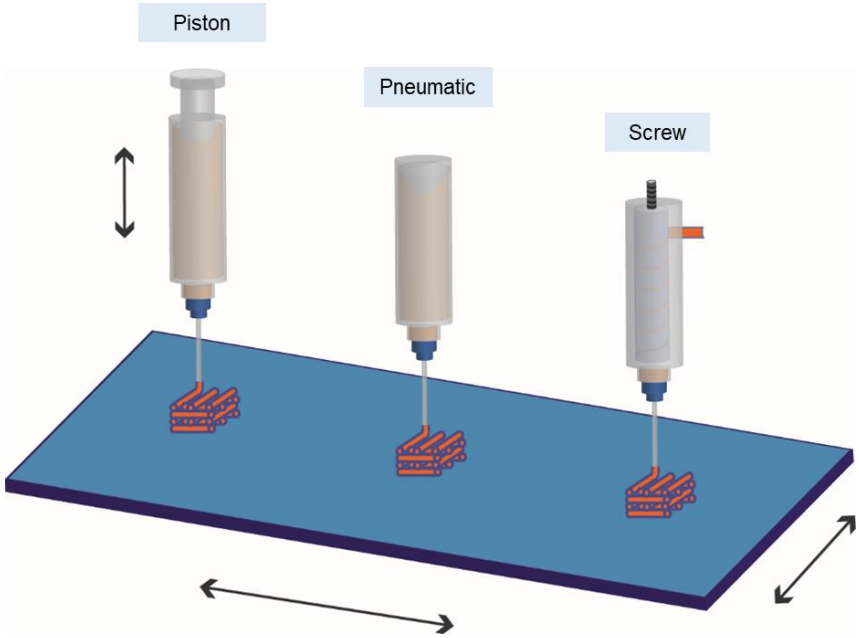

Figure 1.8. Extrusion-based bioprinting.

The extrusion technology for cell printing is based on the simple deposition of gel-like materials loaded with cells in a three-dimensional construct via layer-by-layer printing. Three principal systems are used to print biocompatible materials and can be differentiated based on the plunger that force out the bioink from the syringe. Extrusion uses a piston that is activated by either direct-mechanical (piston) or pneumatic forces. A screw guiding system can be used to extrude thermoplastic materials or to thoroughly mix the bioink while printing.

Extrusion-based cell printing remains a popular approach, given the wide versatility available in the system but still remains limited in resolution [58–60]. Nevertheless, cell printing, based on extrusion techniques, represents an exciting approach for organ printing given, i) the plethora and diversity of compatible materials that can be used, ii) the potential for cell inclusion and, iii) parameter variation available as a consequence of further modulation of printer parameters and scalability [61]. Given the extensive number of hydrogels that can be used in combination with extrusion-based bioprinting platforms, the following section details the range of hydrogel materials, their properties and applications.

1.3 Scaffolds and hydrogels for cell printing

The majority of biomaterials used in cell printing approaches are hydrogels. Hydrogels are highly hydrated, hydrophilic polymer network matrices [62]. Three-dimensional hydrogel matrices (Figure 1.9) can function as an injury site extracellular matrix (ECM) scaffold for stem cell-mediated tissue-regeneration, to deliver bioactive molecules for progenitor cells differentiation, migration and attraction to the damaged site [63]. The high water content of hydrogels can also promote nutrient diffusion and waste removal, while, manipulation of hydrogel properties can enable the rapid or prolonged release of a drug or molecule of interest [64].

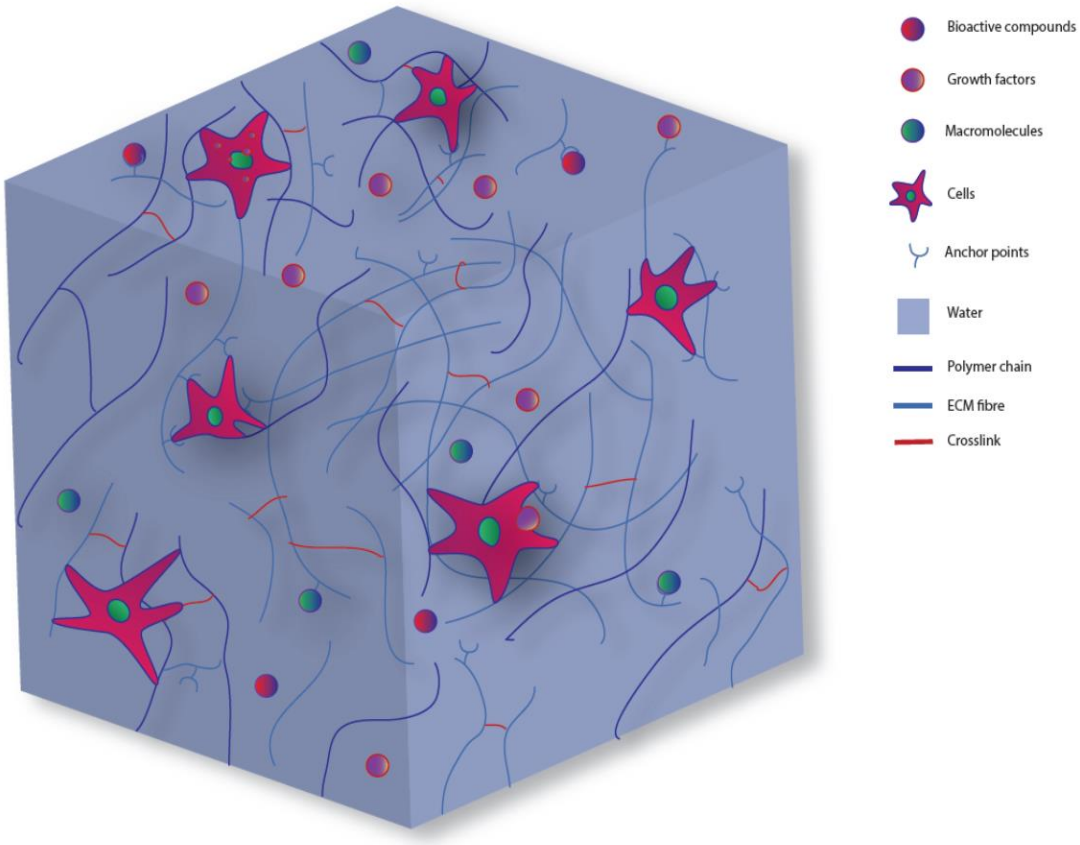

Figure 1.9. Hydrogels resembling extracellular matrix.

Polymeric cell carrier matrices need to mimic the ECM physiological environment that cells experience and sense within the human body. Cells can use filopodia extensions to attach to several anchor-like proteins within the gel matrix or interact with the polymeric chains. Bioactive compounds, growth factors and macromolecules can be included or preserved from natural tissue to stimulate cell activity or differentiation toward a specific lineage.

To be employed as a cell-encapsulation vector for 3D printing applications, hydrogels should possess specific rheological and gelation properties that can be tuned according to the 3D fabrication process [65]. The ultimate purpose for such polymeric matrices is to direct and guide tissue-specific cell lineage formation and to maintain cell proliferation and phenotype [66]. 3D printed scaffolds for tissue regeneration purposes can fabricated by three main approaches including biomaterials alone (*cell-free*), cells alone (*scaffold-free*) or a combination of the two (*cell-laden*).

1.3.1 Cell-free, scaffold-free and cell-laden hydrogel printing

Cell-free (acellular) biomaterial deposition processes, with further post-printing cell addition, remain the most common bioprinting techniques in use [67]. Although printing viscous hydrogels can enable the fine deposition of the material with subsequent cell-seeding, results from acellular approaches are far from ideal. However, recently a novel technique for direct writing (DiW) of polymer solutions via electrospinning has been shown to finely deposit microfibres in three dimensions to allow generation of 3D structures up to 190 µm thick [68]. Indeed, cell-free biomaterials extrusion of superior polymer-content hydrogels can fabricate high resolution printing compared to cell-laden approaches [69]. Nevertheless, acellular approaches still lack the requisite functionality critical for *in vivo* regeneration. Acellular implants have shown tissue ingrowth *in vivo* but with a lower degree of ECM organization compared to cell-laden 3D hydrogel implants [70]. It is important to note that post-printing seeding approaches cannot ensure the requisite cell density, cell spreading, attachment, migration and interaction both *in vitro* and *in vivo*. Acellular 3D printed constructs thus have limited capacity for cell homing, restricting the space available for post-seeded cells. Nevertheless, hydrogel-mediated seeding could represent a promising approach especially in hard tissue regeneration applications. For example, 3D printed cell-free ceramic such as β-tri-calcium phosphate (β-TCP) can be perfused with softer cell-laden hydrogels for effective cell delivery and encapsulation [62,71].

Scaffold-free approaches are promising manufacturing techniques that have been used to engineer 3D constructs exclusively using living cells and the absence of any support or encapsulating biomaterial [49,72–74]. Taniguchi *et al.* [74] used an unconventional Regenova bioprinter to build a fully functional tracheal substitute. Functional multi-cellular organoids (chondrocytes, endothelial cells and mesenchymal stem cells) were run through an array of fine needles using a computer-controlled robotic arm. The organoid printing approach results were promising when constructs were implanted *in vivo*, although not ideal

as a consequence of the high number of spheroids required (384 spheroids for 5 mm long construct), lack of structural integrity (artificial trachea resulted significantly less strong than 8-week old rat trachea) and needed 28 days for full implant maturation.

Cell-laden printing approaches can manufacture biomimetic human-like tissues with stem cells encapsulated in biomaterials able to initiate and stimulate new tissue ingrowth acting as primitive building blocks [75]. The cell-carrier hydrogels are typically doped with GFs, bioactive compounds or macromolecules to aid cell metabolism [62,76]. The hydrogel design should therefore consider both cell microenvironment and printing capabilities. High printing accuracy can be achieved due to tuned gel viscosity reducing strand failure. Nevertheless, the selected biomaterial for cell encapsulation needs to be able to be extruded with minimum applied shear force to avoid cell damage and reduce cell viability [61,77].

1.3.2 Hydrogels - limitations in cell printing applications

1.3.2.1 Natural or Synthetic Hydrogels Can Influence Printability and Cell Behaviour

Natural materials, derived from natural polymers, often convey the added advantage of cytocompatibility and the provision of natural cues to provide a favourable microenvironment for cell differentiation [78]. Synthetic biomaterials manufactured from polymers or blocks of co-polymers, typically yield more consistent and reproducible structures than natural polymers [78]. Synthetic and natural biomaterials have been employed as surfactant agents, bio-carriers and support material for several cell lines [56] and can be applied for cell printing application given their viscoelastic mechanical properties and shear thinning behaviour [56,69]. Additionally, both natural and synthetic hydrogels selected for bioprinting should demonstrate stable gelation conditions to enable even deposition and ensure shape fidelity [79,80].

1.3.2.2 Bioinks lack inbuilt mechanical support

Cell printing can generally produce stable implants but these typically, lack any tissue specific mechanical properties [81]. Support materials are often used to provide further mechanical aid to the final 3D printed tissue substitute. To address this issue, a number of groups have employed a hybrid approach, that is, the simultaneous deposition of a cell-laden hydrogel with a supportive material to generate a mechanically competent 3D printed constructs [35,82–86]. Poly (ε-caprolactone) (PCL) is a synthetic polymer often used as supporting printable materials capable of withstanding a wide range of external loads in comparison to soft and high water-content gels. However, the requisite high extrusion temperature generally makes PCL unsuitable for cell printing [87]. Even as a mechanically stable material, the hard nature of the PCL surface could result in disruption to soft hydrogels providing a non-homogenous environment for cell expansion (altered cell-surface interaction modulating cell proliferation) [35,88].

1.3.2.3 Low polymeric content hydrogels are ideal for cell printing

Hydrogel stiffness, typically correlated with percentage of polymer content, can directly influence cell survival and proliferation rates post-printing. While hydrogel viscosity can be tuned and can increase with polymer concentration [89], care is often required to ensure a cell compatible environment [69] and allow the degradation within a relevant time-frame following implantation. High polymer content hydrogels used for printing can impose higher stress on encapsulated cells than softer hydrogels. Physical stress applied on cells by a stiff hydrogel can prove detrimental for post-print cell viability. Therefore, the optimal biomaterial for cell printing should provide a balance in polymer content ensuring a soft and porous three-dimensional microenvironment where cells can be encapsulated avoiding excessive physical stresses as with high polymer materials [56,90–92]. Hydrogel physical properties such as high polymer content can influence cell survival by hindering nutrient supply and waste removal. Indeed, scaffold porosity is recognised as central to *in vivo* environments to elicit appropriate oxygenation and blood vessel ingrowth. It is well known that scaffold pore sizes can influence rate of diffusion and certain pore sizes may be optimal for revascularization (5 µm), skin (20-125 µm) and bone (100-400 µm) regeneration [38]. The specific spatial distance between cells encapsulated within deposited fibres and the outer oxygen rich regions can influence nutrient and waste diffusion [70]. However, the very nature of hydrogels, being predominantly water, can generally facilitate this exchange,

supporting cells during their proliferation process. Hence, the choice of a hydrogel system with specific physico-chemical properties is crucial for the fabrication of viable and functional constructs for skeletal repair.

1.3.3 Harnessing clay potentials for biofabrication and skeletal repair

Recent studies [93,94] have investigated the use of clay nanoparticles as a novel biomaterial for regenerative purposes. Results suggest a significant potential for nanoclays to be used, alone or in combination with other polymers to i) localise growth factors, ii) aid cell functionality and iii) ameliorate polymers physico-chemical properties [95].

1.3.3.1 Clay and nanocomposites in healthcare and regenerative medicine

Clay minerals, given their high surface reactivity (absorption, cation exchange, swelling), low toxicity, rheological properties and solubility are currently widely used as active excipients in multiple pharmaceutical and cosmetic formulations for oral and topical applications (e.g. dermatological and gastrointestinal protectors, osmotic oral laxatives and aesthetic medicine) [96–98]. Clay materials, among which smectites are a large class, are layered silicate structures crystallised in micro- or nanoparticles naturally possessing an elevated surface reactivity [99]. Nanoclays are formed by atomic subunits that contain minerals found in bone (e.g. silicate, calcium, sodium, aluminium, zinc, iron, and magnesium) [100]. Particularly, smectites structure is based on two tetrahedral silica sheets enclosing an octahedral sheet with cation (e.g. aluminium and magnesium) [101]. Elements substitution within these sheets can alter the general negative charge and tailor the swelling and delamination properties. Dilute smectites (<1 % w/v) show Newtonian flow behaviour, while concentrated dispersions (>1 % w/v) becomes non-Newtonian, with an increase of viscosity exponentially correlated with clay concentration [97].

1.3.3.2 Laponite: a new biomaterial opportunity for tissue engineering

Laponite (LAP), $Na^{+}_{0.7}[(Mg_{5.5}Li_{0.3})Si_8O_{20}(OH)_4]^{-}_{0.7}$) is a synthetic hydrous sodium-lithium-magnesium nanoclay from the smectite class [102] (Figure 1.10).

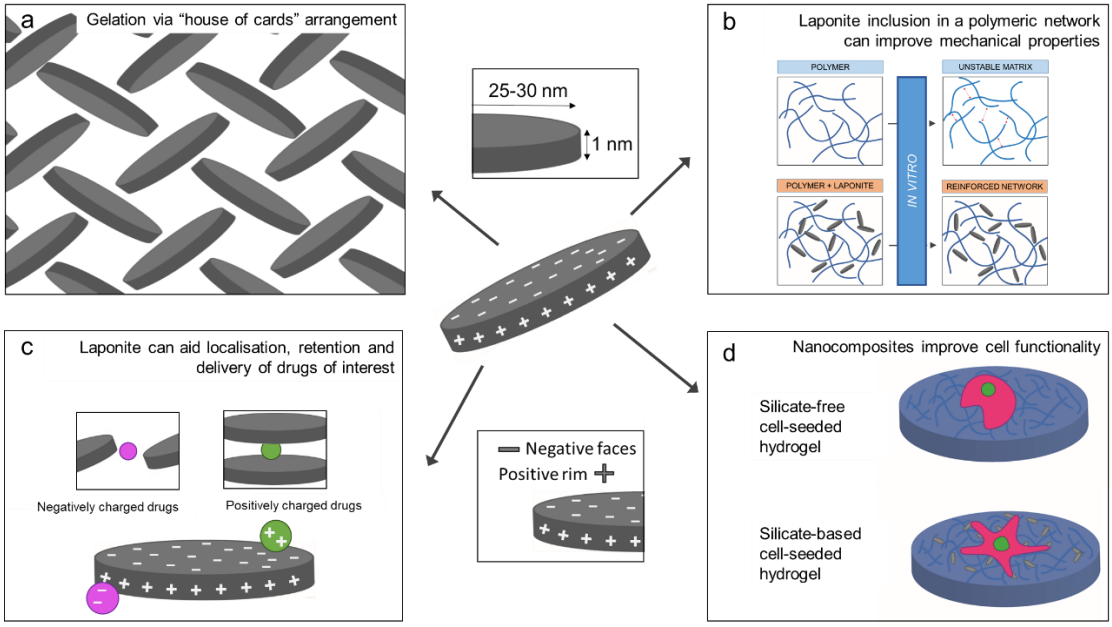

Figure 1.10. Laponite nanoclay.

Schematic summary of Laponite properties. Laponite is a nanosilicate material with a 25-30 nm in diameter and 1 nm in thickness. Laponite presents a positive rim and a negative surface charge. The clay can gelate in suspension assembling its nanodiscs in a "house of cards" (a) structure. When combined with polymeric materials (b), Laponite can alter their mechanical properties. Drugs can be loaded (c) by the combination with the positive and negative charges and their arrangements on the nanodiscs. Nanocomposites can condition (d) the cell functionality by, for instance, altering their attachment on two-dimensional surfaces.

Nanodisc particles of about 25-30 nm diameter and 1 nm thickness that have a large and highly charged surface area with a negative face charge and weak positive rim charge [103]. Face-edge opposite charge attraction allows particle aggregation forming a "house of cards" structure at the microscopic level (Figure 1.10 a). The unique LAP rheological properties such as shear-reversible, thixotropic, shear-thinning characteristics are related to this self-assembling organization of LAP in aqueous solutions. In addition, thixotropic LAP hydrogels are able to regain pre-shear physical network in a time- and temperature-dependent manner [104]. Following high shear stresses, LAP gels can recover their shape after approximately 80 min at 21°C and 20 min at 37°C. During shear-mediated sol-gel

transition, cell encapsulation can be carried out enabling cell delivery in a liquid solution that gelate relatively rapidly depending on the solution ionic concentration [94,95]. Shear properties are translated to nanocomposite materials when Laponite is included within a polymeric network (Figure 1.10 b). Physico-chemical and mechanical properties are then altered and tailored to the required application depending on the clay mass inclusion [101]. Drugs can be efficiently encapsulated and localised in Laponite gels depending on their molecular weight, total net charge and the level of interaction (attraction or repulsion) with the Laponite discs (Figure 1.10 c) [105]. Laponite integration in polymeric networks has been shown to improve the functional response of cells seeded on two-dimensional surfaces [106] or encapsulated [107] in clay-based hydrogels (Figure 1.10 d).

Both alone and in combination with several polymers, Laponite has been used for stem cell encapsulation and fate modulation, drug delivery and most recently, biofabrication. Laponite clay application for these purposes are reported in the following sections.

1.3.3.3 Laponite for stem cell encapsulation, functionality and fate modulation

Laponite nanodiscs have been shown to play a role in influencing human SSCs fate towards bone through Wnt-responsive genes and regulation of Runt-related transcription factor-2 (RUNX-2) [108]. The addition of Laponite limited human SSCs metabolism, possibly as a consequence of particle internalization, although low cytotoxicity was observed compared to other bioactive materials including hydroxyapatite (HAp). Alkaline phosphatase (ALP) activity was found upregulated in Laponite-supplemented conditioning with enhanced production of osteocalcin and osteopontin compared to classical dexamethasone addition [108]. In a recent study, Carrow *et al.* [93] reported the functional impact of clay dispersion on human SSCs identifying more than 4,000 genes and major cellular pathways (e.g. mitogen-activated protein kinase (MAPK)) influenced by cell-clay interaction. The mechanism of cell fate modulation is still unknown, but could be initiated by the degradation of Laponite in aqueous solutions followed by the release of non-toxic products such as Na^+, Mg^{2+} (playing a crucial role in integrin-mediated cell-biomaterial adhesion), $Si(OH)_4$ and Li^+ (indicated to be actively involved in the osteoinduction process) [108]. These Laponite characteristics are promising attributes in the generation of stem cell growth and differentiation microenvironments for bone tissue engineering [103].

1.3.3.4 Laponite for drug delivery

Clay-based gels have been shown to behave as a functional vehicle for drug retention and delivery with preferential clay-protein interactions [105,109]. Laponite typically interacts with molecules via cationic exchange. In addition, hydrophobic and interlamellar mechanisms play a crucial role alongside charge exchange in drug administration and localization [103]. In previous studies, Dawson *et al.* [103] showed the efficacy of Laponite as both an *in vitro* and *in vivo* drug delivery platform and angiogenesis stimulant when combined with vascular endothelial growth factor (VEGF). Enhanced network organization was observed in an *in vitro* tubule-formation assay in the presence of VEGF-coupled LAP and pre-conditioned VEGF-LAP. VEGF pre-incubated LAP showed an increase in number and volume of vessels in bone defect groups compared to controls. Gibbs *et al.* [110] reported Laponite gels functionality in association with physiological doses of bone morphogenetic protein-2 (BMP-2). Harnessing silicate sorptive capacity, BMP-2 activity was preserved and used when Laponite gels were implanted *in vivo*, showing ectopic bone formation even at extremely low dose (40 ng per scaffold) of BMP-2 (clinical dose is in the order of milligrams). An interesting use of Laponite nanodiscs assembled with sodium polyacrilate in nanohydrogel spheres for the delivery of therapeutics has been recently reported [111]. A series of sonication and PBS dispersion allowed the generation of nanohydrogels loaded with drugs. The cargo compounds were released by pH modulation from the nanohydrogel spheres and were found to successfully promote the death of HeLa and MCF-7 cancer cells.

1.3.3.5 Laponite for biofabrication

Laponite has recently gained interest as a nanofiller for biomaterials with regenerative medicine applications [95] and, in particular, as a nanocrosslinker for polymeric chains of printable bioinks [112]. The biocompatible nature, the absence of heavy metals along with its high degree of cationic exchange make this clay a suitable candidate for the enhancement of several characteristics in conventional hydrogels [113]. Rheological data collected from Laponite suspension analysis suggest that Laponite nanodiscs could be useful in cell-printing given the tuneable shear-thinning and thixotropic properties of this material [114–116]. Harnessing shear-thinning properties, the combination of Laponite with a wide library of polymers (reported in Table 1.1) is proving an attractive solution for enhancing bioinks' printability and post-printing shape fidelity. Indeed, remarkable

bioinspired 4D printing has been achieved following Laponite inclusion within nanofibrillated cellulose (NFC)-N,N-dimethylacrylamide (DMAm) or N-isopropylacrylamide (NIPAm) complexes [117]. In 4D bioprinting, progressive tuneable swelling can lead to construct shape modification immediately after printing. Mechanical properties of printed constructs can be tuned by the inclusion of Laponite. For instance, Poly(ethylene glycol) (PEG) and alginate blended with Laponite showed a stretch-relaxation reaching a 300 % strain [118]. Swelling stability of printed structures can be tailored to a specific volume augmentation (growing or shrinking in volume) depending on the concentration of Laponite silicate included in the blend [56,119]. The addition of clay has been shown to further improve the mechanical and physical properties of bioinks, but also to modulate the functionality of clay-protein interactions and entrapment stimulating the cell-laden microenvironment. However, to date, printing attempts using Laponite-based gels have resulted in non-applicable approaches for either *in vitro* or *in vivo* investigations.

Table 1.1. Nanocomposite based on Laponite clay used for conditioning cell functionality, drug delivery or as bioink for 3D printing applications.

Clay	Polymer	Cell conditioning	Drug delivery	Biofabrication
Laponite		[120]	[110]	(support bed) [121,122]
	Poly(ethylene glycol)	[123], hydroxyapatite [124]	[125], poly(lactic acid) [126]	[48], silk fibroin [127], poly(trimethylene carbonate) [119]
	poly(ethylene glycol) diacrylate		chitosan nanoparticles [128]	alginate [118,122]
	Polycaprolactone	[129]	[130]	
	Poly(ethylene oxide)	[125], chitosan [131]		
	Polyvinyl pyrrolidone		[132]	
	N-isopropylacrylamide NIPAm)	[133]		nanofibrillated cellulose [117]
	(N-acryloyl glycinamide)			[134]
	Sodium polyacrylate		[111]	
	Alginate		[135,136]	methylcellulose [56]
	Gelatin	[137]		
	GelMA	[107]		[102], K-Carrageenan [138]
	K-Carrageenan			[139]

1.4 The challenge of cell printing

The particular target tissue and organ of interest, such as bone, will define the selection of cell types required to recapitulate specific biological functions. Cell proliferation rates of the growing tissue substitute need to be tuned to provide the requisite number of cells within the constructs, while specific cell migration abilities must be considered prior to printing. Cell sources and functionality will influence cell encapsulation, as well as loading density. Furthermore, cell functionality post-printing is strongly influenced by a number of printing parameters.

1.4.1 Cell seeding-encapsulation protocols for cell printing can hinder post-printing construct functionality

Seeding porous scaffolds post-printing is a widely used approach in tissue engineering. However, uneven cell distribution produces non-homogenous oxygen gradients from the surface to the core of the scaffold leading to impaired growth [70]. Therefore, technologies such as cell printing with direct patterning and accurate positioning have been evaluated for successful human tissue replication [88].

Incorporation of cells can ensure homogeneous cell distribution compared to routine cell seeding. However, the biomaterial of choice can directly influence cell encapsulation. Thermoresponsive and thixotropic hydrogels are preferable given the hydrogel viscosity can be significantly reduced due to thermal or physical stresses, permitting cell suspension inclusion and ensuring low cell damage [140]. Indeed, significant cell death can occur even prior to printing, during the cell-loading step. Physically stronger gels can be loaded with cells with the help of mechanical methods (mixing, centrifugation or vortexing) ensuring high printing fidelity, nevertheless cell encapsulation still remains a crucial and unresolved issue [141].

1.4.2 Cell printability and printing parameters influence on 3d printed cell-laden constructs

Printability is defined by the rheological properties of the bioink [61]. Prior to printing, a rheological evaluation of the employed hydrogel is essential to understand and tune the biofabrication parameters to obtain high shape fidelity constructs [65]. However, printability is often the result of a combination of a series of evaluations that remove the beneficial use of a specific hydrogel in combination with a cell type. Mammalian stem cells, in contrast to established cell lines are, typically, particularly sensitive to environmental changes and if, for example, forced through a narrow aperture channel, their membrane integrity, capacity to differentiate and proliferate can be hampered [140,142] necessitating careful consideration of forces, printing parameters and protocols that may induce a low or high degree of cell damage after printing.

1.4.2.1 Shear-stress induces cell damage during the printing process

An understanding of the influence of external forces, including shear stress, compression, cavitation, etc. imposed by 3D printing systems on cell viability and proliferation is pivotal in the cell printing process [143]. Shear thinning (viscosity decreased by shear) and immediate gelation properties are ideal parameters for biomaterial cell-carrier selection; while extrusion of biomaterials that present shear-thickening (viscosity increased by shear) characteristics, along with unfavourable gelling mechanisms, can affect cell viability resulting in cell death and injury [140]. During bioink extrusion from a syringe nozzle, cell mechanical disruption is a direct consequence of shear, where fluid at nozzle walls undergoes shear thinning behaviour while remaining in laminar flow.

Shear stress is the specific sum of forces that impose a deformation on a material in a plane parallel to the direction of the stress. These physical forces are of particular interest in cell printing given the shear field that is present at the nozzle is believed to be the main cause of cell damage and loss during printing [61,144,145]. Blaeser *et al.* [144] investigated the shear forces that induce cell damage in a 3D valve-based printing system. By predicting and controlling shear forces applied at the dispensing nozzle, cell survival and proliferation was affected directly by forces in the range between 0.7 and 18 kPa. Shear stress doubled when a more viscous alginate solution (1.5 % w/v) was extruded. L929 mouse fibroblast cell viability when subjected to shear forces lower than 5 kPa was observed to be around

96%, and about 91% when exposed at 5-10 kPa stress. Furthermore, cell survival was dramatically reduced (76%) when cells were exposed to forces greater than 10 kPa. A number of studies have confirmed that shear stress developed within a needle tip during the printing process are the most disruptive for cells [143–146]. However, the effects of these detrimental forces can be attenuated by the inclusion of an appropriate number of cells × mm^{-3} in the bioink passing through the fine nozzle.

1.4.2.2 Cell density is essential for functionality of printed cell-laden constructs

Cell density is a crucial parameter in the development of specific tissue substitutes given the direct influence of printable hydrogel physical properties. Indeed, evidence of a reduction in stiffness of cell-laden hydrogels with an increase of cell density content have been recently reported [147,148]. The number of cells encapsulated for printing can affect multiple outcomes post-printing. Printing low-density cell-laden hydrogels can result in poor tissue integration and ingrowth construct. In contrast, deposition of a material containing a high cell density can lead to cell over-accumulation both in the print head and in a small-deposited area resulting in a reduced space for cells to proliferate and remain viable. Therefore, optimal cell concentration upon encapsulation is required before printing, due to the high percentage of cell mortality after printing that is proportional to nozzle diameter and system pressure employed.

According to the tissue of interest, the cell density employed can vary. Thus, 1-10 × 10^6 cells ml^{-1} has been found to be an optimal concentration for hydrogel encapsulation in bone tissue engineering [62,70]. Cell content can also influence strand deposition since high cell concentration in the bioink can lead to polymer relaxation or strengthen the polymer composition dependent on the material used. As shown in Figure 1.11 a, 3D printed strands that encapsulate various cell densities can lead to different outcomes in functionality. Low-density cell encapsulation (<1 × 10^6 cells ml^{-1}) will result in high cell survival due to the protective action of the bioink in which the cells are encapsulated and increase post-printing proliferation rate. Nevertheless, low cell density can result in reduced cell growth, tissue maturation and integration *in vivo*. Encapsulating at a high cell number (>5 × 10^6 cells ml^{-1}) will result in swollen and unstable 3D printed strands. Furthermore, high cell content can result in pronounced cell hypoxia, cell saturation and disruptive cell-to-cell interaction. These observations suggest the need to select the cell density to address the appropriate biological environment, for example, to facilitate cells anchorage to polymeric matrix

filaments, cell-cell interactions in three dimensions and cell proliferation within the 3D matrix.

1.4.2.3 Nozzle shape, printing orifice and pressure can directly alter printing and construct functionality outcomes

During the printing process, cells are directly exposed to a velocity gradient profile that changes according to the nozzle employed (typically a maximum intensity at the centre of the nozzle leaving a static field around the nozzle wall) and the pressure applied [145]. Therefore, printing parameters need to be adapted according to the desired bioink. For instance, blunt cylindrical nozzles are used to print with high precision, bioinks with and without cells. The cylindrical nozzle design can compromise and affect cells given the high shear stress field that is produced at the luer-lock interface of the nozzle upon printing [90]. Recently, cylindrical nozzles have been substituted with more cell compliant conical-shaped nozzles, as confirmed by recent publications [90,149] where cell viability following extrusion in both types of nozzles was investigated in relation to shear stress and polymer concentration. Printed cells appear to be less affected by shear imposed by conical rather than cylindrical nozzles, showing a 10-fold increase in cell viability when printed with nozzles of identical gauge [90,149].

As illustrated in Figure 1.11 b, different nozzle apertures can be used to print living cells. Medium size nozzle apertures (i.e. 250-500 μm) can ensure increased printing fidelity and high cell survival upon extrusion, as the extruded cells are not affected by the particular force fields that developed at the nozzle walls as a consequence of hydrogel flow. A large nozzle orifice (i.e. >500 μm) can ensure high post-printing cell survival because of the low shear imposed on the printed cells at the expense of printing resolution. Indeed, wider extrusion aperture can lead to production of imprecise and low-resolution constructs. In contrast, a nozzle with a small aperture (i.e. <250 μm) can enable printing of highly precise structures but will impose an elevated stress on printed cells during the printing process. It is thus self-evident that the same numbers of cells in small versus large nozzle environments will be subject to stress imposed by other cells and the repulsive forces from the contact with the nearby nozzle walls.

Recently, Nair *et al.* [143] quantified the short term bioprinting-induced injury experienced by viable cells upon extrusion. Cell fate and morphology were investigated according to the dispensing pressure (5, 10, 20, and 40 psi) and the nozzle diameter (150, 250, and 400μm) parameters used. The study confirmed that viable extruded cell percentage decreased with

increased printing pressure and decreased with a reduction in the nozzle aperture. Aguado *et al.* [150] used human umbilical vein endothelial cells (HUVECs) as a model to investigate the biomaterial protection effect that alginate may provide to stem cells upon needle extrusion. Upon extensional flow, linear fluid velocity can increase rapidly in the nozzle area reaching an almost 300-fold gain during nozzle extrusion causing acute cell death. Indeed, shear rate is estimated to increase during extrusion jumping from 5 s^{-1} to 26 × 10^3 s^{-1}. Interestingy, alginate hydrogel acting as a surfactant agent was found to limit damage to HUVECs induced by elevated pressure compared to cells delivered using buffer as controls.

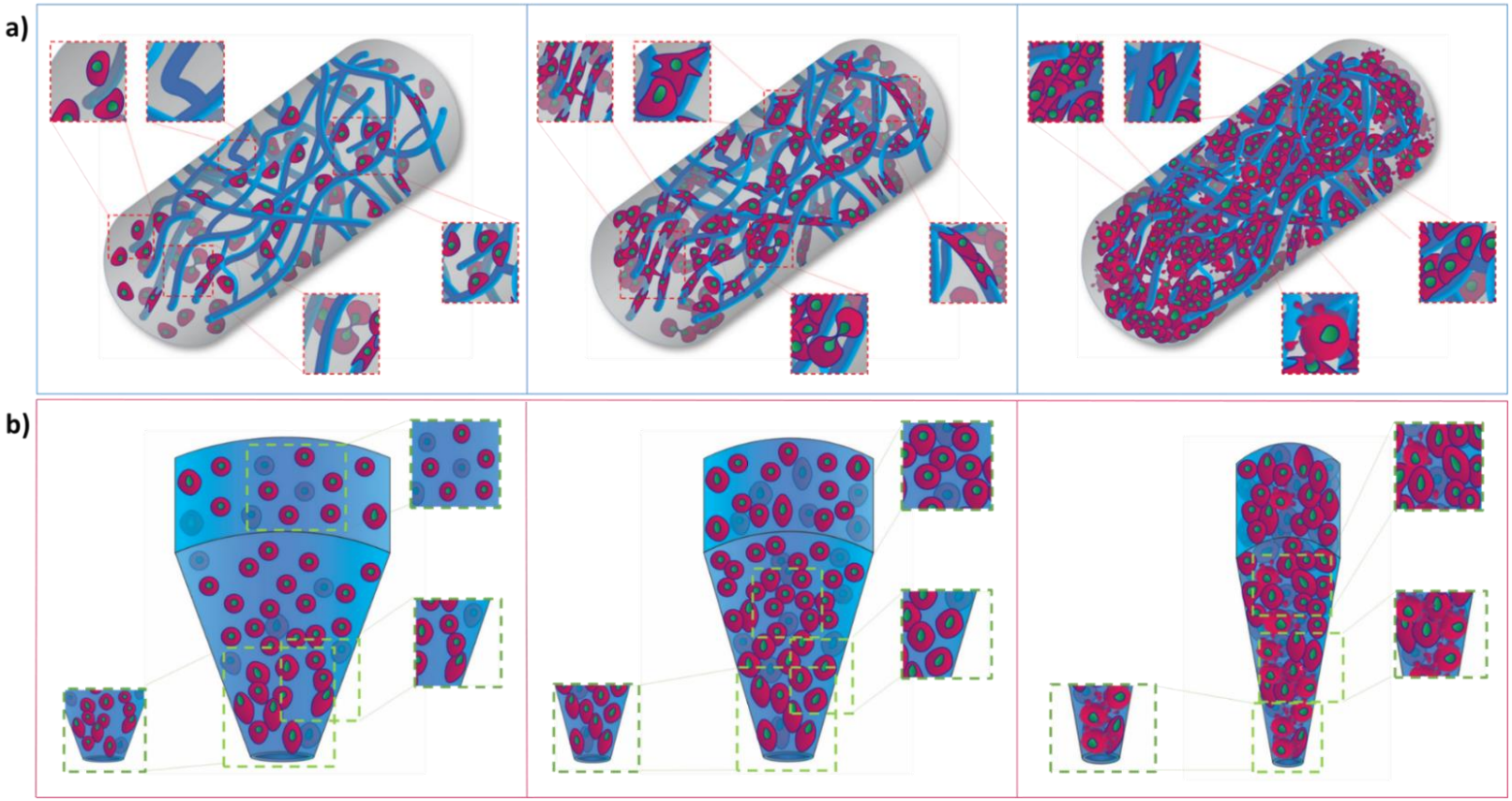

Figure 1.11. Cell seeding density influence on 3D cell-laden biomaterial strands and nozzle extrusion.
Extruded cell-laden filaments can retain a number of cells (red) proportional to the cell seeding density. Bioink polymeric chains (dark blue) concentration and distribution directly influence cell proliferation capability. A lower cell seeding density (left panel) results in poor cell distribution within the printed strand showing low cell-to-cell interaction and a limited proliferation rate. Increasing the cell seeding density (right panel) results in a printed strand filled with cells with a high degree of cell-to-cell interaction and cell death. Proliferation and viability is limited by physical stresses imposed by neighbouring cells. Cell density can be tuned to achieve an even distribution of cell encapsulated within the printed filament (middle panel) in such a way that cells can maintain the required interaction with other cells to remain mitotically active and proliferate. (b) Maintaining constant the number of cells loaded in a printing syringe but changing the nozzle aperture will affect cell printability. Large nozzles (>500µm, left panel) allow limited cell-nozzle walls and cell-to-cell interactions resulting in a widespread distribution of cells in suspension within the bioink. These settings can ensure high cell survival upon extrusion but result in low resolution of the overall construct. In contrast, narrower nozzles (<150µm, right panel) offering smaller surface area for the same number of cells force bioink encapsulated cells to interact with one another resulting in high density at the nozzle aperture. A narrow orifice can produce high resolution, as well as high cell death upon printing. Medium size conical nozzles (150µm-500µm, middle panel) ensure an optimal cells distribution within the nozzle and an increase in print resolution without extensively influencing, cell survival.

1.4.3 Printing parameters and crosslinking methods impact cell viability

A summary of the effects of principal printing parameters including printing pressure and polymer content on cell viability are illustrated in Figure 1.12. Printing pressure can negatively affect cell viability, which is directly altered when printing is carried out with a high polymer content cell-laden material, extruded at high pressure. In contrast, cells will remain viable if low pressure and low polymer content materials are employed. However, a low content hydrogel will not be sufficiently viscous to enable printing and to retain architectural structure upon extrusion.

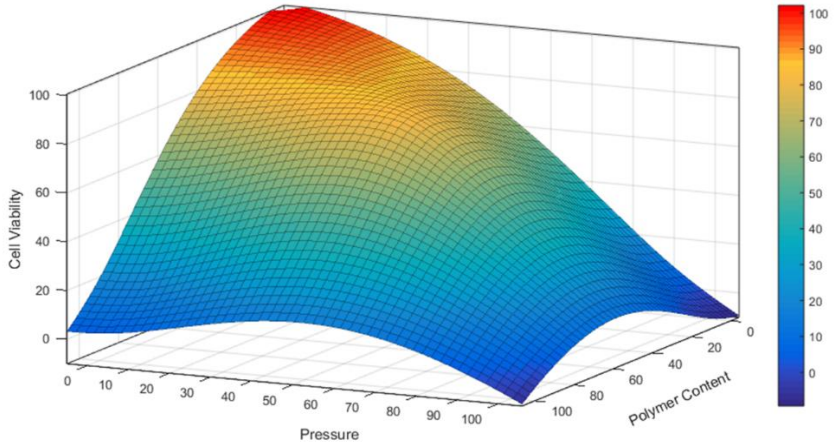

Figure 1.12. Three-dimensional diagram showing the correlation between cell viability and pressure provided by the 3D printing system and bioink polymer content.

Values listed in percentages. The highest cell viability upon printing is observed when a low polymer content hydrogel is used in combination with low pressure. Increasing polymer content and lowering extrusion pressure results in the absence of bioink deposition and reduced cell viability upon printing. High pressure and the use of a low polymer content paste for cell encapsulation produces structurally weak scaffolds. Elevated print pressure and polymer content lead to a, significant decrease and ultimately, a total loss of viable printed cells. 3D model plotted with Matlab (MathWorks, R2018a).

Thus, innovative engineering techniques, biomaterials and cell-seeding densities, are required to produce viable cell-laden scaffolds. Particularly, cross-linking of scaffolds post-printing could provide a reliable methodology for generating enhanced cell viability. Novel crosslinking and printing methods such as visible light-curing [151], secondary covalent crosslinking [152] and free-form (or free-directional) printing [153] have recently attracted interest of the biofabrication community for their mild operating conditions and elevated efficiency in producing highly stable printed structures.

1.5 Stem cell printing: current challenges in a skeletal tissue engineering approach

1.5.1 Printing stem cells to fabricate functional bone tissue

Human-scale tissue 3D printed substitutes have, to date, proved elusive. Indeed, the survival and functionality of the printed cell represents a key challenge in printing large engineered tissue grafts [35,154]. The use of stem cells has been exemplified as a key factor for human tissue regeneration, with significant potential demonstrated in the preparation of a medium to large portions of outer skin tissue [155]. Indeed, over the last few years, stem cells have been successfully incorporated into 3D printing systems allowing precise cell-patterning and development towards tissue microenvironment recapitulation (summarised in Table 1.2).

Physical forces involved in the printing process can influence the functionality of stem cell-laden biofabricated constructs [147]. It is widely accepted that skeletal homeostasis is highly influenced by biophysical signals [156,157] and mechanical cues can direct cell lineage commitment [158]. Thus, fluid flow can activate and regulate intracellular signalling cascades in human SSCs. Shear-triggered increase in calcium divalent ions mediated by MAP kinase ERK1/2 modulate cell proliferation demonstrating a direct effect of physical stresses on regulation of SSCs proliferation and death [159].

As described in “The challenge of cell printing” (section 1.4, page 23), the use of conical nozzles, low pressure values during extrusion and low polymeric bioinks, can limit stem cell damage and preserve viability after printing. However, to print human-scale tissues excellent oxygen exchange is necessary facilitated by appropriate pore connections and a vascular networks. Toward this goal Fedorovich *et al.* [70] investigated the influence of 3D printed constructs on the oxygenation of embedded cells. SSCs were embedded in highly viscous alginate solution and printed in a canonical 0°/90° grid and solid block shapes. Constructs were implanted subcutaneously in immunodeficient mice to investigate hypoxic conditioning over 3D cell-laden hydrogels. As expected, human SSCs experienced superior oxygen deprivation within non-porous constructs producing large quantities of VEGF. SSCs viability decreased considerably from day 3 to 7 when cells were embedded in 3D solid block hydrogels. Oxygenation had a particular influence on SSC osteogenic differentiation guiding oxygen-rich embedded cells towards higher ALP and collagen type I positive staining. Following *in vivo* investigations, solid implants showed unorganized tissue

regeneration with limited tissue infiltration. Indeed, scaffold porosity is recognised as a critical component *in vivo* in eliciting appropriate oxygenation and vessel ingrowth [84].

Bone repair ability has been shown to be sustained through an adequate vascular supply facilitating osteoprogenitor cells recruitment, proliferation and differentiation, gas exchange and bone homeostasis [160,161]. Kolesky *et al.* [79] reported that centimetre-scale bioprinted 3D cell-laden engineered vascularized tissues could be artificially perfused for more than 6 weeks. Complex thick vascularized tissues were created in a modular fashion printing cells-hydrogels and a silicone ink for perfusion chips. Pluronic PF127 was printed to aid network generation and then removed at 4°C leaving an optimal vasculature for HUVECs. Void interconnection between HUVECs vasculature network and SSCs-laden hydrogel was filled with SSCs and human neonatal dermal fibroblasts (HNDFs) encapsulated in a bioink. The authors showed that with an increase in cell density SSCs viability dropped proportionally to distance to the nearest blood vessel. Upon osteogenic conditioning, thick vascularized constructs were noted to differentiate into bone tissue. Furthermore, SSCs were noted to migrate towards vasculature channels suggesting the importance for oxygen exchange within relevant sized tissue.

1.5.2 Fabricating functional large constructs for critical size bone repair

In developing translational biofabrication applications for skeletal tissue regeneration, large 3D constructs at a clinically relevant scale have recently been produced. Critical size implants were fabricated via an automated assembly process [162]. The authors reported the generation of hybrid structures by prefabricating 3D scaffolds from thermoplastic materials which served as a scaffold for subsequently injected “micro-tissues” – cellular aggregates pre-cultured under osteogenic and chondrogenic culture conditions. Complex anatomically shaped constructs such as full-scale osteochondral resurfacing scaffolds could be generated and support long-term micro-tissue fusion, chondrocyte viability and ECM proteins (e.g. glycosaminoglycans (GAGs) and aggrecans) deposition *in vitro*.

A current unresolved challenge in the clinical translation of skeletal biofabrication approaches is the generation of a large 3D tissue analogues *in vivo* [79,163–165]. Daly *et al.* [165] proposed a versatile and scalable approach to direct vascular infiltration within implanted scaffolds during bone repair. A sacrificial hydrogel (Pluronic) was printed to form an intricate yet interconnected structure, before SSC-laden GelMA was cast and UV-cured

to generate a complex micro-porous structure. 3D printed structures were implanted in critical sized femoral defects in a rat model, with major vascularisation of the bone defect core region observed at 4 weeks. Such an implant design showed clear clinical potential, facilitating infiltration of a vasculature to promote and orchestrate endochondral bone regeneration.

Currently, the most advanced application of biofabrication technology to produce a skeletal tissue implant has been reported by Kang *et al.* [35] employing a multi-dispenser arm 3D printer to reproduce highly accurate human-scale implants. Two types of scaffold designs were generated. In “type I” scaffolds (mandible bone and ear-shaped cartilage), PCL materials was deposited in close contact with cell-laden hydrogels, while in “type II” (skeletal muscle) scaffolds, support was arranged mostly on the outer lateral outline and corners. For mandible and calvarial bone regeneration, human amniotic fluid-derived stem cells (hAFSCs) were co-deposited with PCL-TCP composites. A Pluronic 127 mould was utilized for the printed 3D CT-reconstruct printed mandible defect. High cell viability after 24h (91%) and calcium deposition upon osteogenic differentiation induction were detected. Ear cartilage was engineered using scanning data. Both ear cartilage and calvarial bone constructs were implanted into the dorsal subcutaneous spaces of mice, following 10 days of differentiation conditioning *in vitro.* Vascularized tissues were observed after 1 and 5 months with viable cell-laden structures resembling critical-size human organ defects, capable of inducing and sustaining tissue regeneration. This study indicated the importance of biomaterial choice, geometry and printing accuracy, together with hydrogel structure/conditioning to generate a 3D printed organ.

Table 1.2. Cell printing for *in vivo* evaluation. *Implants dimensions were not being clearly state in literature. Dimensions evaluation through image analysis have been performed.

Cell line	*Density*	*Bioink*	*Cell survival*		*Construct Size*	*In vivo*	*Printing*	*Ref.*
SSCs	*in vitro* 5×10^6 cells mL^{-1}	Alginate	d0	89%	10 layers, 1 × 2 cm, 10µm layer	mice, subcutaneous (*in vivo* 1×10^7 cells mL^{-1})	BioScaffolder (SYS+ENG)	[163]
haChs	*in vitro* 3×10^6 cells mL^{-1}							
hCECs	1×10^6 cells mL^{-1}	Gelatin-Alginate + sodium citrate	d0	94.6%	8 layers, 30 × 30 × 3.6mm, 0.8mm layer	X	custom-made	[75]
hChs	1×10^6 cells mL^{-1}	Alginate	d1	90– 94%	20 layers, 20 × 20 × 2mm, 250µm pore size, 750µm layer	X	custom-made: multi-head tissue/organ building system (MtoBS)	[83]
			d7	93.9%				
MG63			d1	90–94%				
			d7	95.6%				
MC3T3-E1	$2.3\text{-}2.8 \times 10^5$ cells mL^{-1}	Alginate	d1-7	84%	27 × 27 × 4.5 mm pore size 488µm layer Alginate: 466µm; PCL: 437µm	X	custom-made (melt pot and dispensing system)	[84]
hMSCs and gMSCs cells	$5–10 \times 10^6$ cells mL^{-1}	Alginate	porous constructs		10 × 10 × 1mm pores 0.8 mm (solid) and 2mm (porous) and 100 µm layer	mice, subcutaneous	BioScaffolder (SYS+ENG)	[70]
			d3 d7	85%				
			solid graft					
			d3	68%				
			d7	41%				
hASCs, hTMSCs and L6	1 to 5×10^6 cells mL^{-1}	decellularized extracellular matrix (dECM)	d1 d7-d14	95% 90%	*hdECM 10 × 10 × 1mm cdECM 6 × 6 × 3mm adECM 10 ×10 × 4mm	X	custom-made: multi-head tissue/organ building system (MtoBS)	[88]
hESC-derived HLCs	1×10^6 cells mL^{-1}	Alginate	d0	*hESCs 86%	not-specified	X	custom-made nanolitre dispensing system	[154]
hiPSC-derived HLCs				hiPSCs 63%				
SSCs, hNDFs and HUVECs	1×10^7 cells mL^{-1}	Gelatin–Fibrinogen (SSCs and hNDFs) Pluronic F127 (HUVECs)	d0	95% (gelatin 95°C)	725 × 650 × 125 mm, 100-410µm diameter nozzle	X	custom-made (4 independent printheads)	[79]
HNDFs	2×10^6 cells mL^{-1}	PLURONIC F127, Gelatin Methacrylate (GelMA)	d0	HNDFs 70%	*10 × 10 mm, 6 layers height	X	custom-made (4 independent printheads)	[161]
			d7	81%				
10T1 / 2s			d0	10T/12 61%				
			d7	82%				
HUVEC								
hAFSCs,	5×10^6 cells mL^{-1}	Gelatin, Hyaluronic Acid, Glycerol, Fibrinogen, Pluronic F127 as sacrificial material	d1	91%	Mandible bone 3.6 × 3 × 1.6 cm	Calvarial bone defect 8 mm diameter × 1.2 mm thickness	Integrated Tissue–Organ Printer (ITOP)	[35]
reChs,	40×10^6 cells mL^{-1}		d1	91%	Ear Cartilage 3.2 × 1.6 × 0.9 cm			
C2C12	3×10^6 cells mL^{-1}		d1	97%	Skeletal muscle 15 × 5 × 1 mm			
HepG2	1.5×10^6 cells mL^{-1}	Gelatin Methacrylamide	d0	> 97%	13 × 13 × 1-3 mm thickness, 150-200 µm layer thickness, and fibres spacing of 350 and 550 µm	X	Bioplotter Envisiontec, GmbH	[90]
gMSCs	2.5×10^5 cels mL^{-1}	Lutrol F127	*Lutrol F 127		20 × 20mm with spacing between fibres of 300 µm and 150 µm layer thickness, 210 µm nozzle	X	Bioplotter Envisiontec, GmbH	[57]
			d0	92%				
		Alginate	*Alginate					
			d0	92%				
			d1	75%				
			d3	80%				
SSCs	2×10^6 cells mL^{-1}	Alginate	d0	84%	- Not reported -	X	custom-made pneumatic extrusion-based bioprinter	[146]

Hypothesis and Aims

The overall hypothesis of this PhD thesis is that Laponite clay properties may be harnessed, in combination with several polymeric materials, to produce bioinks that can print three-dimensionally SSCs, fabricating viable and functional constructs to regenerate bone tissue *in vitro* and *in vivo.*

The project tested five different hypothesis through specific aims:

Hypothesis (I):

Laponite (LAP) can be homogenously blended with alginate and methylcellulose to aid printability. Mechanical properties can be significantly enhanced by clay inclusion along with shear-thinning characteristics, and formulations screened for printability depending on their viscosity. Cell viability can be tested up to 21 days of culture *in vitro* compared to the silicate-free control. Laponite inclusion may enhance drug retention and localisation compared to the silicate-free control.

Aims:

- To blend Laponite with alginate and methylcellulose to produce an optimal formulation for printable hydrogels with specific shear-thinning characteristics;
- To assess optimal formulation printability to produce large constructs;
- To quantify the mechanical properties of the nanocomposite bioinks and final printed constructs;
- To evaluate the long-term cell viability of encapsulated cells the after printing.

Hypothesis (II):

Laponite (LAP) clay blended with alginate and methylcellulose can be loaded with SSCs and viable constructs can be fabricated. SSCs differentiation can be stimulated *in vitro* by the inclusion of Laponite within the printed construct. Chick chorioallantoic membrane (CAM) model can be used to evaluate the potential of printed scaffolds of different sizes to

integrate with vascularised membrane. Laponite absorption capacity can be harnessed to load VEGF before implantation in CAM, HUVECs can be seeded on printed scaffold, or a combination of VEGF and HUVECs can be used to ultimately evaluate angiogenic potential *ex vivo*.

Aims:

- To use the Laponite-alginate-methylcellulose to print SSCs and fabricate cell-laden constructs;
- To assess SSCs viability and functionality when printed in three-dimensional lattice scaffolds;
- To determine the integration on the membrane and angiogenic potential of printed lattice scaffolds of different dimensions after implantation in a chick chorioallantoic membrane model;
- To investigate membrane integration and angiogenic potential of VEGF-absorbed, HUVECs-seeded or the combined effect of these after implantation in an *ex vivo* chorioallantoic membrane model.

Hypothesis (III):

Laponite-alginate-methylcellulose bioink can be used to encapsulate growth factors (e.g. BMP-2) or SSCs (e.g. unselected HBMSCs) to aid bone formation ectopically *in vivo*. Printed scaffolds can improve BMP-2 retention and bone formation compare to alginate gels. SSCs encapsulated in printed bioink can enhance bone formation ectopically in comparison with acellular bulk or printed or cell-laden bulk scaffolds. 3D printed scaffolds can promote a greater effect in bone formation, mineralisation volume and density compare to the bulk constructs.

Aims:

- To investigate the effect of BMP-2-absorbed on printed scaffolds to generate bone tissue *in vivo* after implantation in a subcutaneous mouse model when compared to silicate free-alginate gels;
- To quantify and characterise mineralised scaffolds 4 weeks after implantation;
- To evaluate SSCs-laden printed scaffolds potential to form bone tissue after subcutaneous implantation in an athymic mouse model *in vivo* when compared to cell-free and cast controls;
- To quantify and characterise mineralised scaffolds 8 weeks post-implantation.

Hypothesis (IV):

Laponite (LAP) can be combined with gellan gum (GG) to generate a mechanically improved bioink with tailorable swelling and greater printability. Cell viability and functionality can be sustained up to 21 days *in vitro* and nanosilicate inclusion can ameliorate osteogenic stimuli inducing osteogenic differentiation. Laponite can improve drug absorption and localisation within its matrix, being able to stimulate construct integration and vascular infiltration in an *ex vivo* model.

Aims:

- To blend Laponite with gellan gum (LAP-GG) and quantify the degree of swelling *in vitro*;
- To evaluate printability in air and in agarose of LAP-GG and GG control;
- To quantify viability/proliferation and assess functionality of C2C12 cells printed in agarose;
- To investigate drug analogues absorption while printing from the dispersion of the compound in agarose and consequent release;
- To evaluate integration of printed LAP-GG and GG constructs loaded with VEGF during printing in an *ex vivo* CAM model.

Hypothesis (V):

Laponite (LAP) can be blended with GelMA and visible-light crosslinking technology to synthesize a new bioink with improved printing fidelity. The use of visible-light crosslinking in combination with photoinitiators can allow continuous deposition and crosslinking of LAP-GelMA. Silicate addition can improve functionality of the cell-laden nanocomposite and in combination with drug absorption/release abilities mediated by silicate inclusion, can localised VEGF and stimulate angiogenesis *ex vivo*.

Aims:

- To mix Laponite and GelMA to synthesise and print a novel nanocomposite bioink (LAP-GelMA) with a continuous visible-light curing technology;
- To quantify viability/proliferation and functionality of encapsulated and seeded SSCs;
- To evaluate LAP-GelMA absorption and release of drugs analogues;
- To investigate VEGF-absorbed LAP-GelMA potential for CAM integration and angiogenesis.

Chapter 2 **Materials and Methods**

This chapter details the materials and methods used throughout the entire thesis. Methods specific to chapters are detailed here and linked to the relative chapter.

2.1 Cell culture

All the cell culture procedures presented in this thesis have been carried out with the culture media supplement with 10 % v/v fetal bovine serum (FBS, Lonza) and 100 U ml^{-1} penicillin and 100 µg ml^{-1} streptomycin (1 % v/v Pen/Strep). Media supplemented with 10 % FBS and 1 % v/v Pen/Strep are referred as full media. Cells were kept in humidified chamber (incubator) maintained at 37°C and 5 % CO_2 balanced air. To induce cell detachment and to collect cells prior to experiments, all cells were washed with 1× phosphate buffer saline (PBS) solution and then treated for 45 min with collagenase IV (200 mg ml^{-1}) in serum-free media, incubating the flasks at 37°C and 5 % CO_2. After collagenase solution removal, a washing step with 1× PBS was carried out followed by 1 % (v/v) Trypsin-ethylenediaminetetra-acetic acid (EDTA) (TE) solution treatment for 5-10 min in incubation at 37°C and 5 % CO_2 balanced air unless stated otherwise. Cells were allowed to detach before collection in a 50 ml Falcon tube. To neutralise the TE, the cell suspension was rinsed with a volume of full cell culture media 3× the TE solution, unless stated. The cell suspension was centrifuged at 240 G for 4 min and the supernatant discarded. The cell pellet was suspended in 20 ml of full media and cells counted in a disposable cell counting chambers (Fast Read 102 Counting slides, Immune Systems, UK).

2.1.1 Human telomerase reverse transcriptase mesenchymal stem cells (hTERT-MSCs)

This methodology is reported in Chapter 3 (3.2.6.1 – page 75)

2.1.2 C2C12

This methodology is reported in Chapter 6 (6.2.10 page 165)

2.1.3 Skeletal stem cells

Human bone marrow stromal cells (HBMSCs) were isolated from human patients undergoing routine total hip-replacement surgery with full national ethical approval and following patient consent (Southampton General Hospital) under approval of the Southampton and South West Hampshire Research Ethics Committee (Ref No. 194/99/1). Following the resection of the femoral head, the bone marrow was aspirated and transferred to a sterile 30 ml universal tube. Unselected HBMSCs were isolated from bone marrow aspirates following a standard protocol [166]. In brief, bone marrow aspirate was resuspended and washed in alpha modified eagle's medium (α-MEM) to remove excessive fat, and shaken vigorously to break any bone fragments collected during the aspiration. The content was transferred to a new sterile 50 ml Falcon tube to remove the excessive fat. The operation was repeated several times until most of the fat tissue was removed and resultant bone fragments were white indicating successful cell removal. The resulting cell suspension was then filtered through a 70-µm cell strainer to remove larger bone fragments still present in the suspension. The sample was divided into two tubes and layered at 1:1 (v/v) ratio on a density gradient separating solution (LymphoPrep™, Axis-Shield, UK). Erythrocytes, granulocytes and mononuclear cells were then separated via a density centrifugation at 800 G for 40 min at 18°C.

The bone marrow mononuclear cell (BMMNC) portion was collected with a plastic Pasteur pipette from the layer phase (buffy coat) between the LymphoPrep™ and the cell culture medium. Isolation of Stro-1$^+$ (Chapter 3) or unselected (Chapter 3, 4, 5, 7) skeletal stem cells was subsequently carried out.

For Stro-1$^+$ isolation (Chapter 3) a portion BMMNCs collected from the buffy coat were incubated for 30 min in a blocking buffer solution to reduce non-specific binding of the antibody. Serial incubations at 4°C were carried out maintaining the sample under agitation. After incubation, washes were carried out with MACS buffer. The Stro-1$^+$ fraction as previously reported [167], was collected by magnetic separation of cells labelled with Stro-1 monoclonal antibody (IgM) from mouse hybridoma and rat anti-mouse IgM microbeads. For the isolation and culture of unselected skeletal stem cells (Chapter 3, 4, 5, 7) a second portion of the BMMNCs collected were washed with α-MEM supplemented with penicillin and streptomycin by sequential centrifugation at 240 G for 5 min at 18°C. Cells were resuspended in α-MEM supplemented with 10 % v/v FBS and 1 % v/v Pen/Strep and counted in a disposable cell counting chamber (Neubauer Counting chambers, Immune Systems Ltd).

The cell suspension was plated into 175 cm^2 cell culture flasks (angled neck, non-pyrogenic polystyrene, Corning, UK) and maintained at 37°C and 5 % CO_2 balanced air for 5 days without changing the media to allow selection of the plastic adherent fraction (unselected BMSCs). Cells were then washed with 1× PBS and cultured for cell expansion with α-MEM supplemented with 10 % (v/v) FBS, 100 U ml^{-1} penicillin and 100 µg ml^{-1} streptomycin. Cell monolayers were maintained at 37°C and 5 % CO_2 balanced air. When the cell cultures were approximatively 80 % confluent, cells were passaged to maintain stemness. Cells were harvested for hydrogel inclusion and experimental protocols using collagenase IV (200 mg ml^{-1}) in serum-free media followed by 1 % (v/v) TE solution treatment. Note that all the experiments reported in this thesis were carried out using BMSCs passaged a maximum of two times.

2.1.4 Osteogenic differentiation

Osteogenic cell culture media was prepared from plain media supplemented with 10 % (v/v) FBS, 1 % (v/v) Pen/Strep, 100 µM ascorbate-2-phosphate (AA2P), 10 nM dexamethasone (Dex) and 10 nM vitamin D (1α,25-OH_2-Vit D3). Osteogenic media was prepared before media change of osteogenic conditioned samples. Unless otherwise stated, cells were transferred to osteogenic media conditions after 1 day of culture following plating and cultured for 21 days.

2.2 Biomaterial synthesis

To prepare all the hydrogels described in this PhD thesis, a deionised water (DW) at 20°C with a resistivity of 18.2 MΩ cm was used. Hydrogel materials were all prepared sterile. DW was sterilised by a 0.2 µm filter (Filtropur S 0.2, Sarstedt) sterilisation and UV irradiation for 1h. Biomaterials were all prepared by mixing in graduated beakers sterilised by a bench-top autoclave, unless otherwise indicated. A 22 min cycle at 126°C and 1.4 bar was used.

2.2.1 Laponite

Laponite (LAP) – XLG grade (BYK Additives & Instruments, UK) with the following chemical formula of $Na^{+}_{0.7}[(Mg_{5.5}Li_{0.3})Si_8O_{20}^{-}(OH)_4]^{-}_{0.7}$. To sterilise the Laponite powder, a bench-top autoclave was used. After sterilisation, the Laponite weight needed for a specific formulation (depending on the application and the polymer of inclusion) was loaded in a sterile Falcon tube under a class II sterile hood with controlled laminar flow and weighed on a precision scale. The powder was poured slowly into a beaker with sterile DW stirred at 5 G for at least 6 h with a magnetic stirrer in a class II sterile hood. Addition of Laponite powder to DW was carried out serially, adding a small portion of Laponite and leaving the suspension to stir at least for 3 hours, allowing full dispersion of nanodiscs and clearing of the gel (Figure 2.1). Depending on the formulation, a solid weight percentage (w/v) of Laponite can be included, influencing smectite dispersion and gelation kinetic. Concentrations of Laponite used in this PhD thesis range between 0.5 % w/v (5 mg ml^{-1}) up to 3 % w/v (30 mg ml^{-1}). Laponite suspension gelling at room temperature was further sterilised for 30 mins under UV irradiation.

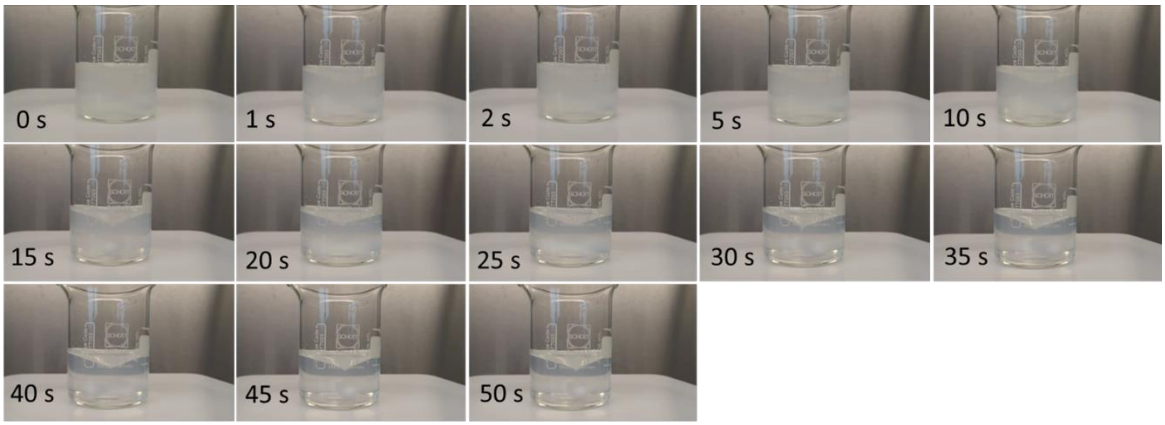

Figure 2.1. Laponite suspension.

Immediately after Laponite addition (0 s) to DW, nanosilicate particles typically result in an opaque solution. After 20 s, Laponite suspension will start to clear, demonstrating Laponite nanoparticles dispersal. By 50 s, Laponite dispersal achieved, evidenced by a water-clear solution. Laponite should be left stirring continuously for at least 3 hours to allow complete dispersion of the nanoparticles in suspension.

2.2.2 Alginate, methylcellulose and alginate-methylcellulose

Alginate (alginic acid sodium salt from brown algae, 71238, Sigma, UK) with a ratio of D-mannuronic acid (M) and L-guluronic acid (G) of 1:2 was sterilised with an autoclaved cycle. Sterile powder was weighed to the correct amount for the specific formulation. Alginate was then added to the stirring DW in a beaker under sterile conditions (class II hood). The alginate was allowed to dissolve in DW under constant stirring 5 G for 3 hours to allow complete dispersion. The final hydrogel solution was irradiated with UV light for 30 min to confirm safe sterilisation.

Methylcellulose powder (M0512, Sigma, USA, molecular weight ≈ 88 000 Da, 4 000 cP) was sterilised using a bench-top autoclave. Methylcellulose was then included in a sterile beaker with sterile DW stirring at 5 G. Dispersion was allowed for 1 h and then stored at 4°C overnight to allow complete dissolution.

Alginate-methylcellulose hydrogel was prepared starting from an alginate solution prepared as detailed above. Methylcellulose powder was then added to the alginate gel and carefully mixed in with a spatula. The alginate-methylcellulose blend was then stored at 4°C overnight to allow complete dispersion of the methylcellulose in the alginate gel.

2.2.3 Gelatin-Methacryloyl

This methodology is reported in Chapter 7 (7.2.2 page 195)

2.2.4 Gellan gum

This methodology is reported in Chapter 6 (6.2.2 page 161)

2.2.5 Human bone extracellular matrix

Human extracellular bone matrix (hECM) was prepared from modified bovine demineralized bone matrix (bDBM) synthesis protocol, reported in details in section 2.3.4 (page 48). Firstly, trabecular bone was collected from femoral head samples obtained from over 50 patients. The trabecular bone component only was isolated by sectioning the femoral head with an IsoMet® diamond saw (Buehler, USA) and using a bone nibbler. Bone fragments were collected and washed 3-4 times with 2 % Pen/Strep in 1× PBS solution. Bone chips were then snap-frozen in liquid nitrogen and crushed with a domestic coffee grinder (Krups F20342). The bone mass was measured and 0.5 M hydrochloric acid (HCl) solution was prepared accordingly. Demineralization was carried out using HCl solution at 25 ml g^{-1} and stirring of bone fragment in HCl for 24 h at room temperature. The fat was routinely skimmed off from the liquid-air interface. A 45-µm stainless steel sieve was used to filter the DBM. A DW flash wash was performed and the DBM mixture was then treated with 1:1 chloroform-methanol solution for 1 h by stirring to extract excess lipid content from DBM. Multiple methanol and DW washes were carried out. Collected DBM was then lyophilized (freeze-dried) overnight and stored at -20°C overnight.

Decellularisation was performed treating DBM material with 0.05 % trypsin and 0.02 % EDTA solution after one further DW wash. Solution was subsequently stirred in an incubator at 37°C for 24 h. A vacuum filter was used to remove any excess solution and a 1× PBS wash performed. The resultant material (referred as hECM) was stirred for 24 h at 4°C in 1 % Pen/Strep solution to remove residual cellular material. hECM was then lyophilized overnight and stored at -20°C. Digestion and solubilisation was then performed. hECM was added to 1mg ml^{-1} pepsin in 0.01 M HCl solution to reach a final concentration of 20 mg hECM/ml solution. The final suspension was then stirred for 96 h at room temperature, to provide a homogeneous solution. Supernatant collected after 830 G centrifugation for 15 min was referred to as the digest solution. Gelation was induced by neutralization of salt concentration and pH adjustment. 0.1 M NaOH and 10× PBS corresponding to one tenth and one ninth of digested volume respectively were added to mixture for neutralization. 1× PBS was then added to adjust the concentration. Procedure is outlined in the following equation (1).

$$\frac{50\ \mu l\ of\ 0.1\ N\ NaOH + 55.5\ \mu l\ of\ 10\ x\ PBS + 394.5\ \mu l\ of\ 1\ x\ PBS}{500\ \mu l\ of\ ECM\ digest\ (20\ mg\ matrix\ /ml)} = 10\ mg/ml \quad (1)$$

Pre-gelled solution was then incubated at 37°C for 1 h.

2.3 Nanocomposite bioinks synthesis and characterisation

2.3.1 Laponite-alginate-methylcellulose

Laponite-alginate-methylcellulose bioinks were all prepared in sterile conditions, by including respectively alginate and methylcellulose in a Laponite dispersion. Laponite (Figure 2.2 a), alginate (Figure 2.2 b) and methylcellulose (Figure 2.2 c) were sterilised by an autoclaving cycle. Powders were weighed under sterile conditions and stored in Falcon tubes (Figure 2.2 d) at 3 % w/v concentration each. A beaker with 20 ml of sterile DW was placed on a magnetic stirrer plate located in a class II laminar flow hood. 0.6 g of sterile Laponite powder was dispersed in DW (Figure 2.2 e) with stirring at 5 G for at least 6 h. 0.6 g of alginate were then included (Figure 2.2 f) and allowed to disperse at 5 G. After at least 2 h, 0.6 g or 1.2 g of methylcellulose was also included (Figure 2.2 f) and mixed with a sterile spatula (Figure 2.3 a). The Laponite-alginate dispersion produced a particularly viscous mixture and the methylcellulose powder cannot be thoroughly mixed (Figure 2.3 b) without physical aid. The bioink resulting from the blending of 3 % w/v Laponite, 3 % w/v alginate and 3 % w/v methylcellulose was referred to as 3-3-3. The final 3-3-3 gel resulted in a non-homogenous mixture as a consequence of undissolved aggregates of methylcellulose. The bioink was stored overnight at 4°C to allow complete methylcellulose inclusion and final homogenous bioink. For all formulations, an additional UV sterilisation cycle of 30 min was used to ensure safe sterile bioink. Gels were then used for printing, mechanical testing and cell-encapsulation purposes.

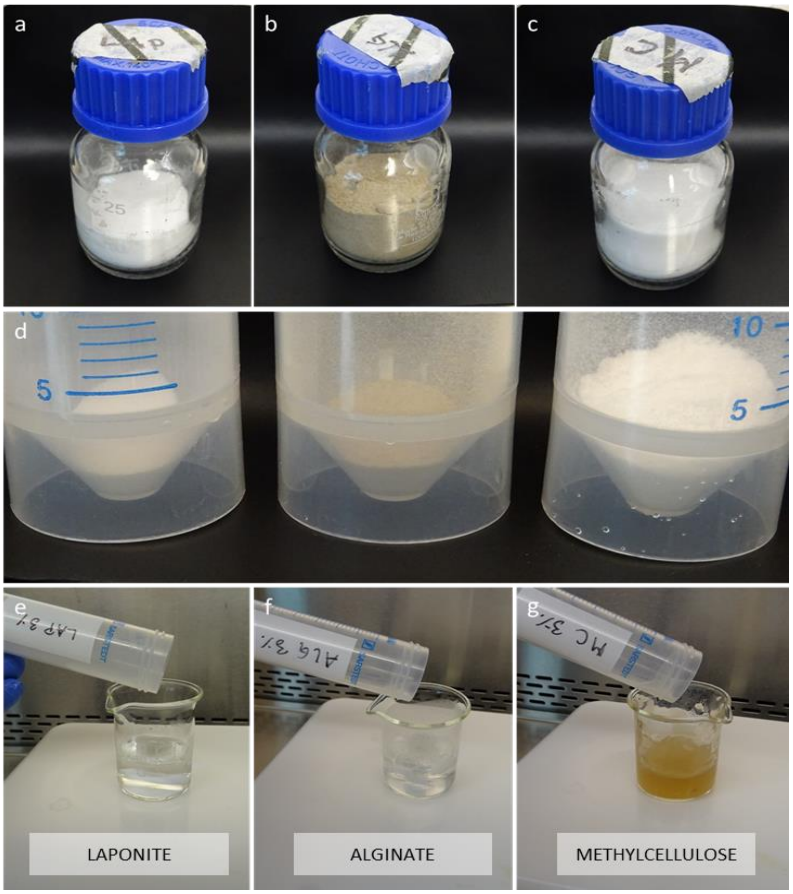

Figure 2.2. Synthesis of Laponite-alginate-methylcellulose bioink.

Autoclaved Laponite (a), alginate, (b) methylcellulose, (c) powder, loaded in glass bottles for long-term storage. (d) Laponite, alginate and methylcellulose powder loaded in sterile falcon tubes ready to be weighed. Laponite (e), alginate (f) and methylcellulose (g) serial addition to deionized water under continuous stirring.

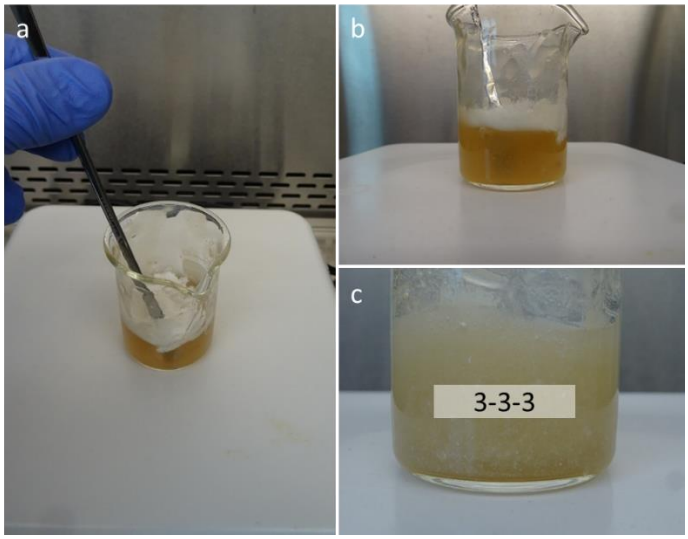

Figure 2.3. Addition of methylcellulose to Laponite-alginate suspension.

Immediately after removal of magnetic stirrer bar, methylcellulose powder can be directly mixed using a sterile spatula (a) addition of methylcellulose powder deposited on top of the suspension (b). Resultant mixture (c) after at least 1 min of stirring with a spatula, the mixture can be stored at 4°C overnight to allow methylcellulose inclusion.

2.3.2 Laponite-gellan gum

This methodology is reported in Chapter 6 (6.2.3 page 161)

2.3.3 Laponite-gelatin methacryloyl

This methodology is reported in Chapter 7 (7.2.3 page 195)

2.3.4 Laponite-demineralised bone matrix-alginate

A gel-like solution of 10 mg ml^{-1} bDBM was prepared as previously described by Sawkins M.J. *et al.* [64]. Briefly, bovine bone granules were demineralized in 0.5 M HCl (25 ml g^{-1} bone) at room temperature for 24 h. Bone particles were suspended in acid while stirring at 5 G. Samples were filtered under vacuum and rinsed in DW. Excess lipids were extracted using chloroform/methanol at a 1:1 ratio for 1h and finally rinsed in methanol and then in DW. Samples were snap frozen and lyophilised to allow storage at -20°C. Lyophilized bDBM was added to 1 mg ml^{-1} pepsin in 0.01 M HCl to give a final suspension of 10 mg ml^{-1} matrix concentration. Alginate (alginic acid, sodium salt, Acros Organics) hydrogel was synthesized through a canonical method by dissolution in DW and continuous mixing without pH alteration. Calcium chloride ($CaCl_2$, >93 % granular anhydrous, Sigma Aldrich) was used post-processing to enable alginate crosslinking.

2.3.5 Rheology

Viscosity of the bioink formulations was measured at constant and increasing shear rates, using a plate rheometer (Rheotest RN 4, Germany or MCR 102, Anton Parr, UK) with a plate-plate distance of 0.1 mm. Non-crosslinked bioinks and their individual components were tested to prove printability. A constant shear rate of 10 s^{-1} was applied, and the

viscosity was measured over time. An amplitude sweep test was carried out to identify the viscoelastic region. The storage and loss modulus were measured over the percentage increase of shear strain. Additional tests are detailed in Chapter 3 (3.2.4 page 74)

2.3.6 Mechanical tests

This methodology is reported in Chapter 3 (3.2.5.3 page 75)

2.3.7 Mass loss and swelling ratio

This methodology is reported in Chapter 6 (6.2.5 page 163)

2.4 Extrusion-based 3D printer: settings and scaffold printing

2.4.1 Bioprinter

A 3D printer built in-house and previously employed for ceramic paste extrusion [55,58,168,169] was adapted to print low viscosity biomaterials and stem cells. The novel bioprinter is represented in Figure 2.4. Printer adjustments consisted in i) table levelling, ii) Z-axis re-structuring, iii) custom-made insulated chamber equipped with UV lamp and sealed doors (to provide adequate sterile environment for cell printing) and iv) coding of new printer input codes. The extrusion-based bioprinter (Figure 2.4 a) was entirely operated by computer-aided motion control (Figure 2.4 b) and was purposely designed to enclose a sterile printing area (Figure 2.4 c).

Figure 2.4. Bioprinter.

The bioprinting system is housed in a vertical enclosed structure (a) that supports the inner mechanism. The outer scaffold frame is covered with corrugated polypropylene insulating sheets. A computer is housed in the lower portion of the printer and controlled by input/output devices (mouse, keyboard and screen) positioned on the front part of the printer (b). The printing area (c) is located on a levelled table and positioned on the central portion of the surface to allow easier levelling. The piston attached to an arm is arranged in a central position to disperse the load on the outer frame.

The bioprinting extrusion system (Figure 2.5 a, b) comprises automated motion control (6K4 motion controller, Parker Hannifin Automation, UK) that can be used to drive motors for X-Y-Z axes and extrusion (pressure). Motion control drives three linear servo motors (XY table and Z axis, YASKAWA, 200W, Micromech Ltd, Essex, UK) and a stepper motor (50,000 steps/rev, Micromech Ltd, Essex, UK) that manoeuvre a fine pitch ball screw converting revolution to linear speed. 100-1 reduction gearbox is employed to decrease stepper motor speed enabling a fine displacement. The upper extrusion motor finely drives the lead screw revolution through a speed reduction gearbox and a load stage press against syringe plunger provides biomaterial paste extrusion. A cell able to read force measurements is located on the load stage to register the force needed for the bioink extrusion. Force measurements are converted in Newtons (N). Three-dimensional printing is the result of Z stage and XY table computer-controlled movements.

The printer was housed in an enclosed cabinet to ensure a sterile environment for printing. Black corrugated polypropylene sheets (4 mm thickness, The Plastic Shop, UK) were used to build the cabinet with fitted doors with clear Perspex positioned for easy access to the printing area. Rubber seals (Bosch Rexroth, UK) were used to prevent rapid heat and air exchange between inner and outer space. Visible and UV light were set in place to visualise and sterilise printing area respectively.

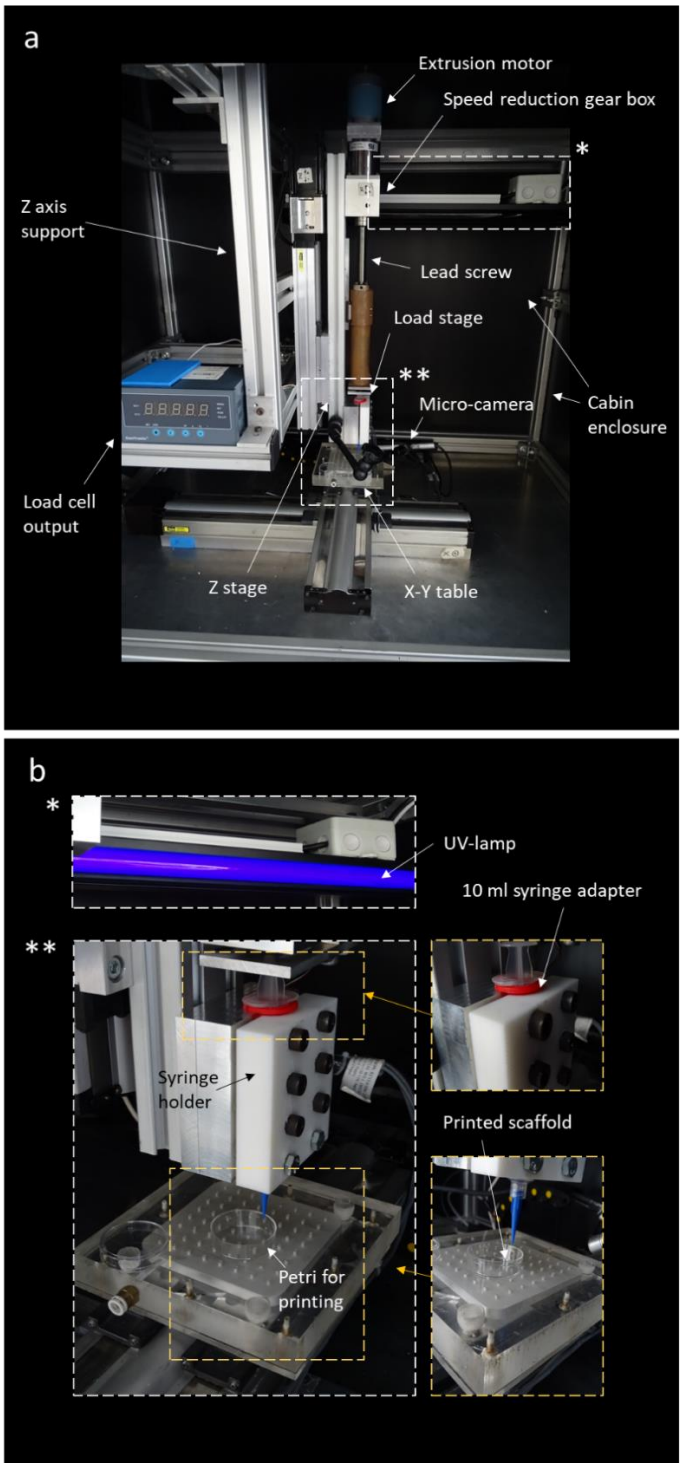

Figure 2.5. 3D extrusion-based printer main setup.

The main printing area (a) is enclosed by a series of propylene sheets and is composed by several moving parts all guided via series of softwares. An X-Y table is fixed onto a series of two motorised axis (X and Y) which controls the movement of the printing bed. The Z stage is mounted on support that house a further axis, moved by an independent motor. On the Z stage is attached an extrusion motor that move, aided by a speed reduction gear box, a lead screw pushing or retracting a load stage that is responsible for the extrusion. The printing area can be monitored by a micro-camera. The area dedicated to the bioink extrusion is sterilised with a UV lamp (*) housed on top of the printing table. The printing process can be carried out on a small portion (**) of the printing cabin where a syringe is fixed in place by a 3D printed holder and an 10 ml syringe adapter – which can be replace with a smaller fitting to include 1 or 5 ml syringes. Printing was carried out in a petri dish located on the X-Y table.

The printing process was entirely controlled using a personal computer and a series of programs (Appendix A Figure 2.1). CompuCam 1.4 (Parker Hannifin Automation, UK) was used to translate CAD files into motion planner language commands and paths (Appendix B Figure 2.2). A 2D structure was drawn by Solidworks software (Software Dassault Systèmes SolidWorks Corp.) and converted into 6K4 Parker language, which is red by the Motion Planner software (Parker Hannifin Automation, UK). The 6K4 code was then imported in LabVIEW custom-made programme into a series of block diagrams (Appendix B Figure 2.3 – 2.11), which represents the base of the programme used for controlling the printer. The frontal panel contained a friendly graphical user interface (GUI) designed with LabVIEW 8.2 (Laboratory Virtual Instrument Engineering Workbench, National Instrument) which is illustrated in Figure 2.6. This LabVIEW program was able to independently control the printing hardware by continuous interaction with the Motion Planner software.

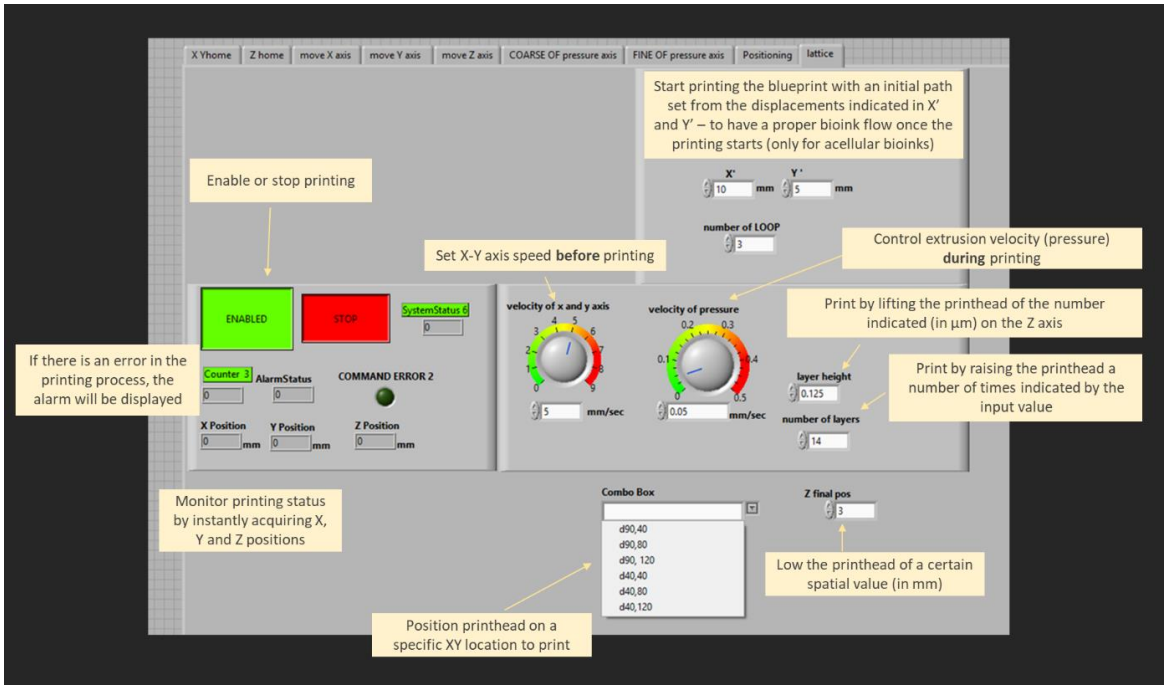

Figure 2.6. Front panel of GUI developed in LabVIEW to control extrusion-based process.

The “lattice” panel allows the user to enable or stop the printing process, closely monitoring the correct functionality of the system with alert system feedbacks. The user can initially set the velocity of the X-Y table and control the extruding pressure during biomaterial deposition. Other parameters that can be set before starting printing are the number of layers, the layer height and the final position of the print head. A tool for precise extrusion of the biomaterial hydrogel is included in the GUI. The printing process can be initialised by the printing of a 0/90° lattice portion that is independently set by the value in displacement along the × (X’) and Y (Y’) axis. The repletion of such lattice path can be set by changing the value in the ‘number of loop’ section.

2.4.2 Acellular scaffolds printing

Scaffolds produced in this thesis were all printed with the in-house built bioprinter reported in paragraph 2.4.1 (page 49), with the exception of Chapter 3 - here a Bioscaffolder 3.1 (GeSiM, Radeberg, Germany) was used, kindly provided by Prof Michael Gelinsky. Acellular printing was carried out using bioinks prepared under sterile conditions.

2.4.2.1 Laponite-alginate-methylcellulose

The 3-3-3 bioink was used for scaffold fabrication. The bioink was loaded in a 10 ml syringe and extruded through conical plastic needles with an inner diameter of 410 µm using compressed air (air pressure: 80–95 kPa) or piston-driven force (25 kN). 3D printing was conducted in air using a Bioscaffolder 3.1 (GeSiM, Radeberg, Germany) for the work reported in Chapter 3, and using a bioprinter reported in Chapter 2 (2.4.1 page 49) for the work illustrated in Chapters 4 and 5. Scaffolds were printed in different dimensions. If not separately detailed within this PhD thesis, scaffolds were printed at 10 × 10 mm^2 with an alternating layer pattern (ABAB, 0°/90°), a layer height of 230 µm and a strand distance of 2 mm. After printing, scaffolds were incubated for 10 min in sterile 100 mM $CaCl_2$ solution to enable crosslinking.

2.4.2.2 Laponite-gellan gum

This methodology is reported in Chapter 6 (6.2.9 page 165)

2.4.2.3 Laponite-GelMA

This methodology is reported in Chapter 7 (7.2.4 page 196)

2.4.3 Fabrication of cast hydrogel discs and films

2.4.3.1 Laponite-alginate-methylcellulose

The methodologies are described in Chapter 5 (5.2.5.1 page 124)

2.4.3.2 Laponite-gellan gum

The methodologies are described in Chapter 6 (6.2.14 page 166 and 6.2.16.1 page 167)

2.4.3.3 Laponite-GelMA

The methodologies are described in Chapter 7 (7.2.6 page 197 and 7.2.10 page 198)

2.4.4 Acellular cast and printed scaffold stability, swelling and printability

2.4.4.1 Laponite-alginate-methylcellulose

This methodology is reported in Chapter 3 (3.2.5.1 page 74 and 3.2.5.2 page 74)

2.4.4.2 Laponite-gellan gum

This methodology is reported in Chapter 6 (6.2.9 page 165)

2.4.5 Printed and cast scaffolds microscopy

2.4.5.1 Laponite-alginate-methylcellulose

This methodology is reported in detail in Chapter 3 (3.2.5.1 page 74)

2.4.5.2 Laponite-gellan gum

This methodology is reported in detail in Chapter 6 (6.2.7 page 164)

2.4.5.3 ECM gels

Scanning electron microscopy (SEM; FEI Quanta 250 FEG, operated in SEM mode) at a voltage of 5 kV (spot size 3) was used to image ECM gels. Prior to SEM, 100 µl samples were dehydrated with a freeze-drier (Lablyo Mini, Froze in Time Ltd., UK) for 12 h and coated with platinum (Q150TES, sputter coater, UK).

2.5 Fabrication, culture and characterisation of cell-laden scaffolds

2.5.1 Encapsulating cells in cast hydrogels

2.5.1.1 Laponite-alginate-methylcellulose

This methodology is reported in detail in Chapter 4 (3.3.8 page 86, 4.2.3 page 99, 5.2.6.1 page 126 and 5.2.6.2 page 127)

2.5.1.2 Laponite-GelMA

This methodology is reported in detail in Chapter 7 (7.2.8 page 198)

2.5.2 Seeding cells on lattice scaffolds and 2D films

2.5.2.1 Laponite-alginate-methylcellulose

This methodology is reported in detail in Chapter 4 (4.2.5 page 100)

2.5.2.2 Laponite-GelMA

This methodology is reported in detail in Chapter 7 (7.2.10 page 198)

2.5.3 Pre-labelling of cells before printing

Cells were suspended at a density of 1×10^6 cells ml^{-1} in serum-free culture medium. Vybrant® DiD (Cell-Labeling Solution, V-22887, Molecular Probes) was then added to the cell suspension. A 5 µl solution of DiD was supplied for each ml of cell suspension (e.g. 25 µl of DiD in 4.975 ml of cell suspension) and mixed by pipetting. Cell suspension supplemented with DiD was incubated for 20 min at 37°C. A centrifugation cycle at 470 G for 5 min was subsequently carried out. The supernatant was removed and the stained cell pellet resuspended in warm serum-free culture media. This washing step was carried out two further times. Cells were then ready to be included in bioinks and printed.

2.5.4 Viability and proliferation in cell-laden discs and printed scaffolds

Viability was quantified from confocal images taken after 1, 7, 14 and 21 days of culture *in vitro*, if not stated otherwise. Samples were first collected and washed twice with 1× PBS. Calcein AM (C3099, Invitrogen, Thermo Fisher Scientific) was diluted in serum-free culture media (0.6 µl per 1 ml of media) and added to each cell-laden scaffold. The scaffolds were then incubated at 37°C and 5 % CO_2 balanced air for 1 h. A repeated wash with 1× PBS was then carried out. Samples were imaged using a confocal scanning microscope (Leica TCS SP5, Leica Microsystems, Wetzlar, Germany). Cell images for viability were pre-stained with a lipophilic dye (DiD) (coloured red) as described in 2.5.3. Calcein AM (abs/em - 488/520 nm) is metabolized in living cells to form a bright green fluorescent product that accumulates in the cytosol. DiD (abs/em – 644/665 nm) is a permanent dye that binds lipoproteins on the cell membrane and is transmitted to daughter cells. As metabolic (living) cells were coloured by both stains, while non-metabolic (dead) cells were only stained by DiD, a differentiation of living compared to all cells was possible. Quantification of living cells was performed by comparing both, the number of Calcein stained cells and DiD stained cells in the Z-stacks of 15 pictures per time point (n=3). Counting was performed with the 'Analyze Particle' tool of ImageJ (1.44p, National Institutes of Health, Bethesda, Maryland, USA). To avoid artefacts of fluorescent Laponite, cell sizes were evaluated to be in dimensions of 20-600 pixel.

Cell density within the scaffolds at different time points was calculated by further analysis of the confocal pictures. Z-stacks were collected of different heights. Therefore, a calculation by normalisation of the number of living cells and the volume of interests was carried out. The resulting value was converted into percentage and plotted with reference to the value corresponding to day 1 (set as 100 %).

2.5.5 Alkaline phosphatase staining

ALP staining was performed on samples cultured *in vitro* and conditioned with basal (full cell culture media) or osteogenic (formulation reported in section 2.1.4, page 42). Media was removed and samples washed two times with 1× PBS. Samples were fixed in 95 % ethanol for 10 min. The ethanol solution was removed and samples washed two times with 1× PBS. The cell-laden and cell monolayer cultures were left to dry for 10 min. In the

meantime, 9.6 ml of DW were mixed with 400 µl Naphtol (AS-MX Phosphate Alkaline Solution, 85-5, Sigma, UK). Fast Violet Salt (F1631 Sigma, UK) was then weighed and 0.0024g were added into the DW-Napthol solution and mixed thoroughly by pipetting. The solution was then pipetted onto samples, which were incubated at 37°C for 1 h. The reaction induced a change of colour in cell-laden scaffolds and cell monolayers controls to red if ALP expression was present. Reaction was then stopped by 1× PBS dilution of the staining solution. Samples were stored at 4°C overnight and imaged with Zeiss Axiovert 200 (Carl Zeiss, Germany) the following day.

2.6 Proteins and growth factors absorption and release

2.6.1 BSA and VEGF loading and release

This methodology is reported in Chapter 3 (3.2.7.1 page 76 and 3.2.7.2 page 76)

2.6.2 BSA and lysozyme absorption and release

Bovine serum albumin (BSA, Sigma-Aldrich) and lysozyme (lysozyme from chicken egg white, lyophilized powder, protein ≥90 %, ≥40,000 units/mg protein Sigma-Aldrich) were solubilised in Hank's balanced salt solution (HBSS, Thermo-Fisher) at 100 µg ml^{-1} and 10 µg ml^{-1} respectively. To correlate the effect of silicate inclusion on the absorption capability, nanocomposites and silicate-free gels were studied. Before absorption, scaffolds were fabricated as indicated in section Chapter 6 (6.2.14 page 166) and 7 (7.2.11 page 199). Absorption and release protocol is shown in Figure 2.7.

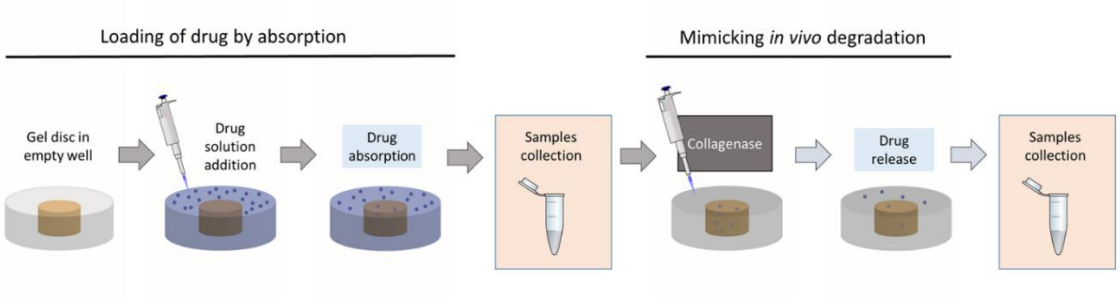

Figure 2.7. Drug absorption and release study.

Fabricated scaffolds were placed in empty wells of a 24-well plate. Drug solutions were added and absorption carried out for 1, 2, 4, 8 and 24 h. Samples were collected. Collagenase solution was added to induce the release of the absorbed drugs. Supernatant was collected. Readings were performed on a microplate reader along with standards for absorption-release kinetic curve preparation.

Cast discs were placed in a 24 well plate. Drug solution was inserted in the well. Scaffolds (n=3) were soaked in BSA or lysozyme solutions for 1, 2, 4, 8, and 24 h. Supernatant (150 µl) was collect to analyse absorption. BSA and lysozyme solutions were replaced with collagenase D (from *Clostridium histolyticum*, Roche Diagnostics GmbH) at 24 h to simulate release in an *in vivo* condition. Samples (150 µl) were collected (n=3) and readings carried out at 1, 2, 4, 8 and 24 h after collagenase addition. Standard curves were prepared using free BSA and lysozyme in HBSS. BSA standards were prepared from 0, 10, 20, 50, 100 µg ml^{-1} solutions. Lysozyme standards were 0, 1, 2, 5, 10 µg ml^{-1} samples. A protein quantification kit (Protein quantification kit – Rapid, Sigma-Aldrich, UK) was used to evaluate absorbed and released BSA and lysozyme. A GloMax Discover microplate reader (Promega) was used to read the solutions in a 96-well plate that reacted with the Coomassie Brilliant Blue (CBB) G solution (150 µl/well). Absorbance of each well at 570-600 nm ($A_{570-600}$) was measured with a microplate reader. Supernatant samples collected from absorbing (A_{abs}), releasing (A_{rel}) or drug-free (A_{nodrug}) fabricated discs were analysed. Absorption/release kinetics were calculated by normalisation of the absorbed or release value by the drug-free biomaterial value. A fitting with the standard curve revealed the BSA or lysozyme absorption and release amount present in solution. Absorption was quantified as the amount of drug present in solution and in contrast to the portion absorbed from discs.

2.6.3 VEGF absorption for release in CAM assay

2.6.3.1 Laponite-alginate-methylcellulose

This methodology is reported in detail in Chapter 4 (4.2.7.1 page 101)

2.6.3.2 Laponite-gellan gum

This methodology is reported in detail in Chapter 6 (6.2.16.1 page 167)

2.6.3.3 Laponite GelMA

This methodology is reported in detail in Chapter 7 (7.2.12.1 page 199)

2.6.4 BMP-2 absorption for release *in vivo*

This methodology is reported in Chapter 5 (5.2.5.3 page 125)

2.6.5 Absorption of drugs in agarose gel by the printed scaffolds in a fluid gel support

This methodology is reported in Chapter 6 (6.2.15 page 167)

2.7 *Ex vivo*

Animal procedures were carried out in accordance with the guidelines and regulations of the Animals Act 1986, UK. Chorioallantoic membrane protocols were conducted under Home Office Approval UK (Project licence – PPL 30/2762). Fertilised eggs were ordered from MedEggs Henry Stewart & Co.Ltd, UK.

2.7.1 Sample fabrication for CAM assay

This methodology is detailed in Chapter 4 (4.2.7.1 page 101), 6 (6.2.16.1 page 167) and 7 (7.2.12.1 page 199)

2.7.2 Implantation in CAM model

Chicken eggs were incubated in a Hatchmaster incubator (Brinsea, UK) for 7 days at 37°C in a 60 % humidified atmosphere and 1 hour rotation. DW was supplemented every two days to ensure the maintenance of a humidified environment. After 7 days, eggs were prepared for implantation. A light torch was used to candle the eggs to assess embryo development and the presence of a vascularised membrane. Eggs were opened serially in a class II culture hood in sterile conditions. One egg was first placed on an egg rack to hold it in place and to allow sectioning of the eggshell (Figure 2.8 a-i). A scalpel was used (under sterile conditions) to open a 1-2 cm^2 window on the eggshell (Figure 2.8 a-ii) unless otherwise stated. The removal of the outer portion revealed the white membrane right below the eggshell (Figure 2.8 a-iii). With the help of flat forceps, the CAM membrane that is located just below the white portion was gently lowered (Figure 2.8 a-iv). An empty window was created (Figure 2.8 a-v) to allow scaffold implantation. Scaffolds reported in section 2.7.1 were implanted (Figure 2.8 b-i) and egg immediately sealed (Figure 2.8 b-ii) with a thin film of transparent and ethanol sterile Parafilm (Bemis™, Parafilm M™, Laboratory Wrapping Film, Fisher Scientific, UK). Labelled tape was then placed at the edge of the Parafilm (Figure 2.8 b-iii). Eggs were then incubated (Figure 2.8 c) in a Hatchmaster incubator for 7 days at 37°C in a 60 % humidified atmosphere without any rotation.

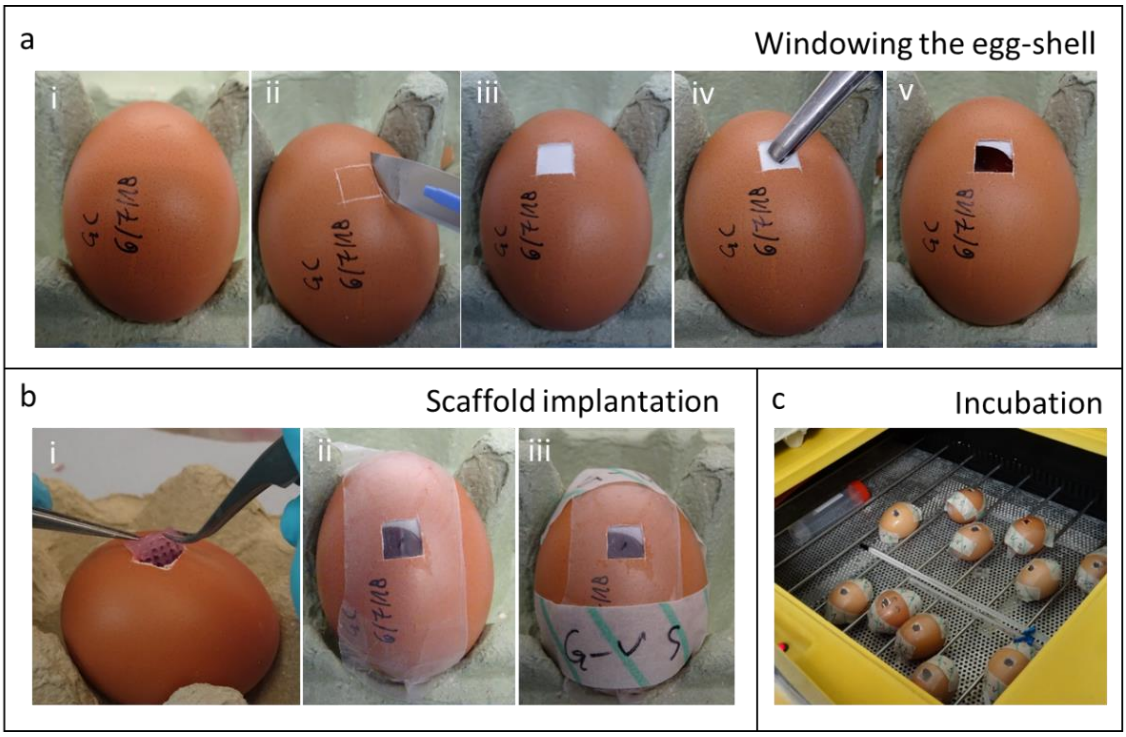

Figure 2.8. Implantation and culture of samples in chicken chorioallantoic membrane model.

To operate a window on the eggshell (a), an egg was candled and placed on a support (a-i), where a window of approximatively 1-2 cm^2 was created with a sterile scalpel (a-ii). The outer portion of the eggshell was removed (a-iii) and a flat forceps was used to lower the outer membrane (a-iv), breaking into the egg and revealing the vascularised membrane (a-v). Scaffolds were implanted on the membrane (b-i) and the window sealed with Parafilm M™ (b-ii) and tape indicating the treatment group (b-iii). Eggs were then incubated (c) in a non-rotational Hatchmaster incubator.

2.7.3 Chalkley score

Samples were incubated in the CAM model for 7 days (Figure 2.9 a-i and a-ii). Implanting 3D printed or cast scaffolds (Figure 2.9 b) can alter the vasculogenesis process and vessels can grow through or in the close vicinity of implanted scaffolds. This infiltration can be evaluated and quantified by Chalkley score assessment. Eggs were opened and chick sacrificed for tissue collection. Scaffolds were examined for Chalkley score after collection from the vascularised membrane. Integrated samples were collected and observed under a stereo light microscope. At 1x magnification, angiogenesis and vessel infiltration were quantified using a Chalkley eyepiece graticule placed in one of the microscope ocular, projected on the scaffold that was being examined and the number of vessels was obtained and registered from 5 independent counts.

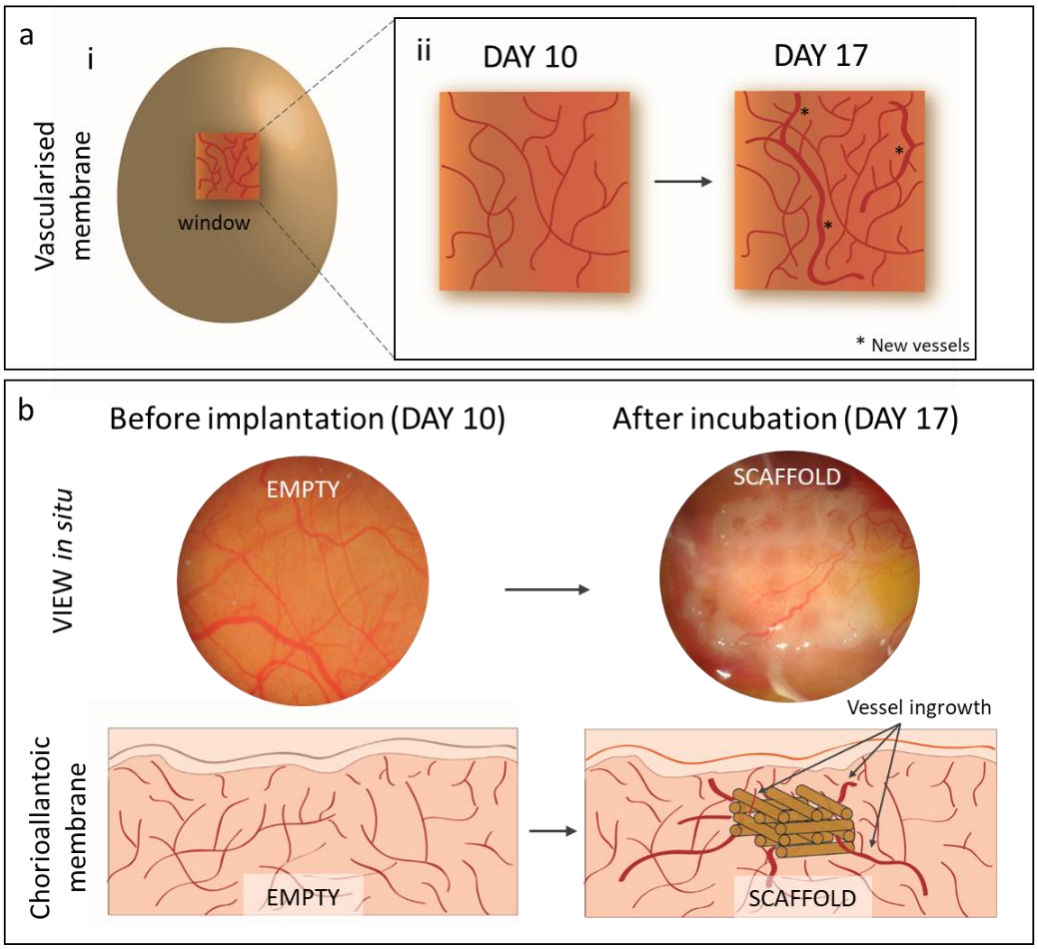

Figure 2.9. Chalkley score can be used to assess angiogenesis and vascular infiltration in implanted scaffolds.

In a developing chicken egg, the CAM vascularised membrane (a-i) can generally increase in number of vessels with the time of incubation (a-ii). Chalkley score can quantify the number of vessels that integrate with the implanted scaffolds after 7 days of incubation (b) which are a direct indication of angiogenesis with the presence of 3D printed or cast scaffolds.

The scores were registered for each integrated sample. The samples that were analysed were embedded in 4 % paraformaldehyde (PFA) overnight and embedded in optimum cutting temperature (OCT) medium the following day.

2.8 *In vivo*

2.8.1 Subcutaneous implantation of BMP-2 loaded 3D printed scaffolds

This methodology is detailed in Chapter 5 (5.2.5 page 124)

2.8.2 Subcutaneous implantation of HBMSCs-laden 3D printed scaffolds

This methodology is detailed in Chapter 5 (5.2.6 page 126)

2.9 Micro computed tomography images

A micro computed tomography (micro-CT) scanner (Bruker Skyscan 1176) was employed to collect all the CT images of scaffolds implanted using two subcutaneous mice models. Micro-CT machine was equipped with a sealed micro-focus X-ray source (20-90 kV, 25 W) and a 4000×2672 pixels detector. Mice were scanned exclusively at 4 weeks for the first subcutaneous implantation in MF-1 mice (5.2.5 page 124) and at 4, 6, and 8 weeks for the second implantation in BALB/c nude mice (5.2.6 page 126). Animals were anaesthetised with Isoflurane (Forane® RX, Abbott, UK) supplied at 5 % to knockout and positioned in the micro-CT machine and maintained under anaesthesia with a fitting mask supplying continuously 2 % Isoflurane with an 1L min^{-1} O_2 flow. An average of three full scans were conducted to obtain CT images from the neck up to the lower posterior portion. Scans were all carried out with a pixel size of 35 µm and an aluminium filter (Al) of 1mm. CT scans of 18 µm were carried out only during the final time point of the *in vivo* investigations (4 and 8 weeks for the implantation in MF-1 and BALB/c, respectively). A nominal resolution of 18 µm equipped with an Al 0.1 mm filter was used to scan *ex vivo* (after isolation and before histological analysis) samples collected from acellular scaffolds implanted subcutaneously in MF-1 mice.

CT representative reconstructions were obtained using NRecon (Bruker) with transfer function that is reported below each reconstruction as reference. Quantitative analysis for new bone formation was carried out using CTAn software v.1.17.7.2 (Bruker) to assess bone volume (BV) and average bone mineral density. Two bone samples from the mice (0.25 g cm^{-3} and 0.75 g cm^{-3} in their average bone density) were used as reference phantoms, scanned with the same parameters as implanted samples.

Similarly, to evaluate scaffolds functionality after 45 days of culture *in vitro*, SSC-laden scaffolds were scanned and details reported in Chapter 4 (4.2.6 page 100).

2.10 Histological analysis

Samples implanted both *ex vivo* or *in vivo* were fixed in 4 % PFA solution overnight at 4°C. Optimal cutting temperature (OCT (125 ml) Thermo Fisher Scientific) medium was then used after 12 h, to embed samples. Cryomold® Biopsy (Sakura Finetek UK Ltd, UK) of 10×10×5 mm, 15×15×5 mm or 25×20×5 mm were used to embed samples with OCT. Samples were stored at -80°C overnight, and sectioning performed the following day. A Cryostat (CM 1850, Leica Biosystems, Germany) was used to produce tissue sections of 8 µm. Kawamoto film's method [170] was used to collect the sections and staining subsequently carried out on cryotape to avoid the need for a demineralisation step. After staining, Super Cryomounting Medium (SCMM) type R3 (Section LAB, Co. Ltd. Japan) was used for mounting. UV light curing was carried out for 30 min to allow photopolymerisation of the SCMM. Slides were stored at room temperature and imaged the following day with a Zeiss Axiovert 200 (Carl Zeiss, Germany) at 2.5×, 5×, 10× and 20× magnification.

2.10.1 Goldner's Trichrome

Slides were hydrated for 10 min under running tap water. Subsequently, the slides were stained with Weigert's haematoxylin solution for 10 min in the dark. Slides were then washed in running tap water for 10 min removed excessive haematoxylin and rinsed four times in 1 % HCl in 70 % ethanol. After a single wash in water for 10 min, a solution of Ponceau-fuchsin-azophloxin (erythrocytes) was used for 5 min. A wash for 15 sec was carried out with 1 % acetic acid. Phosphomolybdic acid/orange G (cytoplasm) was layered

onto the slides for 20 min. A single wash for 15 sec in acetic acid was again performed to remove excess stain. A light green (collagen) solution was used to stain the slides for 5 min. After a final wash in 1 % acetic acid, tape was collected and mounted on a slide with SCMM.

2.10.2 Alcian blue and Sirius red

Slides were hydrated for 10 min under running tap water. Slides were then blotted dry and stained with Weigert's haematoxylin solution for 10 min in the dark. After a single wash in tap water for 10 min, slides were dipped (4 times) in 1 % HCl in 70 % ethanol. Slides were then washed for 10 min in water and stained with 0.5% Alcian blue (stains proteoglycans) for 10 min, molybdophosphoric acid for 10 min and 1% Sirius red (stains collagenous matrix) for 45 min after a further wash for 1 min in water between staining solution addition. After a final wash in running water, tape was removed from the slide and mounted with SCMM.

2.10.3 Von Kossa

Slides were placed in running tap water for 5 min. A drop of silver nitrate (AgNO3) solution was pipetted on each slide. A rack of slide was then set under UV light for 20 min to allow silver nitrate reaction with mineral content. A single wash for 5 min in running tap water was then operated. Sodium thiosulfate was added on slides for 8 min, followed by a wash in tap water for 5 min. Alcian blue and light green were used as counter stains for 1 and 5 min respectively. Sections were then blotted dry and tape removed to be mounted with SCMM to be polymerised and images.

2.11 Statistical analysis

Statistical analysis was performed using GraphPad Prism 7 (Graph Pad Software Inc., La Jolla, CA). Unless otherwise stated, differences in the data were assessed by D'Agostino-Pearson normality test. Both parametric and non-parametric tests were employed. Statistical significance was defined as *$p<0.05$, **$p<0.01$, ***$p<0.001$, ****$p<0.0001$. Non-significant (n.s.) differences were defined as $p>0.05$. The *n* number

reported in the captions represent the independent replicates used in an experiments with analogous conditions. Specific statistical tests and details used to analyse each graph, are reported in the statistical analysis section of each chapter or in the figure legend. When multiple comparison tests were performed for data analysed using one-way and two-way ANOVA, a correction using Tukey, Dunnet, Bonferroni and Sidak testing was carried out.

Chapter 3 Nanocomposite Laponite-alginate-methylcellulose hydrogels for cell-laden bone tissue biofabrication

3.1 Introduction

Typical additive manufacturing methods, such as 3D powder printing or selective laser sintering, are commonly used to build up complex scaffold geometries [171–173], while approaches, including 3D extrusion-based printing [69], offer the opportunity for layer-by-layer fabrication of scaffolds comprising cells or biologically active growth factors. 3D extrusion approaches in particular enable localised arrangement of cells or growth factors within a scaffold [174,175]. In the last few years, the term bioink has been used to describe a cell-containing hydrogel for additive manufacturing technologies that facilitate printing and cell delivery [65]. The parameters to consider for efficacious bioinks preparation include gelation characteristics, viscosity and shear stress as a consequence of the needle gauge employed [65,176]. Tailoring of cell properties can be achieved through addition of biological active peptides to the polymer chains [177,178], or by presentation of an ECM suitable for cell encapsulation [179].

Printing fidelity is focused towards the printing of large-scale, three dimensional constructs [65]. To date, there are two main strategies to achieve biofabricated constructs at clinically relevant dimensions by extrusion-based additive manufacturing that require the use of: i) a stiff support materials (e.g. PCL) processed by fused deposition modelling or, ii) a bioink with sufficient viscosity to preserve scaffold shape post extrusion. Using the latter method, Schütz *et al.* blended 3 % w/v alginate with 9 % w/v methylcellulose to achieve a bioink with a viscosity to enable printing with shape fidelity and good cell viability [69]. As the methylcellulose was not crosslinked, it was washed out and the alginate, crosslinked by cationic calcium ions, retained its shape right after extrusion. However, the high solid content of 12 % w/v limited cell viability while printing and subsequent cell function. Moreover, functionality of the alginate-methylcellulose blend was not demonstrated, possibly because of the inert properties of the composite bioink. Nanosilicates, such as Laponite, offer promise for tissue engineering [180], with the potential to overcome the major hurdles of elevated polymeric bioinks (such as poor cell viability post-printing) and the preservation of physical integrity required to print large scale implants.

Laponite is a synthetic magnesium silicate widely employed as a thickening agent in the cosmetic industry [95,96] and more recently as a novel biomaterial platform for drug delivery [103,126,181] and tissue engineering [95,102,123,133,182,183], both alone and in combination with several polymers. Furthermore, Laponite has been exploited as nanofiller and crosslinker in combination with several synthetic [130,133,184] and natural [102,135,136,183,185] polymers.

The degradation products of Laponite including as Na^{+},Mg^{2+}, $Si(OH)_4$ and Li^{+} are non-toxic [136] and have been shown to play a role in bone metabolism and calcification [186]. Nanocomposite gels are particularly attractive as biomaterials presenting not only enhanced mechanical [187] and self-healing characteristics [188], but also stimuli responsive [133] and biochemical properties [103]. In addition, the facile and effective inclusion achieved by the blending of polymers with nanosilicate, resulted in strong and biocompatible gels.

Alginate is a natural polymer polysaccharide widely used for cell encapsulation and 3D printing applications [177,189,190]. Alginate and Laponite were blended together with 40 % PEGDA by Hong *et al.* [118], generating scaffolds that displayed excellent toughness and elasticity. However, the elevated polymer concentration and lack of *in vitro* investigation for cell inclusion limit the potential application of this bioink for skeletal biofabrication purposes. Methylcellulose has bee proven to be cytocompatible [191,192] and frequently used as filler in polymeric suspensions or solution to aid mechanical stability in aqueous media [193]. Nanoclay-methylcellulose blend has never been reported before and their combination with alginate is here for the first time illustrated.

The current chapter examined a new bioink blend of Laponite, alginate and methylcellulose (Figure 3.1 a) for 3D printing. Laponite was blended with natural biomaterials with the aim to generate a bioink (Figure 3.1 b) for printing (Figure 3.1 c) and cell encapsulation in three-dimensional constructs (Figure 3.1 d).

Hypothesis (I):

Laponite (LAP) can be homogenously blended with alginate and methylcellulose to aid printability. Mechanical properties can be significantly enhanced by clay inclusion along with shear-thinning characteristics, and formulations screened for printability depending on their viscosity. Cell viability can be tested up to 21 days of culture *in vitro* compared to the silicate-free control. Laponite inclusion may enhance drug retention and localisation compared to the silicate-free control.

Aims:

- To blend Laponite with alginate and methylcellulose to produce an optimal formulation for printable hydrogels with specific shear-thinning characteristics;
- To assess optimal formulation printability to produce large constructs;
- To quantify the mechanical properties of the nanocomposite bioinks and final printed constructs;
- To evaluate the long-term cell viability of encapsulated cells the after printing.

Overview of Chapter 3:

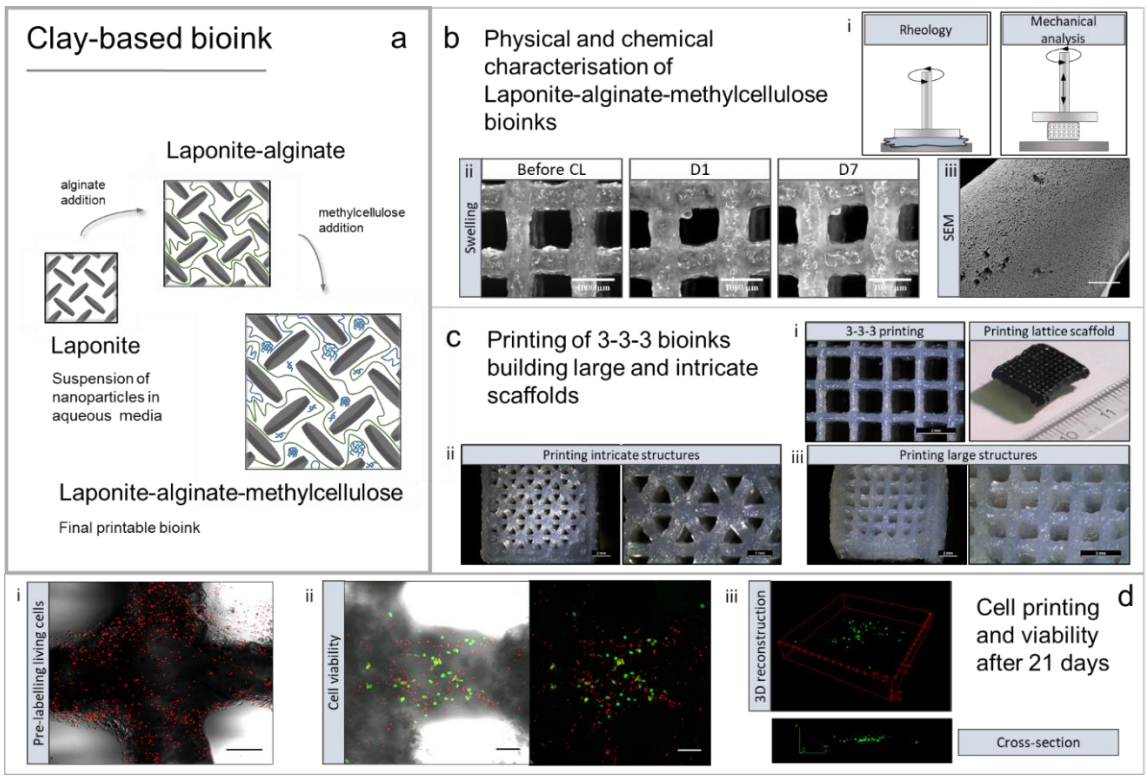

Figure 3.1. Schematic of Laponite-alginate-methylcellulose characterisation and printing.

A clay-based bioink (a) can be synthesised starting from the dispersion of Laponite in aqueous media. Alginate can then be added followed by methylcellulose. The resulting bioink can be tested (b) using rheology and mechanical analysis (b-i), by swelling tests (b-ii) and SEM (b-iii) scanning. An optimal formulation can then be selected for printing simple (c-i), intricate (c-ii) or large (c-iii) lattice scaffolds. Cells can be finally included (d) in the bioink by firstly pre-labelling them (d-i) and finally investigating their viability (d-ii) by Calcein staining or even three-dimensional reconstruction (d-iii) with confocal microscopy. Scale bar: (b-iii) 5 µm, (d-i) 250 µm, (d-ii) 50 µm.

3.2 Methods

3.2.1 Laponite

This methodology is detailed in Chapter 2 (2.2.1 page 43)

3.2.2 Laponite-alginate-methylcellulose bioink

This methodology is reported in Chapter 2 (2.3.1 page 46)

Bioink formulations are shown in Table 3.1. The 3-0-0 formulation (Laponite) was prepared following the protocol detailed in Chapter 2 (2.2.1 page 43). The 0-0-3 (methylcellulose) was synthesised following the protocol in Chapter 2 (2.2.2 page 44). 3-3-0 bioink (Laponite-alginate) was prepared by Laponite dispersion in DW, with consequent inclusion of alginate after 6 h of stirring at 5 G. Alginate powder was allowed to disperse for at least 2 h under constant 5 G shearing. Finally the 3-3-3 and 3-3-6 bioinks (Laponite-alginate-methylcellulose) were prepared following the protocols detailed in Chapter 2 (2.3.1 page 46). All bioinks were stored at 4°C overnight.

Table 3.1. Nomenclature of the tested Laponite-alginate-methylcellulose bioink formulations (all values correspond to % w/v)

Label	*Laponite*	*Alginate*	*Methylcellulose*
3-0-0	3	0	0
0-0-3	0	0	3
3-3-0	3	3	0
3-3-3	3	3	3
3-3-6	3	3	6

3.2.3 Rheology

The methodology used is reported in Chapter 2 (2.3.5 page 48). Other than rheological measurements described in Chapter 2, frequency sweep tests (0.01–100 s^{-1}) were performed on 0-0-3, 3-3-0 and 3-3-3 bioinks and storage modulus and loss modulus were measured.

3.2.4 Scaffold fabrication

This methodology is detailed in Chapter 2 (2.4.2.1 page 53)

3.2.5 Characterisation of printed scaffolds

3.2.5.1 Microscopy

Macroscopic images of the scaffolds were taken with a stereo light microscope (Leica M205 C equipped with DFC295 camera, Germany). Additional analysis was performed using scanning electron microscopy (SEM; Philips XL 30/ESEM, operated in SEM mode) at a voltage of 3 kV (spot size 3) with field emission gun. Prior to SEM, samples were dehydrated through an ascending ethanol series ending in 100 % ethanol and finally by critical point drying. Energy-dispersive X-ray spectroscopy (EDX) mapping was performed at a voltage of 12 kV.

3.2.5.2 Swelling of acellular printed scaffolds in cell culture media

Volumetric swelling of scaffolds was investigated by measuring the strand diameter after incubation in DMEM (Dulbecco's Modified Eagle Medium, Gibco, Thermo Fisher) with

10 % FBS at different time points: before crosslinking, after crosslinking, and after 1, 2, 3, 5, 7, 14 and 21 days. For analysis, pictures of different scaffolds (n=5) were taken using a stereo light microscopy and analysed using ImageJ (1.44p, National Institutes of Health, Bethesda, Maryland, USA).

3.2.5.3 Mechanical tests

To evaluate the mechanical behaviour of the printed 3-3-3 scaffolds, two different geometries were compared: a porous scaffold with a strand distance of 2 mm and a solid scaffold without pores obtained by depositing strands next to each other without a strand gap. Uniaxial compressive tests were applied to scaffolds after 1 day and 21 days of incubation in cell culture medium and Young's modulus and compressive strength were obtained from the data. Furthermore, dynamic mechanical analysis (DMA) was performed to investigate the resistance of the scaffolds against shear stress. Frequency sweep tests ($f = 0.01–10\ s^{-1}$) were applied using a plate rheometer (Rheotest RN 4). Scaffolds were twisted between two plates at a strain of 10 % and the storage moduli measured.

3.2.6 Cell printing

For cell printing, cells were pre-labelled following the protocol reported in Chapter 2 (2.5.3 page 56) and suspended in 100 µl of full media before mixing with the 3-3-3 blend. 3D printing of cell-laden scaffolds was performed with the parameters mentioned in paragraph 3.2.4 (page 74). Cell-laden scaffolds were submerged in full DMEM media and incubated at 37°C and 5 % CO_2. Media changes were undertaken every 2-3 days.

3.2.6.1 Human telomerase reverse transcriptase mesenchymal stem cells (hTERT-MSCs)

A human mesenchymal stem cell line expressing hTERT (human telomerase reverse transcriptase) [194] (hTERT-MSC) was kindly provided by Professor Matthias Schieker (Laboratory of Experimental Surgery and Regenerative Medicine, University Hospital

Munich (LMU), Germany). HTERT-MSC cells were maintained in culture supplemented with full cell culture media (Dulbecco's Modified Eagle Medium (DMEM)), replenished every 3 days and cells passaged at 80 % confluency. Seeding density was maintained at 3×10^3 cells cm^{-2} and cells at passage 2 used for all experiments.

3.2.6.2 Viability and proliferation of hTERT in printed scaffolds

This methodology is reported in Chapter 2 (2.5.4 page 57)

3.2.7 Protein and growth factor release

3.2.7.1 BSA loading and release

BSA (Sigma-Aldrich) was loaded within the 3-3-3 bioink by adding 100µl of BSA stock solution (10 mg ml^{-1}) to 1 g of the bioink. To examine the influence of Laponite, release was compared to a Laponite-free bioink, 0-3-9, which was loaded equally. Immediately after loading, the bioinks were used for printing scaffolds (4 layers, 10×10 mm^2), followed by crosslinking with a 100mM $CaCl_2$ solution for 10 min. Samples (n=5) were incubated in 1ml of Hank's balanced salt solution at 37°C over 21 days. Release solution was replaced after set times (2h, 4h, 1d, 2d, 3d, 5d, 7d, 10d, 14d, 21d). BSA quantities in the supernatants were quantified using Bradford assay using Roti® Nanoquant (Roth, Karlsruhe, Germany) plate reader.

3.2.7.2 VEGF loading and release

3-3-3 and 0-3-9 bioinks were loaded with VEGF (rhVEGF-A165; Biomol, Hamburg, Germany) by mixing 100 µl of VEGF stock solution (100 µg ml^{-1}) to 1 g of the bioink. Immediately after mixing, the VEGF-containing hydrogel bioinks were printed into scaffolds (6 layers, 10×10 mm^2), aiming for a theoretical loading of 700 ng each. After crosslinking

with 100mM $CaCl_2$, samples (n=8) were incubated in 1ml of release medium consisting of Endothelial Cell Basal Medium MV (Promocell, Heidelberg, Germany) supplemented with 15 % FBS and 1% Pen/Strep under cell culture conditions. Supernatants were taken at various time points (2 h, 4 h, 1 d, 2 d, 3 d, 5 d, 7 d) and replaced with fresh medium. Printed scaffolds without VEGF served as negative controls. ELISA using goat anti-human VEGF (Sigma-Aldrich) as capture and biotinylated goat anti-human VEGF (R&D Systems, Minneapolis, USA) as detection antibody was applied as described previously [195].

3.2.8 Statistical analysis

The methodology used is reported in Chapter 2 (2.11 page 66). All values were evaluated by one-way analysis of variance followed by Bonferroni's multiple comparison tests and reported in the figures captions.

3.3 Results

3.3.1 Nanocomposite preparation and evaluation of rheological behaviour

The Laponite-alginate-methylcellulose bioinks were prepared by blending 3 % w/v of Laponite suspension with 3 % w/v of alginate and 3 % w/v and 6 % w/v of methylcellulose, respectively. Viscosities of the different compositions (reported in Table 3.1) are shown in Figure 3.2 a, compared to the Laponite-free control (0-3-9). Autoclaving was chosen as the sterilisation method and performed on the final bioink ('autoclaving of bioink) or on the powders prior to dissolving ('autoclaving of powder'). Viscosities were investigated and compared to non-autoclaved materials ('without autoclaving'). All groups showed that viscosity was not significantly altered following autoclaving of the final bioink. In contrast, autoclaving of the powders before suspension led to significantly ($p<0.001$) lower viscosities.

Pure Laponite bioink (3-0-0) demonstrated a low viscosity of 2–7 Pa s. The addition of alginate (3-3-0) significantly ($p<0.001$) increased the viscosity to 7–18 Pa s. After 3% methylcellulose addition (3-3-3), viscosity was significantly ($p<0.001$) increased to 60–100 Pa s. Further increase of methylcellulose content (3-3-6) led to significantly ($p<0.001$) higher viscosity of 200–250 Pa s. 0-3-9 revealed a viscosity of 42.1 ± 5.2 Pa s, which was lower than the viscosities of the 3-3-3 bioinks. All formulations showed shear thinning effects at increasing shear rates, enabling extrusion through nozzles, evidenced by bioinks without autoclaving in Figure 3.2 b. Subsequently, the bioinks were tested for printing properties. While formulations comprising 3-0-0 and 3-3-0 were not useful in the generation of three-dimensional structures (printed strands collapsed immediately after extrusion), the 3-3-3 bioink allowed printing with high shape fidelity. 3-3-3, sterilised by autoclaving of the powder, could be extruded at lower pressures compared to 3-3-3, which was autoclaved as bioink. As expected, the 3-3-6 blend generated scaffolds with excellent shape fidelity, although required high pneumatic air pressures (>250 kPa) for extrusion, potentially harmful for cell printing. Therefore, a 3-3-3 blend, powder autoclaved, was chosen as a suitable bioink for bioprinting, given the excellent shape fidelity of the printed constructs, as well as the modest pressure (80 kPa) needed for extrusion. Thus, all further results indicated in this chapter, relate to scaffolds fabricated using this 3-3-3 formulation.

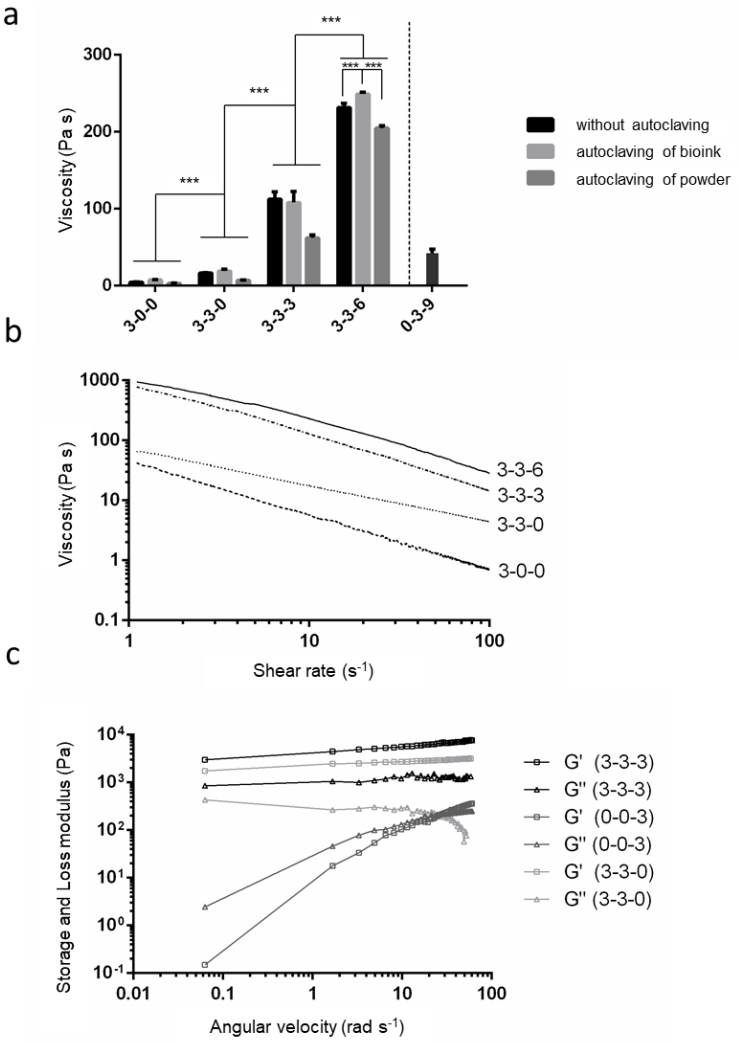

Figure 3.2. Rheological properties of different bioinks consisting of Laponite, alginate and methylcellulose evaluated at room temperature.

Viscosity (a) at a constant shear rate of 10 s^{-1}. The low viscosity of Laponite (3-0-0) was increased by addition of alginate (3-3-0) and further greatly increased by blending with methylcellulose (3-3-3, 3-3-6). (b) Shear thinning of non-autoclaved bioinks at increasing shear rates. (c) Frequency sweep measurements of different bioinks (autoclaved powders). 3-3-3 and 3-3-0 showed a storage modulus (G′) higher than the loss modulus (G′). For pure methylcellulose (0-0-3), a higher loss modulus was observed at lower angular speeds. Statistical significance assessed by one-way ANOVA followed by Bonferroni multiple comparison tests. Mean ± S.D. n=3, ***p<0.001.

Figure 3.2 c, shows the oscillatory frequency sweep tests of the powder autoclaved 3-3-3 blend in comparison to pure methylcellulose (0-0-3) and the blend without methylcellulose (3-3-0). The bioinks revealed viscoelastic behaviour and had been tested at an amplitude in the viscoelastic region, determined by simple amplitude sweep tests. The storage modulus G′ can be seen as an elastic, gelled component, while the loss modulus G describes the viscous, non-gelled component of the bioink. The 3-3-0 and 3-3-3 bioinks displayed a higher storage modulus than loss modulus over a broad range of angular velocities. 0-0-3 displayed a higher loss modulus until an angular velocity of 24.5 s^{-1}. At this

crossover point, the bioink viscous properties are lost and the bioink behaved like an elastic solid, evidenced by the higher shear modulus.

3.3.2 Potential for 3D high-resolution printing using 3-3-3 Laponite-Alginate-Methylcellulose bioink

Printing of the 3-3-3 bioink was successfully performed using a dosing needle (cylindrical blunt) with an inner diameter of 410 µm. After crosslinking, constructs of high accuracy in dimensions suitable for cell culture and clinical applications (20 × 20mm^2) were fabricated (Figure 3.3). Tubular, vessel-like structures (Figure 3.3 a,b) were printed without restrictions at scaffold heights of 2 cm. Cubic structures with 30 layers demonstrated shape preservation even with increasing height (Figure 3.3 c,d).

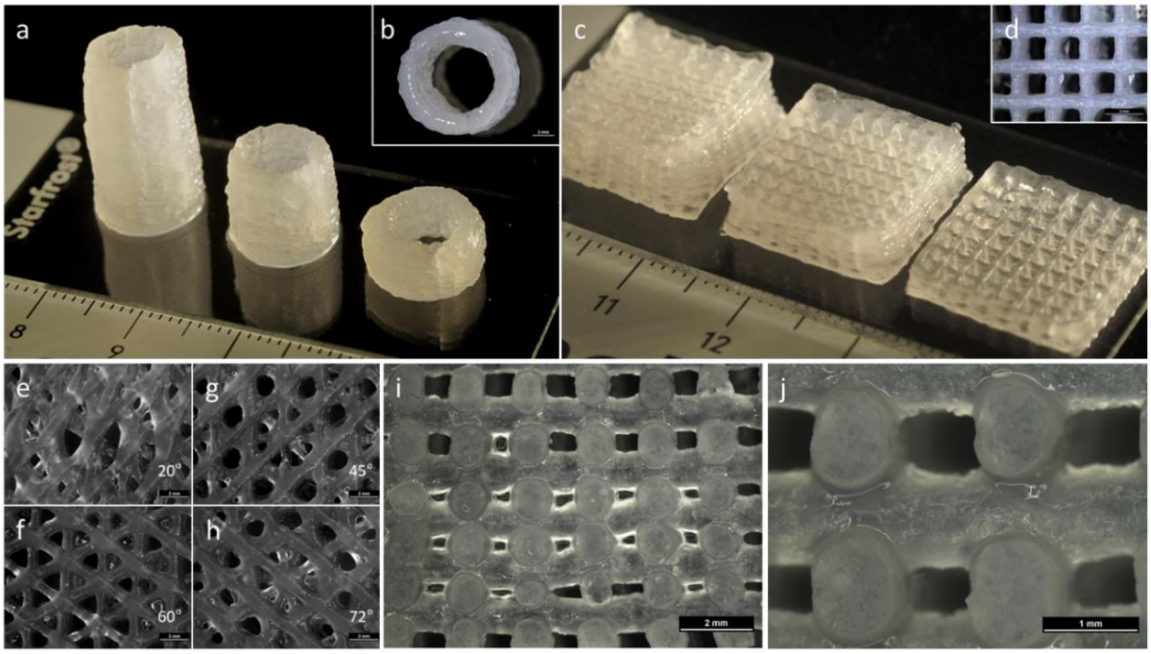

Figure 3.3. Scaffolds printed using 3-3-3 bioink displayed high fidelity at clinically relevant dimensions and shapes.

Tube-like structures (a) with varying heights (2 cm, 1.5 cm, 1 cm). Top view (b) of tube (2 cm). Cubic structures (c) with 30, 20 and 10 layers. Top view (d) of cube (30 layers). Top view (e-h) of scaffolds with different layer orientations. Pores in lateral direction (i,j) in scaffolds with double layers (AABB).

Complex geometries could be fabricated by change of layer orientations (20°, 45°, 60°, 72°), remaining stable after crosslinking and yielding different pore geometries (Figure 3.3 e-h). By changing the stacking sequence from ABAB (0°/90°/0°/90°) to AABB (0°/0°/90°/90°),

pores in lateral direction were formed and remained stable even at profiles with more than 25 layers (Figure 3.3 i,j).

3.3.3 Dynamic Mechanical Analysis revealed stability of 3-3-3 printed highly porous scaffolds

Following incubation over 21 days, it was observed that the printed scaffolds retained their three-dimensional shape. However, scaffold handling changed dramatically, from a flexible and robust phenotype, scaffolds were observed to be soft, with reduced mechanical properties. Mechanical characterisation of 3-3-3 printed scaffolds was carried out to study the reduction in mechanical strength over time and long-term stability of the scaffold. Young's modulus and compressive strength of uniaxial compressive tests were obtained at day 1 and 21 (Figure 3.4 a,b).

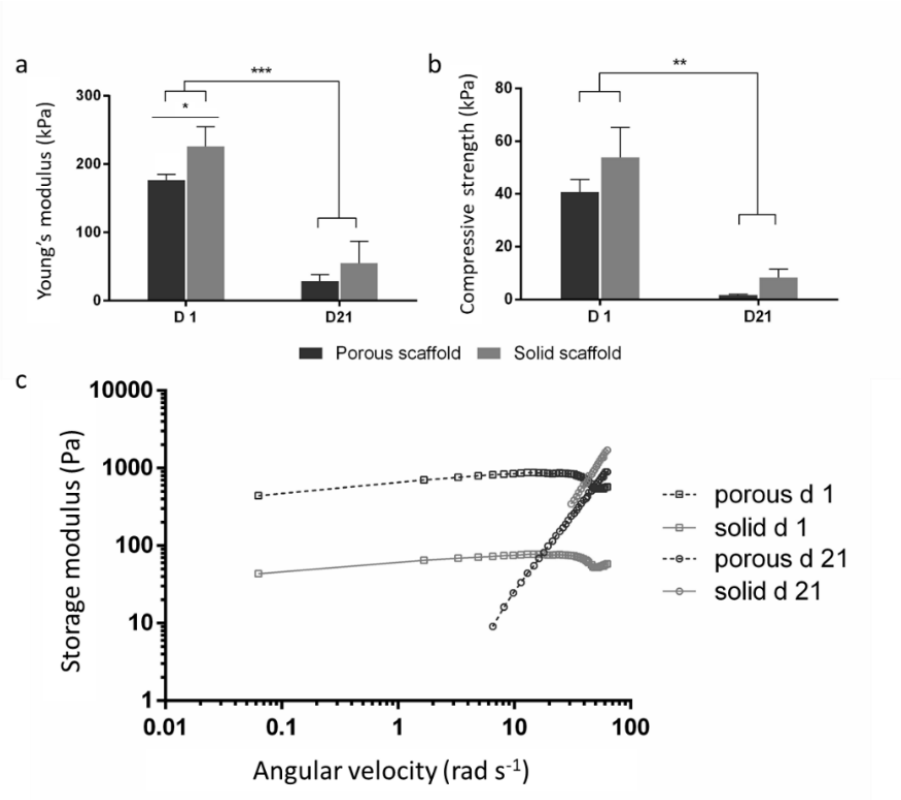

Figure 3.4. Mechanical evaluation of printed porous or solid scaffolds.

Young's modulus (a) and compressive strength (b) of both scaffold types decreased significantly from day 1 to day 21, incubated under cell culture conditions. Oscillatory frequency sweeps (c) revealed a strong change of the crosslinking of the scaffolds during cultivation (n=3). Statistical significance assessed by one-way ANOVA followed by Bonferroni multiple comparison tests. Mean ± S.D. n=5, *p<0.05, **p<0.01, ***p<0.001.

As expected, both the Young's modulus and the compressive strength were higher for non-porous, solid scaffolds compared to porous scaffolds. The Young's moduli decreased significantly ($p<0.001$) from day 1 to day 21 (176 ± 8.9 kPa to 28.6 ± 9.3 kPa (porous) and 226 ± 28.8 kPa to 54 ± 32.3 kPa (solid), respectively) and was found to be significantly ($p<0.05$) different between solid and porous scaffolds at day 1. The compressive strength was noted to change significantly ($p<0.01$) from 40.8 ± 4.7 kPa to 1.6 ± 0.4 kPa (porous) and 53.8 ± 11.4 kPa to 8.4 ± 3.0 kPa (solid). DMA was performed on the scaffolds. After defining the viscoelastic region by amplitude sweeps, oscillatory frequency sweeps were measured.

Data (Figure 3.4 c) obtained at day 1 demonstrated a higher storage modulus for porous scaffolds (~730 Pa) compared to solid scaffolds (~70 Pa). Both curves were relatively constant over the observed range of angular velocities. After 21 days, both the porous and solid scaffolds exhibited increasing storage moduli with linear slopes. The storage moduli of solid scaffolds were noted to be higher than those of the porous scaffolds.

3.3.4 EDX mapping ionic strands content of 3-3-3 printed acellular scaffolds

EDX analysis (Figure 3.5 a) revealed the distribution of Laponite within the printed scaffolds. Spectra analysis (Figure 3.5 b) revealed the elevated presence of silicon (Si) and magnesium (Mg) ions. Further confirmation was evaluated by topographical analysis (Figure 3.5 c-f) showing presence of Si and Mg within printed strands, confirming Laponite inclusion.

However, silicon and magnesium were noted to be heterogeneously distributed evidenced by areas in which these ions could not be detected. Calcium (Ca) detection was related to the crosslinking agent within the mixture after $CaCl_2$ immersion post-printing. The weak sodium (Na) signal (0.73 %), further confirmed the presence of Laponite and alginate in the composite.

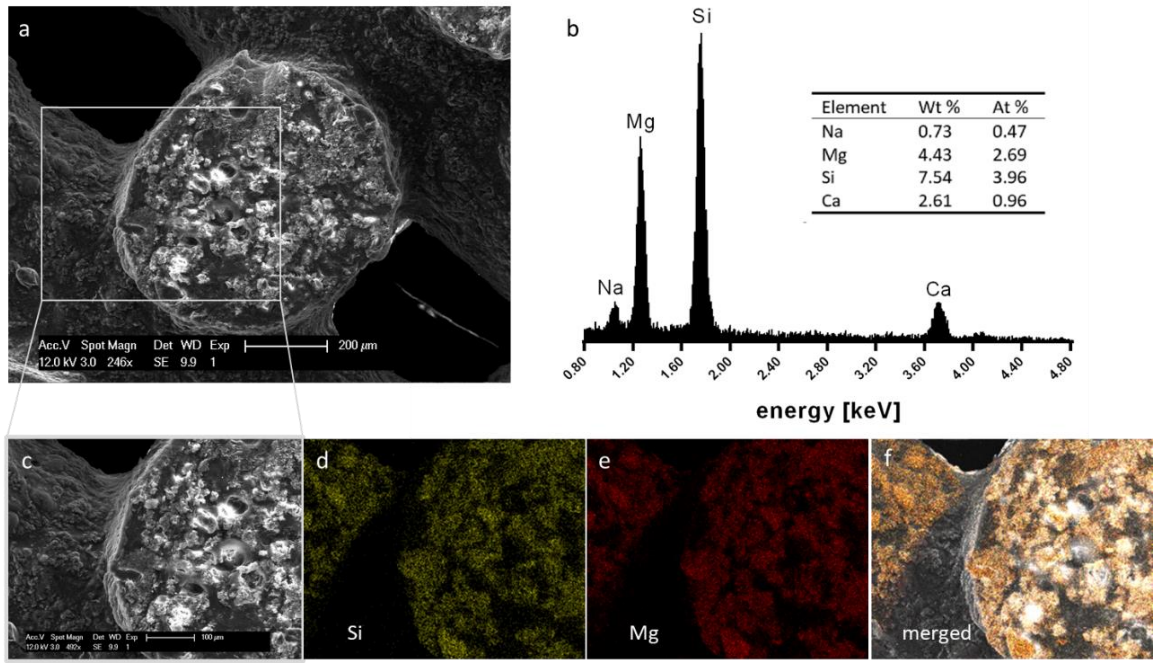

Figure 3.5. EDX mapping of single elements within 3-3-3 printed scaffolds.

Stand cut-out (a) showed internal structures. Spectral analysis (b) revealed elevated presence of Si, Mg and Na can be related to Laponite inclusion. Calcium peak is to be related to crosslinking solution. Close-up to the ROI (c) showed presence of Si (d) and Mg(e) further confirmed by merge result (f).

3.3.5 3D printed 3-3-3 scaffold swelling test elucidate construct stability in aqueous media

Printed 3-3-3 scaffolds were crosslinked using 100mM $CaCl_2$ solution and incubated in cell culture medium over 21 days. At fixed time points, the scaffolds were imaged and strand diameters determined (Figure 3.6 a).

After printing (Figure 3.6 b), the strand diameter was noted to be 420 ± 32 µm, slightly larger than the needle diameter (410 µm). After 10 min incubation in $CaCl_2$ solution, the strand diameter increased significantly ($p<0.001$) to 500 ± 57 µm. Following incubation in cell culture medium, the strands were observed to further swell slightly to a diameter of 548 ± 47 µm and 553 ± 49 µm within the first 2 and 6 h respectively, swelling non significantly up to 555 ± 42 µm after 24 h (day 1, Figure 3.6 c). After day 7, no significant changes in the strand diameter were detected. After 14 days (Figure 3.6 d), strand diameter significantly ($p<0.01$) increased to 607 ± 46 µm, but plateaued and remained constant until day 21. Thus, the strands of printed 3-3-3 scaffolds were observed to swell by approximately 46% after

printing and 20% after crosslinking and subsequent incubation in cell culture medium at physiological conditions (37°C) over 21 days.

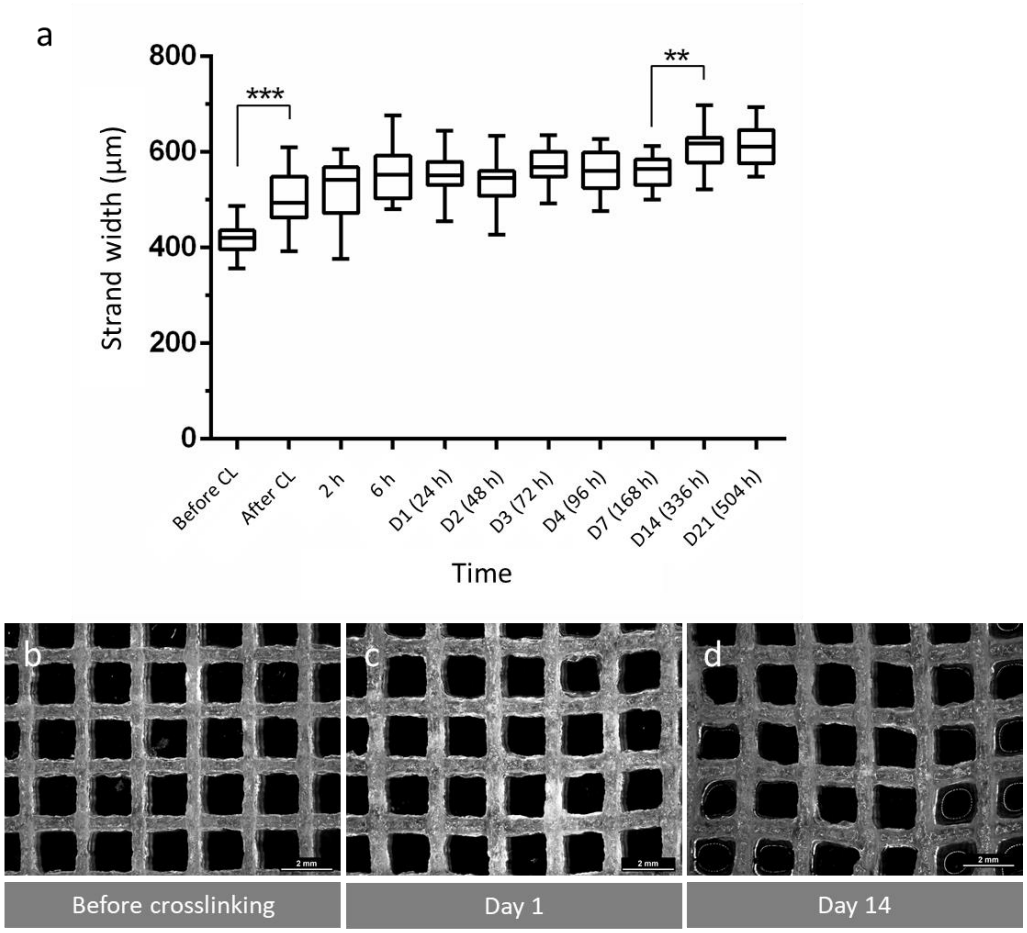

Figure 3.6. Increase in strand diameter over time.

Measurements of strand witdth (a) were plotted against the time points. After printing, crosslinking with $CaCl_2$ was carried out. Measurements were perfomed before (b) and after (c) $CaCl_2$ addition. After 14 days (d), the strand diameter increased slightly, however the scaffolds maintained their defined shape and pores. Statistical significance assessed by one-way ANOVA followed by Bonferroni multiple comparison tests. Mean ± S.D. n=20, **p<0.01, ***p<0.001.

3.3.6 Integrity, fine resolution and elevated porosity of *in vitro* cultured 3D printed scaffolds

SEM analysis of 3-3-3 printed scaffolds revealed differences in the microstructure between the outer surface and the inner structure of the strands.

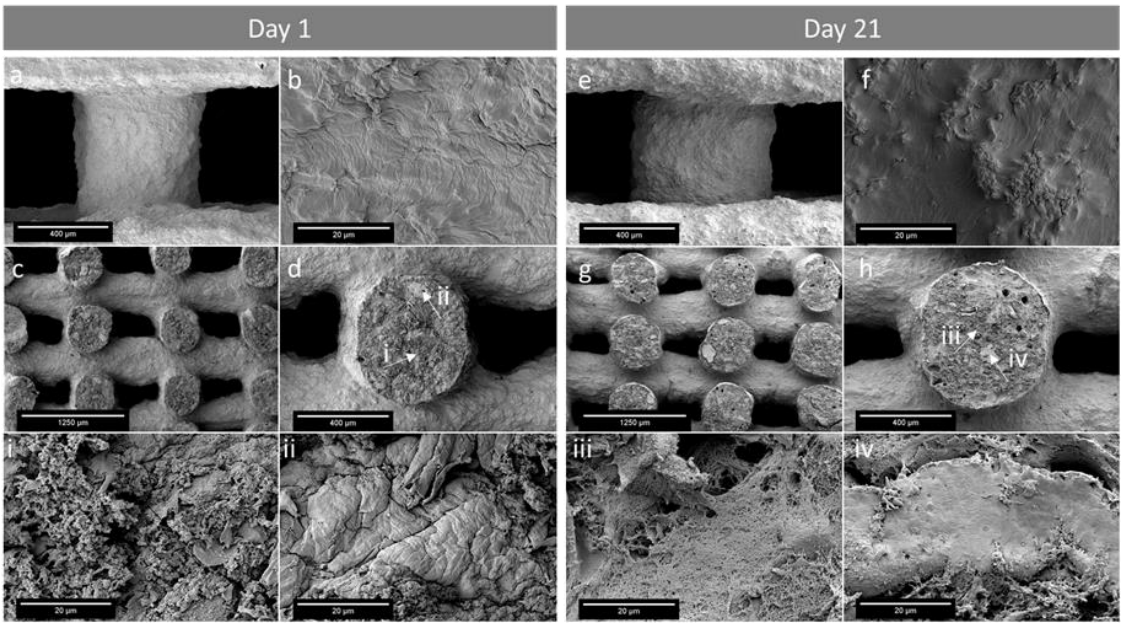

Figure 3.7.SEM photomicrographs of printed 3-3-3 scaffolds after 1 day and 21 days of incubation under cell culture conditions.

The top view (a, b, e, f) revealed strands with low roughness. Side views of cut, double-layered scaffolds (stacking sequence: AABB) (c, d, g, h) showed lateral macropores and a more heterogeneous appearance of the strand cross sections with different areas, marked by white arrows and shown at higher magnification (i, ii, iii, iv). Scale bar: (a,e,d,h) 400 µm, (b,f,i,ii,iii,iv) 20 µm, (c,g) 1250 µm.

Figure 3.7 shows a printed sample from the top view (Figure 3.7 a,b,e,f) with a dense, smooth surface, which did not significantly altered over 21 days. Lateral view (Figure 3.7 c,d,g,h) displayed heterogeneous strand structures with both rough (Figure 3.7 i,iii) and smooth (Figure 3.7 ii,iv) surfaces observed. The rough surfaces appeared porous and netlike, while the smooth surfaces were dense and compact. After 21 days, these areas were still visible although softer in contrast to day 1. Micrographs comparison between day 1 and 21 indicated that the 3D printed 3-3-3 structures degraded through surface erosion dynamics.

3.3.7 BSA and VEGF loading and release from 3D printed scaffolds

To study the growth factor release capabilities of printed 3-3-3 scaffolds, the model proteins BSA and VEGF were used. To evaluate the influence of Laponite, release from a 0-3-9 blend was studied in comparison to 3-3-3 scaffolds. 3-3-3 and 0-3-9 bioinks were loaded with the same amount of BSA (10 mg ml^{-1}) or VEGF (100 µg ml^{-1}) prior to printing.

Cumulative release of BSA over 21 days is shown in Appendix C Figure 3.1 a, b. The 0-3-9 scaffolds were found to show a high initial burst release of 53.8 ± 5.7 µg after 4 h, while BSA released from 3-3-3 scaffolds was observed to be only 2.2 ± 0.7 µg. Up to day 21, only restricted release of BSA from 0-3-9 was measured and the cumulative release increased to a level of 61.7 ± 6.5 µg. In contrast, the cumulative release from 3-3-3 between 4 h and 21 days was found to be higher and after 21 days 18.0 ± 1.5 µg had been released. However, results indicated, that a significant amount of BSA was retained within the 3-3-3 blend. Appendix C Figure 3.1 c, d illustrates the release of VEGF over a period of 7 days. 0-3-9 bioink composition revealed an initial burst release, with 149.0 ± 12.9 ng VEGF measured after 4 h. In contrast, VEGF release from the 3-3-3 scaffolds was 0.26 ± 0.05 ng. While the release of 0-3-9 decreased over time, the cumulative release profile of 3-3-3 was almost linear, indicating a sustained release of VEGF. After 7 days, 0-3-9 showed a total release of 275.7 ± 22.4 ng; while 3-3-3 scaffolds were found to release less (8.3 ± 1.0 ng). As observed for BSA, a significant amount of the growth factor was retained inside the 3-3-3 blend.

3.3.8 Cell-laden constructs preserved morphological properties and cell viability after 21 days

An immortalised human stem cell line (hTERT-MSC) was used to demonstrate the viability of cells encapsulated in 3D printed constructs comprising of 4 layers (Figure 3.8). DiD pre-staining was used to distinguish artefacts from Laponite adsorption and to illustrate cell presence and viability (DiD signal is independent from cell viability) (Figure 3.8: red). Metabolically active, viable cells were evidenced using Calcein (Figure 3.8: green). The cells were observed to be distributed homogeneously over the whole scaffold retaining a round, circular morphology and an absence of cell spreading. For cell viability determination, 3-3-3 scaffolds were compared to a Laponite-free 0-3-9 blend, previously developed [19]. Comparison of the number of living cells (Figure 3.9 a) inside the 3-3-3 blend revealed cell viability had increased from approximately 68.12 ± 10.60 % (day 1), to 75.11 ± 8.34 % (day 7) and 75.71 ± 5.61 % (day 14). After 21 days of culture, hTERT-MSCs were observed to be significantly ($p<0.001$) less viable (65.61 ± 11.33 %). In the Laponite-free control, cell viability was found to be lower than 3-3-3 scaffolds post-printing (63.23 ± 15.62 %, at day 1) and significantly ($p<0.001$) lower after 7 days (60.02 ± 13.39 %) compared to the 3-3-3 blend. Cells were found to be viable after 14 days of culture (78.65 ± 15.56 %) increasing up to 92.23 ± 12.23 % after 21 days.

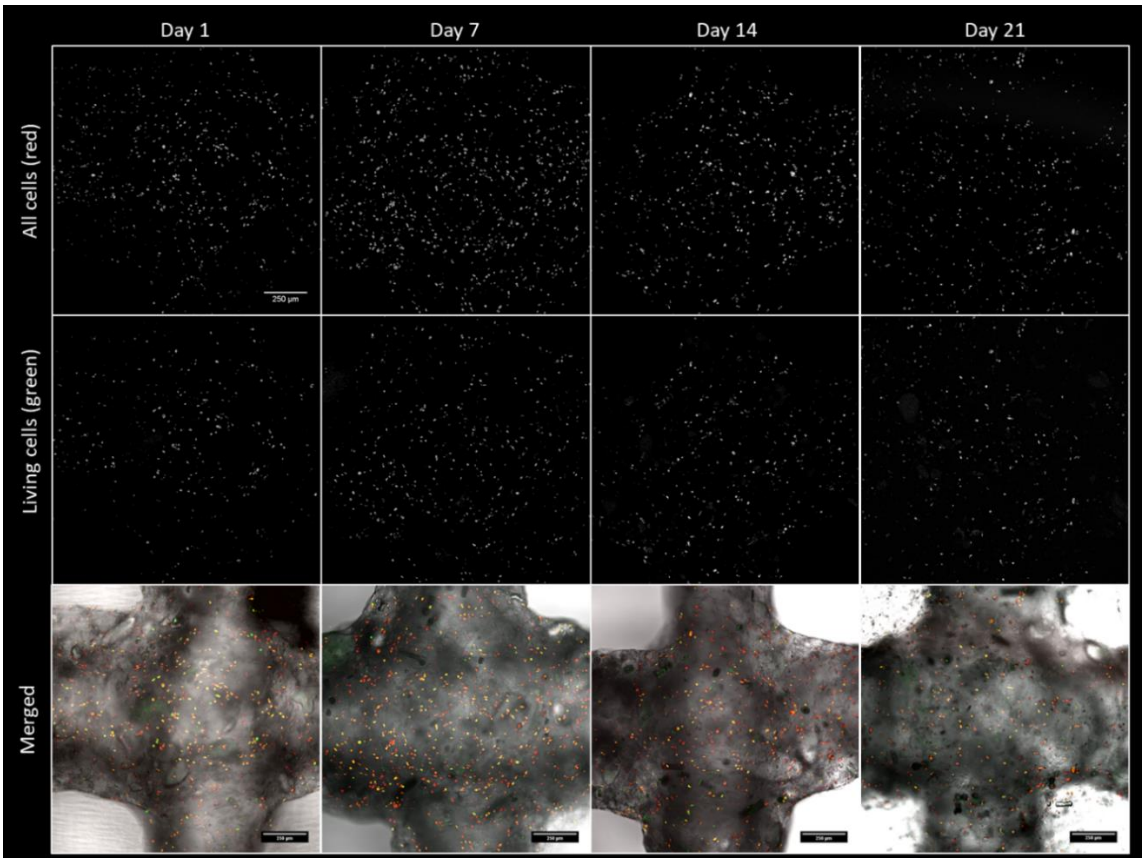

Figure 3.8. hTERT-MSCs-laden printed scaffolds *in vitro* investigation.

Cell-laden scaffolds were cultured for up to 21 days and stained for mitotically active cells at 1, 7, 14 and 21 days. Cells were pre-labelled with DiD (red) before printing. Living cells were stained with Calcein AM (green) at time points. Merged images show not only cell viability but also scaffold integrity. Scale bar: 250 µm.

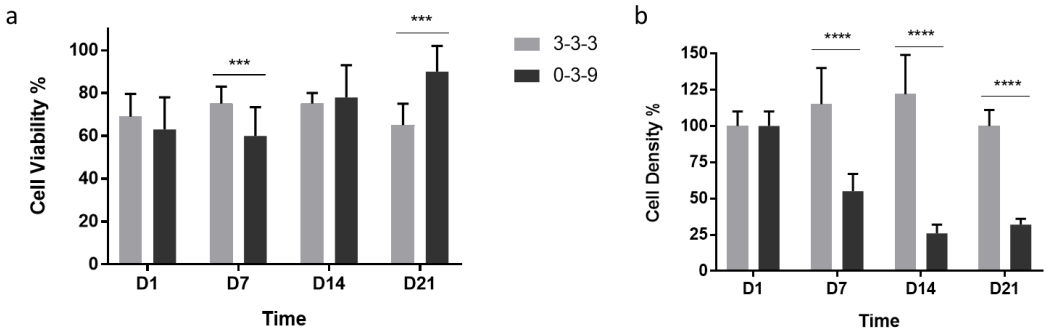

Figure 3.9. Ratio of viable cells in relation to total cell count over 21 days, determined by cell number analysis from confocal pictures.

Cell (a) viability and (b) density quantification of scaffold printed with 3-3-3 or 0-3-9 as control. Cell viability percentages were obtained from the calculated difference between viable and total cells, collected from confocal image analysis. Dead cells were assumed to comprise the fraction not stained with Calcein AM. Cell density was calculated by normalising the number of living cells by the confocal scanning volume. Day 1 was set as 100 %. Statistical significance assessed by one-way ANOVA followed by Bonferroni multiple comparison tests. Mean ± S.D. n=3, ***p<0.001, ****p<0.0001.

The cell density of the printed cell scaffolds of 3-3-3 and 0-3-9 is reported in Figure 3.9 b. Day 1 was set as 100%, and cells were counted and normalised against scanning volume. Cells printed and cultivated in 3-3-3 were found to proliferate from 7 (115.12 ± 25.10 %) up to 14 (122.16 ± 27.68 %) days with a proliferation percentage significantly greater ($p<0.0001$) than Laponite-free control. Cells were found to reach similar confluence levels to day 1 after 21 days (102.79 ± 11.13 %). While the cell density of the 3-3-3 scaffolds was found not to change significantly over time. In contrast, 0-3-9 samples were affected evidenced by the rapid decrease from day 1 to day 7 (55.43 ± 12.19 %) and 14 (26 ± 6.23 %) with a negligible increase observed after 21 days (32.87 ± 4.32 %) compare to 3-3-3 scaffolds ($p<0.0001$).

3.4 Discussion

Extrusion bioprinting can reliably generate three-dimensional structures by spatially controlling biomaterial and cells deposition [196]. However, 3D bioprinting has yet to generate fully viable and structurally stable constructs given the high cell damage observed post extrusion [197]. This could be due to the combined effect of excessive extrusion pressure and bioink viscosity [65]. The novel 3-3-3 composite bioink generated set out to combine physical interaction and integration to provide a reliable low-polymer content bioink for cell printing.

Laponite is a smectite mineral with high potential for cell encapsulation and tissue engineering [95,103], and has recently been used as bioink nanofiller [102,118,119]. Nevertheless, 3D printed structures previously reported showed no extensive beneficial results from Laponite inclusion [102,118,119]. As the excessive shear thinning behaviour of Laponite precludes the generation of 3D structures by printing, blending with alginate and methylcellulose was used to create a printable bioink. Alginate is widely employ as printing material for both, cell-free and cell-laden scaffolds [189,198–200]. Schütz *et al.* described a method for including methylcellulose as a temporary available substance to increase the viscosity of a 3 % alginate bioink while printing, resulting in scaffolds with high shape fidelity and cell vitality [69]. As the methylcellulose was not crosslinked, the methylcellulose dissolved and the crosslinked alginate retained its shape. Lode *et al.* [174] used a similar approach to show, that not just mammalian cells, but also algae could be integrated into a 3D printed scaffold. However, high polymer content could limit cell printing potential due to the high stress that living cells could experience when encapsulated [140]. The 3-3-3 bioink formulation presented in this chapter, aimed to address this issue with methylcellulose content reduced to 3 % (instead of 9 %) and Laponite inclusion to aid drug release and cell-material interactions. Reduced methylcellulose content could be advantageous, as cytotoxicity of methylcellulose has previously been shown [69].

The rheological behaviour of the bioinks was dependent on the sterilization process. Previous data is available for when the individual components are autoclaved, reporting i) a degradation of alginate suspension with a measurable loss of molecular weight leading to decreased viscosities [201], ii) a modulation of Laponite gel aging, enhancing the gel structure [202], and iii) an aggregation of methylcellulose with consequent increase in viscosity [193]. The Laponite aging observations and methylcellulose aggregation explain why autoclaving of the bioinks resulted in increased viscosities of the bioinks. Moreover, the strengthened Laponite network compensated for the observed the loss of viscosity following alginate degradation. The addition of methylcellulose increased the viscosity by gelation of

the polymer chains. However, autoclaving of all three materials before mixing ('autoclaving of powder') inhibited Laponite network formation and aggregation of methylcellulose failed to occur. The reduction in viscosity may be a consequence of the degradation of alginate. Therefore, extrusion of the bioink was carried out to test the printability of the bioink formulations.

Plain Laponite suspension bioinks (3-0-0) as well as a Laponite-alginate combination (3-3-0) bioinks did not enable the generation of three-dimensional structures. In contrast, the addition of 3 % and 6 % methylcellulose (3-3-3 and 3-3-6) resulted in a significant increase in viscosity and allowed the printing of strands with a shape fidelity comparable to the 0-3-9 blend described previously [69]. Finally, the 3-3-3 bioink was chosen as a printing bioink given the favourable viscoelastic properties and high printing fidelity observed. Scaffolds printed from 3-3-3 bioink displayed high shape fidelity. Importantly, through changing the stacking sequence to double layers (AABB), lateral pores were achieved. 3D printed structures were found mechanically stable when cultured in aqueous media. The high adsorption capacity of Laponite did not hinder alginate crosslinking but contributed to stabilising the scaffold when immersed in solution [203]. Indeed, since adsorption can be limited by swelling ratio, methylcellulose may play a crucial role in reducing swelling and Laponite calcium ion adsorption [204]. Limited 3-3-3 swelling, confirmed by measurements of printed lattice scaffolds and SEM micrographs, could be related to Laponite intrinsic adsorption and crosslinking capacities. Indeed, Laponite exfoliated nanodiscs are sensitive to the presence of hydrated positive ions in solution [203]. Therefore, ion exchange reaction can be expected to force Ca^{2+} ions within the Laponite particle interlayers [203]. Negligible post-printing swelling could be achieved through physical and ionic interactions between Laponite nanoparticles and alginate polymeric chains. Indeed, it has been previously shown that Laponite can positively interfere with alginate swelling capacity [135].

The network of the crosslinked 3-3-3 formulation was found to change over time. Alginate is crosslinked by divalent cations like calcium [205], and can interact with Laponite [183]. The zwitterionic charge structure of Laponite presents a range of possible modes of interaction with charged polymers. Furthermore the presence of ions such as calcium can cause aggregation of dispersed clay particles and initiate gelation through particle-particle interactions. [203]. Therefore, a strong mutual influence of the alginate network formation and the Laponite arrangement can be expected. Laponite nanodiscs can interact with guluronic and mannuronic acid groups present on the alginate chain, occupying ionic pockets where calcium ions should be positioned, providing a temporary linkage between long alginate chains. This phenomenon could explain the limited swelling by systematic Ca^{2+} ionic subtraction, aided by non-covalent bonding between Laponite nanodiscs and alginate chains. EDX data clearly demonstrated Laponite inclusion within the composite

bioink evidenced by magnesium and silicon peaks. Furthermore, a migration of calcium ions from the alginate chains to the Laponite particles could occur and result in changes of the network structure which may cause the drop in stiffness and changes of viscoelastic properties after 21 days. In general, mechanical degradation was observed for solid and porous scaffolds. As expected, the non-porous, solid scaffolds revealed higher mechanical strength, than porous scaffolds [206]. The significant drop in Young's moduli and compressive strength illustrate systematic degradation during 21 days of culture. Storage modulus of porous and solid scaffolds indicated a substantial difference in lattice or bulk constructs. Printed structures resulted in a 100-fold higher elastic than solid scaffolds at day 1 reaching a similar trend after 21 days. The changing in slope at day 21 clearly showed a decreasing concentration of biopolymer present in the composite, indicating biodegradation. However, 3-3-3 printed constructs were noted to be physically intact even if mechanical properties were affected.

Initially, cells embedded in the 3-3-3 bioink exhibited higher cell viability (70%–75% active cells) after printing compared to cells suspended in the 0-3-9 blend [69]. In the absence of Laponite, a drop in cell viability was observed at earlier time points in 0-3-9 blends; whereas cell viability was stable across the time course in the 3-3-3 blend. This was reflected in the significantly lower viability in 0-3-9 bioink versus 3-3-3 bioink at day 7. Interestingly, the cells at later time points in 0-3-9 blend displayed a higher proportion of viable cells, albeit at a considerably lower total cell density. These results indicate Laponite inclusion was beneficial for biological function of the bioink. This could be related to the positive influence of Laponite itself, as well as the reduction of the total solid content [65] or the content of methylcellulose. Cell viability was stable over 21 days, without a significant decrease in cell number. Therefore, metabolically inactive, dead cells could likely be a consequence of shear forces during the extrusion process or mixing of the cells with the printing bioink prior to extrusion. Forces involved in the printing process have been shown to cause cell death [144]. Over the culture period of 21 days, cells displayed a round-shaped morphology indicating limited interaction with the blend components. Favourable characteristics of Laponite, including support of cell proliferation or adhesion [102], were not observed. Indeed, alginate is known for its poor cell adhesive properties [207]. Furthermore, the drop of stiffness of the scaffolds could limit cell activity [208]. However, the favourable interactions of Laponite with polarised substances suggested promising options for the loading of growth factors to the material prior or after printing, which could promote cell functions [209].

In this respect, initial steps were made in loading model proteins BSA and VEGF to Laponite-containing 3-3-3 bioink and Laponite-free bioink 0-3-9 before printing and studying their release from printed scaffolds. 0-3-9 was previously found to behave as a simple

alginate-based 3D printed scaffold in culture [69]. Therefore it is expected that the release kinetc upon BSA or VEGF loading will be well represented by the release from an alginate construct which is widely reported in literature [210,211]. The inclusion of Laponite to the hydrogel drastically changed the protein release kinetics. Thus, while 0-3-9 showed a high initial burst release of both growth factors, 3-3-3 compositions displayed limited burst release of proteins. This may be due to the higher inner porosity of 0-3-9, but most likely results from the strong electrostatic binding sites of 3-3-3 as a consequence of the Laponite inclusion [103], absent in the 0-3-9 composition. The electrostatic interaction of Laponite with BSA and VEGF may also explain the smaller differences in the release curves of BSA and VEGF. BSA is negatively charged protein [212], while VEGF displays a positive total charge [213]. Therefore, different bond strengths between the growth factors and Laponite explain the differences between BSA and VEGF release. The results obtained suggest that most of the proteins were still retained inside the 3-3-3 blend after 7 and 21 days, respectively.

Similar effects have been reported by Ding *et al.* [209] following FGF2 loading, who demonstrated, that pure Laponite gels released only negligible amount of growth factor after 35 days. It was shown, that different electrostatic interactions within Laponite blends changed growth factor binding and therefore growth factor release [209]. Dawson *et al.* [103] recently demonstrated the absorption, encapsulation and release of BSA and VEGF from Laponite hydrogels. Release profile of the protein resulted to be significantly lower when compared to the release from alginate controls. This property was harness and in combination with VEGF, Laponite gels were absorbed with VEGF and implanted in a mouse defect helping to stimulate vasculature ingrowth for endochondral ossification aided by vessel sprouting guided by the retention of the compound *in situ*. These results are promising and consistent with the *in vitro* study here reported. These absorption/release ability will be harnessed in Chapter 4 to improve angiogenesis in an *ex vivo* model, and in Chapter 5 to augment bone formation *in vivo*.

3.5 Conclusions

Nanocomposite hydrogels represent an exciting alternative for 3D bioprinting materials. In particular, Laponite silicate is a versatile nanomaterial that can be employed as a filler for multiple polymeric platforms. In this chapter, a novel nanocomposite bioink has been synthesized, evaluated and characterised. The potential of Laponite as a colloidal ligand in alginate and methylcellulose bioink has been fully investigated, allowing reduction of polymeric weight content and the development of a potential bioink for SSCs printing and drug delivery that will be further studied in Chapters 4 and 5.

Autoclaving of the powder was found to be matching the viscoelastic properties of a highly printable bioink, although unable to match the mechanical properties similar to bone tissue post printing. DMA revealed a pre-crosslinked hydrogel that exhibited a dramatic change in mechanical properties once extruded and crosslinked through the addition of $CaCl_2$. Post-printing chemical crosslinking did not affect significantly the swelling characteristics of the printed structure, allowing elevated shape fidelity and shape retention up to 21 days of *in vitro* culture. However, further physico-chemical analysis would be required to fully understand Laponite-alginate-methylcellulose interactions. In the following chapter (Chapter 4), SSCs viability and functionality post-printing will be indeed studied. hTERT-MSCs were used as a cellular model for printability and post-printing viability evaluation. Cells were found to remain viable and to proliferate for up to 21 days of culture. Laponite inclusion was found to highly influence release, entrapping BSA and VEGF, and localising these agents in the printed structure. This could be of advantage and will be further investigated in Chapter 4 and 5 through the evaluation of released drugs *ex vivo* and *in vivo*. The results presented in this chapter, indicate the potential of 3-3-3 as a bioink for cell printing.

Chapter 4 *In vitro* investigation of nanocomposite 3D printed scaffolds for bone regeneration

4.1 Introduction

Stem cell printing is an attractive approach currently advocated for the generation of three-dimensional constructs to repair damaged tissue. Cell-laden 3D printed implants should ideally i) sustain cell viability and promote cell proliferation, ii) result in functional constructs within a short period of time after printing and, iii) stimulate the host microenvironment to aid tissue ingrowth and ultimately tissue infiltration and integration. Indeed, cell printing can be considered as an efficient tool to deposit encapsulated cells in a three-dimensional environment that serve as a temporary support for cell growth and new tissue development [62]. Ideally, printing should be adjusted to allow stem cells to experience the minimum stress in order to preserve their viability following deposition [146,150]. Recent studies have confirmed significant (90%) SSCs viability after extrusion when encapsulated in shear-thinning, thixotropic, injectable hydrogels [146]. In contrast, Fedorovich *et al.* [57] have recently found that bionks (e.g. Lutrol PF127, agarose) that are not mechanically tuned to support cell printing, can induce significant damage to encapsulated cells during the printing process. Shear-thinning hydrogels are attractive given their properties with the ability to shear while extruded and regain their shape upon deposition, while shielding encapsulated cells from damage induced by the printing processes [65].

Laponite, is a clay smectite with a particular division of positive (along edges) and negative (top-bottom surfaces) charges. This anisotropic distribution of the charges allows the nanodiscs to form self-assembled “house-of-cards” structures that are able to dynamically form and break depending on the amount of shear applied to the gel [214]. Laponite rheological properties can be tailored by the addition of polymers (e.g. sodium polyacrilate [114]) or ions (e.g. $CaCl_2$ [215]). Recently, Laponite has been reported to show, in combination with gelatine, shear-thinning behaviour useful for injectability of the mixture to treat haemorrhages [137]. The nanocomposite was found to be able to shear and regain its structure right after extrusion from a fine needle, showing a yield stress of increased value by the addition of greater concentration of clay. Alginate shear-thinning behaviour was recently found to be enhanced by the addition of Laponite dispersion [115]. When low shear is applied, the alginate chains and the Laponite house of cards structure contribute to the significant increase of the nanocomposite viscosity.

Thus, at present, nanocomposite hydrogels are being investigated as bioinks for cell printing [216]. Chimene *et al.* [138] have recently reported the use of a nanosilicate modified bioink for cell printing. Laponite-GelMA-kappa carrageenan bioink provided a shear thinning and highly printable material with the deposition of murine osteoblast cells that maintained their viability for up to 120 days. However, high polymeric content (13 w/v %), UV-mediated

crosslinking proved less successful with the application of an animal cell line lacking functionality and poor TE applications. Peak *et al.* [216] investigated the blending of Laponite with PEG to produce a shear-thinning bioink with the potential to encapsulate and print murine osteoblasts. Moreover, a lack of reports on further functionality studies preclude evaluation of the applications for this nanosilicate-based bioink.

The current chapter has evaluated the viability (*in vitro*) and functionality (*in vitro* and *ex vivo*) of SSCs encapsulated in a novel clay-based hydrogel formulation reported in Chapter 3, where Laponite-alginate-methylcellulose bioink was characterised and mechanical, physical and chemical characteristics determined [56]. However, the lack of a clear demonstration of biological functionality, reporting only the printability of an immortalised stem cell line, indicates the need for further evaluation of the clay-based bioink functionality *in vitro*. Here the 3-3-3 bioink has been applied as a shear-thinning and cell-encapsulating bioink (Figure 4.1 a,b) for rapid cell printing and biofabrication of implantable constructs that can be fabricated in different sizes (Figure 4.1 c) and conditioned with cells and growth factors (Figure 4.1 d) to build on previous work by enhancing the biological functionality of the fabricated scaffold – as demonstrated in *ex vivo* models of angiogenesis.

Hypothesis (II):

Laponite (LAP) clay blended with alginate and methylcellulose can be loaded with SSCs and viable constructs can be fabricated. SSCs differentiation can be stimulated *in vitro* by the inclusion of Laponite within the printed construct. Chick chorioallantoic membrane (CAM) model can be used to evaluate the potential of printed scaffolds of different sizes to integrate with vascularised membrane. Laponite absorption capacity can be harnessed to load VEGF before implantation in CAM, HUVECs can be seeded on printed scaffold, or a combination of VEGF and HUVECs can be used to ultimately evaluate angiogenic potential *ex vivo*.

Aims:

- To use the Laponite-alginate-methylcellulose to print SSCs and fabricate cell-laden constructs;
- To assess SSCs viability and functionality when printed in three-dimensional lattice scaffolds;
- To determine the integration on the membrane and angiogenic potential of printed lattice scaffolds of different dimensions after implantation in a chick chorioallantoic membrane model;
- To investigate membrane integration and angiogenic potential of VEGF-absorbed, HUVECs-seeded or the combined effect of these after implantation in an *ex vivo* chorioallantoic membrane model.

Overview of Chapter 4:

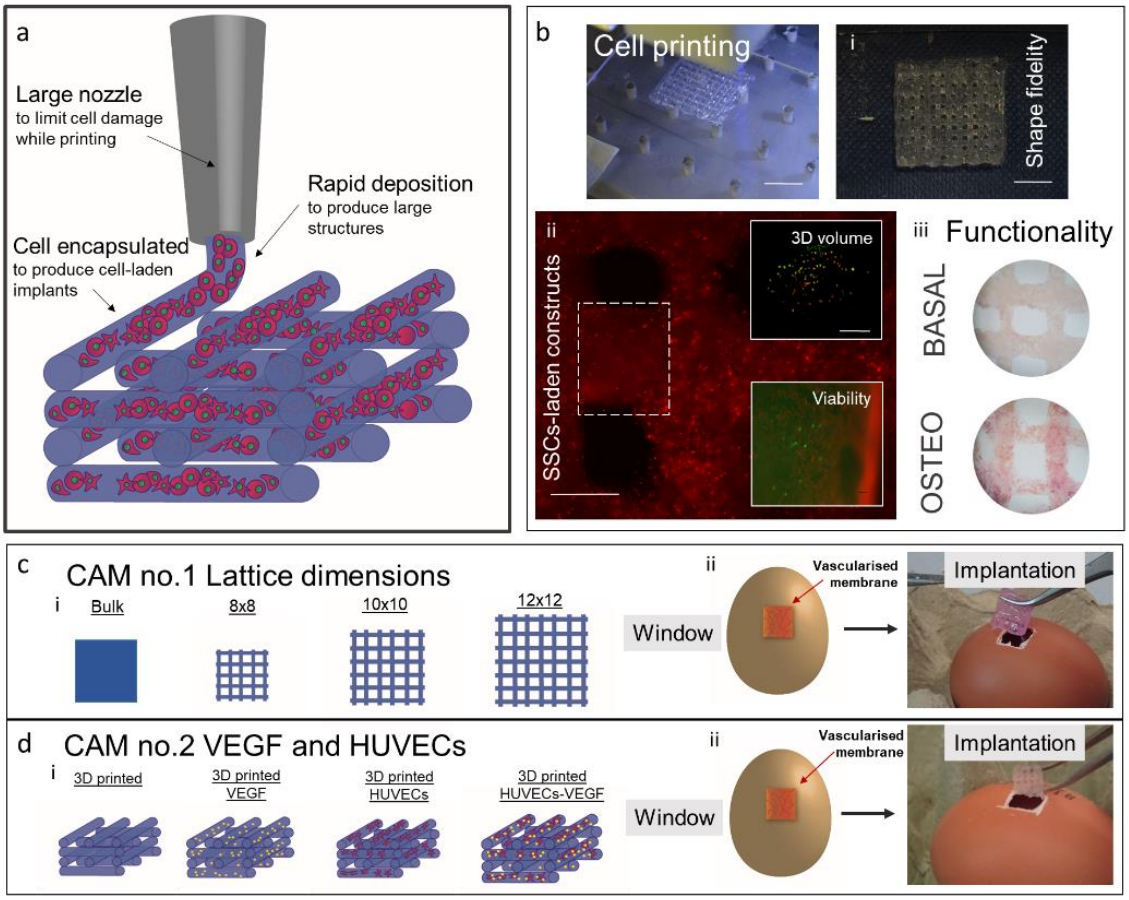

Figure 4.1. Schematic of skeletal stem cell printing.

Three dimensional lattice deposition (a) of SSCs. A large nozzle (410 µm) can be used to allow safe deposition of cells without affecting shape fidelity. Rapid deposition is essential to produce large structures. Cells can be encapsulated in the bioink before printing to deposit cell-laden strands in three-dimensions. Printed SSCs-laden scaffolds (b-i) are regular in shape and (b-ii) large SSC constructs fabricated. Functionality evaluated *in vitro* by alkaline phosphatase staining (b-iii) following culture in basal or osteogenic media. Further functionality assessed using the *ex vivo* CAM model (c). Effect of lattice dimensions (c-i) and VEGF and human umbilical vein endothelial cells (HUVECs) (d-i) when implanted in CAM window (c,d-ii). Scale bar: (b) 5 mm, (b-i) 5 mm, (b-ii) 1 mm, 100 µm, 50 µm.

4.2 Methods

4.2.1 Skeletal stem cell isolation

This methodology is detailed in Chapter 2 (2.1.3 page 41)

4.2.2 Laponite-alginate-methylcellulose bioink synthesis

This methodology is detailed in Chapter 2 (2.3.1 page 2.3.146)

4.2.3 SSCs printing

SSCs were isolated from multiple donors. Unselected hBMSCs and Stro-1^+ from male donors (M68 and M70) for donor variability study and unselected hBMSCs from a female donor (F76) were also used for viability/functionality investigation. The cells were encapsulated in 3-3-3 bioink and printed in a 10 × 10 mm^2 construct. Printing was carried out using an in-house built bioprinter (2.4.1 page 49) to fabricate 4 layer scaffolds with pores of 2 mm. An AA/BB pattern was followed, as detailed in Chapter 2 (2.4.2.1 page 53). Prior to printing, cells were pre-labelled following protocol detailed in Chapter 2 (2.5.3 page 56). A final density of 0.5 × 10^6 cell ml^{-1} (M68 and M70) and 1 × 10^6 cell ml^{-1} (F76) was encapsulated in 3-3-3, mixed with a sterile spatula, and loaded in a 10 ml sterile syringe (Becton Dickinson, BD, UK). A 410 µm conical nozzle (Fisnar Europe, UK) was used to manufacture cell laden scaffolds. Scaffolds for donor variability study were sequentially printed (n=5 per patient) to typically maintain in culture 5 scaffolds to be used in each time point. Scaffolds for viability and functionality investigations were printed (total: n=60) to typically cultivate 5 and 6 scaffolds to be used every time point for viability and functionality (ALP staining and CT scanning), respectively. Scaffolds printed in excess, were maintained in culture *in vitro* as supplementary samples in case of need.

4.2.4 Viability and proliferation of printed SSCs

This methodology is detailed in Chapter 2 (2.5.4 page 57)

4.2.5 SSCs attachment to 3D printed scaffolds

Scaffolds were printed following a protocol detailed in Chapter 2 (2.4.2.1). SSCs from multiple patients (unselected hBMSCs and Stro-1^+ from male (M68 and M70) donors) were isolated following procedure detailed in Chapter 2 (2.1.3 page 41). Scaffolds after printing were allowed to reach swelling stability in full cell culture media for 3 h at 37°C and 5 % CO_2 balanced air. Cells were labelled, prior to seeding, with a red DiD lipophilic dye detailed in Chapter 2 (2.5.3 page 56). Cells were seeded at an initial concentration of 0.3×10^6 cell ml^{-1} and allowed to attach at 37°C and 5 % CO_2 for 1 and 3 days. Scaffolds were then washed with HBSS and fixed with 3.7 % formaldehyde for 60 min at room temperature. Scaffolds were washed with HBSS (×3) to remove excess formaldehyde and a 5 min incubation at room temperature with 0.1 % Triton X100 was carried out. HBSS washes (× 3) were carried out. A solution of 3 % BSA was used for 60 min to block autofluorescence of the scaffold material. BSA solution was then removed. A solution containing 25 µl/ml phalloidin (Alexa Fluor 488 phalloidin, Invitrogen, A12379) in 3 % BSA was then used to stain adherent cells. An incubation of 60 min was carried out. HBSS was then used to wash thoroughly the stained scaffolds. Scaffolds were maintained in fresh HBSS and imaged right after with a confocal laser scanning microscope (Leica TCS SP5, Leica Microsystems, Wetzlar, Germany).

4.2.6 SSC-laden scaffolds functionality *in vitro*

This methodology is detailed in Chapter 2 (2.1.4 page 42, 2.5.5 page 57 and 2.9 page 64). Scaffolds were produced with the same cell density (F76) reported in the paragraph 4.2.3. Bulk scaffolds were generated by cell-laden 3-3-3 bioink loading in a 2.5 ml sterile syringe (Becton Dickinson, BD, UK) and slip tip removed with a sterile scalpel. The cell-laden bioink was extruded and 100 µl cylinders were produced, collected with a scalpel and

immediately crosslinked for 10 min in 10 mM $CaCl_2$ solution. Initial weight of the cylinders was registered and recorded (n=3, 0.05 ± 0.02 g) for the generation of 3D printed scaffolds of similar weight (n=3, 0.06 ± 0.03 g). Bulk alginate cell-laden constructs of similar weight (n=3, 0.06 ± 0.02 g) and cultured in osteogenic conditions, were chosen as control. Scans were analysed in by normalisation with cell-free 3-3-3 and alginate materials. CT scanning was carried out using Al 0.1 mm filter and 18 µm resolution.

4.2.7 CAM assay

4.2.7.1 Sample fabrication

Scaffolds were printed using sterile 3-3-3 bioink, prepared following protocol reported in Chapter 2 (2.3.1 page 46). For a first CAM study, scaffolds of different dimensions, with 8, 10 and 12 mm side length, were fabricated (n=6 for each treatment group). Scaffolds were fabricated, stored at 4°C and implanted the next day. For a second CAM study, scaffolds were produced with a 10 × 10 mm lattice base area and 2.5 mm pores. Acellular scaffolds (n=6 for each treatment group) were divided into four groups: i) 3D printed (n=6), ii) 3D printed loaded with VEGF (n=6), iii) 3D printed seeded with HUVECs (n=6) and iv) 3D printed seeded with VEGF and loaded with HUVECs (n=6). Scaffolds were then allowed to reach swelling stability in full cell culture media for 3 h at 37°C and 5 % CO_2 balanced air. HUVECs were seeded at a density of 0.6×10^6 cell ml^{-1} onto printed scaffolds (n=12). Seeded scaffolds were placed onto a rocket shaker at 37°C and 5 % CO_2 balanced air overnight. For the first 3 h of incubation, the cell suspension was regularly collected and pipetted again onto the scaffold to allow a greater number of HUVECs to attach. After 16 h, seeded scaffolds were washed with HBSS. Recombinant human VEGF 165 (Peptrotech, USA) was diluted to 100 µg ml^{-1} in HBSS solution and pipetted onto the printed scaffolds. VEGF was absorbed onto printed scaffolds (n=12) for 60 min (being VEGF half-life reported to be 90 min at room temperature) maintaining well plates in close contact with ice. HBSS was used to wash out unbound VEGF. All scaffolds were left to dry 10 min before implantation, avoiding retention of any residual solution.

4.2.7.2 Implantation, extraction and Chalkley score

This methodology is detailed in Chapter 2 (2.7.2 page 61 and 2.7.3 page 62)

4.2.8 Histological analysis

This methodology and specific staining are reported in Chapter 2 (2.10 page 65 and 2.10.1 page 65)

4.2.9 Statistical analysis

This methodology is detailed in Chapter 2 (2.11 page 66). Statistical evaluation of quantitative results is reported within the caption of the representative figures.

4.3 Results

4.3.1 Printing of SSCs in Laponite-Alginate-Methylcellulose hydrogel preserved viability and proliferation

HBMSCs were encapsulated at a low density (< 0.5 × 10^6 cell ml^{-1}) and printed using the 3-3-3 hydrogel. Two donors were selected to compare donor variation. Viability (Figure 4.2 a) was investigated via analysis of confocal stack images of cell-laden 3D printed scaffolds. Unselected HBMSCs from patient 1 showed an increase in viability from 73.07 ± 2.30 % (day 1) to 77.62 ± 4.21 % after 7 and 85.78 ± 5.04 % after 21 days ($p<0.01$). Similarly, HBMSCs from patient 2, printed in 3-3-3 hydrogel, showed an increase in viability from day 1 (78.33 ± 2.07 %), 7 (81.65 ± 3.05 %) up to 21 (86.84 ± 7.46 %) ($p<0.05$). Stro-1^+ were encapsulated and printed in 3-3-3 hydrogels to harness the skeletal differentiation potential of the selected HBMSCs population. Stro-1^+ cells from the first donor were viable after printing with an estimated viability of 84.00 ± 4.04 %, 86.81 ± 6.24 % and 92.30 ± 9.18 % after 1, 7 and 21 days, respectively. Selected Stro-1^+ population of cells from the second donor were printed and viability investigated at day 1 (84.84 ± 1.92 %), 7 (87.18 ± 4.85 %) and 21 (92.46 ± 9.28 %). A significant difference was found between the unselected BMSCs from the first donor and Stro-1^+ cells from first ($p<0.05$) and the second ($p<0.01$) donor at day 1. A further significant difference was found after 7 days between the unselected cells from the first donor and the selected population from the second donor ($p<0.01$).

Cell density (Figure 4.2 b) was investigated to give an indication of SSC proliferation potential after printing. Basal value on day 1 was set as 100 % and analysis at 7, 14 and 21 days determined. HBMSCs from patient 1 were highly proliferative at 7 days (247.36 ± 1.12 %) and 14 (328.94 ± 2.97 %) after printing ($p<0.0001$). A significant increase ($p<0.0001$) in cell proliferation was observed after 21 days of culture (736.84 ± 1.36 %). Proliferation of HBMSCs from the second patient were found to be significantly increased ($p<0.0001$) from 7 (161.70 ± 1.37 %) and 14 days (240.42 ± 2.08 %) up to 21 days (491.48 ± 2.76 %) following printing. Stro-1^+ cell populations isolated from the first patient initially slowed in proliferation (71.09 ± 0.82 % after 7 days), but reached a significant increase ($p<0.0001$) at 193.65 ± 2.82 % and 365.71 ± 3.40 % after 14 and 21 days respectively. Selected Stro-1^+ cells from the second donor reached 155.35 ± 2.38 % after 7 days of culture. However, cell-laden scaffolds appeared not to proliferate after 14 days (146.43 ± 1.03 %) and to then double, reaching a significant difference ($p<0.0001$) after 21 days of culture (301.34 ± 3.44 %).

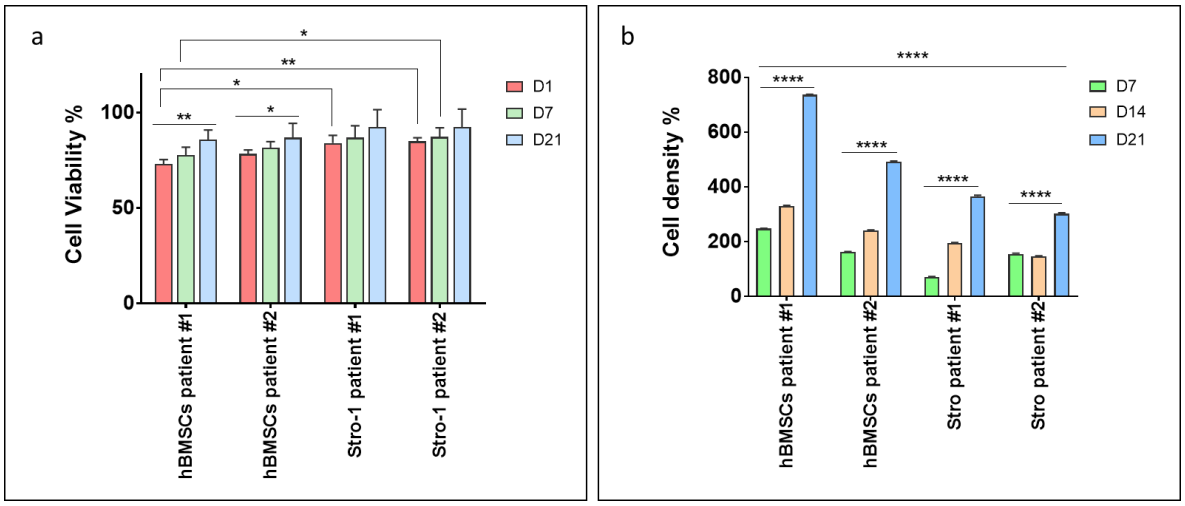

Figure 4.2. SSC-laden scaffolds viability and proliferation over 21 days.

Donor and selected compared to non-selected SSCs was investigated. Cell viability (a) was determined from confocal stack images of SSC-laden scaffolds. Statistical significance assessed by two-way ANOVA followed by Tukey's (a) and Dunnett's (b) multiple comparison tests. Mean ± S.D. n=5, *p<0.05, **p<0.01, ****p<0.0001.

Attachment of SSCs onto 3-3-3 scaffolds was carried out to determine the ability of the scaffold to sustain cell adhesion and spreading as well as encapsulation. Cells were seeded without any mechanical aid (e.g. bioreactors, stirring plate) onto 3D printed scaffolds at low density (< 0.5×10^6 cell ml^{-1}) to investigate attachment and proliferation potential. Static seeding was performed by inserting cell suspension on top of the printed lattice scaffold and left to attach by simple gravitational forces. HBMSCs isolated from patient 1 and patient 2 were found to attach to the 3-3-3 printed scaffold after 1 day of static seeding (Figure 4.3 a,b and Figure 4.3 c,d, respectively). After 7 days of incubation at 37°C and 5 % CO_2, scaffolds seeded with patient 1 (Figure 4.3 e,f) and patient 2 (Figure 4.3 g,h) cells were imaged. Proliferation of unselected HBMSCSs from the second donor compared to the first patient was observed. Stro-1^+ stem cells from patient 1 (Appendix C Figure 4.1 a,b) and patient 2 (Appendix C Figure 4.1 c,d) were also investigated for attachment on 3-3-3 scaffolds. After 1 day, single cells were observed on the scaffold due to the initial static low density seeding. After 7 days, Stro-1^+ cells from the first donor (Appendix C Figure 4.1 e,f) displayed limited proliferation, whereas cells from the second donor (Appendix C Figure 4.1 g,h) appeared static with no apparent proliferation.

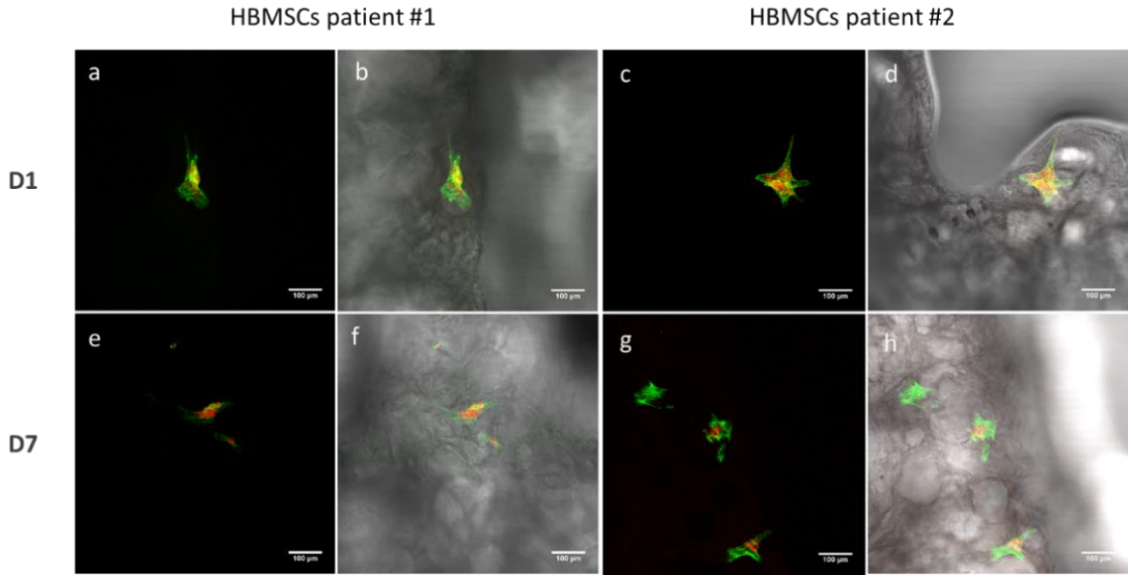

Figure 4.3. 3D printed scaffolds seeded with HBMSCs.

Seeding was carried out at a low density to assess cell attachment. Scaffolds were fixed and imaged by confocal microscopy following staining with Alexa fluor 488 (phalloidin) after a pre-stain with Vybrant DiD (red). After 1 day, scaffolds seeded with HBMSCs from patient 1 (a,b) and patient 2 (c,d) donor were imaged. Incubated for 7 days, scaffolds seeded with HBMSCs from patient 1 (e,f) and patient 2 (g,h) donors were assessed for proliferation. Scale bar: (a-h) 100 µm.

4.3.2 *In vitro* SSCs-laden nanocomposite characterisation display viability, sustained proliferation and immediate functionality

To evaluate functionality, other than viability and proliferation, HBMSCs from a single donor were encapsulated into 3-3-3 hydrogel at elevated seeding density (1×10^6 cell ml^{-1}). As undertaken in Chapter 3, DiD (red) labelling solution was used to stain cells prior to encapsulation in the 3-3-3 paste. DiD signal was considered independent from cell viability calculations. Constructs were maintained in culture and imaged at 1 (Figure 4.4 a), 7 (Figure 4.4 b), 14 (Figure 4.4 c) and 21 (Figure 4.4 d) days.

Cells were observed to preserve a rounded morphology for up to 21 days, showing no evident signs of cell spreading in three-dimensions. HBMSCs viability (Figure 4.4 e) was quantified following image analysis processing. Viability was measured at day 1 (81.08 ± 13.32 %), day 7 (88.05 ± 6.77 %), day 14 (88.33 ± 9.17 %) and day 21 (88.79 ± 8.02 %). After 7 days of culture, the density of HBMSCs encapsulated in 3-3-3 (Figure 4.4 f) was found to be significantly higher ($p<0.0001$) than at day 1 (152.09 ± 13.39 %). Following a further 7 days of culture, the cell density was observed to significantly decrease ($p<0.0001$) (day 14, 108.96 ± 7.09 %) and to subsequently plateau after 21 days (119.18 ± 11.60 %).

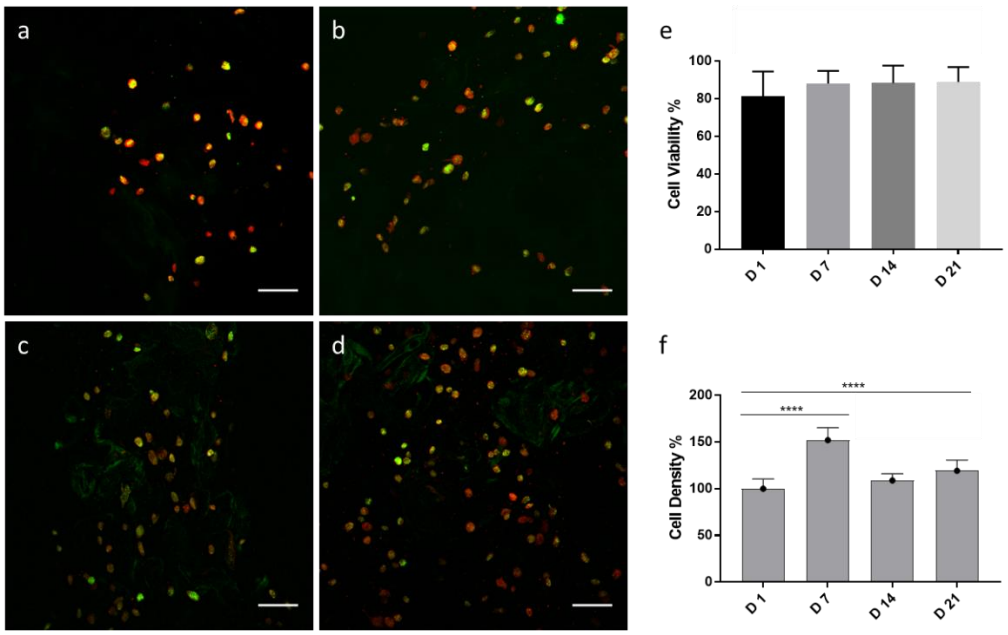

Figure 4.4. HBMSCs-laden 3D printed nanocomposite scaffolds *in vitro* viability.

Confocal microscopic images of SSCs-laden scaffolds at (a) 1, (b) 7, (c) 14 and (d) 21 days of *in vitro* incubation. All cells were stained with DiD labelling solution (red) while mitotically active cells were stained with Calcein AM (green). Cell viability (e) and (f) density quantification. Cell viability percentages were obtained from the calculated difference between viable and total cells. Dead cells were assumed to comprise the fraction not stained with Calcein AM. Scale bar: 100 µm. Statistical significance assessed by one-way ANOVA followed by Tukey's multiple comparison tests. Mean ± S.D. n=3, ****p<0.0001.

HBMSCs encapsulated in 3-3-3 were printed and investigated for differentiation *in vitro*. ALP staining was performed on cell-laden 3D structures after 1, 7 and 21 days of culture in basal (Figure 4.5 a-i) and osteogenic (Figure 4.6 a-i) conditions. Full cross-sections of 3D deposited fibres illustrated ALP expression decreased from 1 to 21 days (Figure 4.5 a-c) following culture in basal media. 3-3-3 constructs in basal media showed extensive expression of ALP at day 1 (Figure 4.5 d) particularly localised in areas of high cell density (Figure 4.5 e). After 7 days (Figure 4.5 f) ALP expression decreased, with a lack of staining throughout the 3D structure (Figure 4.5 g). At day 21 of culture in basal media (Figure 4.5 h) scaffolds showed limited ALP staining with cells coalescing into cluster shapes (Figure 4.5 i). ALP expression of osteogenic conditioned scaffolds resulted in a decrease from day 1 (Figure 4.6 a) to day 7 (Figure 4.6 b) and 21 (Figure 4.6 c). When cultured in osteogenic media, scaffolds displayed a higher degree of ALP staining at day 1 (Figure 4.6 d) compared to basal media (Figure 4.5 d). HBMSCs-laden scaffolds presented increased staining in proximity to cells encapsulated within 3-3-3 material (Figure 4.6 e). Scaffolds cultured for 7 days (Figure 4.6 f) showed limited signs of ALP expression, localised only in numbers of cell clusters (Figure 4.6 g). After 21 days of culture in

osteogenic conditions (Figure 4.6 h) encapsulated cells displayed negligible ALP staining (Figure 4.6 i).

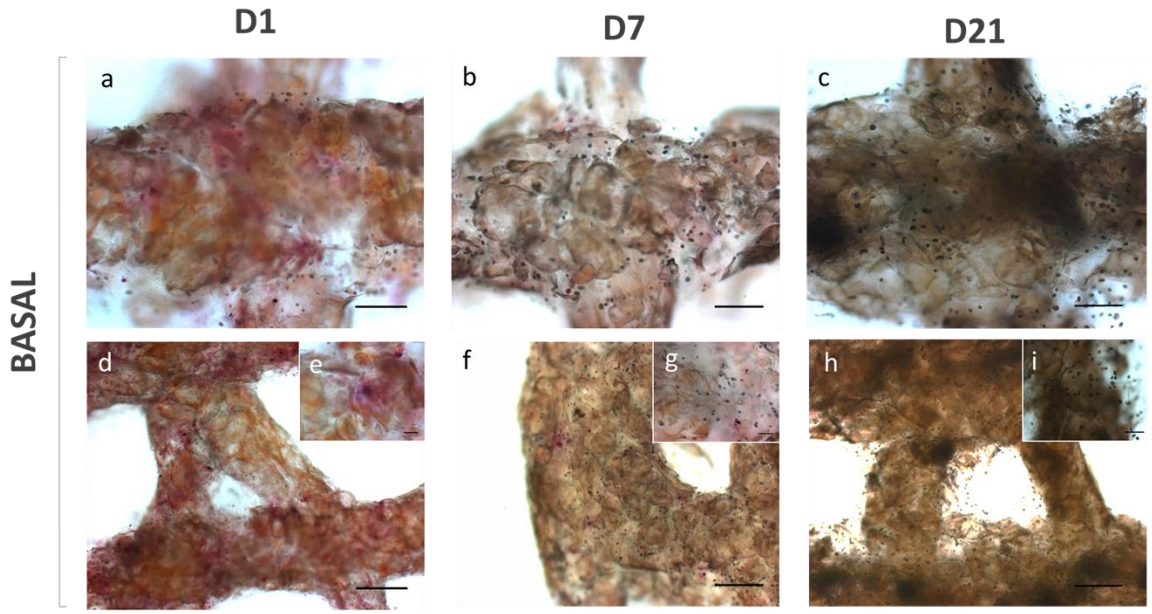

Figure 4.5. Alkaline phosphatase expression of HBMSCs-laden lattice scaffolds cultured in basal media.

Cross-sections of printed strands imaged after (a) 1, (b) 7 and (c) 21 days. Magnified brightfield images of basal cultured scaffolds show ALP staining at (d,e) day 1, (f,g) 7 and 21 (h,i). Scale bar: (a-c) 250 µm, (d,f,h) 500 µm, (e,g,i) 50 µm.

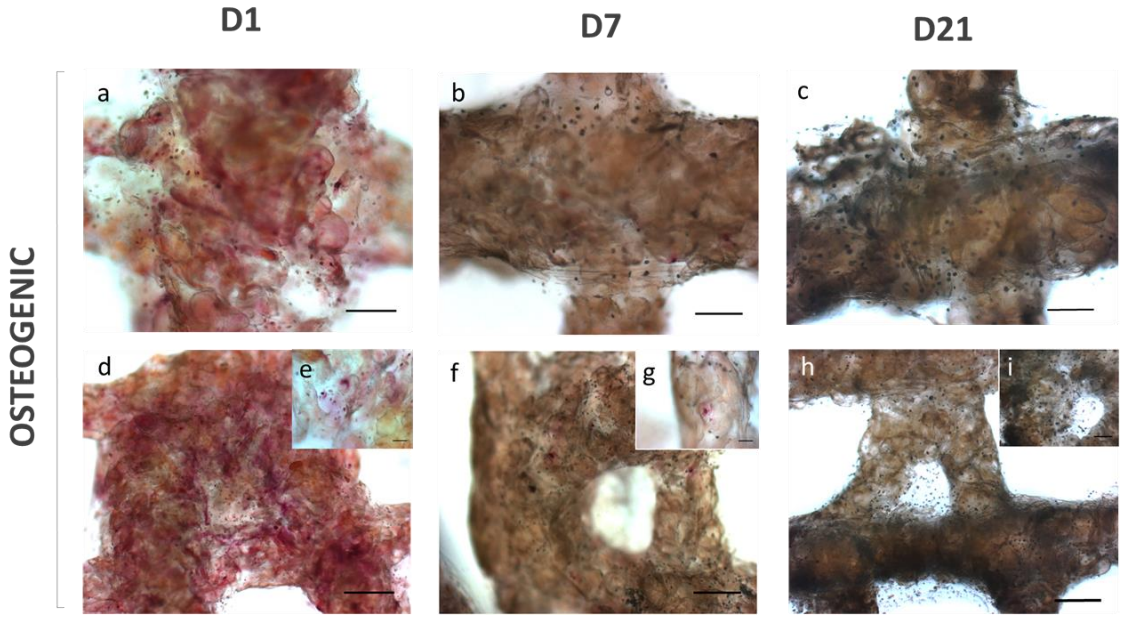

Figure 4.6. Alkaline phosphatase expression of HBMSCs-laden lattice scaffolds cultured in osteogenic media.

Cross-sections of printed strands were imaged after (a) 1, (b) 7 and (c) 21 days. Magnified brightfield images of osteogenic cultured scaffolds show ALP staining at (d,e) day 1, (f,g) 7 and 21 (h,i). Scale bar: (a-c) 250 µm, (d,f,h) 500 µm, (e,g,i) 50 µm.

To further assess the functionality of 3D printed scaffolds, long-term culture was performed and mineral deposition was quantified via micro-CT of printed scaffolds cultured in basal (figure 4.7 a) and osteogenic (Figure 4.7 b) media, and bulk scaffolds maintained in basal (Figure 4.7 c) and osteogenic (Figure 4.7 d) media.

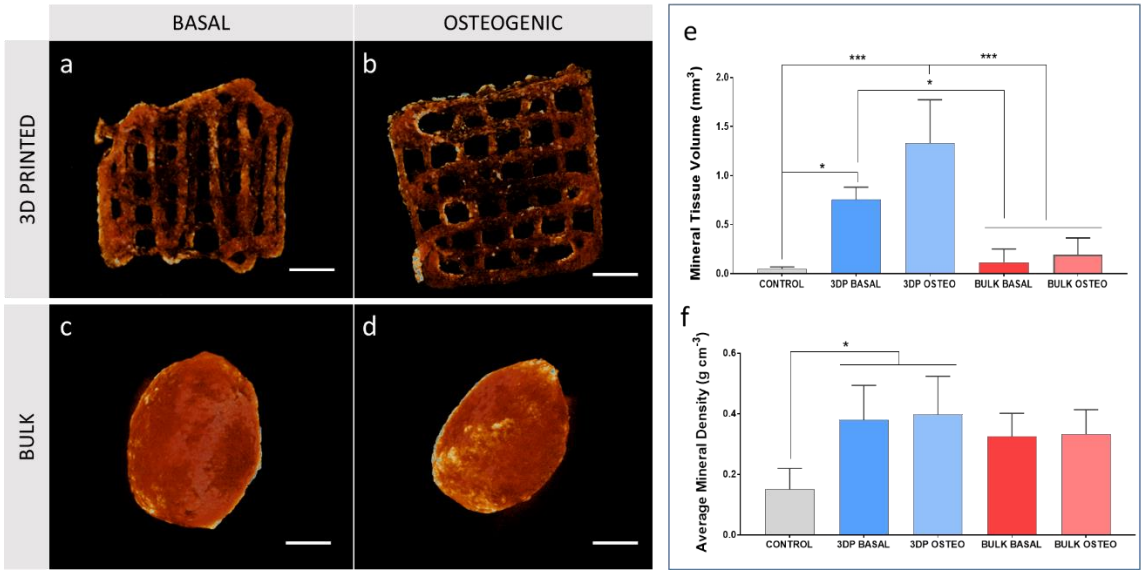

Figure 4.7. Functionality assessment using micro-CT analysis after 45 days of culture *in vitro*.

Scaffolds were 3D printed and cultured in basal (a) and osteogenic (b) media. Control scaffolds were fabricated in a bulk shape and cultured in basal (c) and osteogenic (d) media. Mineral volume (e) and average mineral density (f) were quantified via CTAn analysis. Scale bar: (a-d) 2 mm. Statistical significance assessed by one-way ANOVA with Tukey's multiple comparison tests. Mean ± S.D. n=3, *p<0.05, ***p<0.001.

Mineral tissue volume measurements (Figure 4.7 e) revealed1.33 ± 0.44 mm^3 of mineral content in cell-laden 3D printed scaffolds cultured under osteogenic conditions significantly greater ($p<0.001$) than control (0.05 ± 0.02 mm^3) and bulk cast gels cultured in basal (0.11 ± 0.13 mm^3) and osteogenic (0.19 ± 0.17 mm^3) media. Basal conditioning of cell-laden 3-3-3 printed scaffolds resulted in 0.75 ± 0.12 mm^3 of mineral deposition, significantly greater ($p<0.05$) than control and bulk basal samples. Basal 3D printed scaffolds were found to show a significantly ($p<0.05$) greater mineral volume than control. Average mineral density analysis (Figure 4.7 f) revealed a similar average density between basal (0.38 ± 0.11 g cm^{-3}) and osteogenic (0.39 ± 0.12 g cm^{-3}) conditioned 3D scaffolds and basal (0.32 ± 0.07 g cm^{-3}) and osteogenic (0.33 ± 0.08 g cm^{-3}) bulk scaffolds. The average mineral density of basal and osteogenic conditioned 3D printed scaffolds resulted significantly greater ($p<0.05$) compared to control (0.15 ± 0.07 g cm^{-3}).

4.3.3 3-3-3 bioink functionality evaluation using an *ex vivo* chorioallantoic (CAM) model

Acellular 3D printed scaffolds were implanted in the vascularised CAM of a 10 day old developing chick embryo. Cast bulk scaffolds (Figure 4.8 a) were used as a control. Scaffolds of increasing size (8 × 8 mm (Figure 4.8 b), 10 × 10 mm (Figure 4.8 c) and 12 × 12 mm (Figure 4.8 d)) were implanted through a 1 cm^2 window on the eggshell.

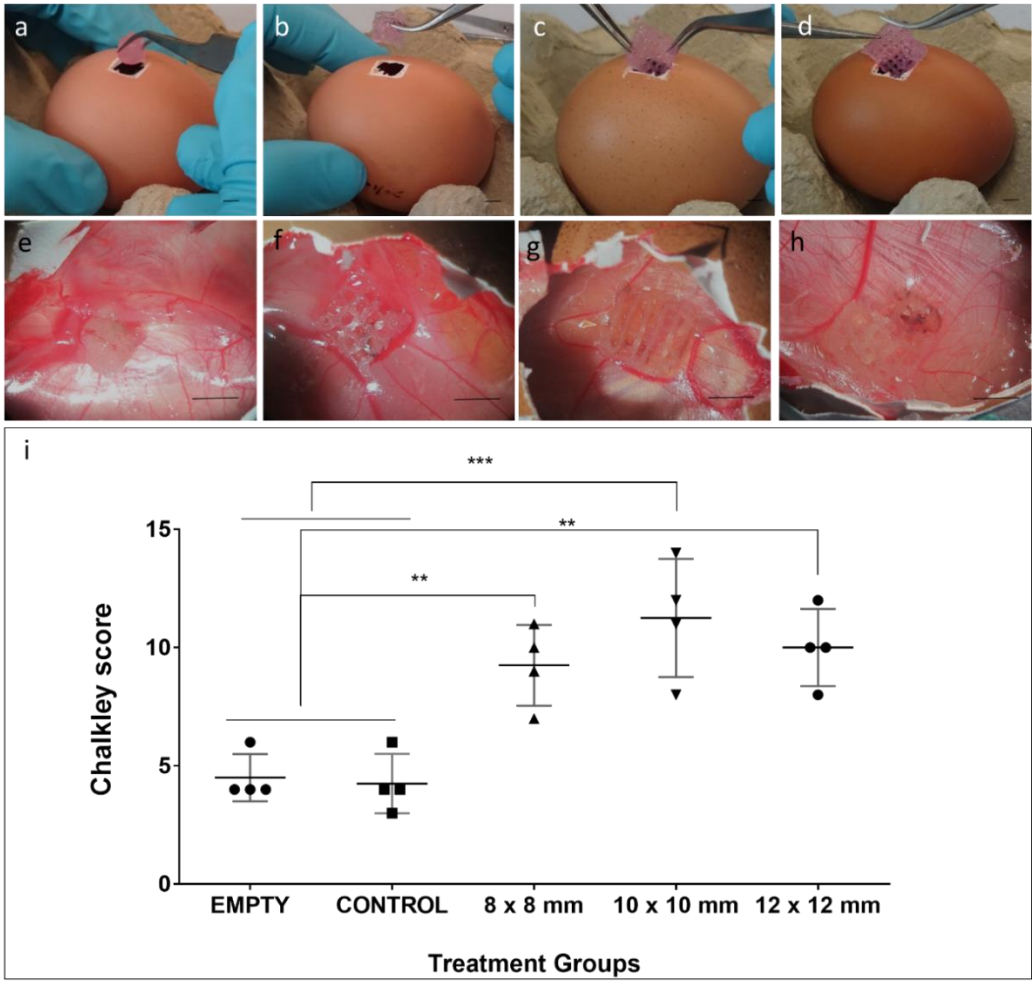

Figure 4.8. *Ex vivo* implantation study of acellular scaffolds in CAM model.

(a) Control bulk, (b) 8 × 8 mm, (c) 10 × 10 mm and (d) 12 × 12 mm 3D printed 3-3-3 scaffolds implanted in 10 day old developing chicken embryo. Macrographs of (e) bulk, (f) 8 × 8 mm, (g) 10 × 10 mm and (h) 12 × 12 mm scaffolds. Chalkley score (i) analysis performed on vascularised scaffolds. Scale bar: (a-d) 10 mm, (e-h) 5 mm. Statistical significance assessed by one-way ANOVA followed by Tukey's multiple comparison tests. Mean ± S.D. n=4, **p<0.01,***p<0.001.

After 7 days of incubation, control (Figure 4.8 e), 8 × 8 mm (Figure 4.8 f), 10 × 10 mm (Figure 4.8 g) and 12 × 12 mm (Figure 4.8 h) samples were assessed by Chalkley score for angiogenic activity (Figure 4.8 i). The score revealed a significant difference ($p<0.001$) between 10 × 10 mm group (11.25 ± 2.50) compared to the empty (4.50 ± 1.00) and control (4.25 ± 1.25) groups. Remaining groups (8 × 8 mm and 12 × 12 mm) scored 9.25 ± 1.71 and 10 ± 1.63 respectively, indicating reduced integration, but significantly higher vascular infiltration compared to empty and control groups ($p<0.01$).

Extracted samples were stained with Goldner's Trichrome (Figure 4.9).

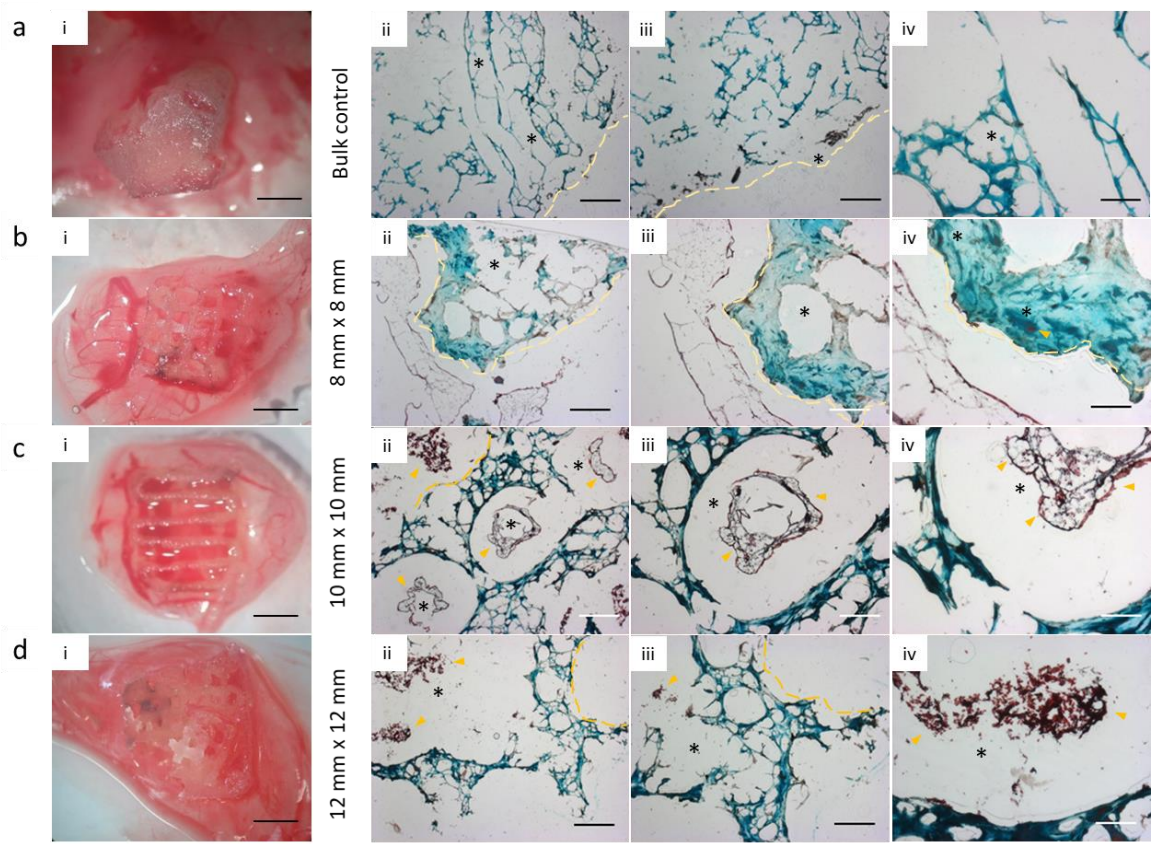

Figure 4.9. Histological analysis of CAM integrated 3D scaffolds.

Goldner's Trichrome staining was carried out on each group, and images were taken for (a-i,ii,iii,iv) bulk control, (b-i,ii,iii,iv) 8 × 8 mm, (c-i,ii,iii,iv) 10 × 10 mm and (d-i,ii,iii,iv) 12 × 12 mm scaffolds. Yellow line delimitate scaffold and CAM interface, asterisks (*) in area of interests indicate vessels infiltrating printed pores, yellow arrows indicate intrinsic microporosity and erithrocytes in vessels near or through the 3-3-3 bioink. Scale bar: (a-i, b-i, c-i, d-i) 5mm, (a-ii, b-ii, c-ii, d-ii) 500 µm, (a-iii, b-iii, c-iii, d-iii) 250 µm, (a-iv, b-iv, c-iv, d-iv) 100 µm.

Control bulk scaffolds (Figure 4.9 a-i) revealed a porous internal structure (Figure 4.9 a-ii) with small vessels around the sample (Figure 4.9 a-iii) and negligible capillary penetration through the structure (Figure 4.9 a-iv). 8 × 8 mm scaffolds (Figure 4.9 b-i) showed limited blood vessel penetration (Figure 4.9 b-ii) through large pores (Figure 4.9 b-iii) but displayed a small number of capillaries integrated in the internal lattice structure (Figure 4.9 b-iv). 10

× 10 mm scaffolds (Figure 4.9 c-i) were found to be penetrated by major vessels throughout the pores of the scaffold (Figure 4.9 c-ii). Vessels within the pores appeared collapsed (Figure 4.9 c-iii), but maintained an intact endothelial layer. Interestingly, inner strand structures were not penetrated by capillaries (Figure 4.9 c-iv). 12 × 12 mm scaffolds (Figure 4.9 d-i) were integrated with the CAM. Vessels were found extensively in the large 12 mm^2 structure (Figure 4.9 d-ii) with capillaries penetrating through the printed strands (Figure 4.9 d-iii). Blood vessels were found within the pores and erythrocytes were visible (Figure 4.9 d-iv).

To investigate the functional effect of the angiogenic stimulant (VEGF) and endothelial cells (HUVECs) on 3D printed scaffolds, constructs were implanted into a CAM model.

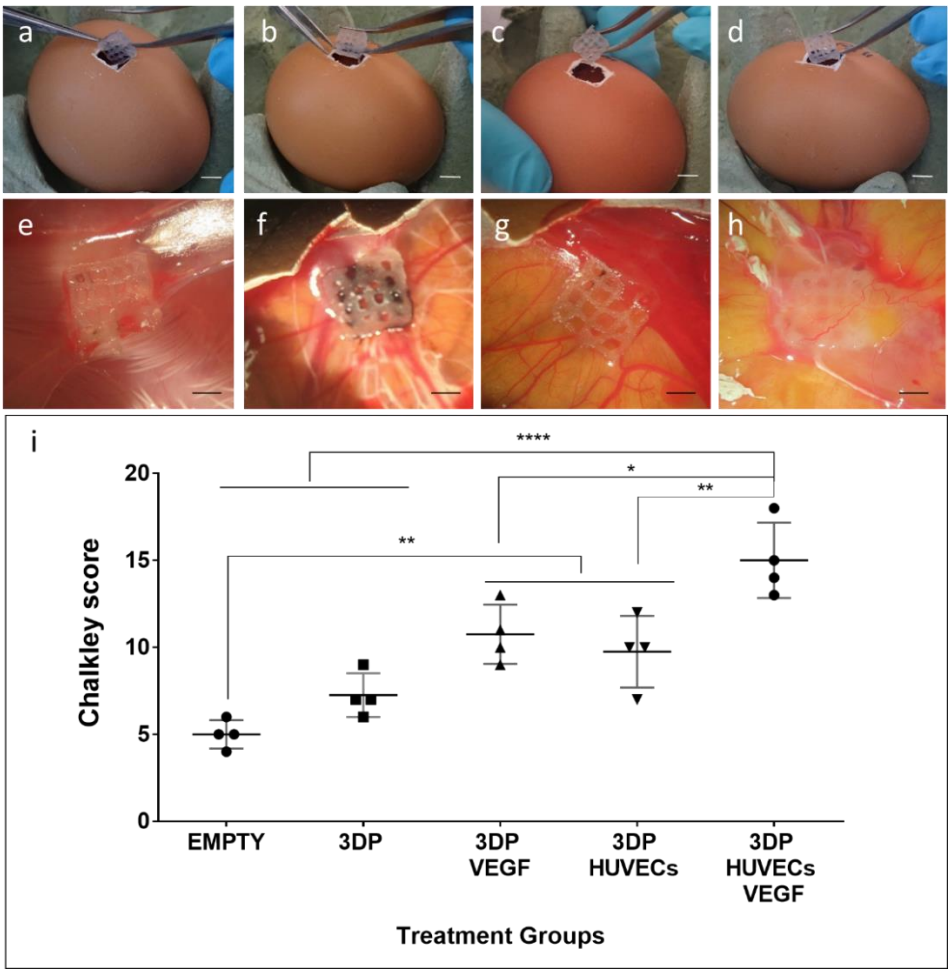

Figure 4.10. *Ex vivo* implantation study of VEGF and HUVECs conditioned scaffolds in CAM model.

(a) 3D printed control, (b) 3D printed scaffold loaded with VEGF, (c) 3D printed scaffold seeded with HUVECs and (d) 3D printed scaffold loaded with VEGF and seeded with HUVECs imaged following implantation in a 10 days old developing chicken embryo. Macrographs of (e) 3D printed control, (f) 3D printed scaffold loaded with VEGF, (g) 3D printed scaffold seeded with HUVECs and (h) 3D printed scaffold loaded with VEGF and seeded with HUVECs. Chalkley score (i) analysis performed on vascularised scaffolds. Scale bar: (a-d) 10 mm, (e-h) 5 mm. Statistical significance assessed by one-way ANOVA followed by Tukey's multiple comparison tests. Mean ± S.D. n=4, *p<0.05, **p<0.01, ****p<0.0001.

VEGF was loaded at 100 µg ml^{-1} into the bioink and HUVECS were seeded at low density (0.5×10^6 cells/scaffold). 3D printed blank scaffolds were implanted as control, (Figure 4.10 a), loaded with VEGF (Figure 4.10 b), seeded with HUVECs (Figure 4.10 c) or scaffolds were loaded with VEGF and seeded with HUVECs (Figure 4.10 d) – samples were run on the CAM for 7 days. 3D printed control scaffolds, (Figure 4.10 e), loaded with VEGF (Figure 4.10 f), seeded with HUVECs (Figure 4.10 g) and scaffold loaded with VEGF and seeded with HUVECs (Figure 4.10 h) were extracted and analysed for vascularisation as determined by the Chalkley score test (Figure 4.10 i). Scaffolds with VEGF (10.75 ± 1.71) and HUVECs alone (9.75 ± 2.06) displayed the highest infiltration of blood vessels ($p<0.01$) than egg samples lacking any scaffold (empty). 3D printed scaffolds loaded with VEGF and seeded with HUVECs (15.01 ± 2.16) showed a significant ($p<0.0001$) difference in vascular penetration compared to empty (5.00 ± 0.81) and control 3D printed scaffolds (7.25 ± 1.26). Combined VEGF and HUVECs with printed scaffolds resulted in a significantly greater effect than HUVECs seeded ($p<0.01$) and VEGF loaded alone ($p<0.05$).

Histological analysis of integrated samples revealed the limited penetration of blood vessels into the 3D printed control (Figure 4.11 a-i) scaffolds with some pores filled with clotted blood vessels (Figure 4.11 a-ii, a-iv) and areas lacking capillary penetration. VEGF-loaded scaffolds (Figure 4.11 b-i) were found to be infiltrated with vessels (Figure 4.11 b-ii) that displayed a clotted phenotype and lacked thin epithelial surrounding tissue found in Figure 4.9 c-iii. However, the presence of minor vessels penetrating through the printed structure (Figure 4.11 b-iii) and erythrocytes filling blood vessels (Figure 4.11 b-iv) confirmed scaffold integration and blood vessel penetration. HUVECs-seeded samples (Figure 4.11 c-i) were found to be extensively infiltrated by clotted vessels (Figure 4.11 c-ii) throughout the lattice pores with infiltration of minor capillaries (Figure 4.11 c-iii) within the inner printed structure. Major pores were observed displaying an irregular shape as a consequence of remodelling and *in vivo* degradation, filled with major blood vessels that were noted to be extensively clotted (Figure 4.11 c-iv).

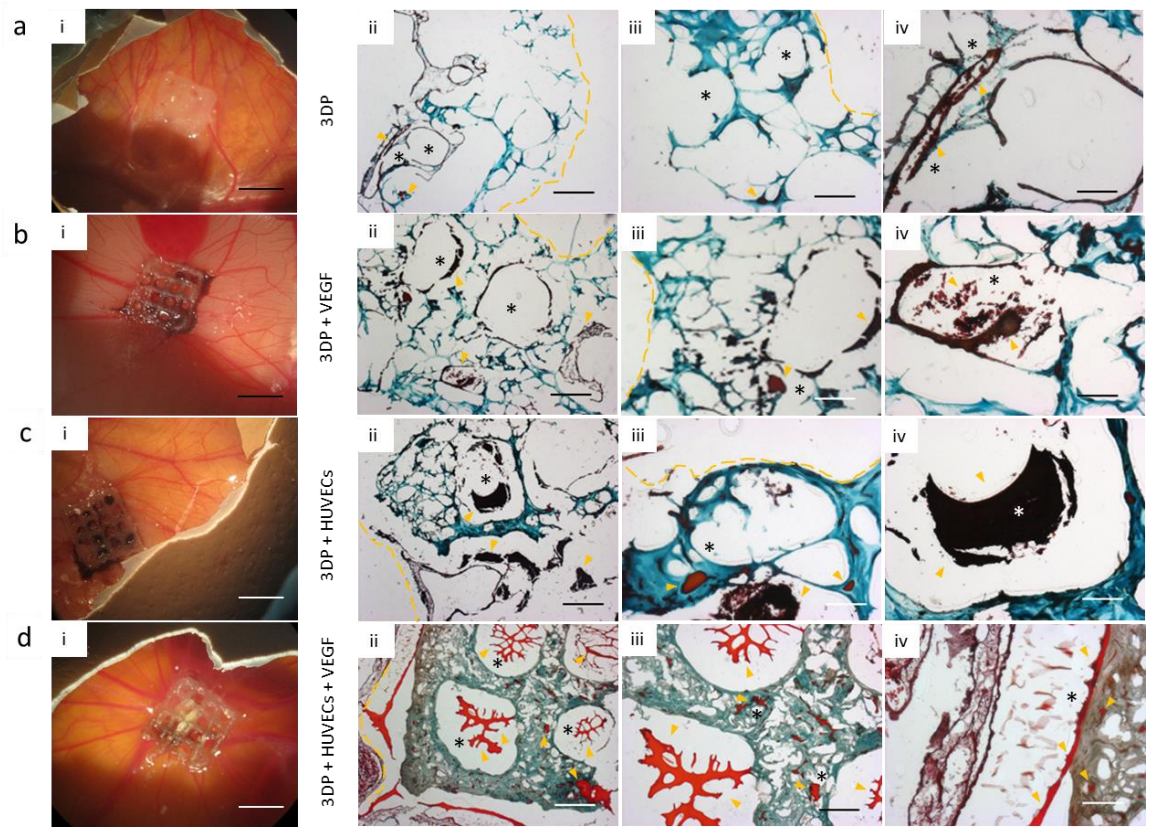

Figure 4.11. Histological analysis of CAM integrated 3D scaffolds.

Goldner's Trichrome staining performed for each group, and images were taken for (a-i,ii,iii,iv) 3D printed control, (b-i,ii,iii,iv) 3D printed scaffold loaded with VEGF, (c-i,ii,iii,iv) 3D printed scaffold seeded with HUVECs and (d-i,ii,iii,iv) 3D printed scaffold loaded with VEGF and seeded with HUVECs. Yellow line delimitate scaffold and CAM interface, asterisks (*) in area of interests indicate vessels infiltrating printed pores, yellow arrows indicate intrinsic microporosity and erithrocytes in vessels near or through the 3-3-3 bioink. Scale bar: (a-i, b-i, c-i, d-i) 5mm, (a-ii, b-ii, c-ii, d-ii) 500 µm, (a-iii, b-iii, c-iii, d-iii) 250 µm, (a-iv, b-iv, c-iv, d-iv) 100 µm.

3D printed scaffolds loaded with VEGF and seeded with HUVECs (Figure 4.11 d-i) were integrated with the CAM membrane (Figure 4.11 d-ii) with major vessels penetrating the pores of the printed structure (Figure 4.11 d-iii). Extensive penetration throughout the printed structure was visible with minor capillaries integrated with the scaffold cross-section (Figure 4.11 d-iii). Scaffolds were found blended with the CAM in the outer portion of the samples, with major vessels surrounding the scaffolds (Figure 4.11 d-iv) indicating the vascularisation of the inner, as well as the outer, portion of the printed construct.

4.4 Discussion

A clay-based hydrogel (3-3-3) developed and characterised in Chapter 3, has been utilised here for the first time as a bioink for SSCs delivery and three-dimensional cell-laden construct fabrication. The viscoelastic properties of the 3-3-3 were employed as the main characteristic for delivery of the bioink to generate large 3D scaffolds. The clay bioink allowed the fabrication of large structures 8 × 8 mm, 10 × 10 mm and 12 × 12 mm useful for further *in vivo* testing and potential future clinical application. The limited damage after printing of SSC populations confirmed following viability and proliferation assessments established the protective mechanism that the viscoelastic properties of the 3-3-3 provided to the encapsulated stem cells.

To investigate HBMSCs survival following printing, stem cells were encapsulated at a low density (< 0.5×10^6 cell ml^{-1}). Initially, a low cell-to-polymer ratio was chosen to evaluate viability and proliferative potential of HBMSCs from two patients as well as to assess donor-to-donor variability. As reported previously, cells entrapped in a three-dimensional matrix can start a degradation process by digestion of the surrounding hydrogel network occurs [62]. Cells will naturally tend to proliferate and aggregate forming intricate connections within a gel. Therefore, a low initial cell encapsulation density offers the potential to study the proliferative capacity of a cell population. In this study, cells remained viable after culture over 21 days regardless of donor or primary cell selection (unselected or Stro-1^+). Donor variability was expected to impair the initial viability of scaffolds due to a difference in proliferation rate observed during expansion and as previously reported *in vitro* [217]. However, the current results suggest similarity in viability percentage and attachment throughout the entire *in vitro* study even at the early stages (day 1). Nevertheless, when the cell density was evaluated, unselected HBMSCs from patient 1 proliferated at a higher rate compared to the selected Stro-1^+ portion and SSCs isolated from a second donor. Unselected HBMSCs displayed enhanced proliferation reaching higher cell encapsulated density independently from the particular donor. Stro-1^+ cell proliferation was observed within the printed lattice, but at a reduced rate, suggesting a smaller portion of selected cells remained viable compared to a similar fraction of unselected HBMSCs.

Further studies on encapsulation using high cell numbers (≥ 1×10^6 cells ml^{-1}) was carried out as high cell density can significantly affect the rheological properties of a bioink and consequently printability [148] and viability of fabricated cell-laden constructs [90]. Unselected HBMSCs from a single donor were encapsulated in 3-3-3 bioink at 1×10^6 cell ml^{-1} to evaluate post-printing viability and functionality. HBMSCs survived printing even at a high density and remained viable after 21 days of culture. Thus, a clay-based bioink

proved a reliable platform for cell delivery, preserving viability post-printing with minimal cell damage observed. Cell density was noted to increase linearly up to 7 days of culture and plateau at day 14. This phenomenon has been reported in the literature [218] where cells encapsulated at high density escape the soft hydrogel network. As a consequence, after 14 days of culture the number of cells mm^{-3} was found lower than post-printing. Interestingly, viability was not affected by this decrease in cell density. Cells present in the lattice structure were viable from day 14 to day 21 of culture.

Encapsulated cells were functional up to day 21 of culture *in vitro* when stimulated with basal and osteogenic media. This is notable, since enhanced ALP expression is rarely reported in SSCs-laden constructs at early time points (e.g. 3 days) [57] and, typically, is found extensively at later time points (between 1 and 2 weeks) [70,219]. ALP is an early osteogenic marker, expressed by HBMSCs during early cell culture [220]. Early expression of ALP and its decrease over time has been reported as necessary for bone nodule formation [221]. Interestingly, nodules were observed in 3D printed scaffolds by day 21 with a simultaneous significant reduction in the number of ALP stained encapsulated cells suggesting differentiation of encapsulated SSCs. Basal cultures of bone marrow stromal cells have been reported to express a highly decreased ALP expression at 20-25 days as compared to early (3-7 days) cell culture populations. Recently, Carrow *et al.* [93] reported a significant increase in ALP activity of SSCs cultured in the presence of nanodispersion of Laponite in the cell culture media, suggesting that the clay silicate biomaterial could promote osteogenic activity in cultured cells even in standard culturing techniques. Alginate/methylcellulose blend [69] was shown to be functionally active and to promote SSCs differentiation toward the adipogenic lineage. Combinatory effects of matrix stiffness (alginate/methylcellulose) and clay-mediated induction suggest the 3-3-3 bioink supports osteogenic differentiation of encapsulated SSCs cultured in osteogenic media. Functionality was further confirmed by micro CT scans of 3D printed scaffolds compare to a bulk control. Interestingly, the average mineral density was similar for all the samples and treatment groups indicating a uniform mineral deposition over 45 days *in vitro* culture of HBMSCs-laden constructs. Although Laponite mineralisation has not been fully understood *in vitro* [94], alginate gels have been found to show mineral deposition in the presence of calcium phosphates [222]. Discussion over mineralisation of 3-3-3 bioink will be carried out in details in Chapter 5.

Essential for bone formation is the presence of a vasculature within the bone forming construct [160]. The potential of 3D printed scaffolds to sustain vessel ingrowth and integration with host tissue were assessed using the chick chorioallantoic membrane model. Implantation of scaffolds with different dimensions proved the efficacy of a 10 mm^2 surfaced lattice structure with vessels penetrating through major pores. Indeed, vascular penetration

has been reported to occur in scaffolds with interconnected porosity, that might stimulate angiogenesis, even in absence of angiogenesis-inducing additives [223]. Moreover, it is known that three-dimensional scaffolds with larger pore sizes, greater porosity and increased pore size distribution can result in increased vascularisation [224]. Interestingly, when 3-3-3 printed scaffolds were implanted, micro-vasculature could be observed penetrating the printed fibres after 7 days of incubation, indicating further integration with the CAM and major advantages of 3D printed constructs. Indeed, neovascularisation was found in large (2 mm) printed pores and in fibre micro-porosity. The addition of VEGF or HUVECs was carried out to further stimulate integration and angiogenesis. 10 mm^2 lattice surface scaffolds were loaded with VEGF (similar to Chapter 3, 100 µg ml^{-1}) and resulted in integration with the CAM, with major blood vessels directly adherent to the scaffold with blood clots near the surface facing the CAM. Clotting of blood vessels was reported even in 3D printed samples seeded with endothelial cells. This phenomenon could be linked to excessive functional stimuli for the blood vessels of the chick membrane which could clot in the absence of anti-clotting agents. In particular, VEGF is known to stimulate vascular permeability [225], therefore a localisation of excessive VEGF might have induced the leakage of the CAM membrane capillaries forming the cloth as a consequence.

Stimuli such as VEGF and HUVECs can be further optimised to allow vascular induction reducing the leakage of blood vessels [226]. Dual HUVECs-seeded and VEGF-loaded scaffolds resulted in significant integration, with blood vessel penetration through major pores without clotting. Beneficial effect of VEGF on HUVECs have been previously reported [227]. Particularly, Dawson *et al.* [103] tested the effect of VEGF localisation in Laponite on HUVECs tubule formation and *in vivo*. Results in this chapter suggest the ability of clay-gel to stimulate angiogenesis both *in vitro* and *in vivo* following a brief exposure to VEGF. Similarly, 3-3-3 printed scaffolds were found to positively mediate HUVECs to absorbed VEGF exposure, functionally stimulating a greater membrane integration and neovascularisation as demonstrated by Chalkley score and histological analysis. However, fixative method (4% PFA), embedding (OCT medium) and cryosectioning induced the major vessels to collapse within the pores of the scaffold. Nevertheless, major vessels remained visible and were found to surround the scaffold structure. Micro-vasculature was found to extensively penetrate the printed scaffold, throughout the printed fibres, confirming superior integration of the implanted scaffolds.

4.5 Conclusions

The potential to print stem cells, preserving cell viability, proliferation and functionality is a key unmet challenge for the biofabrication approach to regenerative medicine. Clay-based bioinks offer an attractive vehicle for printing SSCs in three-dimensional constructs. In this chapter, the biofabrication potential of 3-3-3 bioink to sustain SSCs viability and functionality has been observed. Unselected and Stro-1^+ cells were viable after printing over 21 days, proliferating over time when encapsulated at low density. SSCs seeding on 3D printed 3-3-3 scaffolds showed rapid attachment of SSCs on printed structures. Encapsulation at an elevated density of HBMSCs resulted in stable viability for up to 21 days and maintenance of proliferative capacity over 7 days. Functionality of high-density scaffolds over 21 days resulted in a rapid HBMSCs differentiation within 24 hours of culture, with an extensive decrease of ALP expression up to 21 days. An *ex vivo* chick model was used for the first time to test biocompatibility of 3-3-3 scaffolds and their angiogenic potential when loaded with VEGF and seeded with HUVECs. A 10 mm^2 lattice surface was found to be optimal for integration. VEGF stimulated angiogenesis and HUVECs improved integration. Their combined effect on 3-3-3 scaffolds integration showed greater vessel penetration between interconnected printed pores and micro-vasculature infiltration within the printed structure.

Scaffold dimensions were found to affect the functional response *ex vivo,* therefore possibly an important consideration for *in vivo* studies. This finding would require further investigation since implantable printed scaffolds would results of different sizes depending on the defect region to repair. Moreover, the possibility to include high numbers of primary cells (1×10^6 cell ml^{-1}) would require long-term expansion of SSCs that could affect cell viability-functionality and delay possible implantation in the patient as needed. The current chapter has demonstrated the potential for a 3-3-3 bioink for further *in vivo* investigation. This is reported in the next chapter.

Chapter 5 *In vivo* evaluation of nanocomposite 3D printed scaffolds for bone regeneration

5.1 Introduction

Skeletal regeneration using innovative tissue engineering approaches has received considerable attention in recent years. Computer-aided cell and biomaterial deposition has shown great capacity in manufacturing complex and hierarchically organised constructs able to closely mimic bone structure [56]. Thus, printed constructs can be used to replace damaged tissue or as an *in vitro* drug screening platform [228]. Engineered tissues need to be tested in pre-clinical models to validate safety and efficacy of the tissue-like construct. For istance, the *in vivo* subcutaneous bone formation assay can be use for testing *de novo* bone formation where new mineralised tissue is formed in a contained envirornment (the implanted scaffold) after the stimulation of mineral deposition aid by chemical, physical or cellular cues [229,230]. Recently, *in vitro* model that may help replace, reduce and refine *in vivo* animal models have been developed and proven efficacious [231]. However, *in vivo* subcutaneous model still remain the gold standard for pre-clinical testing [232].

Acellular strategies are typically attractive, relying on the intrinsic functional properties of the printed material to attract host cells aiming for tissue integration [233]. A hyper-elastic bone (HB) construct printed with a blend made of poly(lactic-co-glycolic acid), PCL and hydroxyapatite (PLGA/PCL/HAp) has recently shown great potential for *in vivo* application [234]. The synthetic printed scaffold displayed tissue infiltration in a murine subcutaneous implant, bone ingrowth in a rat spinal fusion model and new bone formation in a macaque calvarial defect. These results suggested evidences for clinical potential as a bone cement substitute. However, this innovative acellular approach reported only limited bone ingrowth (aided by the inclusion of BMP-2 in the spinal fusion model) especially when implanted subcutaneously, possibly due to the inert properties of the material.

Pivotal for skeletal regeneration is the presence of SSCs, shown to actively participate in bone repair when encapsulated in functional hydrogel networks [235]. Biofabrication platforms alone [236] appear insufficient to aid complete and functional regeneration of bone tissue, and new bioinks are needed to allow the inclusion of SSCs within the implantable construct [148].

An attractive biofabrication solution to manufacture hard tissue implants is the co-deposition of thermoplastic fibres along cell-laden [86] bioinks. A rigid thermoplastic material can be layered in close proximity to cell-laden bioinks to aid further support during implantation, tissue remodelling and regeneration. Moreover, thermoplastic polymers are often non-functional, serving exclusively as a support material. The elevated temperature of deposition (60°C), required in the application of such thermoplastic polymers has not yet been entirely proven safe for cell-laden bioinks deposited next to the polymeric hard strand. Efficacious ectopic bone formation has been reported in biofabricated scaffolds implanted

in a mouse model [237]. PCL-reinforced alginate-based scaffolds were fabricated including non-human SSCs within an alginate bioink. The PCL-bioink constructs, implanted subcutaneously in a murine model, showed elevated bone volume formation when compared to bioink (PCL-free) scaffolds after 12 weeks implantation. However, the requisite for: i) SSCs from xenogenic sources (raising the risk of implant rejection), ii) high cell numbers (20×10^6 cells ml^{-1}) and iii) pre-implantation culture for cartilage differentiation for 4 weeks (to guide endochondral bone formation) preclude immediate clinical translation of such an approach. As bioprinted tissues develop *in vivo*, the tissue should be amenable to remodelling, facilitating the formation of structures driven by cellular and physiological requirements [196]. Hydrogel-like biomaterials can actively facilitate this process with the inclusion of a drug delivery system (e.g. plasmid DNA [238]) or living stem cells (e.g. HBMSCs [57]).

In this chapter, three-dimensional scaffolds fabricated with a 3-3-3 hydrogel bioink (developed in Chapter 3 and assessed for *in vitro* and *ex vivo* functionality in Chapter 4) were examined *in vivo.* This chapter will detail the large 3D printed constructs (Figure 5.1 a) fabricated (acellular and comprising BMP-2 or HBMSCs) and implanted subcutaneously in murine models (Figure 5.1 b,c) to evaluate ectopic bone formation.

Hypothesis (III):

Laponite-alginate-methylcellulose bioink can be used to encapsulate growth factors (e.g. BMP-2) or SSCs (e.g. unselected HBMSCs) to aid bone formation ectopically *in vivo*. Printed scaffolds can improve BMP-2 retention and bone formation compare to alginate gels. SSCs encapsulated in printed bioink can enhance bone formation ectopically in comparison with acellular bulk or printed or cell-laden bulk scaffolds. 3D printed scaffolds can promote a greater effect in bone formation, mineralisation volume and density compare to the bulk constructs.

Aims:

- To investigate the effect of BMP-2-absorbed on printed scaffolds to generate bone tissue *in vivo* after implantation in a subcutaneous mouse model when compared to silicate free-alginate gels;
- To quantify and characterise mineralised scaffolds 4 weeks after implantation;
- To evaluate SSCs-laden printed scaffolds potential to form bone tissue after subcutaneous implantation in an athymic mouse model *in vivo* when compared to cell-free and cast controls;
- To quantify and characterise mineralised scaffolds 8 weeks post-implantation.

Overview of Chapter 5:

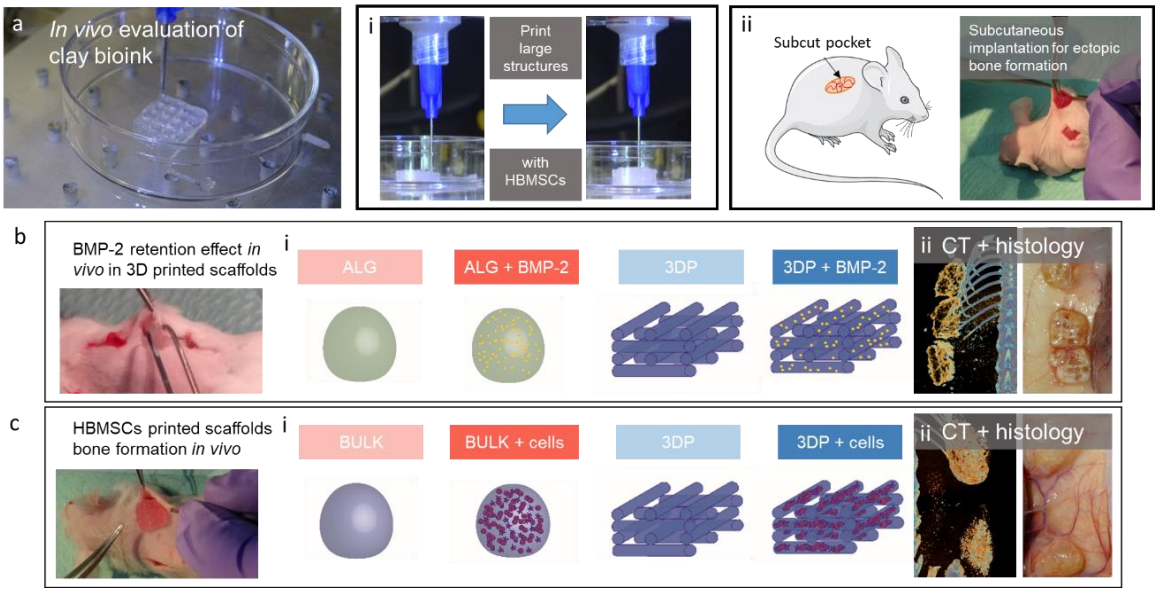

Figure 5.1. *In vivo* implantation of 3D printed scaffolds for ectopic bone formation investigation.

Large Laponite-alginate-methylcellulose (3-3-3) 3D printed structures laden with HBMSCs (a-i) were fabricated via layer-by-layer deposition. Implants were inserted subcutaneously (a-ii) in mice for ectopic bone formation investigations. Two studies were carried out. The first (b) investigated (i) BMP-2 effect comparing drug-free controls and bulk alginate with Laponite-alginate-methylcellulose 3D printed scaffolds loaded with BMP-2. CT images were acquired after 28 days (ii) and scaffolds were extracted and analysed histologically. The second (c) study investigated the effects of HBMSCs encapsulated (i) in bulk controls or in 3D printed scaffolds. CT images and histological analysis (ii) were performed to confirm bone formation at ectopic loci.

5.2 Methods

All animal procedures reported in this chapter were carried out with prior received ethical approval and carried out in accordance with the regulations as laid down in the Animals (Scientific Procedures) Act 1986. As part of the application for a project licence under which to perform the animal work (PPL numbers: 30/2880 & P96B16FBD), animal procedures in this study were reviewed and approved by the Scientific Review Group, part of the Animal Welfare and Ethical Review Body at the University of Southampton. All the *in vivo* studies detailed were carried out under the personal license numbered I7C4C7DE5.

5.2.1 Skeletal stem cells isolation

This methodology is detailed in Chapter 2 (2.1.3 page 41)

5.2.2 Alginate

This methodology is detailed in Chapter 2 (2.2.2 page 44)

5.2.3 Laponite-alginate-methylcellulose bioink

This methodology is reported in Chapter 2 (2.3.1 page 46)

5.2.4 Bioprinting system

This methodology is reported in Chapter 2 (2.4.1 page 49)

5.2.5 Subcutaneous implantation of BMP-2 loaded 3D printed scaffolds

5.2.5.1 Preparation of bulk alginate for BMP-2 delivery *in vivo*

Bulk alginate gel scaffolds were fabricated as negative (BMP-2 free) and positive (loaded with BMP-2) controls for functional mineralisation *in vivo*. Alginate 3 % w/v solution was prepared as reported in Chapter 2 (2.2.2 page 44) and pipetted into a sterile 2 ml Eppendorf tube. Alginate was deposited on the bottom of the tube. A solution of 100 mM of $CaCl_2$ was then gently pipetted (500 µl) on top of the gel and left to crosslink for 10 min. After 5 min, 250 µl of the $CaCl_2$ solution was used to crosslink the portion of the gel in contact with the bottom of the tube, by inserting the pipette tip on the side and then on the bottom of the bulk alginate gel. Crosslinking solutions was then removed, and scaffolds were washed (×5) with HBSS. Scaffolds were then blotted dry and weighed to confirm their weight consistent with 3D printed scaffolds. Alginate bulk scaffolds were found at 0.164 ± 0.02 g and of a similar weight with lattice scaffolds. A total of n=12 samples was produced. Only n=6 samples were planned for the implantation. Scaffolds were kept dry at 4°C overnight in a solution-free well plate for BMP-2 loading and scaffold implantation the following day.

5.2.5.2 Preparation of 3D printed 3-3-3 scaffolds for BMP-2 delivery *in vivo*

3D printed scaffolds were fabricated with an in-house built bioprinter (2.4.1 page 49) using 3-3-3 as bioink. A sterile 410 µm cylindrical blunt nozzle was used. Scaffolds were printed at 3 mm s^{-1} with an extrusion force of 45-55 kN, building a 8 × 8 mm^2 lattice network with a total of 15 layers. Scaffolds (n=12) were printed sequentially and crosslinked with 100 mM of $CaCl_2$ for 10 min after printing. Crosslinking solutions was then removed, and scaffolds were washed (x 5) with HBSS 1x. The weight of the scaffolds was registered to be 0.165 ± 0.03 g. A total of n=12 samples was produced. Only n=6 samples were planned to be used for implantation. Scaffolds were stored dry at 4°C overnight in a well plate for BMP-2 loading and scaffold implantation the following day.

5.2.5.3 BMP-2 loading and implantation of scaffolds in MF-1 mice

This animal study was conducted in compliance with ethical approval and in accordance with institutional guidelines. Animals had ad libitum access to standard mouse chow and water at all times. *In vivo* experimental design consisted in the implantation of n=3 scaffolds of 4 treatment group and a single sham control in a total of n=4 MF-1 mice. Treatment groups were: i) alginate, ii) alginate absorbed with BMP-2, iii) 3D printed 3-3-3 and iv) 3D printed 3-3-3 absorbed with BMP-2. A BMP-2 solution was diluted to reach a 10 µg ml^{-1} concentration. Solution was then left to absorb on alginate bulk and 3D printed 3-3-3 scaffolds for 1 h prior to implantation. Scaffolds were maintained in ice during loading of BMP-2, transportation to the surgical site and implantation to avoid BMP-2 degradation. Scaffolds were blotted dry after a wash with HBSS. Mice were first weighed and then sedated with anaesthetic/analgesic (fentanyl-fluanisone (Hypnorm; Janssen-Cilag Ltd.) and midazolam (Hypnovel; Roche Ltd.) in a 1:1 dilution in DW) operating an intraperitoneal injection of 10 ml kg^{-1}. A limit of 250 µl of anaesthetic/analgesic was considered. A total of 3 midline dorsal incisions per side were made after shaving and an ethanol sterilisation of the outer skin. A total of n=3 printed scaffolds with BMP-2 and n=3 printed scaffolds BMP-2 free were implanted on each side and wounds closed with clips. A total of n=3 printed scaffolds with BMP-2 and n=3 printed scaffolds BMP-2 free were implanted on each side and wounds closed with Michel suture clips. A scheme illustrated in Table 5.1 reports location of implants in mice. Scaffolds were implanted sequentially. Right after each single surgical procedure mice were housed in a temperature-controlled cage (with optimal temperature of 28°C) until complete restoration of motor functions. Mice were then housed in cages and monitored three-times a week up to 4 weeks.

Table 5.1. *In vivo* implantation of BMP-2 loaded and free scaffolds subcutaneously in mice

Mouse #	*Mouse weight (g)*	*Experiment*	
		Left side	*Right side*
1	34.4	3D printed + BMP-2	3D printed
2	32.2	3D printed	3D printed + BMP-2
3	34.3	Alginate bulk	Alginate bulk + BMP-2
4	35.7	Alginate bulk + BMP-2	Alginate bulk
5	33.2	Sham control	

5.2.5.4 Samples collection and end of experimental protocol *in vivo*

After CT scanning, illustrated in 5.2.7 page 129, mice anesthetised were sacrificed for samples extraction. An incision was operated on middle line on the spine to collect macroscopic image of integrated scaffolds. Samples were then collected and stored in 4 % PFA solution at 4°C overnight, before OCT embedding and sectioning.

5.2.6 Subcutaneous implantation of HBMSC-laden 3D printed scaffolds

5.2.6.1 Preparation of bulk 3-3-3 for HBMSCs-encapsulation for *in vivo* implantation

Bulk hydrogels either acellular or with encapsulated HBMSCs, were fabricated as control for functional bone formation *in vivo*. 3-3-3 bioink was prepared as illustrated in Chapter 2 (2.3.1 page 46) and divided into two groups: i) acellular or ii) cell-laden scaffolds with 1×10^6 cell ml^{-1}. Bioink groups were divided into 3 ml slip tip syringes (BD Plastipak, UK). Syringe tips were then removed with a sterile scalpel and 200 µl cylinders were extruded from the circular aperture. Cylinders were collected with a scalpel and immediately crosslinked in 10 mM $CaCl_2$ for 10 min, washed (×5) with HBSS. Bulk scaffolds (n=3) were blotted dry and weighed to confirm similar mass to the 3D printed scaffolds. The acellular and cell-laden bulk scaffolds were weighed resulting 0.163 ± 0.74 g and 0.162 ± 0.81 g respectively. A total of n=12 samples for each treatment group (acellular and cell-laden) were produced. Only n=9 were the samples per group that were used for the implantation. The remaining scaffolds (n=3) were maintained in culture *in vitro* for further comparison after 8 weeks. Scaffolds were incubated at 37°C and 5 % CO_2 overnight and implanted the following day.

5.2.6.2 Preparation of 3D printed HBMSC-laden 3-3-3 scaffolds for *in vivo* implantation

Bioink formulation (3-3-3) was prepared as illustrated in Chapter 2 (2.3.1 page 46). 3D printed scaffolds were printed with an in-house built bioprinter (5.2.4 page 123). A sterile cylindrical nozzle with 410 µm of internal diameter was used to print 15 layer scaffolds. Scaffolds were fabricated at 2.5 mm s^{-1} with an average extrusion force of 55 kN, printing n=12 scaffolds of 8 × 8 mm^2 lattice scaffolds. Scaffolds were fabricated sequentially and crosslinked for 10 min with 100 mM $CaCl_2$. Solution was then removed and scaffolds washed (x 5) with HBSS. To register the weight of 3D printed scaffolds, n=3 cell-laden and n=3 acellular printed scaffolds were blotted dry and weighed registering 0.162 ± 0.04 g and 0.163 ± 0.34 g for acellular and cell-laden scaffolds respectively. n=12 samples were produced for acellular and cell-laden printed 3-3-3 scaffolds. Samples for implantation (n=9) were stored at 37°C and 5 % CO_2 balanced air overnight and implanted the following day. The remaining samples (n=3) were kept in culture *in vitro* for further comparison after 8 weeks.

5.2.6.3 Implantation of scaffolds in BALB/c mice

This animal study was conducted in compliance with ethical approval and in accordance with institutional guidelines. The study consisted in the implantation of n=9 scaffolds of 4 treatment groups in n=9 BALB/c athymic mice. Male athymic immunodeficient mice were purchased from Envigo, UK and acclimatised for a minimum of 1 week prior to experimentation. Animals had ad libitum access to standard mouse chow and water at all times. Treatment groups, all realised using the 3-3-3 bioink were: i) bulk, ii) bulk with encapsulated cells, iii) 3D printed and iv) 3D printed with encapsulated cells. Scaffolds were washed with serum-free media and maintained in the same media during surgery. Scaffolds were then blotted dry after a single wash with HBSS. Mice weights were registered and an anaesthetic/analgesic (fentanyl-fluanisone (Hypnorm, Janssen-Cilag Ltd.) and midazolam (Hypnovel, Roche Ltd.) – hypnorm: 1:3 dilution in DW, hypnovel 1:1 dilution in DW (10ml kg^{-1})) was administered with an intraperitoneal injection, using up to 250 µl of anaesthetic depending on the weight of the animal. A total of 2 midline dorsal incisions for each side were applied. A total of n=8 printed scaffolds for each treatment group were implanted, two for each side, in a randomised distribution as reported in Table 5.2. Incisions were sutured with sterile metal Michel clips. Scaffolds were implanted sequentially. An overall number of

n=32 scaffolds were implanted in the subcutaneous pocket of n=9 mice. Lastly, n=1 scaffolds for each treatment group were implanted in a single mouse to be monitored, from the day of implantation (0 weeks), via micro-CT imaging. Sutures instead of metal clips were applied to avoid interference with CT readings. After each surgical intervention, mice were housed temporally in a temperature-controlled and ventilated cage with a desired temperature maintained at 28°C. Once anaesthetic effects were found withdrawing, animals were housed in ventilated cages and monitored three-times a week up to 8 weeks.

Table 5.2. *In vivo* implantation of BMP-2 loaded and free scaffolds subcutaneously in mice

Mouse #	*Mouse weight (g)*	*Experiment*			
		Left side		*Right side*	
1	27.9	Bulk		Bulk + cells	
2	27.3	3D printed		3D printed + cells	
3	28.2	3D printed		Bulk	
4	30.9	Bulk + cells		3D printed	
5	33.0	3D printed + cells		Bulk	
6	26.75	Bulk + cells		3D printed	
7	24.8	3D printed + cells		Bulk + cells	
8	27.6	Bulk		3D printed + cells	
		Top left	*Bottom left*	*Top right*	*Bottom right*
9	29.4	Bulk	Bulk + cells	3D printed	3D printed + cells

5.2.6.4 Samples collection and end of experimental protocol *in vivo*

Anesthetised mice were sacrificed before CT scans at 8 weeks post implantation. CT scan methodologies are reported in 5.2.7 (page 129). A middle line incision was made and macroscopic images of integrated scaffolds were taken. Samples were collected and stored in 4 % PFA solution at 4°C overnight. Samples were then embedded in OCT and sectioned.

5.2.7 Micro computed tomography images

This methodology is reported in detail in Chapter 2 (2.9 page 64)

5.2.8 Histological analysis

This methodology is reported in detail Chapter 2 (2.10 page 65)

5.2.9 Statistical analysis

This methodology is detailed in Chapter 2 (2.11 page 66). Statistical evaluation of quantitative results is reported within the caption of the representative figures.

5.3 Results

5.3.1 *In vivo* evaluation of BMP-2-loaded nanosilicate-based scaffolds resulted in ectopic bone formation

To test the *in vivo* functionality of the 3-3-3 bioink, 3D scaffolds were fabricated and implanted subcutaneously in mice. BMP-2 was loaded within the scaffolds to investigate the capacity for the 3-3-3 bioink for retention and localisation potential for the growth factors of interest for skeletal regeneration (Figure 5.2).

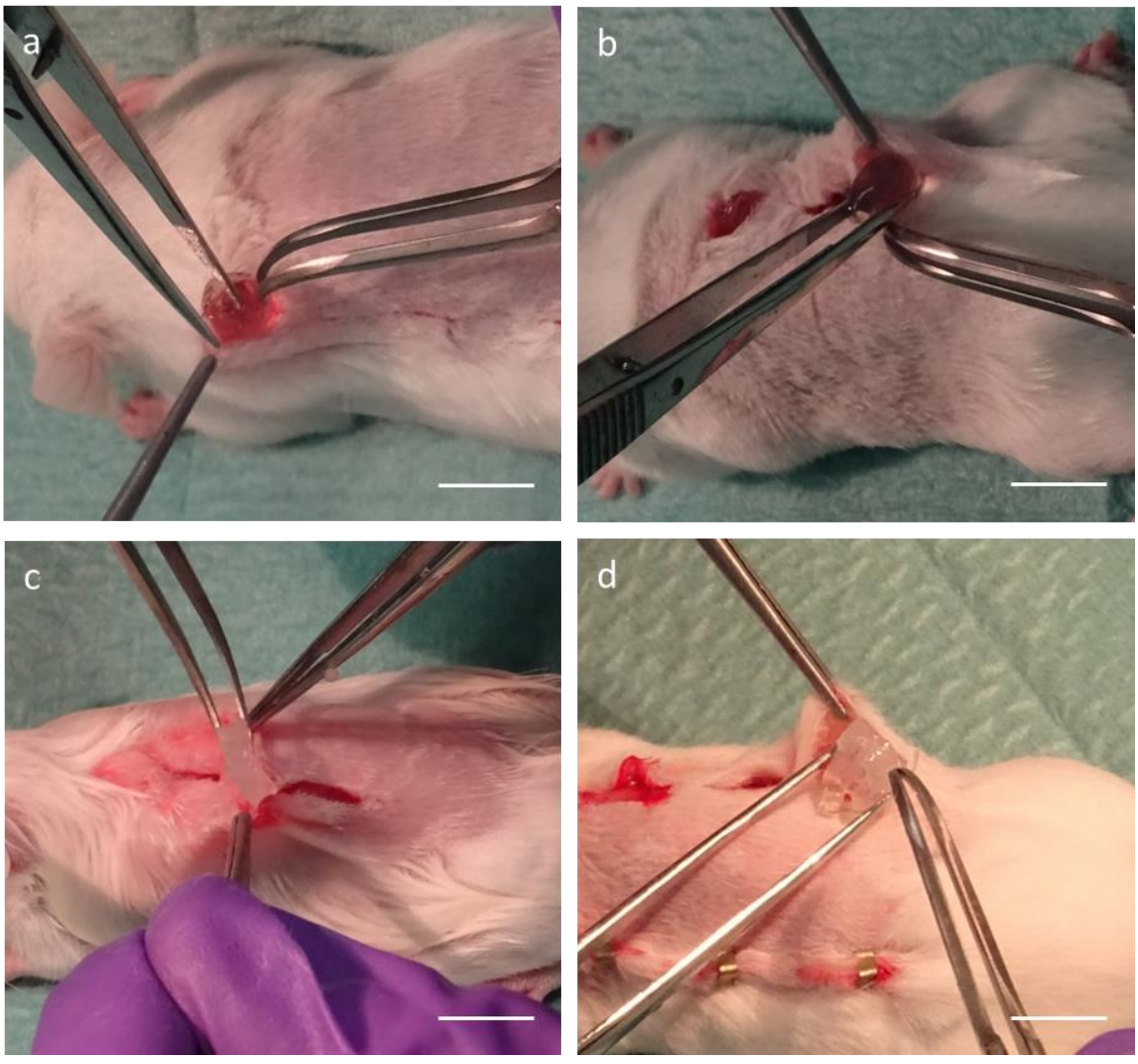

Figure 5.2. *In vivo* implantation of 3D scaffolds for ectopic bone formation.

Bulk free (a) or scaffold loaded with BMP-2 (b) were implanted as negative and positive control samples. 3D printed scaffolds free of growth factors (c) and BMP-2 loaded constructs (d) implanted to assess bone formation *in vivo*. Scale bar: 10 mm.

Bulk scaffolds (Figure 5.2 a) were set as negative control. Bulk scaffolds loaded with BMP-2 (Figure 5.2 b) served as a positive control. 3D printed drug-free and BMP-2 loaded scaffolds (Figure 5.2 c,d) were implanted to assess bone ectopic formation *in vivo*. Mice were sacrificed after 4 weeks and scaffolds scanned *in situ* via micro-CT and data extracted (Figure 5.3). The drug-free bulk alginate negative controls retained their spherical appearance (Figure 5.3 a-i). CT images confirmed limited mineral in the bulk scaffolds. In contrast, the BMP-2 loaded bulk alginate (Figure 5.3 b-i) samples displayed a conserved spherical shape and greater mineralisation after 4 weeks (Figure 5.3 b-ii) compared to BMP-2-free alginate.

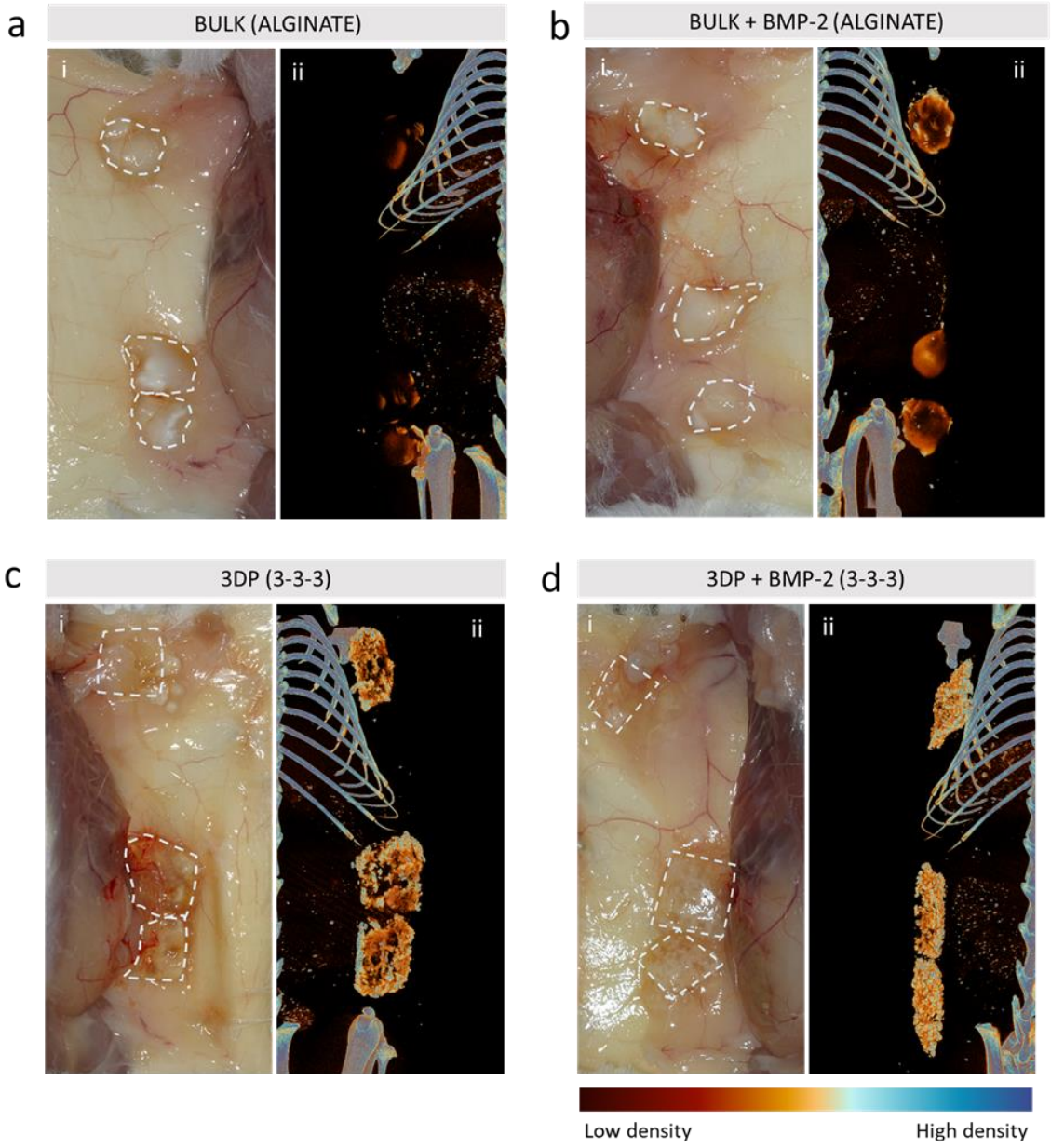

Figure 5.3. Comparison of *in vivo* mineralised scaffolds and CT images 4 weeks after implantation.

Control alginate bulk (a), alginate loaded BMP-2 (b), 3D printed 3-3-3 (c) and 3D printed 3-3-3 loaded with BMP-2 (d) scaffolds showed *in vivo* (i) and CT reconstruction (ii) respectively. Bone density scale indicates low density bone as dark red and high density bone as blue.

The 3D printed scaffolds were found partially degraded but still retained their lattice structure (Figure 5.3 c-i) and mineralisation could be observed (Figure 5.3 c-ii). The BMP-2 3-3-3 scaffolds displayed altered morphology from the original spherical implant (Figure 5.3 d-i) and were highly mineralised (Figure 5.3 d-ii).

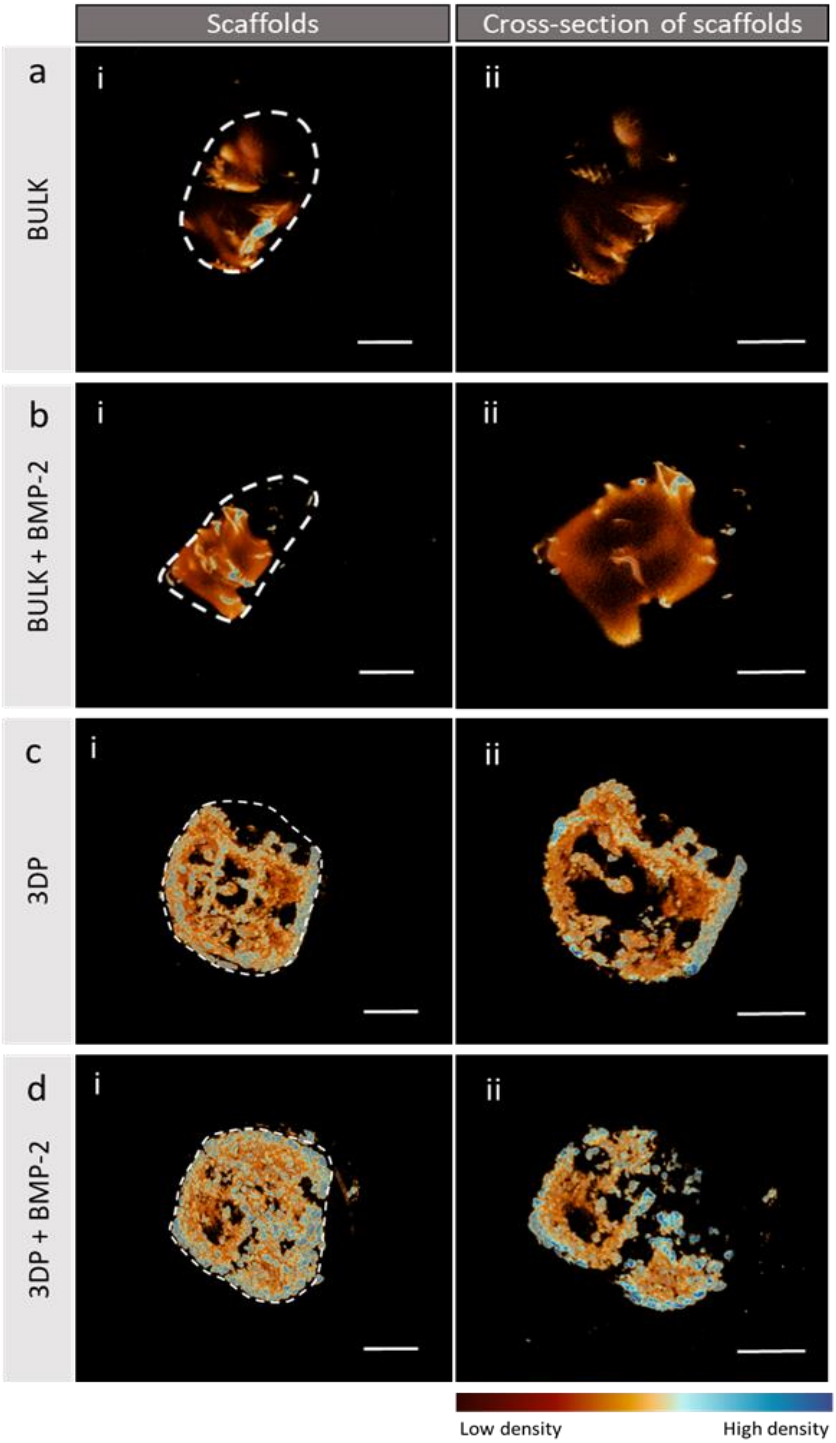

Figure 5.4. Comparison of extracted scaffolds under high resolution CT.

Control bulk (a) alginate loaded BMP-2 (b), 3D printed 3-3-3 (c) and 3D printed 3-3-3 loaded with BMP-2 (d) scaffolds reconstructions in full view (i) and cross-section (ii) respectively. Scale bar: 5 mm. Bone density scale indicates low density bone as dark red and high density bone as blue.

Scaffolds were collected after 28 days and scanned at high-resolution (18 µm). Bulk BMP-2-free scaffolds were observed to be partially mineralised on the outside of the sample (Figure 5.4 a-i) whilst remaining uncalcified at the core (Figure 5.4 a-ii). The BMP-2 bulk alginate implants showed higher mineralisation than bulk control on the outer surface (Figure 5.4 b-i) and core (Figure 5.4 b-ii). The 3D printed scaffolds showed higher mineralisation on the outer (Figure 5.4 c-i) and inner (Figure 5.4 c-ii) surfaces than bulk BMP-2 and BMP-2 free controls. BMP-2 loaded 3D printed constructs showed extensive high-density mineralised tissue on the outer (Figure 5.4 d-i) and inner (Figure 5.4 d-ii) core of the construct compared to BMP-2 free printed scaffolds and bulk controls.

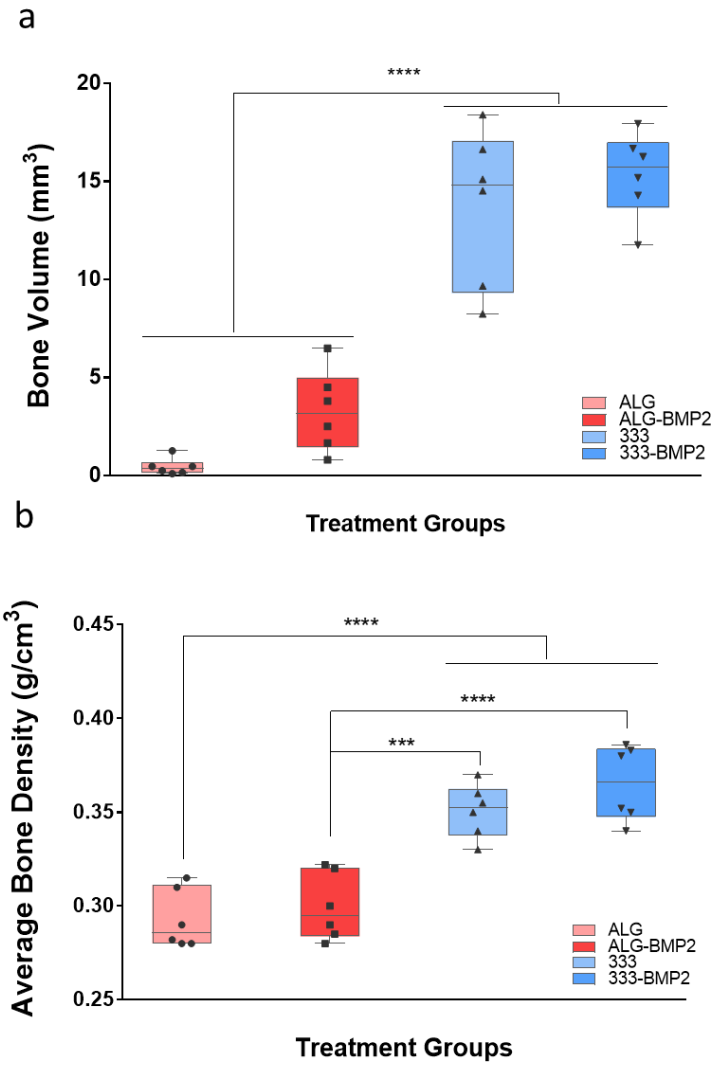

Figure 5.5. Quantitative analysis of *in vivo* implanted scaffolds after 4 weeks.

Bone volume (a) and average bone density (b) of three-dimensional constructs implanted *in vivo.* Statistical significance assessed by one-way ANOVA followed by Tukey's multiple comparison tests. Mean ± S.D., n=4, ***p<0.001, ****p<0.0001.

Bone volume (Figure 5.5 a) and average bone density (Figure 5.5 b) were quantified across all implanted scaffolds. 3D printed scaffolds loaded with BMP-2 (15.34 ± 2.16 mm^3) and drug-free (13.75 ± 3.98 mm^3) showed significantly higher bone volume ($p<0.0001$) than BMP-2 loaded and free alginate controls (3.28 ± 2.07 mm^3, 0.44 ± 0.42 mm^3) respectively. Average bone density analysis revealed BMP-2 loaded (0.36 ± 0.02 mm^3) 3D printed scaffolds generated significantly higher bone density than drug-loaded (0.29 ± 0.02 mm^3) and free (0.29 ± 0.01 mm^3) bulk control scaffolds ($p<0.0001$). Surprisingly, the 3D printed drug-free scaffolds (0.35 ± 0.01 mm^3) showed significantly higher average bone density in comparison to BMP-2-loaded alginate bulk control ($p<0.001$) and bulk drug-free scaffolds ($p<0.0001$).

Histological analysis using Alcian blue/Sirius red staining of BMP-2-free bulk alginate scaffolds extracted after 4 weeks revealed limited GAGs present in the sample area (Figure 5.6 a-i) surrounded by a discrete layer of collagen (Figure 5.6 a-ii). Collagen was found, organised in a randomly aligned fashion (Figure 5.6 a-iii) on the outer surface of the scaffolds with concentrated integration of GAGs at the core of the scaffold (Figure 5.6 a-iii). BMP-2-loaded bulk alginate was integrated with the surrounding tissue (Figure 5.6 b-i). The samples were surrounded by a discrete layer of collagen (Figure 5.6 b-ii) with limited integration across the tissue (Figure 5.6 b-iii) and larger GAGs presence in the core of the scaffolds compare to BMP-2-free alginate (Figure 5.6 a-i). Drug-free 3D printed scaffolds did not retain their lattice shape (Figure 5.6 c-i) and were observed to degrade over 28 days *in vivo*. GAGs penetration was enhanced (Figure 5.6 c-ii) compared to the bulk (Figure 5.6 a-ii) and BMP-2-bulk (Figure 5.6 b-ii) controls. BMP-2 loaded on the 3D printed scaffold (Figure 5.6 d-i) displayed collagen deposition on the outer (Figure 5.6 d-ii) and inner (Figure 5.6 d-iii, iv) surfaces of the sample. Collagenous tissue was observed across and penetrating the large printed structure, infiltrating the scaffold with considerably greater deposition compared to bulk (Figure 5.6 a-i), bulk with BMP-2 (Figure 5.6 b-i) and drug-free printed (Figure 5.6 c-i) scaffolds.

Goldner's Trichrome staining on bulk alginate scaffolds (Figure 5.7 a-i) confirmed poor integration (Figure 5.7 a-ii) with limited collagen presence (Figure 5.7 a-iii) and confirmed blood vessels only partially surrounding the scaffold (Figure 5.7 a-iv).BMP-2-loaded alginate bulk scaffolds (Figure 5.7 b-i) were integrated with tissue with a fine layer of collagen on the outside of the scaffold (Figure 5.7 b-ii) with limited penetration throughout the scaffold (Figure 5.7 b-iii) and minor vessels in the marginal areas within the scaffold (Figure 5.7 b-iv). 3D printed BMP-2-free scaffolds (Figure 5.7 c-i) were observed to be integrated with the host tissue with collagenous surrounding tissue (Figure 5.7 c-ii) in close vicinity together with small (Figure 5.7 c-iii) and major (Figure 5.7 c-iv) vessel networks integrated throughout. BMP-2 3D printed scaffolds (Figure 5.7 d-i) were integrated in the proximity of

major vessels (Figure 5.7 d-ii) present in the scaffold surroundings (Figure 5.7 d-iii) with evidence of major collagenous tissue penetration (Figure 5.7 d-iv).

Mineral deposition was evidenced and analysed using von Kossa staining. Bulk alginate scaffolds (Figure 5.8 a-i) were observed to be poorly integrated (Figure 5.8 a-ii) with scattered discrete areas of (Figure 5.8 a-iii) mineralised tissue. Individual mineral deposits were found only in limited regions on the outer surface of the scaffolds (Figure 5.8 a-iv). BMP-2 alginate scaffolds (Figure 5.8 b-i) displayed limited mineral deposition (Figure 5.8 b-ii) with only one discrete region (Figure 5.8 b-iii) on the outer surface of the scaffolds showing mineralised tissue (Figure 5.8 b-iv). 3D printed scaffolds (Figure 5.8 c-i) were extensively mineralised (Figure 5.8 c-ii) with elevated mineral deposition (Figure 5.8 c-iii) on the internal scaffold region localised near the scaffold-tissue interface (Figure 5.8 c-iv). BMP-2 3D printed scaffolds (Figure 5.8 d-i) showed extensive mineralisation across the entire scaffold (Figure 5.8 d-ii) including the scaffold core. Large areas of mineral deposition were observed internally at the scaffold-tissue interface (Figure 5.8 d-iii) evidenced by the areas of large mineral nodules (Figure 5.8 d-iv).

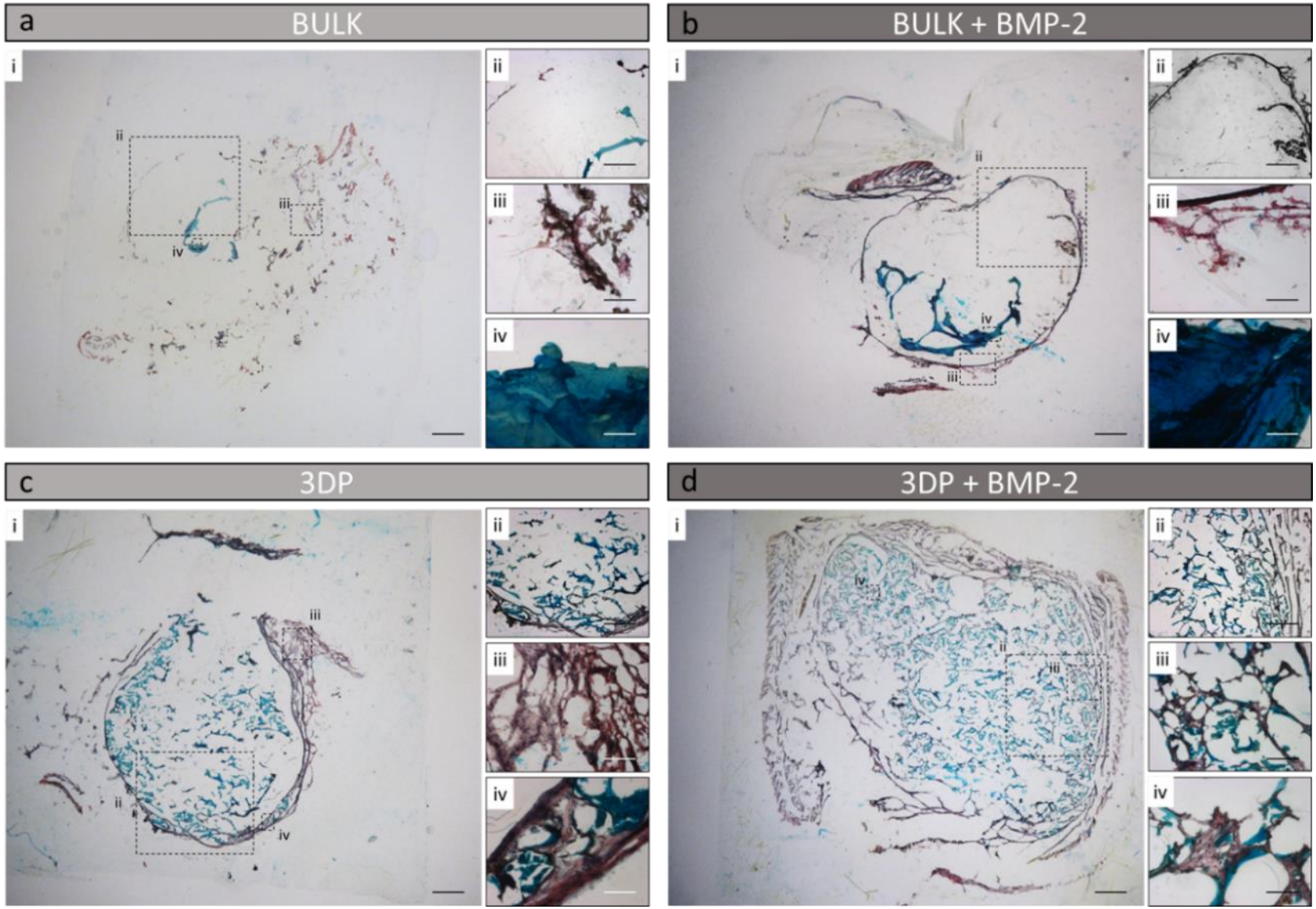

Figure 5.6. Histological analysis of implanted 3-3-3 scaffolds.

Alcian blue/Sirius red staining was performed on bulk (a), bulk BMP-2-loaded (b) controls and 3D printed (c), 3D printed BMP-2-loaded (d). Histological process stained black for nuclei, blue for glycosaminoglycans and other polysaccharides, red for collagen. Scale bar: (i) 1 mm, (ii) 500 µm, (iii) 100 µm, (iv) 50 µm.

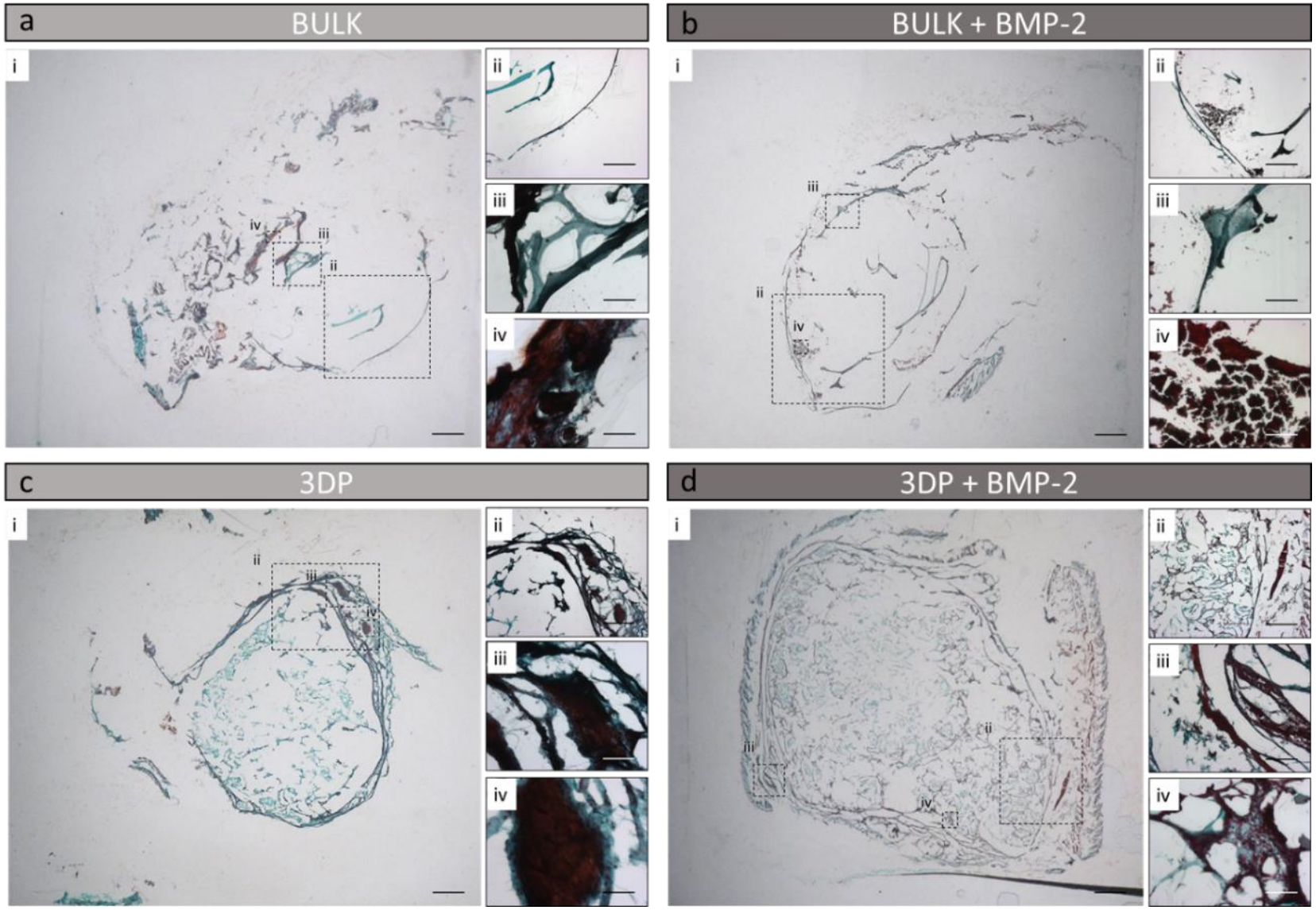

Figure 5.7. Histological analysis of implanted scaffolds.

Goldner's Trichrome staining was performed on bulk (a), bulk BMP-2-loaded (b) controls and 3D printed (c), 3D printed BMP-2-loaded (d). Histological process stained black for nuclei, red for erythrocytes, orange/bright red for cytoplasm, green for collagen. Scale bar: (i) 1 mm, (ii) 500 µm, (iii) 100 µm, (iv) 50 µm.

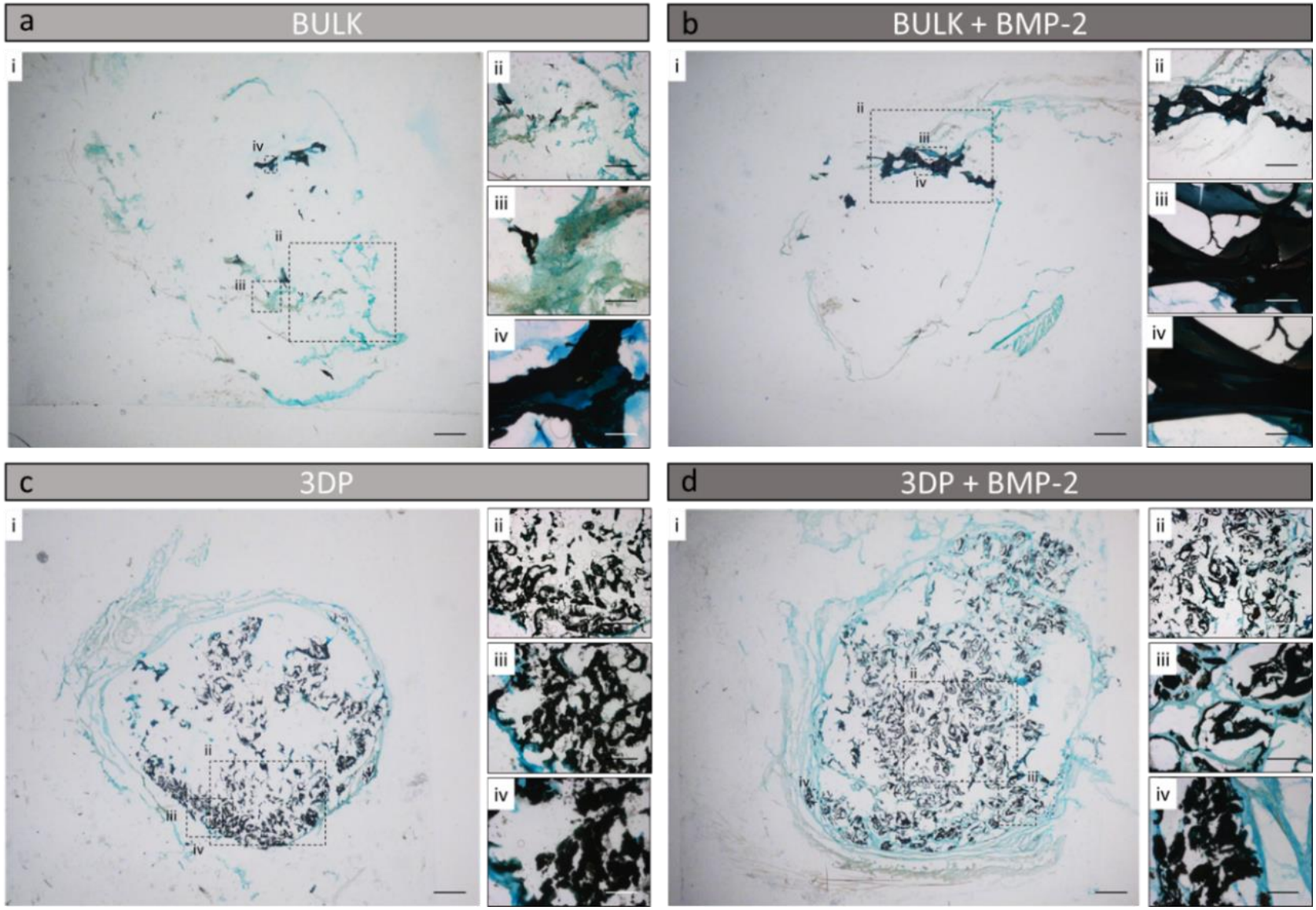

Figure 5.8. Histological analysis of implanted scaffolds.

Von Kossa staining was performed on bulk (a), bulk BMP-2-loaded (b) controls and 3D printed, (c) 3D printed BMP-2-loaded (d). Histological process stained black for mineralised tissue, green/blue (alcian blue counterstain) for polysaccharides. Scale bar: (i) 1 mm, (ii) 500 µm, (iii) 100 µm, (iv) 50 µm.

5.3.2 *In vivo* implantation of HBMSC-laden revealed significant bone formation

To evaluate the potential of HBMSC-laden 3D printed scaffolds to generate *de novo* bone tissue *in vivo*, acellular and cell-laden lattice and bulk scaffolds were fabricated and implanted in athymic mice. Bulk (Figure 5.9 a) and 3D printed (Figure 5.9 b) HBMSC -laden 3-3-3 were used to investigate the potential of cell encapsulated 3D clay-based structures to produce bone *de novo*. Controls used in the study included acellular bulk and 3D printed scaffolds. Scaffolds (n=9) were implanted in pairs on each side of mice in a randomised order (Figure 5.9 c).

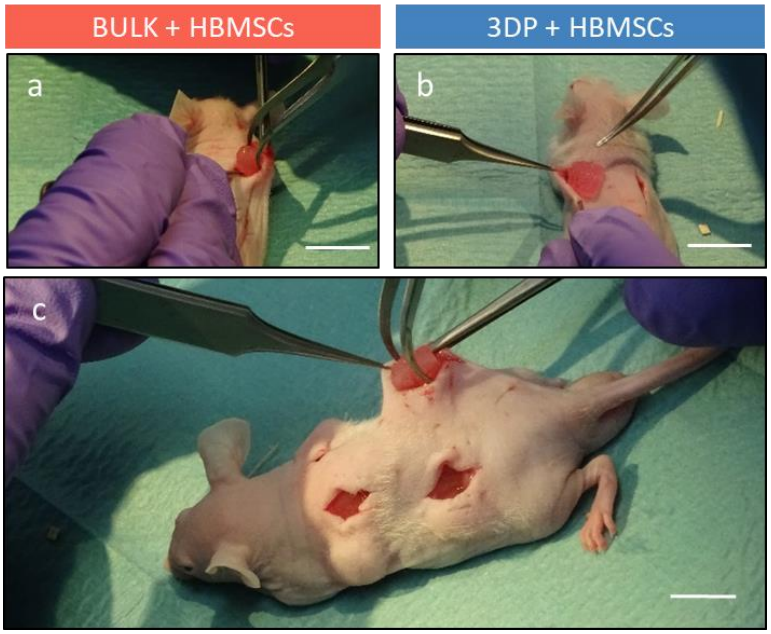

Figure 5.9. *In vivo* implantation in athymic mice of acellular and cell-laden scaffolds.

HBMSC-laden bulk (a) and 3D printed (b) scaffolds implantation (four scaffolds per mouse, two in each side in a randomised order). Scale bar: 20 mm.

A portion of the scaffolds (n=3) was retained in culture, *in vitro*, to investigate the degradation profile of the constructs for the duration of the *in vivo* investigation. *In vitro* control scaffolds were cultured up to 8 weeks at 37°C, 5 % CO_2 balanced air. Acellular (Appendix C Figure 5.1 a) and cell-laden bulk 3-3-3 (Appendix C Figure 5.1 b) scaffolds retained their spherical morphology following 8 weeks of culture. Acellular 3D printed 3-3-3 (Appendix C Figure 5.1 c) were observed to partially degrade, but the scaffold lattice structure was conserved. HBMSCs encapsulated in 3-3-3 bioink, printed and cultured for 8 weeks displayed considerable degradation with relatively few pores still visible (Appendix C Figure 5.1 d).

Four treatment groups (bulk, bulk + HBMSCs, 3D printed, and 3D printed + HBMSCs) were implanted in each mouse and implanted scaffolds were assessed for mineral deposition using temporal CT scanning within the same animals from implantation (0 weeks) through to 8 weeks. Particularly, one sample of each treatment group was implanted in a single animal to investigate bone formation in a unique host, from implantation to 8 weeks. Bulk (cranial posterior evaluation) and HBMSC-laden bulk (caudal posterior evaluation) were scanned at implantation, 2, 4, 6 and 8 weeks (Appendix C Figure 5.2). CT images revealed the absence of any mineral deposition at implantation. After 2 weeks, HBMSC-laden scaffolds showed initial formation of mineral nodules, while the bulk scaffold displayed no mineral deposition, which was evident even after 4 weeks. Following 6 weeks of implantation, bulk acellular scaffolds displayed mineralised tissue as did the HBMSC-laden bulk scaffolds. Mineralisation was observed on the surface of the scaffolds (exclusively) after 6 weeks. At 8 weeks, the scaffolds displayed extensive mineralisation and had started to degrade in comparison to 6-weeks samples. Similarly, implanted 3D printed (cranial posterior) and HBMSC-laden

3D printed (caudal posterior) scaffolds were scanned at implantation and after 2, 4, 6 and 8 weeks (Appendix C Figure 5.3). Acellular and cell-laden 3D printed scaffolds displayed detectable mineralisation after 2 weeks. 3D printed scaffolds differed from the bulk controls with cluster-like mineralisation observed. At 4 weeks post-implantation, both acellular and HBMSC-laden scaffolds displayed extensive mineralisation, with the mineral content observed to accrue over the 8 weeks. Acellular printed scaffolds showed rapid mineralisation with a significant increase between 4 and 6 weeks. 3D printed HBMSCs encapsulated scaffolds increased in mineral density over 8 weeks, with only modest changes between weeks 6 and 8.

CT images of implanted bulk (Figure 5.10), HBMSC-laden bulk (Figure 5.11), 3D printed (Figure 5.12) and HBMSC-laden printed (Figure 5.13) scaffolds were collected from 8 mice and analysed over the implantation period to compare bone volume changes within each treatment group.

Bulk acellular 3-3-3 scaffolds (Figure 5.10 a) were mineralised on the outer surface after 8 weeks from implantation. Full-field view of the scaffold (Figure 5.10 b) revealed mineral deposition across the entire outer surface with discrete high mineral density regions. Inner CT scan of bulk sample (Figure 5.10 c) revealed a non-mineralised core. HBMSC-laden bulk 3-3-3 (Figure 5.11 a and Figure 5.11b) showed mineral deposition on the outer surface with reduced mineralisation at the core (Figure 5.11 c). Acellular 3D printed 3-3-3 scaffolds (Figure 5.12 a) displayed rapid mineral deposition up to 8 weeks, with increased mineral

density. Mineral deposition appeared expressed in a cluster-like fashion (Figure 5.12 b) and was also observed within the inner core of the printed scaffold (Figure 5.12 c). HBMSC-laden 3D printed 3-3-3 scaffolds (Figure 5.13 a) showed extensive mineralisation within the 3D scaffolds. CT images revealed bone volume and the density clearly increased over time with the HBMSC-laden 3D printed 3-3-3 scaffolds fully mineralised (Figure 5.13 b) even within the core of the constructs (Figure 5.13 c).

Full comparison analysis of bone volume (Figure 5.14 a) and average bone density (Figure 5.14 b) of treatment groups was determined and acellular bulk (2.52 ± 1.73 mm^3), loaded with stem cells (2.79 ± 2.92 mm^3), 3D printed (3.01 ± 2.30 mm^3) and HBMSC-laden printed (7.66 ± 2.80 mm^3) implants showed non-significant differences in bone volume after 2 weeks of implantation. At 4 weeks, 3D printed scaffolds loaded with HBMSCs (26.41 ± 7.62 mm^3) showed significant differences in bone volume with acellular bulk (7.80 ± 3.06 mm^3), 3D printed (8.12 ± 4.24 mm^3) ($p<0.001$) and HBMSC-laden bulk (6.38 ± 4.92 mm^3) ($p<0.0001$) constructs. After 6 weeks cell-laden 3D printed resulted in significant ($p<0.0001$) bone formation (40.77 ± 13.40 mm^3) compared to acellular (12.43 ± 4.438 mm^3) and cellular (9.81 ± 8.76 mm^3) bulk controls and HBMSC-free printed (13.15 ± 5.39 mm^3) scaffolds. Within 8 weeks of implantation, HBMSC-laden printed scaffolds showed significant ($p<0.0001$) differences in bone volume formation (56.49 ± 15.11 mm^3) in comparison to acellular bulk (15.91 ± 8.57 mm^3) and printed (18.11 ± 5.66 mm^3) as well as HBMSC-laden (13.36 ± 9.20 mm^3) bulk scaffolds.

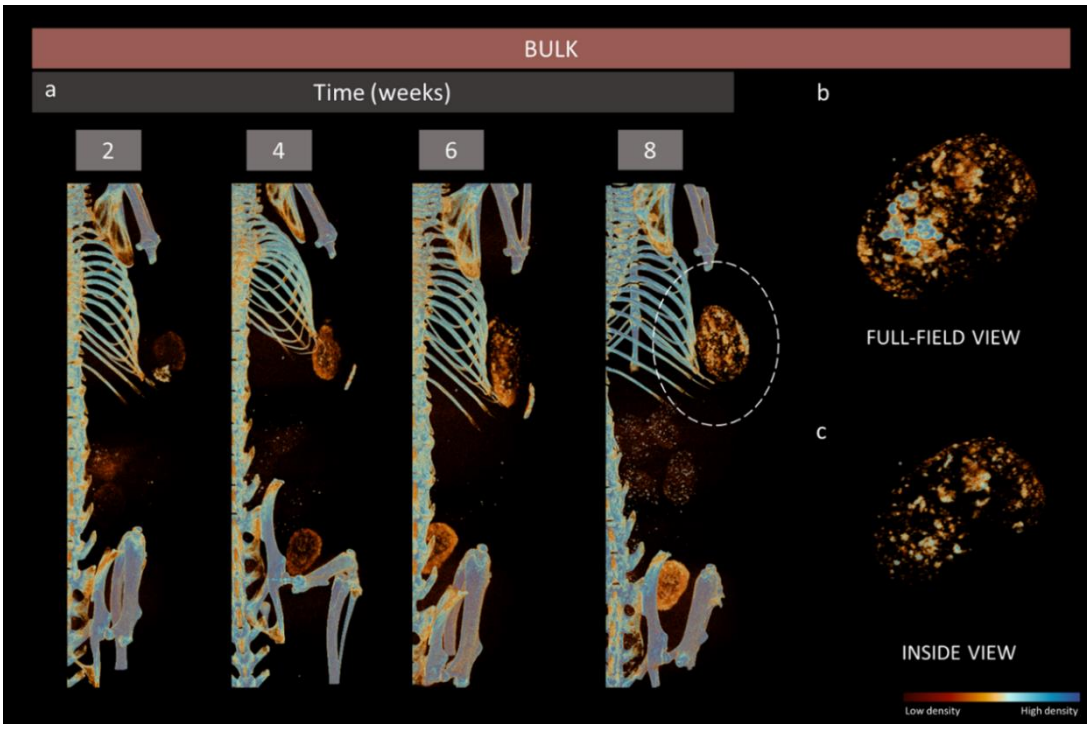

Figure 5.10. CT analysis of acellular bulk 3D scaffolds.

Posterior CT images (a) of bulk scaffolds at 2, 4, 6 and 8 weeks. Full-field top (b) and inside (c) view of selected scaffold. Bone volume quantification (d) of bulk scaffolds over 8 weeks after implantation. Bone density scale indicates low density bone as dark red and high-density bone as blue.

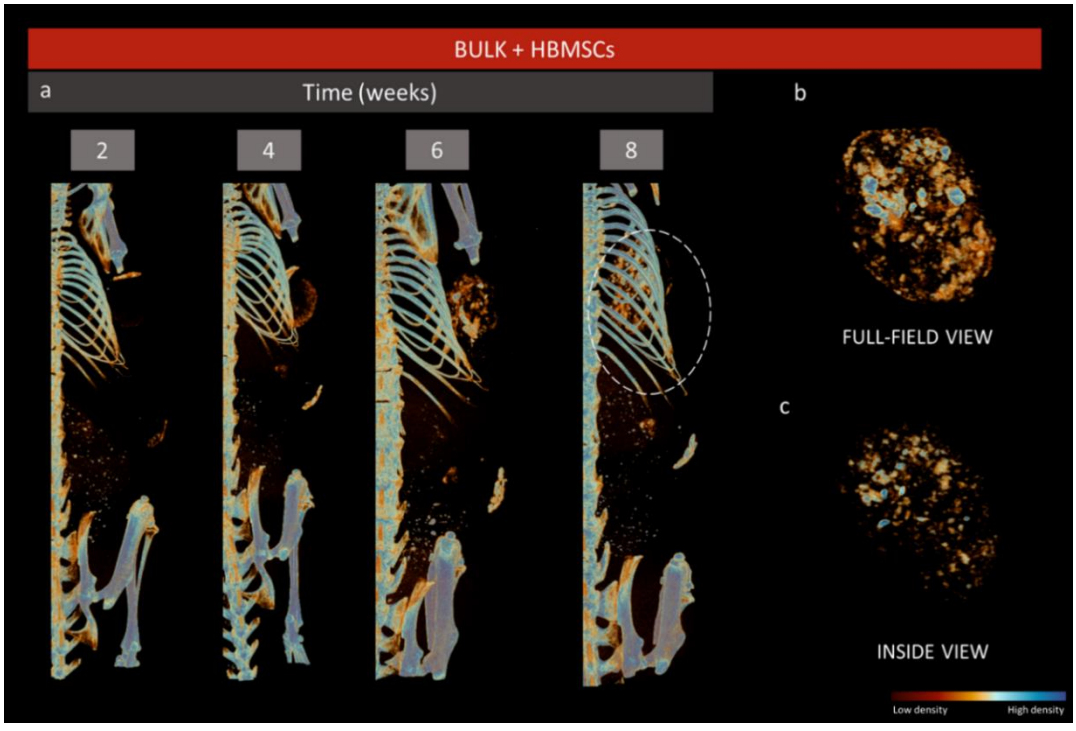

Figure 5.11. CT analysis of HBMSC-laden bulk 3D scaffolds.

Posterior CT images (a) of HBMSC-laden bulk scaffolds at 2, 4, 6 and 8 weeks. Full-field top (b) and inside (c) view of selected scaffold. Bone volume quantification (d) of HBMSC-laden bulk scaffolds over 8 weeks after implantation. Bone density scale indicates low density bone as dark red and high-density bone as blue

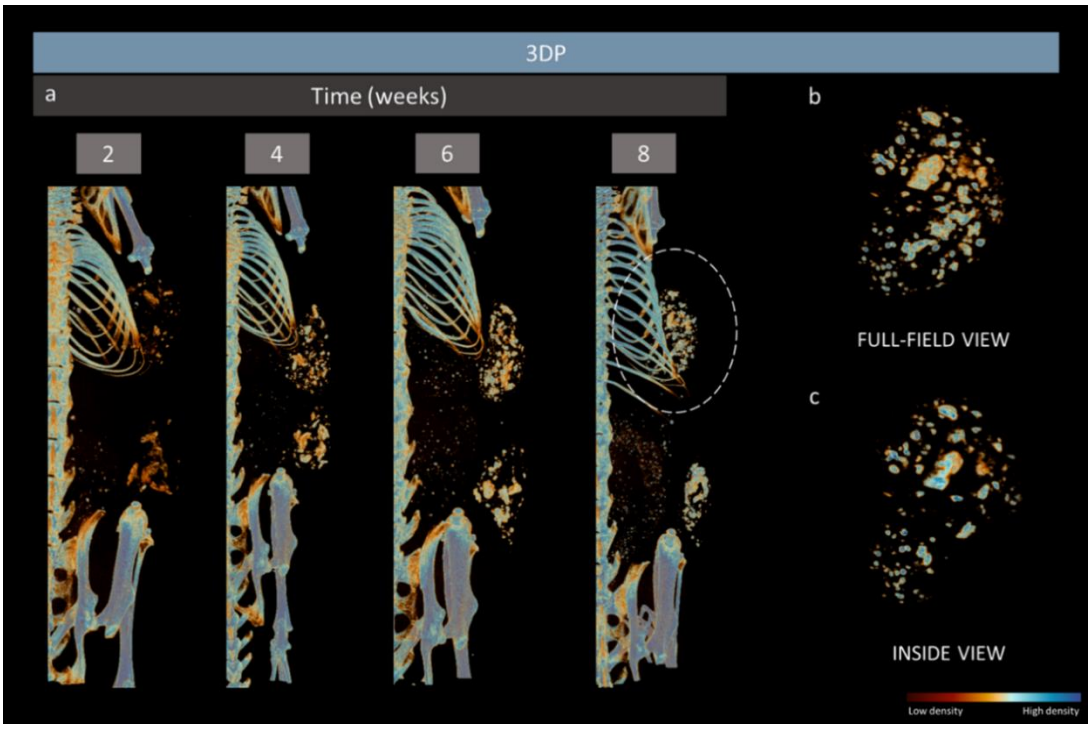

Figure 5.12. CT analysis of acellular 3D printed scaffolds.

Posterior CT images (a) of 3D printed scaffolds at 2, 4, 6 and 8 weeks. Full-field top (b) and inside (c) view of selected scaffold. Bone volume quantification (d) of 3D printed scaffolds over 8 weeks after implantation. Bone density scale indicates low density bone as dark red and high-density bone as blue

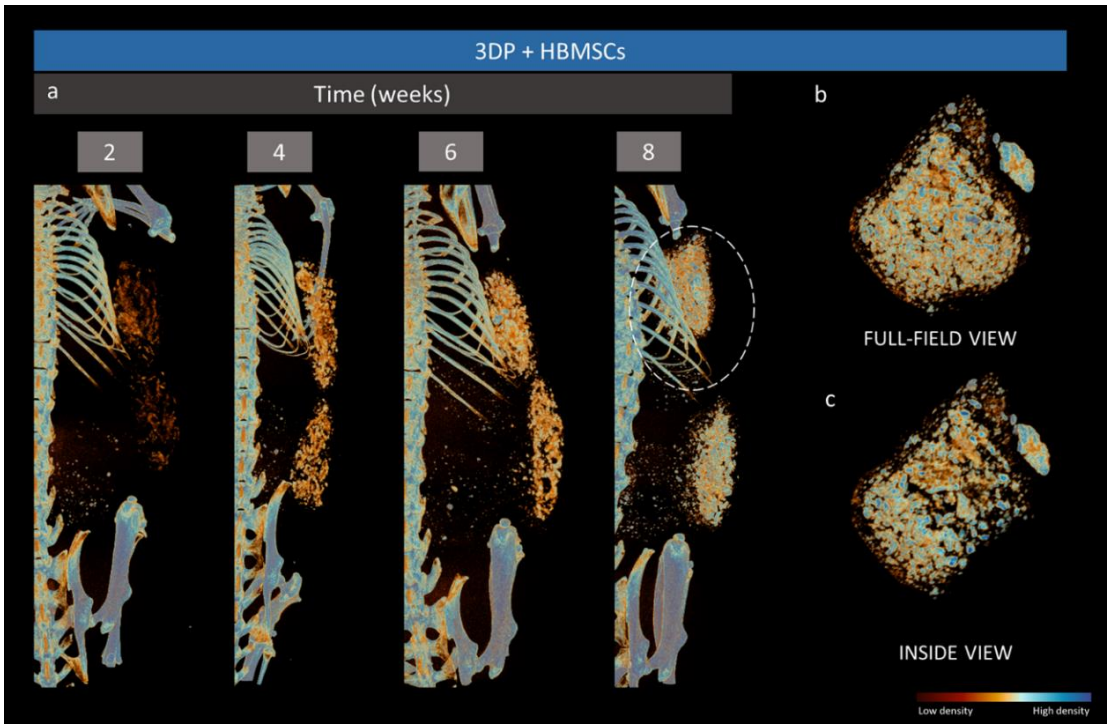

Figure 5.13. CT analysis of bulk HBMSC-laden 3D scaffolds.

Posterior CT images (a) of HBMSC-laden 3D scaffolds at 2, 4, 6 and 8 weeks. Full-field top (b) and inside (c) view of selected scaffold. Bone volume quantification (d) of HBMSC-laden 3D scaffolds over 8 weeks after implantation. Bone density scale indicates low density bone as dark red and high-density bone as blue.

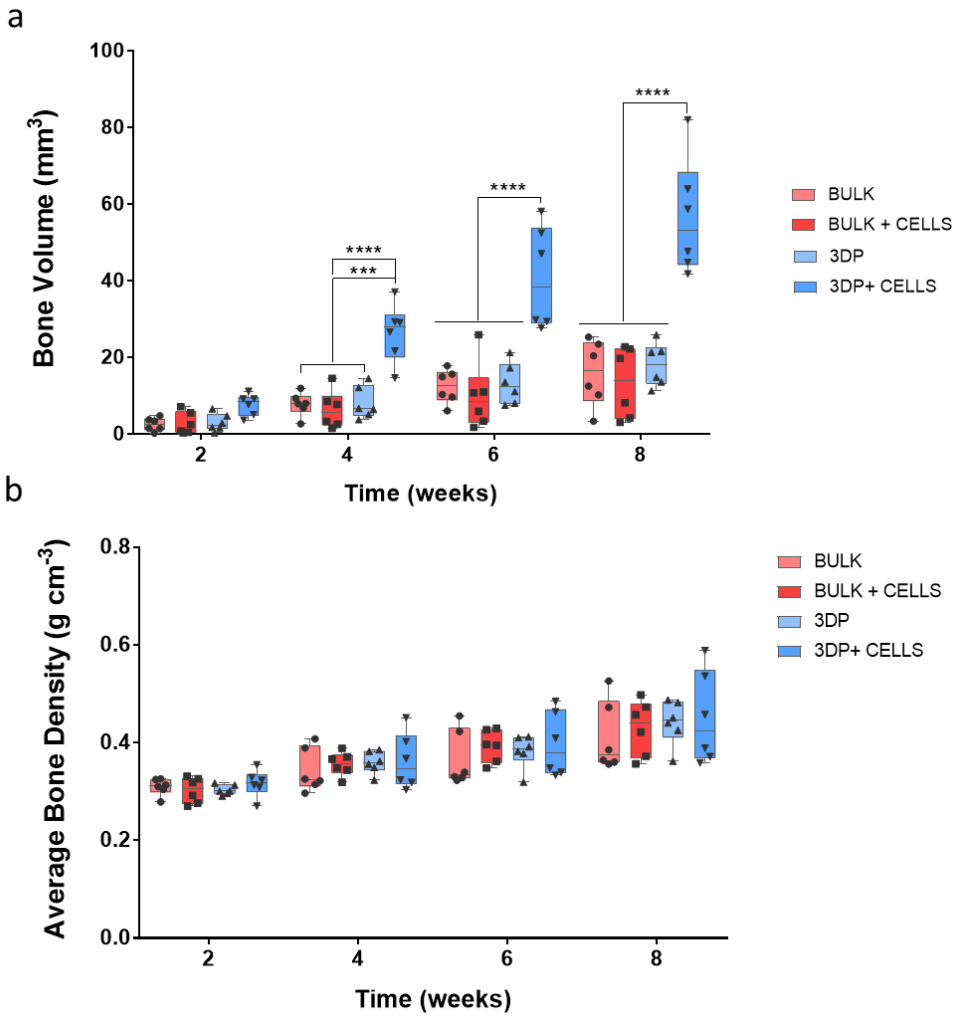

Figure 5.14. Quantitative analysis of *in vivo* implanted HBMSC-laden scaffolds after 8 weeks.

Bone volume (a) and average bone density (b) of three-dimensional constructs implanted *in vivo* were analysed by treatment conditions, including bulk, bulk with HBMSCs, 3D printed, and 3D printed with HBMSCs. Statistical significance assessed by two-way ANOVA followed by Tukey's multiple comparison tests. Mean ± S.D., n=6, *p<0.05, **p<0.01, ***p<0.001, ****p<0.0001.

Data reported in Appendix C Figure 5.4 a illustrate the changes in bone volume from 2 weeks through to 8 weeks of implantation. Acellular bulk scaffolds showed a significant increase in bone volume at 6 ($p<0.01$) and 8 ($p<0.0001$) weeks respectively compared to the 2 weeks scan. As expected bone volume increased significantly over 4 to 8 weeks ($p<0.05$). HBMSCs-laden bulk scaffolds showed a significant increase in bone volume at 8 weeks ($p<0.01$) compared to initial scan at 2 weeks. However, a non-significant growth was reported at 4 and 6 weeks compared to 8 weeks analysis. Acellular 3D printed scaffolds displayed significantly augmented bone volume at 8 weeks compared to 2 ($p<0.0001$) and 4 ($p<0.01$) week scan sets. A significant increment ($p<0.01$) was found after 6 weeks of implantation. HBMSCs-laden printed scaffolds showed significant increase in bone volume ($p<0.0001$) at all the time points examined.

Average bone density (Figure 5.14 b) was evaluated following CT scans. No significant differences were found between treatment groups at 2, 4, 6 and 8 weeks after implantation. Appendix C Figure 5.4 b indicates the quantitative changes in bone density each week for each treatment group. Acellular bulk scaffolds showed a linear increase in bone density from 0.31 ± 0.01 g cm^{-3}, 0.34 ± 0.04 g cm^{-3}, 0.36 ± 0.05 g cm^{-3} up to 0.41 ± 0.07 g cm^{-3} at 2, 4, 6 and 8 weeks respectively, with a significant increase in density from 2 up to 8 weeks ($p<0.01$). HBMSC-laden bulk scaffolds showed a similar increase in bone density over 8 weeks ($p<0.001$). The average density increased from 0.30 ± 0.02 g cm^{-3} at 2 weeks, 0.35 ± 0.02 g cm^{-3} at 4 weeks, 0.39 ± 0.032 g cm^{-3} at 6 weeks through to 0.43 ± 0.05 g cm^{-3} at 8 weeks. Bone density was also found significantly increased ($p<0.01$) after 6 weeks. Acellular 3D printed scaffolds showed significant changes in density between 2 and 8 weeks ($p<0.001$) resulting in 0.30 ± 0.01 g cm^{-3} after 2 weeks, 0.36 ± 0.02 g cm^{-3} after 4 weeks, 0.38 ± 0.03 g cm^{-3} after 6 weeks and 0.44 ± 0.04 g cm^{-3} after 8 weeks. 3D printed scaffolds were found to show significant increase ($p<0.05$) in average bone density after 6 weeks (compared to 2 weeks) and after 8 weeks (compared to 4 weeks) post-implantation. HBMSC-laden 3D printed scaffolds displayed significantly increased mineral density after 8 weeks ($p<0.001$) (0.31 ± 0.02 g cm^{-3}, 0.36 ± 0.05 g cm^{-3}, 0.39 ± 0.06 g cm^{-3} and 0.45 ± 0.09 g cm^{-3} after 2, 4, 6 and 8 weeks respectively). Bone density was found significantly higher ($p<0.05$) after 6 and 8 weeks compared to 2 and 4 weeks, respectively.

Bulk scaffolds stained for Alcian blue/Sirius red (Figure 5.15 a-i) displayed limited GAGs distribution (Figure 5.15 a-ii) and were surrounded by a layer of collagen over the entire scaffold (Figure 5.15 a-iii). GAGs were found present, extensively, within the sample (Figure 5.15 a-iv) with limited or no staining for collagen within the core of the implanted sample. Bulk control loaded with HBMSCs (Figure 5.15 b-i) displayed a paucity of GAGs (Figure 5.15 b-ii) comparable to the acellular control. A collagenous thin layer encapsulated the sample (Figure 5.15 b-iii) with discrete processes suggesting enhanced integration compared to the acellular bulk scaffolds. A tight interaction with the external collagen layer (Figure 5.15 b-iv) was observed in HBMSC-laden bulk scaffolds. Acellular 3D printed samples stained strongly for Alcian blue/Sirius red (Figure 5.15 c-i). Scaffolds were observed to be degraded and integrated with the surrounding tissue (Figure 5.15 c-ii,iii) with collagenous tissue present inside the scaffold constructs (Figure 5.15 c-iv). HBMSC-laden 3D printed implants (Figure 5.15 d-i) displayed high levels of GAGs resulting in a compact tissue-like structure (Figure 5.15 d-ii). Integration with surrounding tissue was observed extensively (Figure 5.15 d-iii, iv) with collagenous tissue throughout in the core of the scaffold.

Implants were stained with Goldner's Trichrome to determine if blood vessels were present in the mineralised tissue. Bulk controls (Figure 5.16 a-i) while integrated with the host tissue (Figure 5.16 a-ii,iii) displayed limited vessel structures (Figure 5.16 a-iv). HBMSC-laden bulk scaffolds (Figure 5.16 b-i) were fully integrated (Figure 5.16 b-ii) with vessel rich tissue (Figure 5.16 b-iii), although limited capillary infiltration (Figure 5.16 b-iv) was observed. Acellular 3D printed scaffolds (Figure 5.16 c-i) were noted to be integrated with the surrounding host tissue (Figure 5.16 c-ii) with blood vessels on the periphery of the samples (Figure 5.16 c-iii) and erythrocytes entrapped in surrounding tissue (Figure 5.16 c-iv). 3D printed cell-laden constructs (Figure 5.16 d-i) contained extensive collagenous tissue (Figure 5.16 d-ii) with major vessels across the inner region of the scaffold (Figure 5.16 d-iii,iv).

Von Kossa staining was carried out to assess mineral deposition in implanted scaffolds. Acellular bulk controls (Figure 5.17 a-i) were found mineralised with scattered mineral nodules (Figure 5.17 a-ii) in the inner surfaces of the scaffold and more (Figure 5.17 a-iii) and less dense (Figure 5.17 a-iv) nodules on the outer surface. Similarly, cellular bulk scaffolds (Figure 5.17 b-i) presented an even distribution of inner mineral deposition (Figure 5.17 b-ii,iii) with highly concentrated mineral cores (Figure 5.17 b-iv). 3D printed scaffolds were found mineralised (Figure 5.17 c-i), but poorly within the core (Figure 5.17 c-ii). Cluster-like nodules were found evenly distributed in the whole scaffold (Figure 5.17 c-iii,iv). Cell-laden scaffolds (Figure 5.17 d-i) were found mineralised in cluster-like deposited nodules (Figure 5.17 d-ii) that were found preferentially located on the outer surface of the scaffold (Figure 5.17 d-iii,iv).

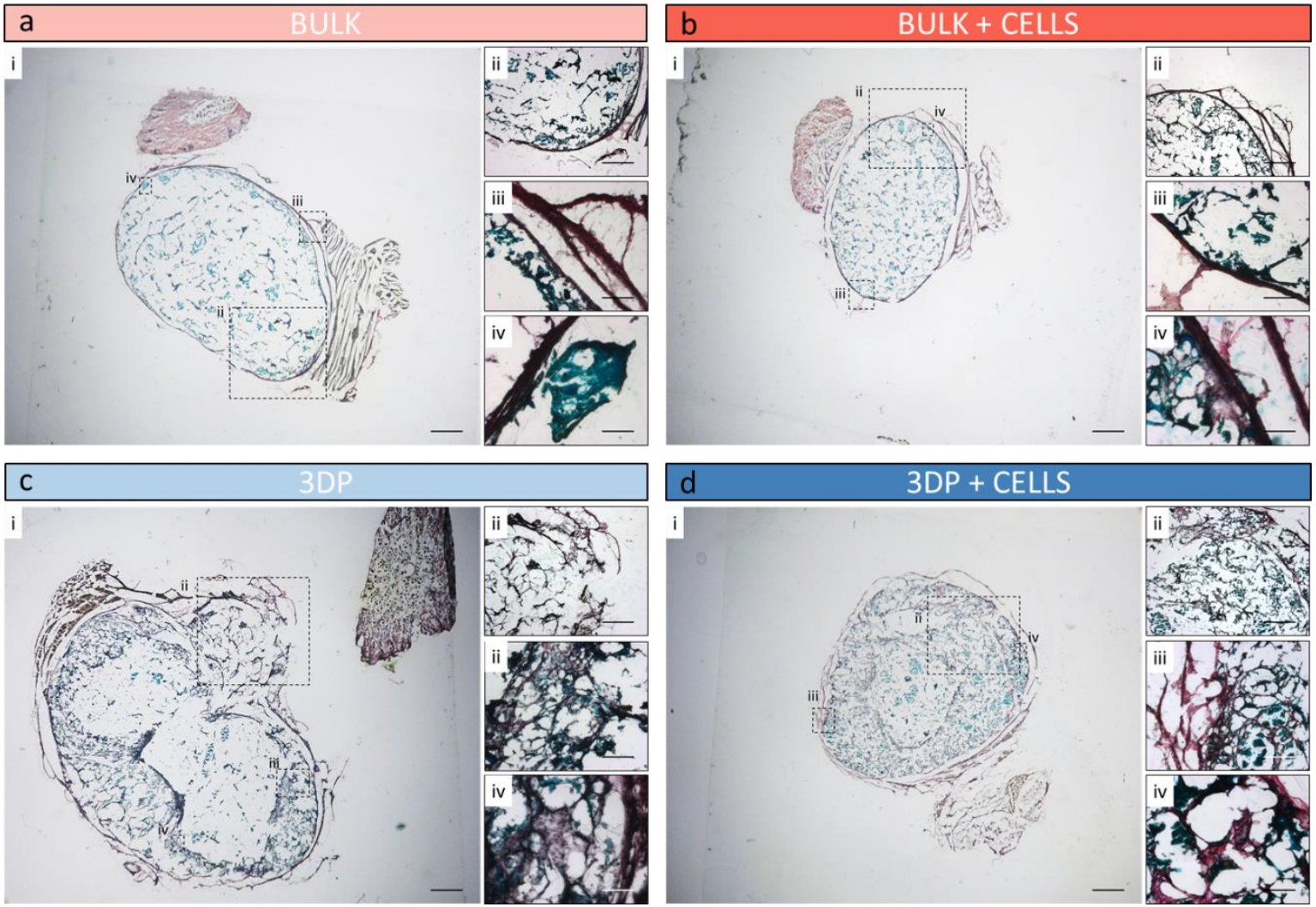

Figure 5.15. Histological analysis of implanted scaffolds.

Alcian blue/Sirius red staining was performed on bulk (a) and HBMSC-laden bulk (b) controls, acellular 3D printed (c) and HBMSC-laden 3D printed scaffolds (d). Histological process stained black for nuclei, blue for glycosaminoglycans and other polysaccharides, red for collagen. Scale bar: (i) 1 mm, (ii) 500 µm, (iii) 100 µm, (iv) 50 µm.

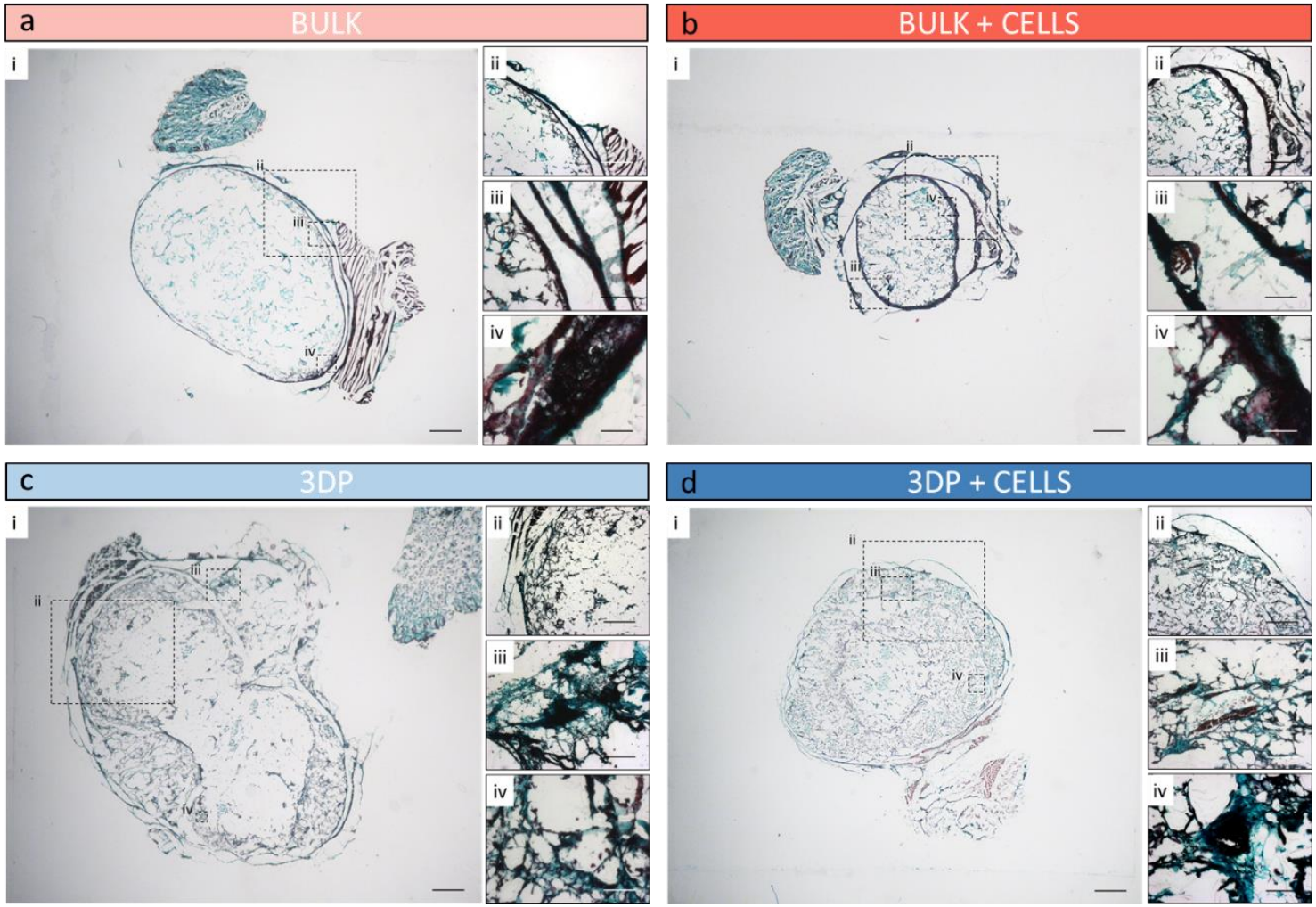

Figure 5.16. Histological analysis of implanted scaffolds.

Goldner's Trichrome staining was performed on bulk (a) and HBMSC-laden bulk (b) controls, acellular 3D printed (c) and HBMSC-laden 3D printed scaffolds (d). Histological process stained black for nuclei, red for erythrocytes, orange/bright red for cytoplasm, green for collagen. Scale bar: (i) 1 mm, (ii) 500 µm, (iii) 100 µm, (iv) 50 µm.

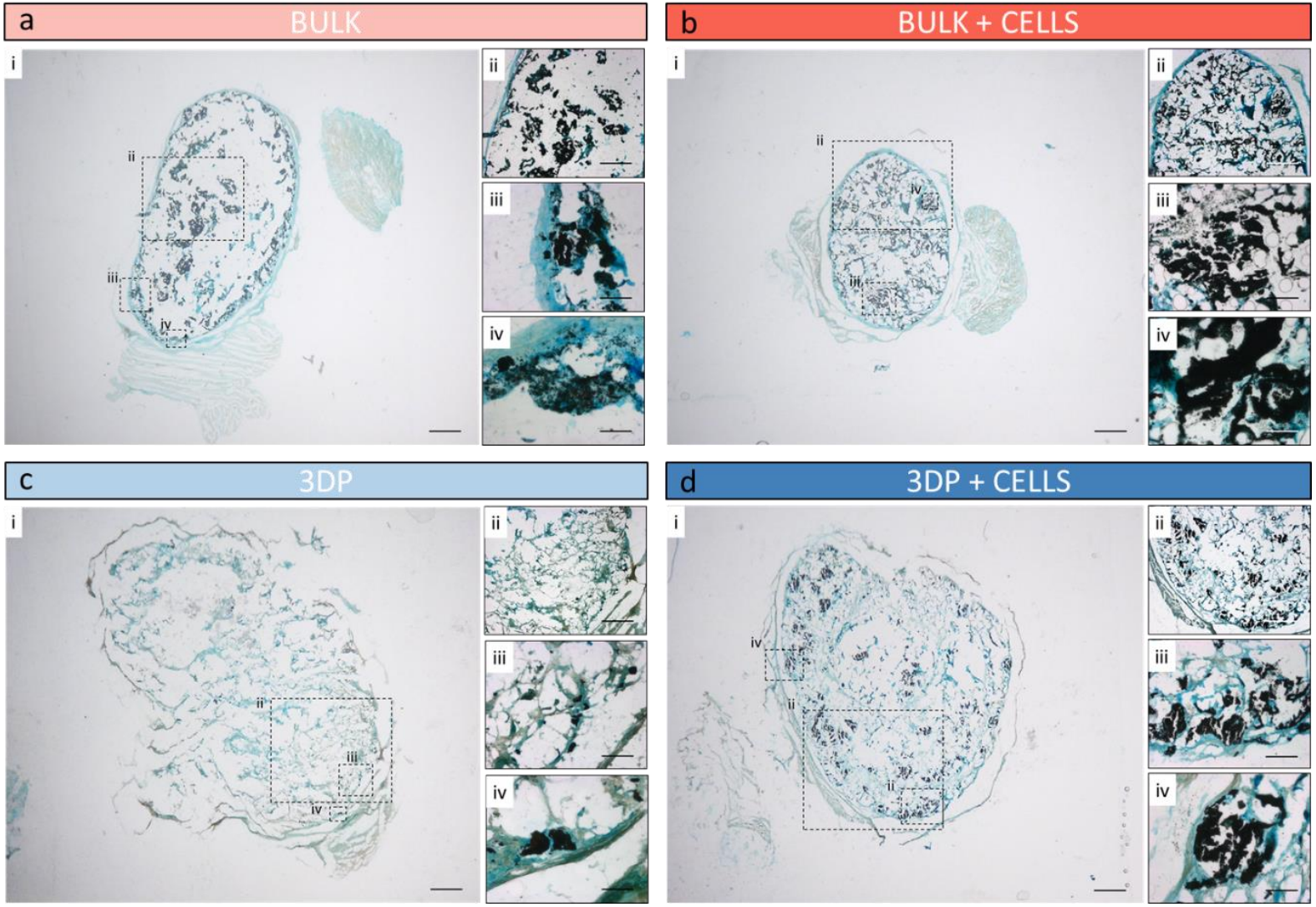

Figure 5.17. Histological analysis of implanted scaffolds.

Von Kossa staining was performed on bulk (a) and HBMSC-laden bulk (b) controls, acellular 3D printed (c) and HBMSC-laden 3D printed scaffolds (d). Histological process stained black for mineralised tissue, green/blue (Alcian blue counterstain) for polysaccharides. Scale bar: (i) 1 mm, (ii) 500 µm, (iii) 100 µm, (iv) 50 µm.

5.4 Discussion

Biofabrication offers new approaches to tissue regeneration, screening and indeed approaches to reduce animal experimentation [239]. However, scarcity of essential *in vivo* studies of safety and efficacy of 3D printed scaffolds for bone formation are hampering the pace of this process, preventing the clinical translation of a number of biofabricated constructs, tested exclusively *in vitro*. Ectopic bone formation model results are particularly useful in evaluating novel osteoinductive biomaterials, bone stimulating growth factors and skeletal-forming stem cells [16,229]. Indeed, ectopic bone formation systems have been shown to be an appropriate model for its robustness and the possibility to screen the efficacy of constructs and bioactive factors for bone formation [240,241]. Inspired by previous results obtained in similar mice models [110], bulk alginate drug-free and loaded with BMP-2 were used as negative and positive control scaffolds.

Alginate is a naturally occurring polysaccharide with excellent biocompatibility and biodegradability properties and, importantly is approved by the Food and Drug Administration (FDA) as a bone void filler device in combination with human demineralised bone matrix [242]. Sodium alginate release properties are well known and widely used in drug delivery [243–245] exhibiting an elevated drug-loading efficiency [246] paired with a tuneable release profile [76] depending on the molecular weight used, but generally matching a burst-release mechanism. Imitating a clinical scenario, following a previous employed protocol [110], alginate controls and 3D printed 3-3-3 scaffolds were soaked in BMP-2 allowing absorption of the drug within the gel matrix. CT scans collected after 4 weeks of implantation revealed limited mineral deposit of drug-free alginate compared to BMP-2 loaded control, which showed a mineral deposition particularly concentrated on the outer surface of the bulk scaffold. Bulk alginate scaffolds were found to be spherical in shape after 4 weeks *in vivo* showing limited degradation. Furthermore, cross-sectional view of CT images demonstrated limited internal mineralisation of the bulk controls, with limited higher density in BMP-2 bulk than drug-free bulk alginate scaffolds. In contrast, 3D printed drug-free 3-3-3 scaffolds showed extensive and evenly distributed mineral deposit throughout the entire lattice constructs. Similar mineral deposits were found in implanted BMP-2-loaded 3D printed scaffolds. Printed scaffolds were found to be physically degraded with only partial conservation of their lattice structure. CT images of 3D printed scaffolds revealed a full mineral lattice structure with superior shape retention in the drug-free scaffolds. This was due to the localised mineralisation auto-induced by the clay content, with spontaneous mineral deposition resulting in mineralised strands. Clay-mediated

mineral deposition has not been reported *in vivo*. Shi *et al.* [94] showed an enhanced mineral deposition *in vitro* of cell-laden Laponite gels, providing an insight in the inherent Laponite bioactivity. Over 3 weeks, the matrix reorganization and mineral deposition in FBS-absorbed cell-laden clay gels were observed superficially and within the capsule core, suggesting an increase of calcium phosphate, confirmed by EDX analysis. Similarly, the clay-based constructs in this study displayed spontaneous mineralisation even in the absence of bone formation agents (e.g. BMP-2). 3D printed scaffolds supplemented with BMP-2 were found to show a higher mineral density and distribution, losing their lattice structure to the mineral tissue, which was observed to fill the open pores of the scaffold. Interestingly, BMP-2 loaded scaffolds were found to exhibit a higher mineral density distribution within the printed implant. Quantitative analysis of mineral volume and density revealed the superior capacity of printed 3-3-3 to generate larger volume of mineral tissue compared to equal bulk volumes of alginate gels loaded or free of BMP-2, showing promising potential for clinical translation [110,247]

Histological staining was carried out to confirm mineralisation and bone formation after 4 weeks. Alginate bulk scaffolds (control) resulted in poor integration with surrounding tissue, showed limited collagenous staining and surrounding capillaries. Mineralisation was observed to be localised to a single area on the outer surface of the samples. Similarly, BMP-2 loaded samples were found to be poorly integrated with limited vascularisation and mineralisation concentrated in larger areas than the BMP-2 free control, but still on the periphery. Interestingly, 3D printed scaffolds showed higher integration and mineralisation compare to controls. Vasculature was found close to the implant with few major vessels, suggesting the growth of vessels around the drug-free implant, confirming the functionality of acellular 3-3-3 scaffolds. BMP-2 loaded printed scaffolds were found extensively integrated. However, a fibrotic capsule appear to be localised on the outer region of the scaffolds, suggesting an inflammatory response of the host to the implanted constructs after 4 weeks [248]. Nevertheless, major vessels were found in close proximity and within the printed implants indicating a vascular rich environment, particularly suitable for bone formation [160]. Mineral deposition was found evenly distributed in drug-free and BMP-2 loaded 3-3-3 scaffolds, with highly mineralised outer surfaces compare to the core of the implant. However, BMP-2 loaded samples were found to show greater mineralised tissue within the inner portion of the scaffold, matching CT scan results and suggesting greater potential for bone formation when 3-3-3 printed scaffolds are absorbed with BMP-2 right before implantation [110,249].

HBMSCs were encapsulated in 3-3-3, printed and implanted in athymic mice to evaluate safety and efficacy of cell-laden 3-3-3 constructs. Furthermore, a comparison between bulk and 3D printed porous lattice structure was considered in the study,

hypothesizing the beneficial implantation of a cell-laden porous three-dimensional structure. Athymic nude mice [229,250,251] are used as a model for hosting human cells and testing their efficacy as a pre-clinical model. Showing spontaneous deletion in the *Foxn1* gene with an inhibited immune system due to the reduction of T-cells numbers [251], athymic mice are ideal for implantation of cell-laden scaffolds, as proven in previous studies [72,252–254].

Cell-laden printed constructs were compared with acellular scaffolds and bulk casted controls (acellular and cell-laden). Interestingly, an 8-week study of bone forming 3D printed scaffolds has never been attempted before. Therefore, scaffold controls were cultured *in vitro* for 8 weeks to evaluate their integrity. Bulk acellular and cell-laden scaffolds were not influenced by 8 weeks of culture at 37°C and 5 % CO_2 balanced air. Bulk scaffolds remained resistant to degradation. However, HBMSC-laden bulk scaffolds appeared more translucent than acellular controls, suggesting limited degradation, possibly caused by encapsulated HBMSCs [62]. However, these scaffolds remained intact, with negligible leakage of material or cracking, typical of bulk degrading constructs. 3D printed structures were partially degraded after 8 weeks of culture. HBMSC-laden printed scaffolds were remodelled with closed pores and were smaller compared to cell-free controls following implantation. Hydrogel degradation can be influenced by a number of factors that include the number of polymeric chains and linkages, biomaterial chemistry, cell inclusion and *in vivo* micro-environment [62,255]. Cushing *et al.* [256] have shown that encapsulated human HBMSCs are able to actively remodel the hydrogel core environment to enable migration and form cell-to-cell junctions, triggering differentiation. In the remodelling process, cells degrade the soft hydrogel material to create more space for interaction. This degradation can be tuned so as not to affect the overall structural integrity of the 3D printed scaffold.

To date, an *in vivo* investigation and comparison of acellular and cell-laden bulk and 3D printed scaffolds has not been carried out. However, few recent studies have demonstrated the beneficial results of SSCs seeding or inclusion in printed scaffolds [163,165,237] demonstrating greater bone deposition [163] and vascularisation [237]. In this chapter, a clear indication of advantages in printing SSCs in lattice structure has been demonstrated. Scaffolds were implanted subcutaneously with at least two different treatment groups per mouse, in a randomised arrangement, to prevent cross-talk and influence bone formation. CT scans were performed at 2, 4, 6 and 8 weeks after implantation, revealing a rapid growth of mineral deposition in all groups. Overall, 3D lattice constructs showed a higher bone volume and density compared to the bulk controls. As mentioned previously, the clay and alginate portions of the 3-3-3 tends to increase its mineral content over time. Significant mineral volume deposition was observed to occur mainly in the outer surface of the bulk scaffold, with limited mineral content on the inside.

This result suggests a slow and irregular mineralisation of bulk 3-3-3 scaffolds similarly to results obtain in the first *in vivo* study. Bulk scaffolds are not allowing tissue penetration and appear to mineralise exclusively on the outer surface, independently from HBMSCs inclusion. On the contrary, the highly porous 3D printed lattice structure showed an elevated mineral deposition and possibly a different mechanism from the mineralisation of bulk controls. While bulk scaffolds showed an evenly distributed average mineral density, acellular 3D printed scaffolds were found to show a higher density cluster network, comparable in density to the skeletal bones of the mouse. Indeed, the printed structures were observed, as reported in the first *in vivo* study as well, to undergo a mineralisation process with cluster-like high density mineral formation with limited low-density deposition and significant porosity, making the measured volume and density similar to the bulk controls. HBMSC-laden 3D printed 3-3-3 constructs were found to follow a cluster mineralisation process, but showed a significant larger mineralised volume compared to the printed acellular controls. A great difference in bone volume and average density of the mineralised tissue was found when cell-laden lattice scaffolds were compared with acellular and cellular bulk controls, suggesting a clear and significant advantage of the open porous lattice structure never reported before. The mineral density was found to be well distributed within the scaffold with an elevated number of high-density clusters and a diffuse low-density matrix to encapsulate them. The bone formation mechanism can be related to the acellular clay-based 3D printed scaffolds with a high-density cluster-like arrangement due to the clay content. However, the lower density matrix surrounding the clusters was not found in the acellular printed controls, suggesting a novel remodelling and bioactive functional activity of the encapsulated HBMSCs.

Interestingly, histological analysis confirmed greater bone tissue content in cell-laden 3D printed structures compared to bulk controls and acellular printed scaffolds. However, mineral depositions were found consistently greater in bulk acellular and cellular structures respect to printed structures. On the contrary, 3D printed scaffolds were found to be rich in bone tissue as per Sirius red staining through to the core of the implant, and highly present in cell-laden constructs compared to acellular scaffolds. Importantly, blood vessels were found to infiltrate the printed structure which either collapsed or integrated with host tissue after 8 weeks, therefore it was difficult to estimate the specific area of vessel infiltration. Nevertheless, HBMSC-laden printed scaffolds showed a higher number of larger vessels present in the core of the scaffold, suggesting the formation of a rudimentary marrow cavity.

5.5 Conclusions

In this chapter, the *in vivo* investigation of safety and efficacy of 3D printed 3-3-3 scaffolds was carried out. Initially, BMP-2 was absorbed onto alginate controls and 3D printed 3-3-3 scaffolds implanted in mice and compared to drug-free controls. After 4 weeks, 3D printed constructs showed significantly higher bone volume and density independent of the loaded BMP-2. Scaffolds were highly mineralised compared to bulk alginate controls and bone tissue was found in the 3D printed implants proving functionality of 3D printed 3-3-3 scaffolds *in vivo*. A further animal model was employed to investigate HBMSCs efficacy in producing bone *de novo* when encapsulated and printed in 3-3-3 hydrogel. HBMSC-laden 3D printed scaffolds were found to exhibit significantly higher bone volume compared to the acellular lattice structures. Comparison with acellular and HBMSC-laden bulk 3-3-3 scaffolds further confirmed 3D printed constructs superior ability in forming bone ectopically. These results finally suggest *in vivo* functionality of 3D printed clay-based scaffolds for large bone volume formation.

Further studies are needed to elucidate the mechanism(s) of mineralisation and bone formation (intramembranous or endochondral). The lack of either *in vitro* or *in vivo* studies on the spontaneous mineralisation capacity of Laponite make this the first study to investigate such process. However, further confirmation with technologies including atomic absorption spectroscopy and EDX will be needed to identify mineral deposition process and its origin in clay-based bioink. Furthermore, immunohistological staining will aid collagen specificity (type I) for bone tissue, confirming functional mineral tissue formation.

Moreover, the extrusion of 3-3-3 is simple and effective for the immediate production of cell-laden implants. However, more clinically relevant size scaffolds are needed and the extrusion-based technology in air is limiting the possibility to produce such implants. A novel technological approach to 3D print cells in a supporting bath for the fabrication of clinically relevant scaffolds is reported in the next chapter.

Chapter 6 Printing bone in a gel: using clay gels to print skeletal stem cells

6.1 Introduction

Printing cells in three dimensions has proved challenging when the aim is to fabricate large structures to fill critical tissue defects [9]. Hydrogels are attractive biomaterials to use in the printing of cells and to build-up three-dimensional structures [61,80]. Printed scaffold should either be functional or able to be functionalised following printing. Functionality can depend on i) the inherent bioactivity of the hydrogel, ii) inclusion of cells, and iii) retention of growth factors. The hydrogel should be able to be extruded with high precision, enabling the fabrication of complex three-dimensional structures that maintain their shape in culture. Generally, hydrogel formulations are excellent in their swelling capacity; being able to absorb water and significantly increase their volume [257]. However, for bioprinting applications, bioinks ideally are required to display minimal swelling capacity post-printing and preserve their shape indefinitely, unless undergoing degradation.

Indeed, printing reported in Chapters 3, 4 and 5 showed discrete printing abilities and swelling of the bioink. Nevertheless, the ability to build large structures was limited to 30 layers maintaining open porosity and structural integrity. Clinical-size constructs have been previously fabricated [153,258–263] by printing bioinks within a temporary support material. This novel technology is called free-form printing and have been shown to be particularly useful for producing large and complex structures that would otherwise be impossible if fabricated in air. Hinton *et al.* [258], demonstrated that the extrusion of the hydrophobic polydimethylsiloxane (PDMS) in a hydrophilic carbopol (poly (acrylic acid)) bed resulted in high shape fidelity of the construct, with the possibility to fabricate hollow and complex vasculature structures. However, the lack of further study of PDMS biocompatibility and carbopol bed functionality, limited the free-form printing application using this approach.

Recently, Moxon *et al.* [259] detailed the ability to extrude free-form bioink into a cytocompatible gel bath enabling support and further crosslinking of the bioink. The bioink of choice was gellan gum (GG) [264,265], a polysaccharide material that has been shown to be highly biocompatible [266], supporting cell viability and functionality *in vitro* [267]. GG is a popular biomaterial of microbial origin (from *Sphingomonas elodea*) and due to its advantageous physicochemical properties, GG has been widely used as additive for pharmaceutical products [268]. Gellan gum is a FDA and European Union (E418) approved with significant potential for tissue engineering applications [269]. The support bath consisted in an agarose fluid gels. Agarose is a popular polymeric biomaterial that is able to form inert hydrogel network widely used for cell encapsulation [270,271]. The fluid gel prepared by Moxon *et al.* [259] consisted of an heterogeneous suspension of particles with sizes in the range of 2-11 μm which was particularly suitable for its final thixotropic

properties. Indeed, the agarose fluid gel was able, at the same time, to support the extruded GG bioink prior to crosslinking and allow the free movement of the printing nozzle by self-healing right after. GG at low concentration could be precisely deposited in 3D generating complex structures. A complex double layered osteochondral plug was generated by depositing a gellan gum solution loaded with HAp to mimic bone and gellan gum as the cartilage mimicking layer. The resulting constructs were functional, but lacked shape fidelity, and only *in vitro* investigations were performed.

GG is easily tuneable in its mechanical properties by the change of the system temperature [272]. This particular property is appealing for the chemical and physical modification of this polymeric material [113]. Laponite (LAP) has been shown to be an excellent filler for hydrogels that aim to function as bioinks for biofabrication applications [56,118,122]. Pacelli *et al.* [113] recently reported the physico-chemical and drug-delivery properties of LAP-GG hydrogels, demonstrating that; i) Laponite induced an increase in viscosity of the final polymeric solution, ii) stabilised the GG network, and iii) modulated the release of a model drug (ofloxacin). However, functional studies on encapsulated cells were not implemented and the use of a methacrylate-modified GG, crosslinked by UV-light is far from ideal for cell encapsulation purposes.

In this chapter, the use of a nanocomposite bioink (LAP-GG) (Figure 6.1 a) that could be extruded in a tailored functional agarose fluid gel (Figure 6.1 b) has been examined. Specifically, this chapter will examine the potential to fabricate large constructs (> 10 mm) (Figure 6.1 c) and cell-laden scaffolds (Figure 6.1 d) and functionality examined within an *ex vivo* model (Figure 6.1 e) to investigate membrane integration and angiogenic potential.

Hypothesis (IV):

Laponite (LAP) can be combined with gellan gum (GG) to generate a mechanically improved bioink with tailorable swelling and greater printability. Cell viability and functionality can be sustained up to 21 days *in vitro* and nanosilicate inclusion can ameliorate osteogenic stimuli inducing osteogenic differentiation. Laponite can improve drug absorption and localisation within its matrix, being able to stimulate construct integration and vascular infiltration in an *ex vivo* model.

Aims:

- To blend Laponite with gellan gum (LAP-GG) and quantify the degree of swelling *in vitro*;
- To evaluate printability in air and in agarose of LAP-GG and GG control;

- To quantify viability/proliferation and assess functionality of C2C12 cells printed in agarose;
- To investigate drug analogues absorption while printing from the dispersion of the compound in agarose and consequent release;
- To evaluate integration of printed LAP-GG and GG constructs loaded with VEGF during printing in an *ex vivo* CAM model.

Overview of Chapter 6:

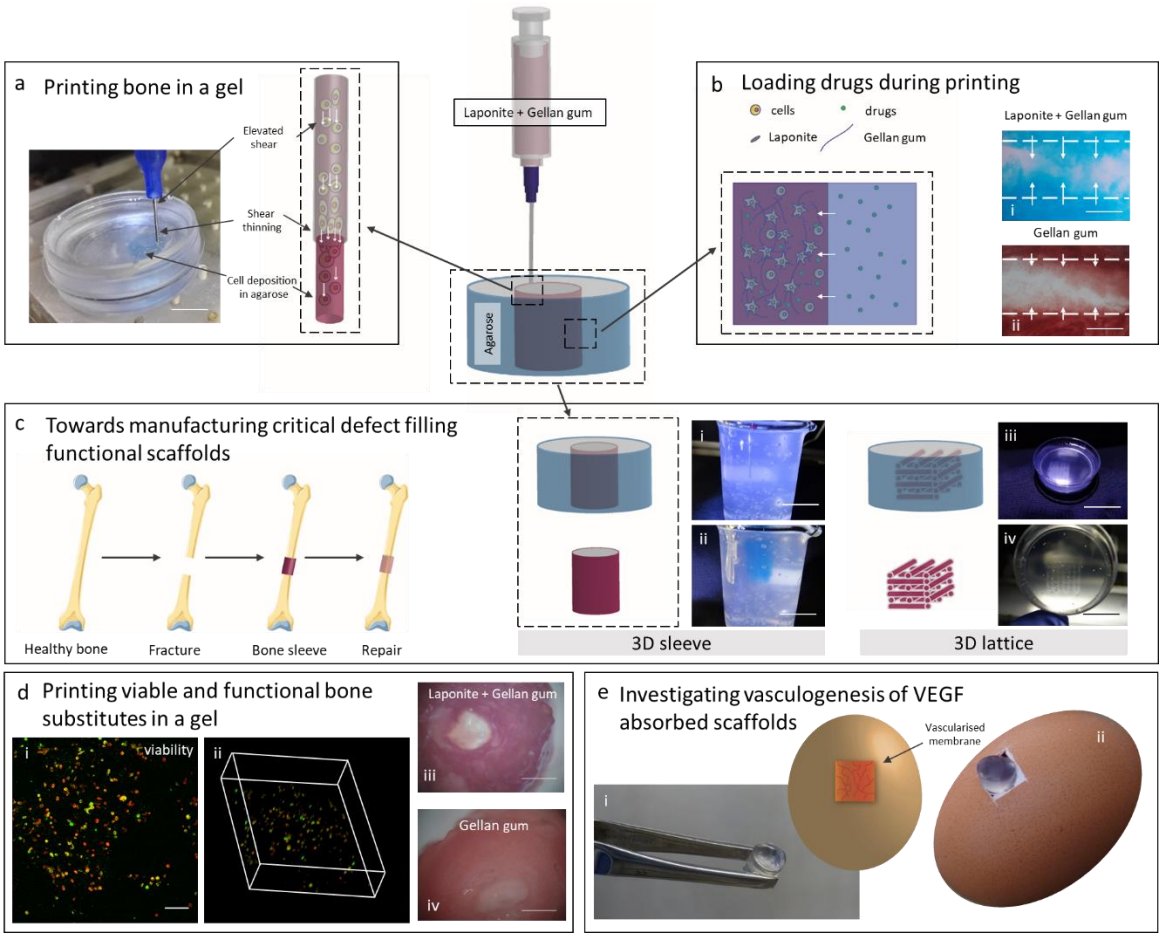

Figure 6.1. Schematic of LAP-GG printing in agarose fluid gel for skeletal tissue engineering.

Extrusion of LAP-GG in agarose bed can produce three-dimensional structures (a). Low polymeric content of the nanosilicate bioink can shield cells from damage and preserve the viability right after extrusion. The agarose fluid gel can allow loading of compounds of interests during printing (b) both in LAP-GG and in GG control. LAP-GG bioink can be loaded with greater penetration of the compound in the printed strand. LAP-GG extrusion in self-healing agarose support can be used to fabricate large functional structures (c) such as 3D sleeve (i,ii) and 3D lattice (iii,iv) structures to fill critical bone defects. Cells can be printed when encapsulated in LAP-GG (d) and their viability (i,ii) and functionality (iii,iv) assessed to investigate bone formation potential. Integration with chick membrane model and vascular penetration (e) can be investigated when printed scaffolds are implanted in the vascularised membrane of a developing chick. Scale bar: (a) 5 mm, (b-i,ii) 100 µm, (c-i,ii) 20 mm, (c-iii) 20 mm, (c-iv) 10 mm, (d-i) 100 µm, (d-iii,iv) 2 mm.

6.2 Methods

6.2.1 Laponite

This methodology is detailed in Chapter 2 (2.2.1 page 43)

6.2.2 Gellan gum

Low acyl gellan gum (GG) was allowed to dissolve in DW at different concentrations, as described by a previously reported protocol [259]. Hydrogels were prepared based on w/v percentage formulations. DW was left to stir at 5 G and heated at 60°C before adding GG and leaving it to stir for 1 h at constant shear and temperature. The increase of solution transparency confirmed GG complete dispersion. GG gel was allowed to cool down at room temperature for 2 h before using it for rheological, printing or other studies.

6.2.3 Laponite-gellan gum

Laponite-gellan gum (LAP-GG) was prepared from a Laponite suspension prepared following a detailed protocol reported in the paragraph 2.2.1 (page 43). Briefly, DW was left to stir at 5 G (Figure 6.2 a) and Laponite was added slowly (Figure 6.2 b) to reach clear dispersion after 6 h (Figure 6.2 c). Sterile GG powder was then added to the Laponite suspension and heated at 60°C (Figure 6.2 d). GG integration in Laponite suspension was carried out at a constant 5 G shearing at 60°C for 1 h. Final LAP-GG suspension results homogenous and amber in colour (Figure 6.2 e) ready for printing (Figure 6.2 f). If stored at room temperature, the LAP-GG bioink hardens and therefore results not printable (Figure 6.2 g,h). Weight content of Laponite and gellan gum depend on the w/v formulations reported in the Table 6.1. LAP-GG bioink with 7.5 % w/v GG and 1 % w/v Laponite was considered for all the experiments reported in Chapter 6, excluding the sol fraction and mass loss study, used for screening of optimal bioink concentration.

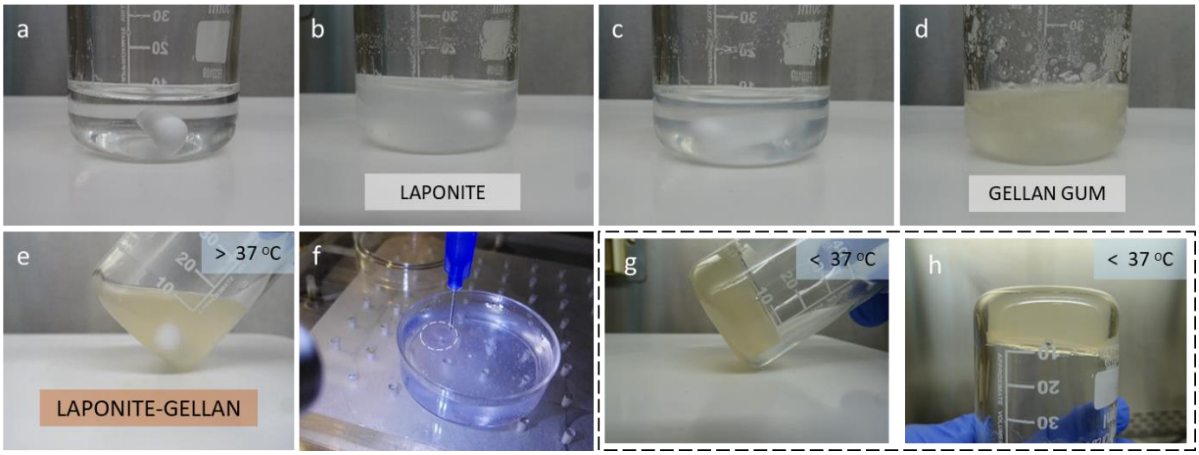

Figure 6.2. Synthesis of Laponite-gellan gum bioink.

DW was allowed to stir (a) and Laponite added (b) slowly to allow full dispersion of nanoparticles (c). Gellan gum was then added (d) and allowed to solubilise in heated Laponite suspension, leaving a homogeneous bioink (e) that can be immediately use in combination with agarose fluid gel for free-form printing (f). LAP-GG gel stored at a temperature below 37°C will harden (g) and gel (h).

Table 6.1. Nomenclature of the tested Laponite - gellan gum bioinks formulations (all values correspond to % w/v)

Label	*Laponite (L)*	*Gellan gum (G)*
G1	0	1
L0.5G1	0.5	1
L1G1	1	1
G2	0	2
L0.5G2	0.5	2
L1G2	1	2
LAP-GG bioink	1	7.5

6.2.4 Agarose fluid gel

Fluid gel was prepared as previously described [259]. Briefly a 0.5 % w/v solution of agarose (Genetic analysis grade, Fisher Bioreagents, UK) was autoclaved right after agarose addition to 300 ml of DW. The solution was then allowed to cool down from 85°C to 20°C under constant shear (20 G) by a magnetic stirrer. This shearing has been shown

to create an angular velocity of 74 rad s^{-1}. The solution was then sterilised under UV irradiation for 1 h.

6.2.5 Mass loss and swelling ratio

Mass loss and swelling studies were performed on the GG and LAP-GG discs to study the effect of nanosilicate incorporation into GG hydrogels. GG and LAP-GG discs were prepared by pipetting 500 µl of hydrogel bioinks in their fluid form into 2 ml sterile Eppendorf tubes. A solution of 1 M $CaCl_2$ was then pipetted in each tube and allowed to crosslink the gels for 10 min. All samples were weighed immediately before ($m_{initial}$) and after cross-linking ($m_{initial,t0}$) to obtain initial wet mass, and three samples were lyophilized to obtain their dry weights ($m_{dry,t0}$). The actual macromere fraction was then calculated using equation (2)

$$actual\ macromer\ fraction = \frac{m_{dry,t0}}{m_{initial,t0}} \quad (2)$$

The remaining samples were incubated in a PBS bath at 37°C to allow swelling and the soluble fraction to leach out of the hydrogel network. After 1 day the samples were weighed again ($m_{swollen}$). The samples were then lyophilized and weighed a last time (m_{dry}). The sol fraction was defined as the mass loss after 1 day and was calculated using equation (3) and (4). Mass swelling ratio (q) was calculated using equation (5).

$$m_{initial,dry} = m_{initial}\ (actual\ macromer\ fraction) \quad (3)$$

$$sol\ fraction = \frac{m_{initial.dry} - m_{dry}}{m_{initial,dry}}\ 100\% \quad (4)$$

$$q = \frac{m_{swollen}}{m_{dry}} \quad (5)$$

6.2.6 Swelling in air and in agarose

To evaluate bioinks swelling behaviour when printed in agarose fluid gel, GG and LAP-GG fibres were extruded from a 250 µm cylindrical blunt nozzle. Strands were deposited in a 2 mm thick agarose fluid gel. Measurements were carried out on GG (n=3) and LAP-GG (n=3) strands imaged with a stereo light microscope before (immediately after printing) and after crosslinking with 1 M $CaCl_2$ for 10 min. Further measurements were acquired 1, 3 and 24 h after printing similarly to previous study [113]. All measurements were analysed with ROI macro plugin and analyse measurements in Image J (1.44p, National Institutes of Health, Bethesda, Maryland, USA) was used as the analysing software.

To evaluate whole scaffolds swelling, a 5 mm hollow cylindrical structure was printed in agarose and in air. Measurements of the internal (pore) and outer diameter were carried out on images acquired with a stereo light microscope. Image J (1.44p, National Institutes of Health, Bethesda, Maryland, USA) was used as the analysis software.

6.2.7 Microscopy of cast gels and cell attachment

C2C12 cells were seeded at a density of 0.1×10^6 cell ml^{-1} onto 100 µl LAP-GG and GG gels plated in wells of a 96-well plate. Cells were cultured for 24 h to allow attachment with full media as reported later in 6.2.10. Scanning electron microscopy (SEM; FEI Quanta 250 FEG, operated in SEM mode) at a voltage of 5 kV (spot size 3) was used to image acellular and cellular gels. Prior to SEM, samples were dehydrated with a freeze-drier (Lablyo Mini, Froze in Time Ltd., UK) for 12 h and coated with platinum (Q150TES, sputter coater, UK).

6.2.8 Rheology

This methodology that tested i) viscosity of LAP-GG bioink (7.5 % w/v GG and 1 % w/v LAP) and its individual components and ii) storage and loss moduli over shear strain is reported in detail in Chapter 2 (2.3.5 page 48)

6.2.9 Acellular printing of gellan gum and gellan gum – Laponite

Printing of acellular GG and LAP-GG was carried out both in air and in agarose. A 5 ml agarose fluid gel bed was prepared for in agarose extrusion. GG and LAP-GG bioinks were tagged with orange and blue dye solutions respectively to be visualised during extrusion in agarose. A hollow cylindrical shape of 5 mm in diameter was used as blueprint. Printing was carried out at 2.5 mm s^{-1} depositing 10 layers with an average layer height set to 300 µm distance. A 1 M $CaCl_2$ solution was used to crosslink GG and LAP-GG for 10 min.

6.2.10 C2C12 cell culture

The immortalized mouse myoblast cell line C2C12 (mouse C3H, muscle) were obtained from the European Collection of Authenticated Cell Cultures, Public Health England, Porton Down, Salisbury, SP4 0JG, UK (cat number: ECACC 91031101). The cells were maintained in culture supplemented with full cell culture media (Dulbecco's Modified Eagle Medium (DMEM)), replenished every 3 days and cells passaged when reaching a maximum confluency of 80-90%. Seeding density was kept constant to 1×10^3 cells cm^{-2}. Cells were used for experiments at their twelfth passage.

6.2.11 C2C12 cell printing in agarose fluid gel

Cell-laden scaffolds were fabricated with GG and LAP-GG bioinks reported in 6.2.2 (page 161) and 6.2.3 (page 161). C2C12 cells were expanded for 14 days. A total of 5×10^6 cell ml^{-1} were pre-labelled with protocol reported in Chapter 2 (2.5.3 page 56) encapsulated in GG and LAP-GG and printed. Printing was carried out in agarose fluid gel prepared following protocol outlined in 6.2.4. The extrusion of hollow cylinders (5 mm in diameter and 10 layers high) were fabricated with a constant printing speed of 2.5 mm s^{-1} and pressure of 11.5 kN. Printed scaffolds were crosslinked for 10 min with 1 M $CaCl_2$, subsequently washed with HBSS and incubated in full cell culture media at 37°C and 5 % CO_2 balanced air up to 21 days. Scaffolds printed with the two bioinks were divided into two

further groups to obtain scaffolds for cell viability (n=9 cell-laden and n=9 acellular) and functionality (n=12 cell-laden and n=12 acellular) investigations.

6.2.12 Viability of cell-laden printed scaffolds

Viability at day 1, 7 and 21 was investigated by Calcein AM staining and confocal imaging of n=3 samples per time point. This methodology is detailed in Chapter 2 (2.5.4 page 57).

6.2.13 Functionality of cell-laden printed scaffolds

Functionality was evaluated by ALP staining, detailed in Chapter 2 (2.5.5 page 57). Culture was carried out at 37°C and 5 % CO_2 with basal or osteogenic media (detailed in 2.1.4 page 42). Mean intensity units of each image were calculated using Image J software, by analysing ROI with the “density” tool present in Fiji (1.44p, National Institutes of Health, Bethesda, Maryland, USA).

6.2.14 Drug analogues absorption and release

This methodology is detailed in Chapter 2 (2.6.2 page 58). Discs of LAP-GG and GG were fabricated as following. Both heated GG and LAP-GG solutions were pipetted at 300 µl into a sterile 2 ml Eppendorf. After 5 min to allow cooling of the solution, 500 µl of 1 M $CaCl_2$ solution were inserted in both GG and LAP-GG gels. Collection and dispersion of the solution by the lower portion of the gels in the Eppendorf were carried out. After 10 min for crosslinking of the nanosilicate gels, gels were removed, and a sterile scalpel was used to remove the conical end that was naturally cast because of the Eppendorf morphology, aiming to produce a cylinder of theoretical 400 µl. Discs of such volume were used in the absorption/release protocol.

6.2.15 Simulation of absorption of drugs in agarose gel by the printed scaffolds in the fluid gel support

To investigate the possibility to solubilise drugs in the agarose fluid gel and induce the absorption of the drugs in the bioink during and after printing, orange and blue colouring dyes were used to tag the agarose gel and print GG and LAP-GG respectively. Scaffolds produced following protocols detailed in section 6.3.8. Fibres extruded from a 250 µm nozzle were deposited in coloured agarose. A stereo and an inverted (Zeiss Axiovert 200) microscopes were used to image the printed structures and visually evaluate penetration by sectioning of the strands at the extremity and in a median portion with a sterile scalpel.

6.2.16 CAM assay

6.2.16.1 Sample fabrication

Scaffolds were printed using sterile LAP-GG and GG bioinks. Using absorbing methods described in 6.2.15 (page 167), VEGF (recombinant human VEGF 165, PeproTech USA) was solubilised at 100 µg ml^{-1} in a solution of 0.5 % w/v agarose fluid gel. Printing was performed by depositing a 20-layer high bulk cylinder of 10 mm in diameter. A total of n=8 scaffolds were fabricated with LAP-GG or GG for VEGF absorption. A remaining n=8 constructs were printed with LAP-GG or GG in VEGF-free agarose. Crosslinking of scaffolds (10 min exposure to 1 M $CaCl_2$ solution) was carried out after 15 min. Both printed GG and LAP-GG cylinders were maintained in agarose loaded with VEGF- for 30 min prior to collection and a single wash with HBSS. Scaffolds were implanted right after

6.2.16.2 Implantation, extraction and Chalkley score

This methodology is detailed in Chapter 2 (2.7.2 page 61 and 2.7.3 page 62)

6.2.17 Histological analysis

This methodology and specific staining are reported in Chapter 2 (2.10.1 page 65)

6.2.18 Statistical analysis

This methodology is detailed in Chapter 2 (2.11 page 66). Statistical evaluation of quantitative results is reported within the caption of the representative figures.

6.3 Results

6.3.1 Physical characterisation of gellan gum – Laponite nanocomposite

To test the ability of nanosilicate-modified hydrogels to withstand swelling forces, the physical properties of cast gels were investigated. Sol fraction content (Figure 6.3 a) and mass swelling ratio (Figure 6.3 b) of the LAP-GG formulations were calculated. PBS and HBSS were used as solutions to test the LAP-GG physical characteristics depending on the ionic content. A series of formulations were tested by maintaining GG content between 1 % and 2 % w/v, and serially changing the LAP content from 0.5 and 1 % w/v. In PBS, sol fraction (Figure 6.3 a) showed a high value for G1 (99.79 ± 0.16 %), L0.5 G1 (99.66 ± 0.17 %), L1G1 (99.44 ± 0.48 %), G2 (99.38 ± 0.48%), L0.5G2 (99.67 ± 0.04 %) and L1G2 (99.02 ± 0.18 %). Sol fractions of GG and LAP-GG immersed in HBSS showed no significant changes. Addition of Laponite to 1 % w/v of gellan gum showed a linear decrease in sol fraction from 92.62 ± 7.28 % (G1), to 87.56 ± 3.02 % (L0.5G1) and 87.43 ± 1.66 % (L1G1). However, a non-linear trend was observed when 2 % w/v of gellan gum was investigated. G2 sol fraction was 85.23 ± 7.50 % and the addition of 0.5 % w/v and 1 % w/v LAP raised the sol content to 93.81 ± 2.27 % and 82.71 ± 4.04 % respectively. Finally, there was a significant increase in sol fraction when L0.5G1 ($p<0.01$), L1G1 ($p<0.01$), G2 ($p<0.001$) and L1G2 ($p<0.0001$) were immersed in PBS compared to HBSS.

The mass swelling ratio (Figure 6.3 b) in PBS was found to increase with the addition of Laponite to gellan gum from 35.86 ± 10.32 % (G1), to 37.92 ± 5.05 % (L0.5G1) and up to 42.82 ± 3.58 % (L1G1). Particularly, L1G1 resulted significantly greater ($p<0.05$) than L0.5G2 and L1G2. However, the inclusion of nanosilicate, in gellan gum, induced a decrease of the swelling ratio from 28.88 ± 7.61 % (G2), to 20.73 ± 6.52 % (L0.5G2) and 21.53 ± 0.57 % (L1G2), resulting in lower ratio compared to L1G1. Assessment of swelling ratio in HBSS showed a significantly reduced magnitude in swelling compared to PBS conditioning, for all formulations ($p<0.0001$). Laponite inclusion induced a decrease in swelling ratio from $1.65 \times 10^{-2} \pm 0.36 \times 10^{-2}$ % (G1), to $0.58 \times 10^{-2} \pm 0.15 \times 10^{-2}$ % (L0.5G1) up to $0.74 \times 10^{-2} \pm 0.08 \times 10^{-2}$ % (L1G1). When 2 % w/v of gellan gum was used, the mass swelling ratio ($1.20 \times 10^{-2} \pm 0.55 \times 10^{-2}$ %) increased with the addition of 0.5 % w/v LAP ($2.26 \times 10^{-2} \pm 0.50 \times 10^{-2}$ %) and 1 % w/v LAP ($2.46 \times 10^{-2} \pm 0.99 \times 10^{-2}$ %). L0.5G2 and L1G2 presented a significantly ($p<0.05$) higher mass swelling ratio than L0.5G1 and L1G1.

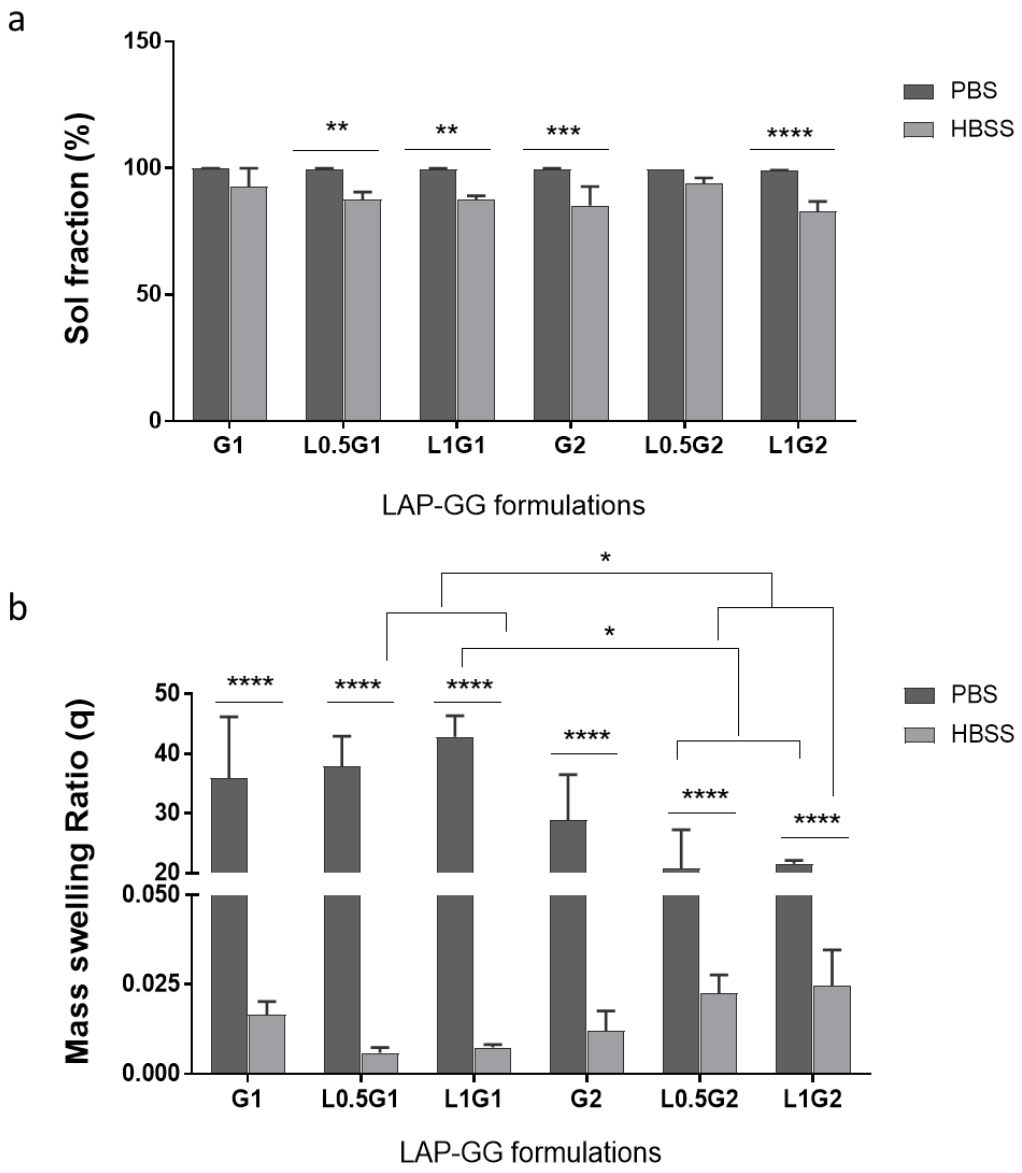

Figure 6.3. Physical characterisation of wet and dry nanosilicate composite gels in PBS and HBSS.

Sol fraction (a) of series of LAP-GG formulations and controls evaluated in PBS or in HBSS. Mass swelling ratio (b) of LAP-GG gels compositions and controls in PBS and HBSS. Statistical significance assessed by two-way ANOVA followed by Sidak's multiple comparison tests. Mean ± S.D. n=6 *p<0.05, **p<0.01, ***p<0.001, ****p<0.0001. For simplicity, Laponite was labelled as L and gellan gum as G, with the subsequent number indicating the % w/v.

To validate the sol fraction and mass swelling studies and to investigate the bioink print fidelity, GG and LAP-GG were printed in air (Figure 6.4 a,b) or in agarose gel (Figure 6.4 c,d) and strands measured for swelling over 24h.

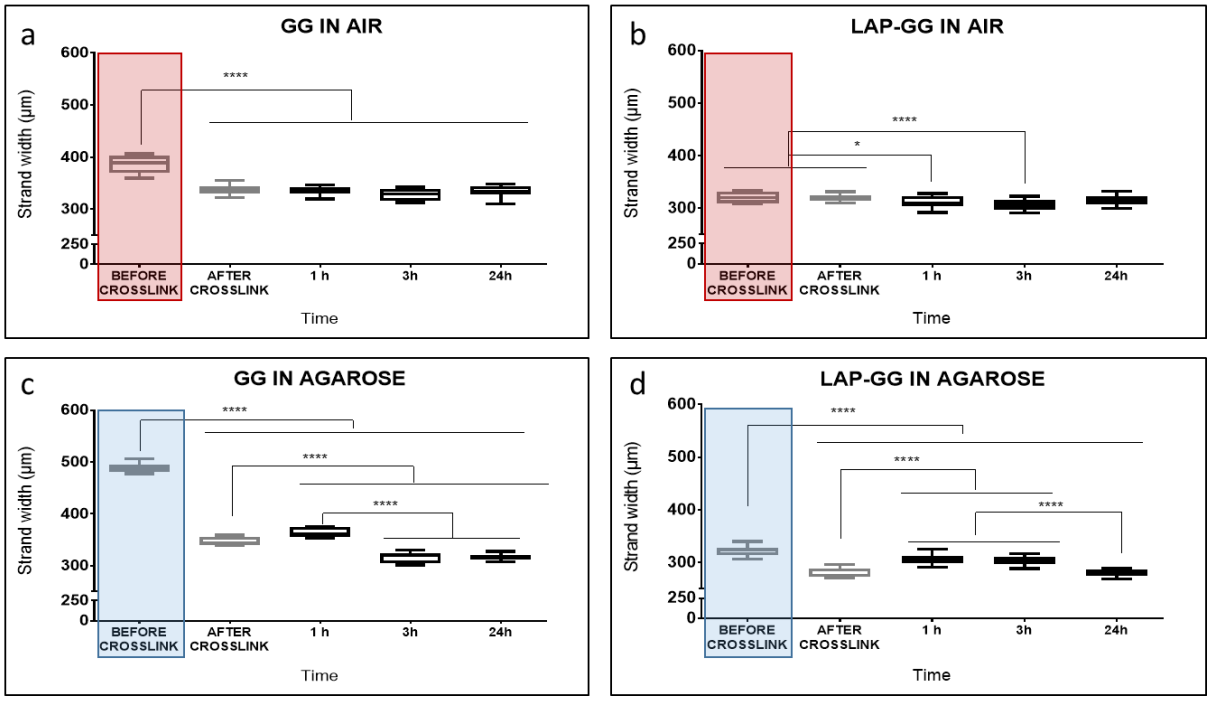

Figure 6.4. Printed fibre diameter swelling measurements over 24 h after printing.

Measurements were collected for GG (a) and LAP-GG (b) printed in air. Fibre size for printed GG (c) and LAP-GG (d) printed in agarose. Statistical significance assessed by two-way ANOVA followed by Tukey's multiple comparison tests. Mean ± S.D. n=3, *p<0.05, ****p<0.0001.

A bioink formulation of 2 % w/v content in GG and 1% LAP was selected for all further characterisation studies reported in this chapter. GG and LAP-GG fibres (Appendix C Figure 6.1 a) were printed in an agarose bed (Appendix C Figure 6.1 b) with a cylindrical nozzle of 250 µm (Appendix C Figure 6.1 c) to generate a 250 µm deposited strand. GG printing in air (Figure 6.4 a) resulted in a swollen fibre before printing (387.20 ± 17.69 µm), significantly larger ($p<0.0001$) than immediately after crosslinking (337.91 ± 9.61 µm), 1h (335.60 ± 8.20 µm), 3h (328.70 ± 11.37 µm) and 24h (333.63 ± 11.76 µm).

LAP-GG when printed in air (Figure 6.4 b), showed a lower degree of swelling compared to GG (320.52 ± 10.42 µm) and a comparable dimension of strand size immediately after crosslinking (319.41 ± 7.32 µm). A significant decrease in strand diameter was registered after 1h (311.80 ± 11.78 µm) ($p<0.05$), 3h (306.70 ± 10.73 µm) and 24h (315.02 ± 9.87 µm) ($p<0.0001$).

A significant degree of swelling and a decrease in strand diameter was observed when GG was printed in an agarose gel bed (Figure 6.4 c). After extrusion a deposited strand of 488.72 ± 9.28 µm was measured significantly greater ($p<0.0001$) in lateral dimensions. After $CaCl_2$ crosslinking (347.75 ± 8.01 µm), the strand was found to significantly decrease ($p<0.0001$) in diameter. However, after only 1h the diameter had significantly swollen

(364.12 ± 9.21 µm) compared to strands before and after crosslinking (p<0.0001), after 3h (316.10 ± 10.49 µm) and 24h (316.60 ± 6.19 µm) (p<0.0001).

LAP-GG (Figure 6.4 d) generated a significantly lower degree of swelling immediately before crosslinking (322.65 ± 9.99 µm) (p<0.0001) compared to GG bioink. LAP-GG displayed a significantly decreased fibre diameter (282.60 ± 8.95 µm) (p<0.0001) after crosslinking. A significant swelling after 1h (305.90 ± 10.21 µm) (p<0.0001) was found, consistent with GG swelling kinetics. After 3h, the strand diameter was unchanged (303.52 ± 8.81 µm) and subsequently decreased after 24 h (280.41 ± 7.08 µm). Interestingly, the LAP-GG printed fibres before crosslinking were found to be significantly smaller (p<0.0001) in diameter compared to GG, both in air (Appendix C Figure 6.2 a) and agarose (Appendix C Figure 6.2 b).

LAP-GG bioink rheological properties were investigated before extrusion and viscosity measurements (Figure 6.5 a) determined to investigate bioink printability. Single components and final LAP-GG blends were tested for viscosity. Laponite showed a low viscosity profile (0.92 Pa s) compared to GG (182.35 Pa s). LAP-GG components were observed to decrease linearly with an increase in shear rate (from 0.1 to 100 s^{-1}). LAP-GG nanocomposites exhibited a higher viscosity (257.82 Pa s) than GG alone, despite only containing 1 % w/v of Laponite solid content.

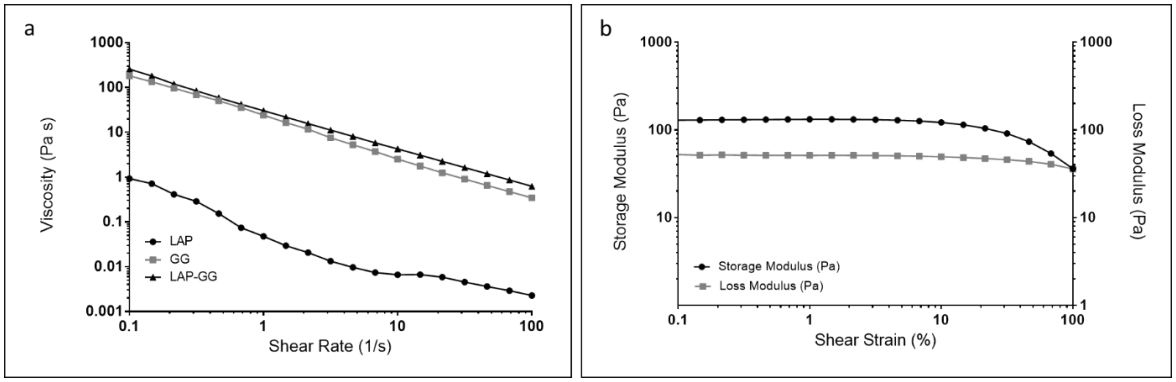

Figure 6.5. Rheological characterisation of pre-crosslinked LAP-GG bioink.

Viscosity (a) drop by the change of shear rate was registered for LAP, GG, LAP-GG. Storage and loss moduli (b) of LAP-GG bioink measured depending on the percentage change in shear strain.

The decreasing trend of LAP-GG viscosity, with increasing shear rate, was different compared to GG. Storage and loss moduli (Figure 6.5 b) of the LAP-GG bioink were measured according to the percentage change of the shear strain. The storage modulus was stable (131.02 Pa) up to 3.16 % in strain, but subsequently decreased up to 36.13 Pa

when 100 % shear was reached. The loss modulus was found to linearly decrease from 52.57 Pa to 35.90 Pa.

SEM images of cast GG and LAP-GG gels (Figure 6.6) were acquired and analysed. GG discs (Figure 6.6 a) displayed a less porous internal architecture compared to LAP-GG (Figure 6.6 b), further confirmed by examination at higher magnification (Figure 6.6 c and d respectively). Cell attachment showed a similar morphology for GG (Figure 6.6 e) and LAP-GG (Figure 6.6 f).

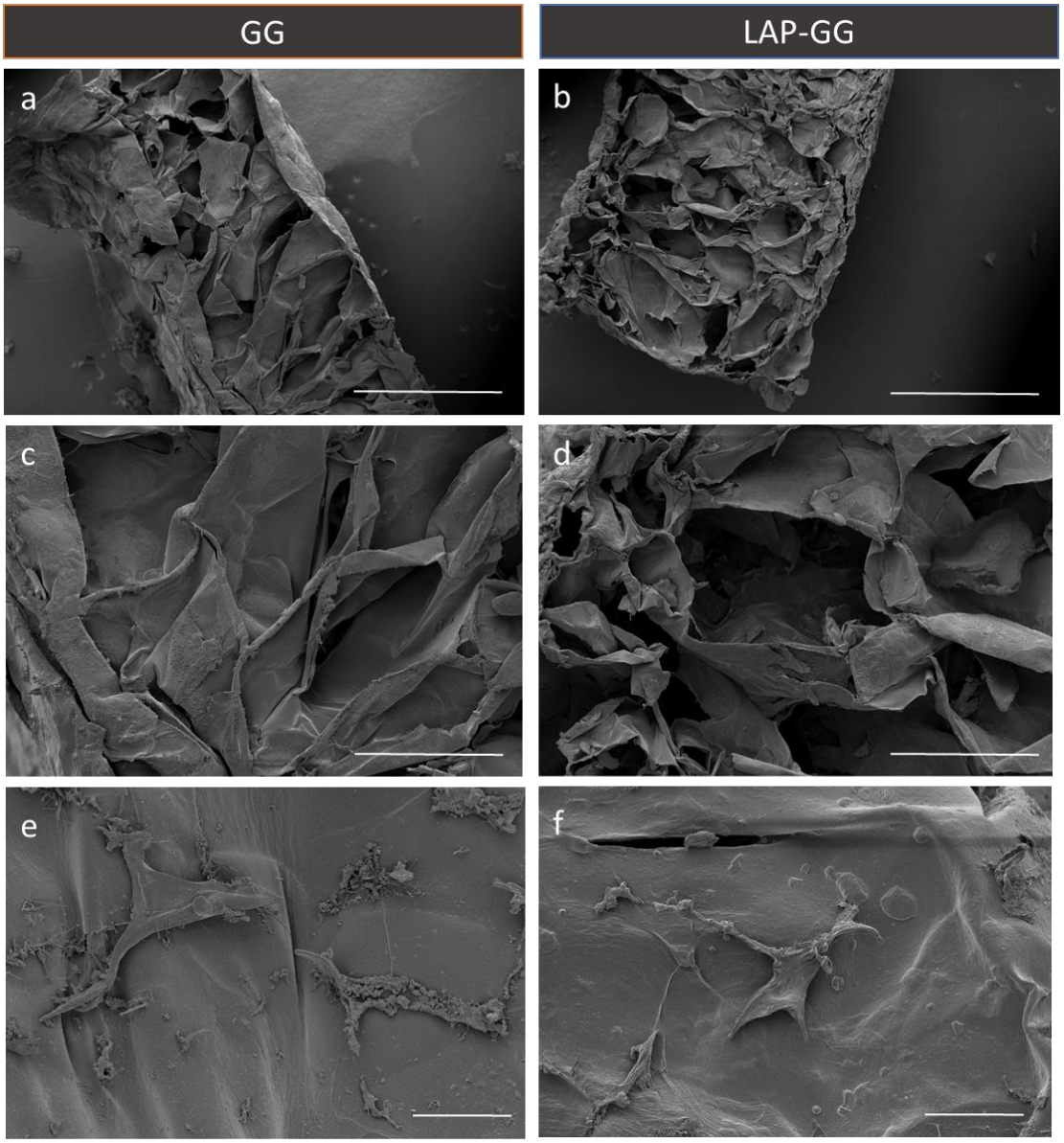

Figure 6.6. SEM micrographs of bulk gels.

Micrographs of GG (a,c) and LAP-GG (b,d) showing internal open porosity. C2CC12 seeded on GG (e) and LAP-GG (f) under SEM. Scale bar: (a,b) 1mm, (c,d) 300 µm, (e,f) 100 µm.

6.3.2 Printing acellular scaffolds in a fluid gel

To investigate the effect of LAP addition to GG on printing accuracy, GG and LAP-GG were deposited in agarose and in air (Figure 6.7). Extrusion of GG in agarose medium (Figure 6.7 a) resulted in an initial formation of a cylindrical shape, which swelled immediately after, until the central pore was occluded (Figure 6.7 b). When GG was extruded in air (Figure 6.7 c), the printed construct collapsed immediately after a few initial layers, resulting in a failed scaffold (Figure 6.7 d). LAP-GG was observed to be highly printable in agarose (Figure 6.7 e) and layer-by-layer deposition resulted in a high-resolution construct (Figure 6.7 f) that closely represented the blueprint file. However, when LAP-GG was extruded in air, the structure was found to be unstable (Figure 6.7 g), partially collapsing under its own weight (Figure 6.7 h).

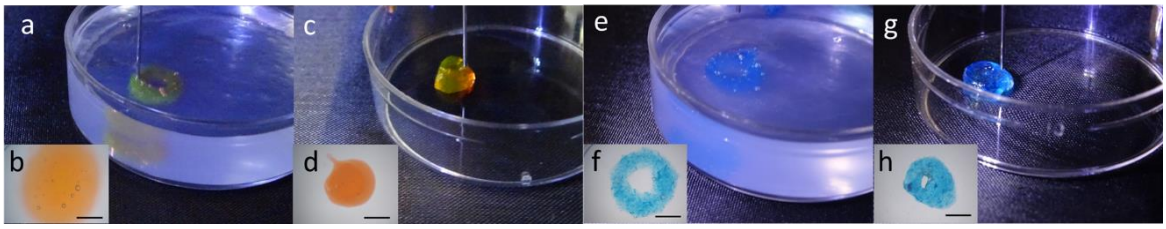

Figure 6.7. Extrusion of acellular LAP-GG and GG structures in agarose or in air.

GG can be extruded in agarose gel (a,b) or air (c,d) into circular shape. LAP-GG deposited in agarose (e,f) and in air (g,h). Scale bar: (b,d,f,h) 2 mm.

Measurements were conducted on cylindrical-shaped 3D constructs (Figure 6.8 a) to investigate print fidelity. GG (orange, left) and LAP-GG (blue, right) were extruded in agarose and in air, and the central pore (Figure 6.8 b) and overall scaffold diameters (Figure 6.8 c) examined.

GG could not be extruded without immediate swelling resulting in a collapsed central pore. Extrusion of LAP-GG bioink resulted in the fabrication of cylindrical scaffolds with 1.85 ± 0.12 mm and 1.15 ± 0.19 mm as main channel dimension in agarose and in air, respectively. Cylindrical-shaped scaffolds showed significantly greater inner pore than constructs fabricated with GG hydrogel ($p<0.0001$). GG and LAP-GG constructs were found to show similar outer diameter when extruded in agarose (Figure 6.8 c, 6.57 ± 0.24 mm and 6.36 ± 0.23 mm, respectively). However, when printed in air, GG displayed a significantly ($p<0.0001$) larger overall diameter (7.85 ± 0.28 mm) compared to constructs printed with LAP-GG bioink (6.24 ± 0.42 mm).

Larger cylindrical constructs could be printed in the agarose gel using the LAP-GG bioink (Appendix C Figure 6.3 a). As proof-of-concept, a 30 mm high three-dimensional sleeve structure was printed (Appendix C Figure 6.3 b,c), showing fidelity to the blueprint and elevated printability in the agarose gel.

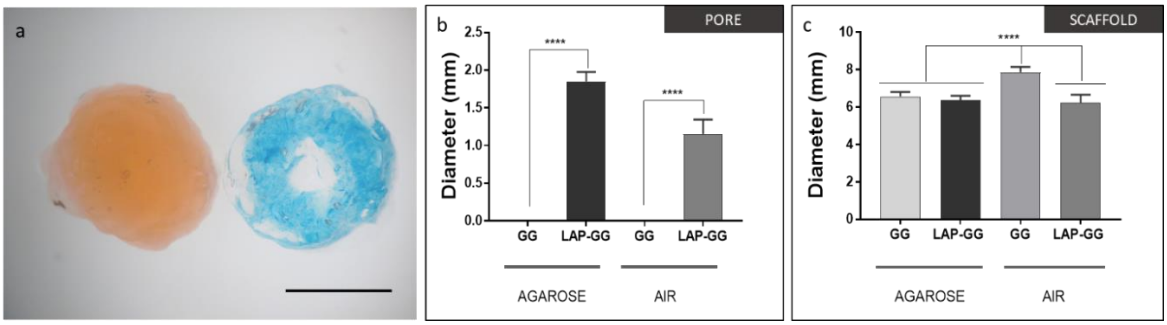

Figure 6.8. Shape fidelity evaluation.

Macrographs showing dyed and printed GG (orange) and LAP-GG (blue) structures. Measurements of inner pore (b) and overall scaffold diameter (c) on samples printed in agarose fluid gel or in air. Statistical significance assessed by one-way ANOVA followed by Tukey's multiple comparison tests. Scale bar: (a) 5 mm. Mean ± S.D. n=6, ****p<0.0001.

6.3.3 Cell viability, proliferation and functionality of printed C2C12 cells *in vitro*

Viability of C2C12 myoblast-laden printed scaffolds was evaluated after 1, 7 and 21 days from fabricated constructs. Confocal images (Figure 6.9 a,b), show representative images of cells encapsulated in GG (Figure 6.9 ai-iii) and LAP-GG (Figure 6.9 b-i-iii) printed fibres after 1, 7 and 21 days of culture *in vitro*.

Quantitative analysis (Figure 6.9 c) revealed a non-significant decrease in cell viability when C2C12 were encapsulated and printed in GG. C2C12 cells remained viable 24 h after printing (84.93 ± 10.33 %). After 7 days, cell viability was registered at 81.13 ± 6.55 %, decreasing to 78.96 ± 12.92 % after 21 days. The LAP-GG nanocomposite bioink preserved cell viability after 1 (80.00 ± 15.75 %) up to 7 (79.05 ± 11.67 %) days of culture *in vitro*. C2C12 cells remained viable over 21 days (84.05 ± 6.14 %).

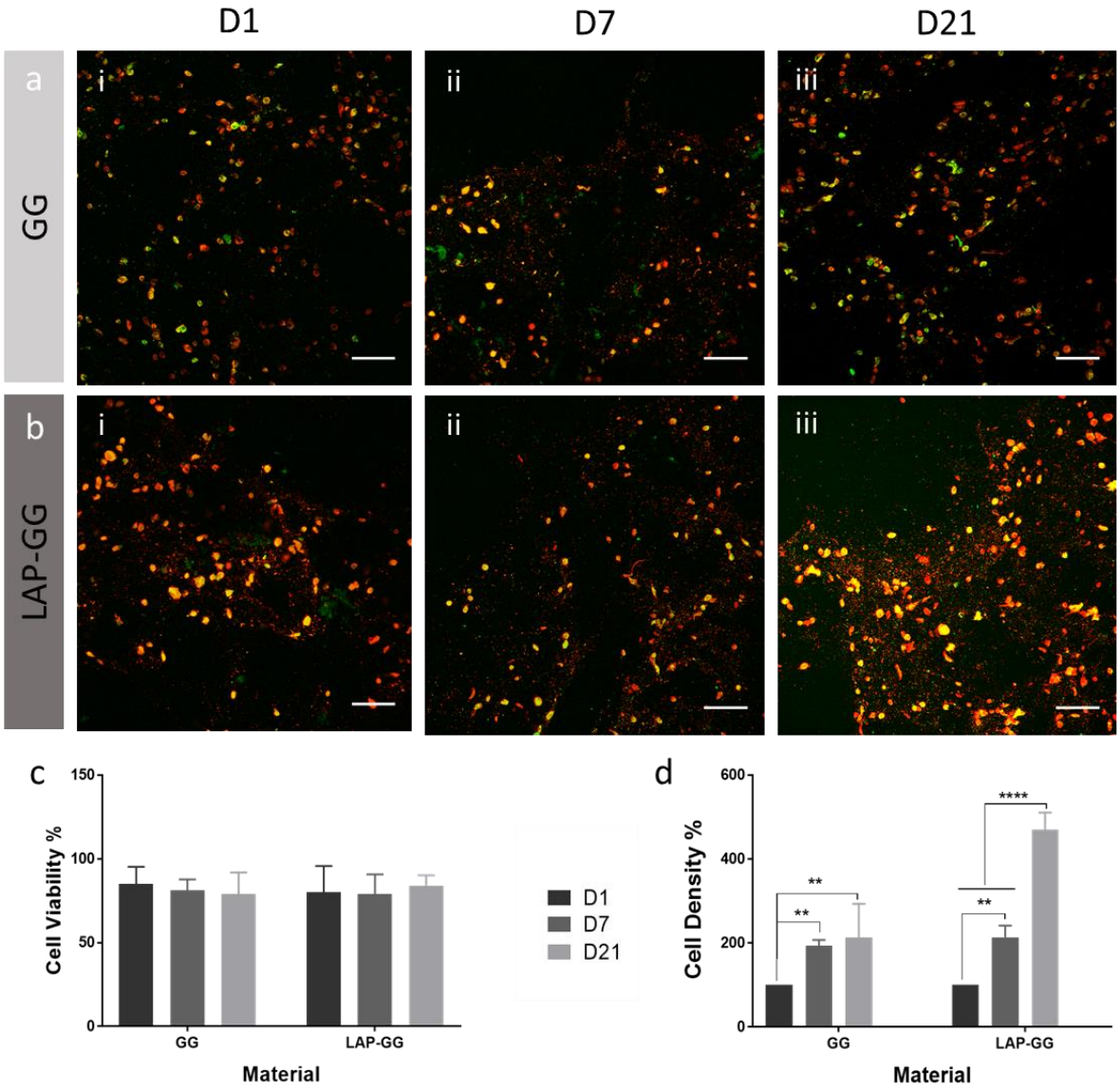

Figure 6.9. Cell viability evaluation of printed C2C12 cells.

Confocal microscopy images of C2C12-laden GG (a) and LAP-GG (b) scaffolds at (i) 1, (ii) 7 and (iii) 21 days. All cells were stained with DiD solution (red) with mitotically active cells stained with Calcein AM (green). Cell (c) viability and (d) density were quantified from confocal images. Cell viability percentages were obtained from the calculated difference between living and total numbers of cells. Dead cells were assumed to comprise cells not stained with Calcein AM. Scale bar: (a-d) 100 µm. Statistical significance assessed by two-way ANOVA followed by Tukey's multiple comparison tests. Mean ± S.D. n=3, **p<0.01, **** p<0.0001.

Cell density (Figure 6.9 d) of the printed constructs was evaluated to study the proliferative potentials of printed C2C12 either in GG or in LAP-GG bioinks. Data analysis was carried out with cell density after 1 day of culture set as the baseline (100 %). Cell-laden GG showed a linear and significant increase in cell density, reaching 194 ± 13 % density ($p<0.01$) after 7 days of culture and 213 ± 79 % ($p<0.01$) after 21 days. LAP-GG bioink were found to

sustain a significant increase ($p<0.01$) in cell number after 7 days of culture (213 ± 28 %) and proliferating significantly ($p<0.0001$) up to 471 ± 40 % after 21 days.

C2C12 cell-laden printed scaffolds were evaluated for their functional potential. Scaffolds fabricated with GG and LAP-GG bioink were cultured for 1, 7 and 21 days in basal (Figure 6.10) and osteogenic (Figure 6.11) media. Results showed that basal conditioning of GG encapsulated C2C12 cells showed limited ALP staining after 1 (Figure 6.10 a) and 7 (Figure 6.10 b) days, with expression of ALP after 21 days (Figure 6.10 c) *in vitro*. LAP-GG cultured in basal media showed ALP expression after 1 day of culture (Figure 6.10 d) and increasing intensity after 7 (Figure 6.10 e) and 21 days (Figure 6.10 f).

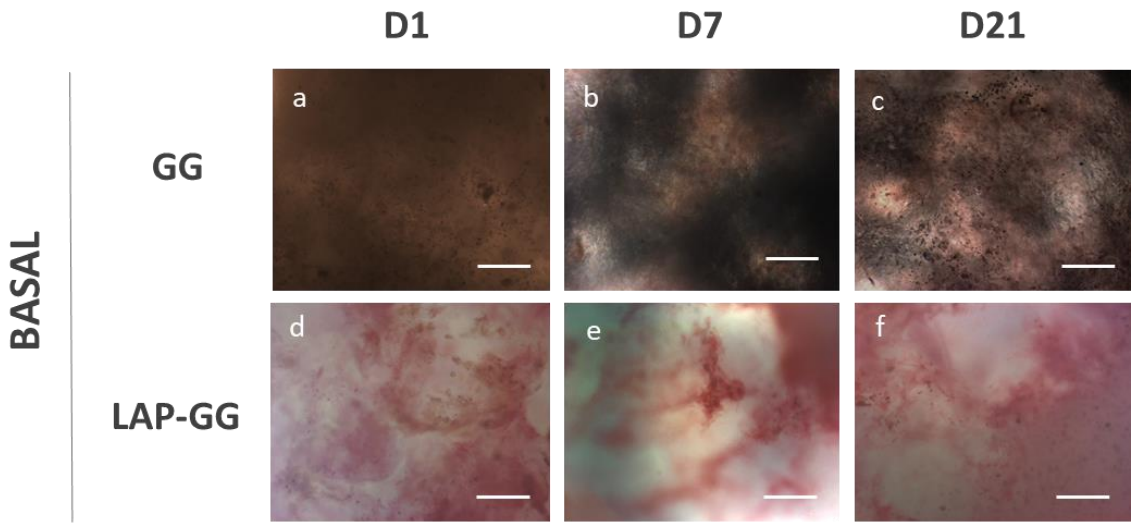

Figure 6.10. Functional evaluation of basal conditioned printed scaffolds.

GG printed scaffolds imaged after 1 (a), 7 (b) and 21 (c) days of culture in basal media. LAP-GG printed scaffolds cultured in basal media imaged at 1 (d), 7 (e) and 21 (f) days of culture. Scale bar: (a-f) 100 µm

Osteogenic conditioned GG scaffolds were found to be positively stained for ALP after 1 day (Figure 6.11 a) with reduced intensity after 7 days (Figure 6.11 b) of culture *in vitro*. C2C12 cell-laden GG scaffolds were extensively stained with a light red colour indicating diffuse ALP expression. Noticeably darker cell agglomerates were found throughout the entire scaffold construct, suggesting mineralised nodules (Figure 6.11 c). LAP-GG scaffolds stained intensely for ALP after 1 (Figure 6.11 d), 7 (Figure 6.11 e) and 21 (Figure 6.11 f) days of culture. An increase in colour intensity and localisation of the staining in a fibrous-like pattern was observed from day 1 to day 21 of culture. Dark and localised nodules could be observed in LAP-GG constructs maintained in culture for 21 days.

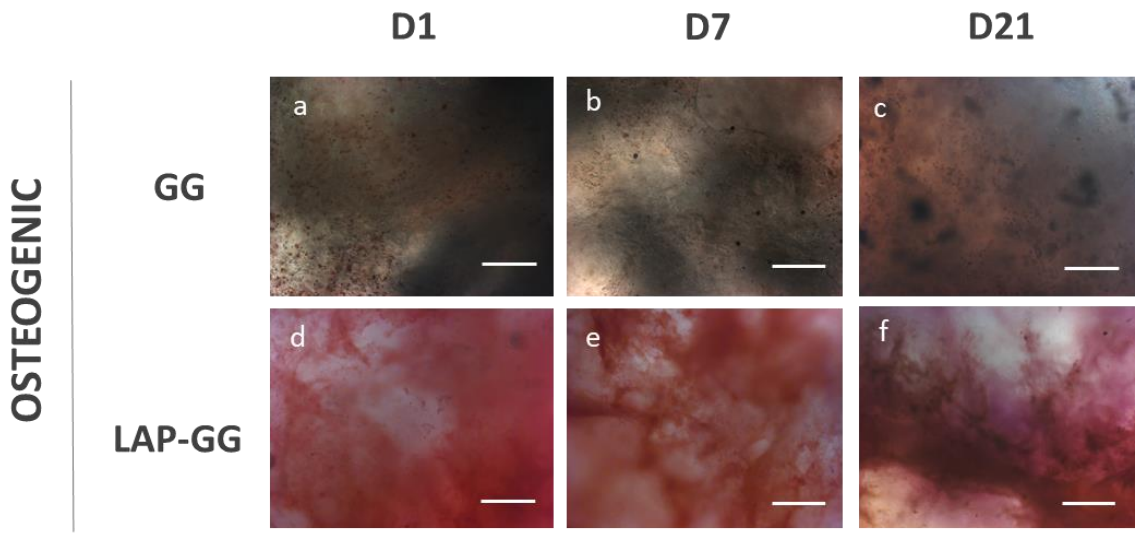

Figure 6.11. Functional evaluation of osteogenic conditioned printed scaffolds.

GG printed scaffolds imaged after 1 (a), 7 (b) and 21 (c) days of culture in osteogenic media. LAP-GG printed scaffolds cultured in osteogenic media imaged at 1 (d), 7 (e) and 21 (f) days of culture. Scale bar: (a-f) 100 µm

Quantitative analysis of ALP staining images confirmed that cell-laden LAP-GG scaffolds cultured in basal condition (Appendix C Figure 6.4 a) showed significantly enhanced ALP activity after 1 ($p<0.01$), 7 ($p<0.0001$) and 21 ($p<0.0001$) days compared to cell-free control scaffolds. Cells encapsulated in LAP-GG showed significantly enhanced activity compared to silicate-free GG after 7 and 21 ($p<0.0001$) days of culture. A significant ($p<0.01$) difference in ALP expression was found in GG cellular samples compared to acellular after 21 days of culture in basal conditions. Osteogenic conditioning (Appendix C Figure 6.4 b) of cell-laden LAP-GG was found to elicit significant ALP expression compared to the cell-free control after 1 ($p<0.05$), 7 and 21 ($p<0.0001$) days in culture post printing. Significant differences were found between cell-laden LAP-GG and GG following culture in osteogenic media, with LAP-GG showing significantly greater intensity of ALP staining after 7 and 21 ($p<0.0001$) days. Similarly to basal conditioned samples, osteogenic-stimulated cell-laden GG were found to express significantly ($p<0.001$) higher level of ALP after 21 days of culture.

6.3.4 Drug absorption/release from nanosilicated gellan gum bioink

The potential for localisation and retention of drugs was tested on GG and LAP-GG constructs *in vitro*. BMP-2 and VEGF analogues (lysozyme and BSA, respectively) were used to model the loading and release profiles of functional osteoinductive and angiogenic compounds respectively.

Figure 6.12 a illustrates the physical changes of gels in a 1× PBS solution. During absorption, cast gels were immersed in PBS-based drug solution. GG showed transparency for up to 24 h of culture, while the LAP-GG scaffold was observed to be opaque. Following collagenase treatment to induce drug release, scaffolds were degraded. GG gels were degraded on the outer surface after only 4 h *in vitro* with further degradation after 24 h. GG cast gels were observed to be opaque after 28 h of incubation. LAP-GG opacity was observed to increase and degraded on the outer surface after 48 h of incubation in collagenase solution.

Lysozyme solution (10 μg ml^{-1}) was incubated with the gels to facilitate absorption over 24 h. The solution concentration was subsequently measured as a surrogate marker of gel absorption. GG cast gels showed a slow absorbance profile (Figure 6.12 b) resulting in 8.429 ± 0.20 μg ml^{-1} and 8.17 ± 0.51 μg ml^{-1} in solution after 1 h and 2 h, respectively. After 4 h, the GG gel showed the first peak of absorption (5.52 ± 0.84 μg ml^{-1}). Lysozyme was released back into solution after a further 4 h (6.61 ± 0.81 μg ml^{-1}). Finally, after 24 h of incubation, GG showed continued absorption (2.01 ± 1.17 μg ml^{-1}). LAP-GG displayed similar kinetics. In contrast, lysozyme absorption was noted to be significantly faster after only 1 h (1.42 ± 0.20 μg ml^{-1}), followed by fractional release at 2 h (2.21 ± 0.26 μg ml^{-1}), 4 h (3.69 ± 0.84 μg ml^{-1}) and 8 h (3.85 ± 1.94 μg ml^{-1}). Absorption was then resumed up to 24 h (0.50 ± 0.38 μg ml^{-1}). Collagenase solution replaced lysozyme solution after 24 h. GG (Figure 6.12 c) was found to release the majority of the absorbed lysozyme after 1 h (7.11 ± 0.87 μg ml^{-1}) with a reduction in lysozyme release rate after 2 h (8.36 ± 1.77 μg ml^{-1}) and 4 h (8.36 ± 1.38 μg ml^{-1}). At 8 h, the lysozyme started to be resorbed (8.24 ± 1.66 μg ml^{-1}), which continued for up to 24 h (6.71 ± 1.28 μg ml^{-1}). In contrast, LAP-GG showed a continued release profile, with the highest rate at 1 h (2.25 ± 0.48 μg ml^{-1}), followed by reduction at 2 h (3.48 ± 1.29 μg ml^{-1}), 4 h (4.25 ± 1.77 μg ml^{-1}), 8 h (5.14 ± 0.87 μg ml^{-1}) and 24 h (8.44 ± 1.38 μg ml^{-1}).

BSA was absorbed onto GG and LAP-GG at an initial solution of 100 μg ml^{-1} (Figure 6.12 d). GG displayed rapid absorbance kinetic with peak of absorbance at 1 h (65.53 ± 1.50 μg ml^{-1}), plateau at 2 h (64.57 ± 2.89 μg ml^{-1}), before resumption at 4 h (47.49 ± 1.92 μg ml^{-1}), with little more absorption at 8 h (43.25 ± 3.80 μg ml^{-1}) and 24 h (40.30 ± 1.55 μg ml^{-1}). LAP-

GG displayed similar absorption kinetics to GG, with rapid adsorption of BSA after 1 h (68.39 ± 1.50 µg ml^{-1}) that stopped at 2h (68.07 ± 2.89 µg ml^{-1}), before resumption at 4 h (47.91 ± 1.92 µg ml^{-1}), LAP-GG was then found to absorb only modest amount of BSA at 8 h (48.90 ±3.80 µg ml^{-1}) and 24 h (43.33 ± 1.55 µg ml^{-1}). Release of BSA after the addition of collagenase solution (Figure 6.12 e) showed the greatest localisation capacity of LAP-GG compared to GG.

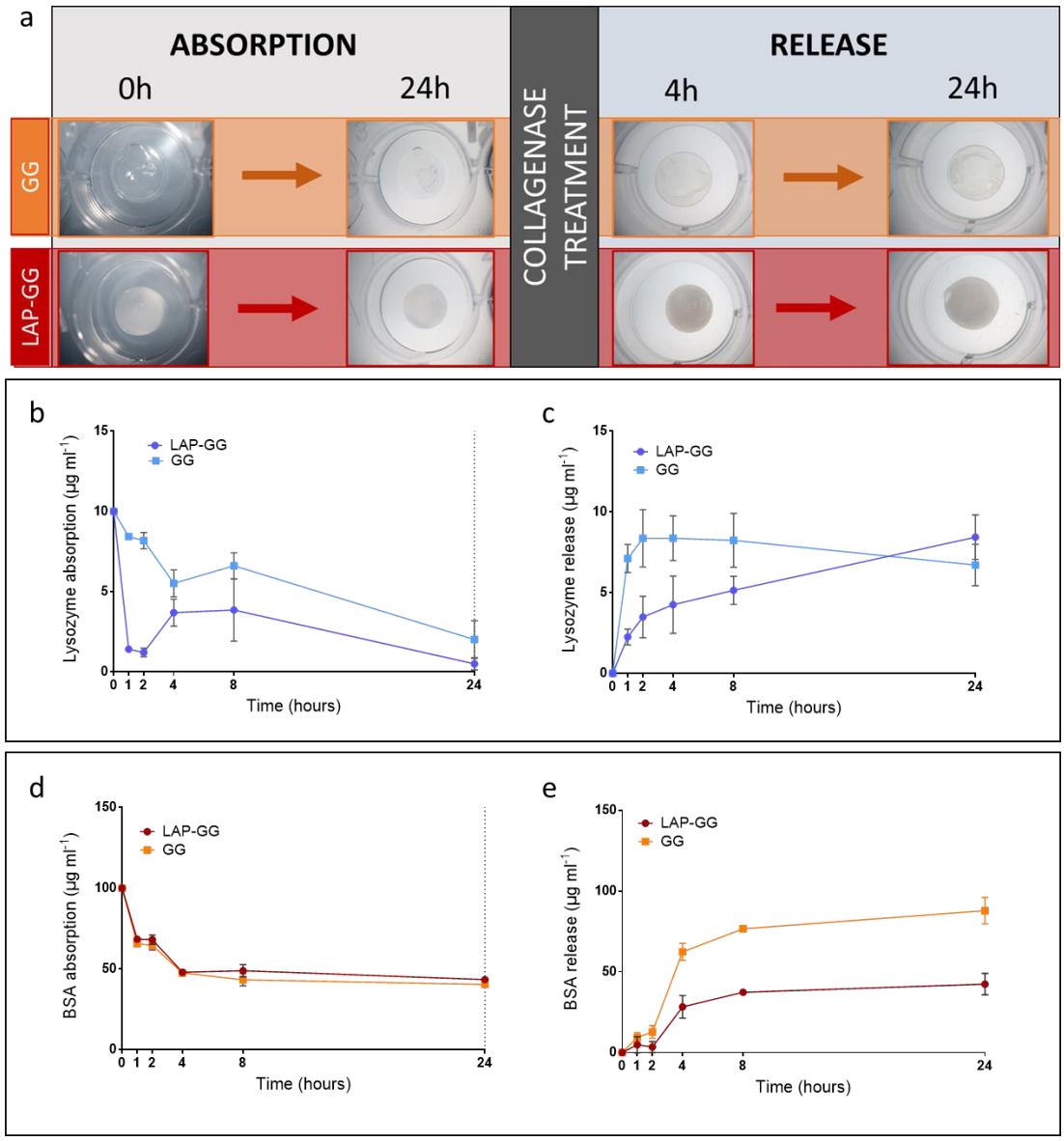

Figure 6.12. Drug absorption/release kinetics of gellan gum-silicate hydrogels.

Schematic of absorption/release study (a) and appearance of GG and LAP-GG gels. Absorption was performed for 24 hours. Collagenase solution was then used to replace drug-containing solution to induce hydrogel digestion over 24 hours. Lysozyme absorption (b) and release (c) were performed for 24 hours, respectively. BSA absorption (d) and release (e) were performed for 24 hours, respectively.

Laponite-free GG digestion with collagenase solution produced a linear release from 1 h (9.38 ± 2.99 µg ml^{-1}), 2 h (12.74 ± 4.00 µg ml^{-1}), 4 h (62.36 ± 5.32 µg ml^{-1}), 8 h (76.64 ± 2.08 µg ml^{-1}), up to 24 h (87.89 ± 8.18 µg ml^{-1}). In contrast, LAP-GG was found to release a negligible amount of BSA after 1 h (4.83 ± 5.03 µg ml^{-1}) and 2 h (3.44 ± 3.48 µg ml^{-1}). After 4 h, LAP-GG was found to start releasing the BSA absorbed (28.33 ± 6.99 µg ml^{-1}), showing a sustained release at 8 h (37.37 ± 2.08 µg ml^{-1}) up to 24 h (42.39 ± 6.68 µg ml^{-1}).

6.3.5 CAM assay of VEGF-absorbed Laponite - gellan gum printed constructs

To test the potential to load drugs solubilised in the agarose gel bed while printing GG or GG-LAP, a bright dye (red and blue, respectively) was used to colour the agarose gel and absorption of the dye was investigated after printing and crosslinking of the scaffold.

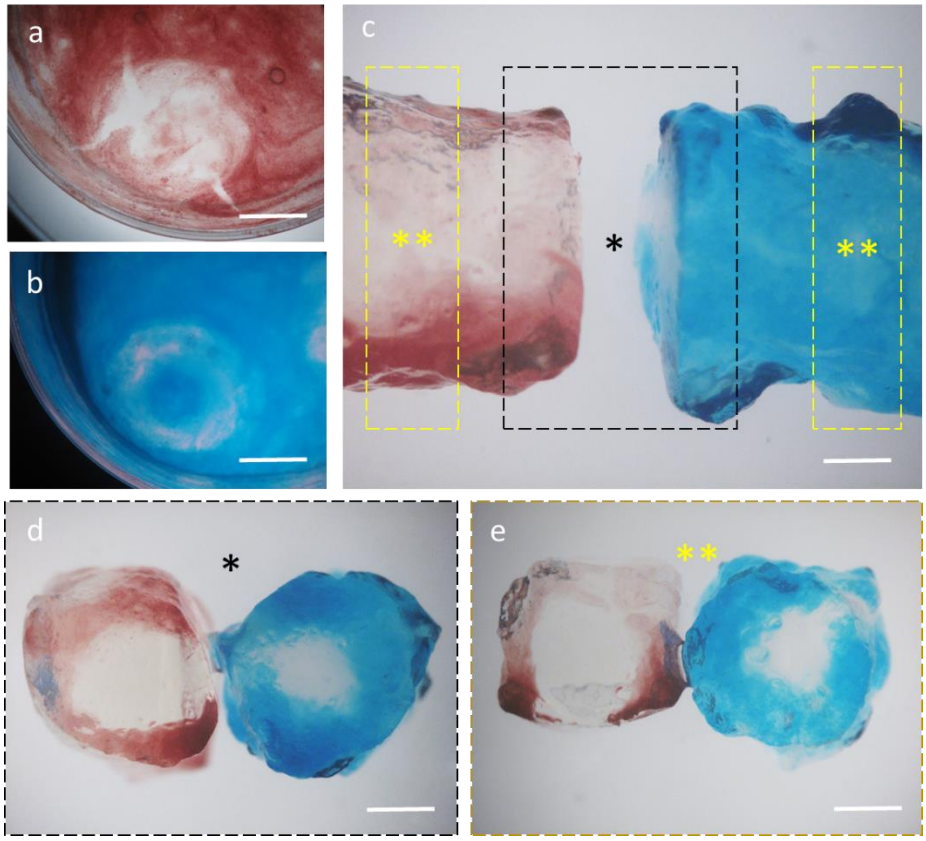

Figure 6.13. Absorption of drugs while printing.

GG (a) and LAP-GG (b) bioinks were printed in agarose tagged with red and blue dye respectively. Single fibres could be printed and retrieved and visually investigated for dye absorption (c). GG and LAP-GG macroscopic images showing comparison of GG and LAP-GG starting end of the fibre (d) and inner slices (e). Scale bar: (a,b) 3 mm, (c) 100 µm (d,e) 200 µm

GG (Figure 6.13 a) was printed in a red dyed agarose gel into a cylindrical shape. LAP-GG (Figure 6.13 b) was extruded in a cylindrical scaffold into an agarose gel bed coloured in blue. The core pore was found to remain intact after crosslinking. Single strands (410 µm in diameter) of GG and LAP-GG were extruded into red and blue agarose respectively (Figure 6.13 c). The top extrusion points (*) and areas at the centre of the strands (**) were imaged to evaluate dye penetration. For the top portion of the strand (Figure 6.13 d) of GG bioink (red), the dye was loaded on the outer rim of the strand, leaving a blank core. LAP-GG (blue) strands were extensively loaded for a larger portion than GG, with the strand inner portion only partially loaded with the dye. Central portions of the strands were imaged to confirm dye absorption (Figure 6.13 e). GG (red) fibre was present on the outer surface of the strand leaving the core of the strand dye-free. LAP-GG (blue) formed fibres with the blue dye on the outer portion of the strand leaving a reduced dye-free core compared to GG control.

Loading VEGF solubilised in agarose onto printed scaffolds was performed during extrusion of bulk cylindrical GG and LAP-GG bioink in the fluid gel. 3D constructs loaded with VEGF or HBSS (control) were implanted in a CAM model to evaluate vasculogenesis and integration of the scaffolds with the CAM. GG (Figure 6.14 a), LAP-GG (Figure 6.14 b), GG-VEGF (Figure 6.14 c) and LAP-GG-VEGF (Figure 6.14 d) scaffolds were implanted on the chorioallantoic membrane of the developing chick (as in Chapter 4).

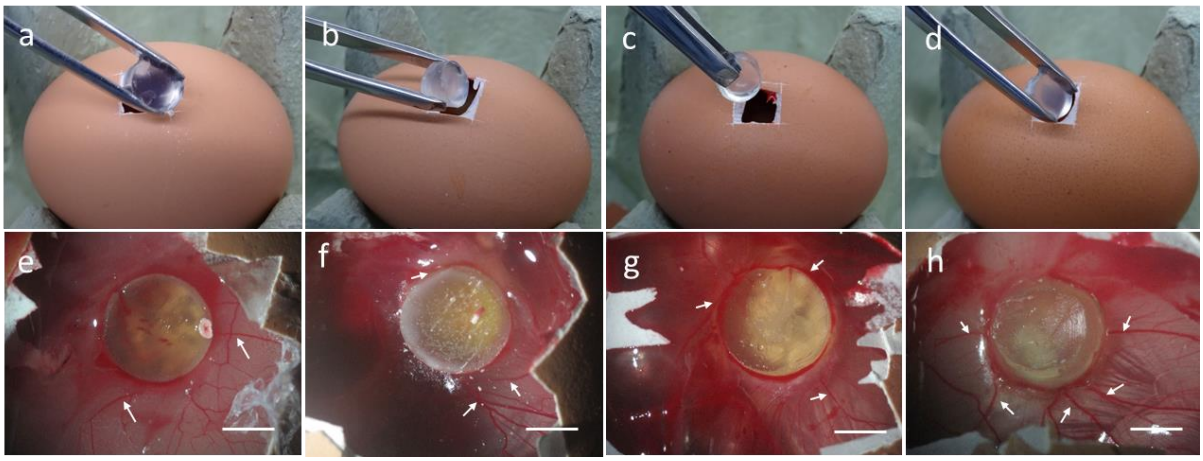

Figure 6.14. CAM assay to evaluate VEGF-absorbed cast hydrogel potential for vasculogenesis and scaffold-CAM integration.

Implantation of GG (a), LAP-GG (b), GG+VEGF (c) and LAP-GG+VEGF (d). Vascular integration assessment of GG (e), LAP-GG (f), GG+VEGF (g) and LAP-GG+VEGF (h) after 7 days of incubation. Arrows indicated major afferent vessels to the implanted scaffold. Scale bar: (e-h) 5 mm.

GG (Figure 6.14 e) was found to integrate and displayed clear vascularisation. Scaffold transparency allowed evaluation of penetrating vessels (small in number) through the structure. Membrane vessels were directed toward the sample (arrows). LAP-GG samples (Figure 6.14 f) were observed to integrate with the membrane. Blood vessels were found present around the outer surface of the construct (arrow) with major vessels converged towards the integrated sample (arrow). VEGF absorbed on GG (Figure 6.14 g) produced no significant effects although the sample was integrated with vessels around the sample (arrows) and minor capillaries around the construct (arrow). LAP-GG samples absorbed with VEGF (Figure 6.14 h) resulted in integration after 7 days of incubation. Vessels were found around the construct, with major vessels (arrows) converging towards the construct.

Chalkley scores (Figure 6.15) confirmed the minimal integration and vessel convergence of GG constructs. LAP-GG and VEGF-absorbed GG showed no significant differences in membrane integration. LAP-GG-VEGF was found to significantly integrate with the CAM compared to GG control ($p<0.0001$), LAP-GG and GG-VEGF ($p<0.01$).

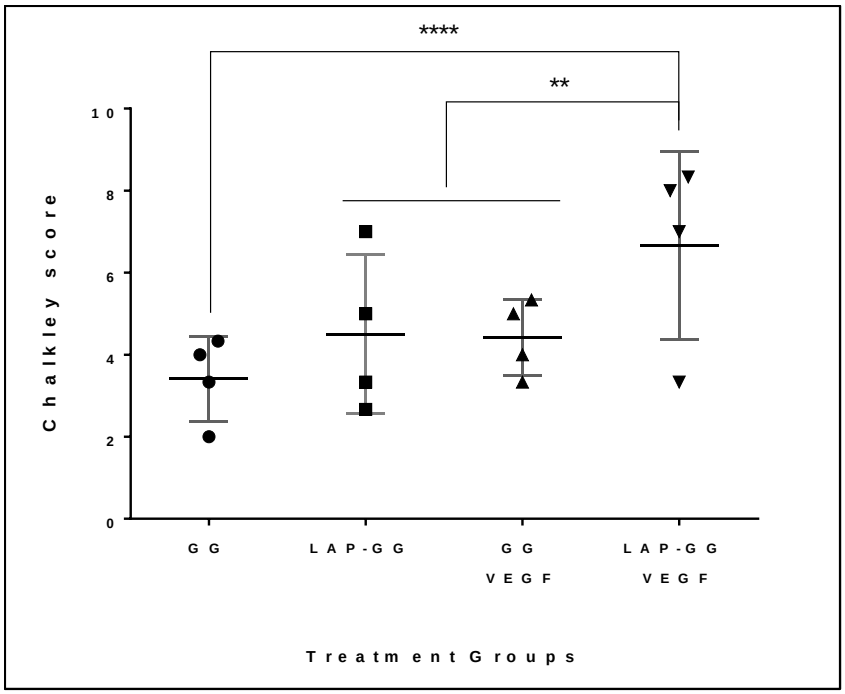

Figure 6.15. Chalkley scoring for implanted scaffolds.

Vascular penetration evaluation of implanted GG and LAP-GG, drug-free or absorbed VEGF groups. Statistical significance assessed by two-way ANOVA followed by Tukey's multiple comparison tests. Mean ± S.D. n=4 **p<0.01, ****p<0.0001.

6.4 Discussion

Recent advances in bioprinting technology have shown the potential of using a secondary gel to print a soft bioink to provide a support before post-printing crosslinking [153]. This novel 3D printing application has been recently defined as free-directional (or omnidirectional) printing [153,273]. This technology has been recently adopted by Highley *et al.* [260] using adamantane (Ad) and β-cyclodextrin (β-CD) to functionalise hyaluronic acid (Ad–HA and CD–HA, respectively) to synthesise a bioink (supramolecular gel) capable of high precision deposition when printed in the same gel. SSCs could be printed into a gel bed containing 3T3 fibroblasts, maintaining high (>90 %) viability. However, the purpose of the inclusion of fibroblasts in the gel medium was unclear and neither culture nor functionality studies were carried out in these studies. Grafting of methacrylates on HA macromers allowed selective UV crosslinking of printed gel, but induced toxicity to the encapsulated cells.

To augment free-form printing functionality, Laponite can be used to aid printability [122], shape fidelity [138], mechanical properties [118], cell viability and drug delivery [56]. Jin *et al.* [262] recently reported on the use of a Laponite gel formulation as a support bed for printing soft alginate-gelatin material. Bioink composition, viscoelastic properties, printing parameters and Laponite concentration influenced printability and construct shape fidelity. However, bioink deposition was highly dependent on the concentration of the Laponite bed (2-4 % w/v) resulting in printed filaments with well-defined shapes with limited swelling avoiding to specify an optimal printability window or functional properties.

In this chapter, a nanocomposite bioink was used to aid printability and functionality of a common biomaterial (gellan gum) printed in an agarose fluid gel bed. Gellan gum is a low-cost, non-animal derived polysaccharide widely reported in the tissue engineering literature for its biocompatible and drug delivery properties [266]. GG can gelate depending on the ambient temperature present. Polymeric chains in the GG network can crosslink in a double-helix following a decrease in the temperature in a thermo-reversible transition [267]. However, GG has been combined with several other polymers or fillers (e.g. alginate [198], GelMA [86,274,275], carbon nanotubes [269]) to generate multifunctional hydrogel platforms for printing applications [276].

Gel stability is profoundly influenced by pH and ionic strength of the submerging medium [113]. The effect of Laponite addition on GG swelling ability, sol fraction and mass loss were investigated. Sol fraction is defined as the loss of mass after 1 day of incubation in a solution [151]. Mass swelling ratio is calculated from the quotient of the swollen over the dry mass

of the gel [151]. PBS and HBSS were used as a solution containing a different ionic content. PBS was used at 1× concentration without Ca or Mg, while HBSS at 1× was used as it contains Ca^{2+} and Mg^{2+} ions. The sol fraction was found not to show significant differences between LAP-GG formulations and controls, either in PBS or in HBSS. However, formulations L0.5G1, L1G1, G2 and L1G2 showed a significant increase in sol fraction percentage when immersed in PBS compared to HBSS solutions. These results suggest the possibility of PBS to induce greater swelling, possibly forcing the release of Ca ions from crosslinked LAP-GG because of the difference in molarity [76].

Mass swelling ratio was found influenced by the ionic content of the PBS and HBSS solutions. Interestingly, LAP-GG formulations conditioned by the incubation in PBS, induced the swelling of cast gels. In contrast, calcium-rich HBSS conditioned scaffolds were limited in their swelling behaviour. These results were in agreement with Pacelli *et al.* [113] who reported the enhanced swelling of LAP-GG in deionized water compared to a solution of sodium chloride (NaCl). Possibly, the positive Na can contrast the negative surface of Laponite nanoparticles that otherwise would interact strongly with the rest of the Laponite negative charge inducing a repulsive action. Grasdalen *et al.* [264] studied the rigidity (N cm^{-2}) of gellan gum material in the presence of different ions. $CaCl_2$ was found to influence GG positively compared to a solution without any salt, limiting the swelling range suggesting a tighter polymeric network.

Investigation of swelling properties of LAP-GG and GG showed that the addition of only 1 w/v % of nanosilicate could regulate the swelling behaviour of the bioink, as initially confirmed by the sol fraction, mass loss investigation and reported in a previous study [113]. LAP-GG displayed reduced swelling compared to GG when printed in air. Critically, LAP-GG showed significantly lower swelling than GG when printed in agarose, as a consequence of Laponite inclusion, confirming the hypothesis the Laponite nanoparticles interact closely with gellan polymeric chains in the gel matrix. These results suggest the possibility to use a nanosilicate reinforced bioink to improve printing fidelity in a fluid gel medium. Furthermore, mechanical properties were enhanced, as evidenced by viscosity measurements that showed the higher viscous behaviour of LAP-GG bioink compared to the GG control. Increased pressure was required to extrude the nanocomposite gel, compared to GG, to achieve similar shear, demonstrating higher viscosity after deposition, resulting in greater printing fidelity after deposition [65]. The storage modulus decrease was noted after 10 % shear, showing a limited printability window.

A relaxed structure was observed in LAP-GG constructs in comparison to the silicate-free GG control, previously reported to show limited internal porosity [266,277]. Silicate-free GG was denser with a lower degree of internal porosity. Larger internal pores were evident in LAP-GG three-dimensional constructs, suggesting a repulsive action of Laponite nanodiscs

inclusion in GG network as confirmed by the mass swelling ratio results. Printing of acellular bioinks was influenced by the swelling behaviour of the gels pre- and post-crosslinking in air and in agarose. Results clearly show the higher resolution achieved by Laponite inclusion both in air and in agarose.

C2C12 were used as a cell line model for their particular sensitivity of differentiation towards bone lineage as previously shown [278]. Cells were allowed to attach onto LAP-GG and GG two-dimensional films. Seeded cells were found to attach and spread on the surfaces of the materials, showing similar morphology. As previously reported [123], Laponite addition can ameliorate cell attachment even at low concentration. The fibroblastic-like morphology of C2C12 cells seeded onto LAP-GG suggested enhanced properties for cell attachment. Further studies would be needed to confirm attachment and proliferation on LAP-GG and GG surfaces. C2C12 cells encapsulated and printed in LAP-GG proliferated more rapidly after 7 days of culture compared to the GG control. This has been previously reported [218] and similar effects will be detailed in Chapter 7 for HBMSCs encapsulated in a different bioink formulation. Cells encapsulated in the soft GG bioink can potentially escape and proliferate on the tissue culture plastic. In contrast, nanocomposite LAP-GG with enhanced mechanical properties to GG, show higher cell retention capacity due to the stiffer matrix retaining cells in the scaffold network. High cell retention and viability provide evidence for the functional potential of LAP-GG. Indeed, in osteogenic media, cells were found to express significantly greater ALP staining. Particularly, osteogenic conditioning of cell-laden LAP-GG scaffolds were found stained intensely for ALP. Douglas *et al.* [266] recently reported the use of a ALP-gellan gum hydrogel mineralisation protocol *in vitro.* ALP enzyme inclusion in GG network resulted in mineralisation when incubated in media conditioned with calcium phosphate (CaP) and magnesium glycerolphosphate (MgGP). GG gels were found extensively mineralised depending on both Ca and Mg concentration in solution. Particularly, osteoblast attachment and proliferation were found upregulated for Mg-conditioned gels. Similarly, both GG and LAP-GG were crosslinked with 1M $CaCl_2$. Residual Ca ions entrapped in the gel network, can be of help in guiding mineralisation. However, GG hydrogels appeared to show greater functionality in basal and osteogenic media when Laponite nanosilicate containing a small percentage of Mg ions was included in the blend. Laponite has been proven active in modelling stem cell differentiation, particularly upregulating ALP production and matrix mineralisation (CaP) [93].

Laponite has been shown, alone [103] or when blended with polymeric materials (e.g. alginate-methylcellulose [56], PEG-PLA [126], pH-sensitive poly(N-vinylpyrrolidone) (PVP) [132]), to aid the localisation of drugs of interests [109]. Compounds can be retained *in situ* to better functionally stimulate the local microenvironment [103]. Lysozyme and BSA were used as BMP-2 and VEGF analogues drugs (as also reported in Chapter 7). Lysozyme

absorption/release kinetics showed the possibility to rapidly load a greater amount of compound in LAP-GG and a lower sustained release over time compared to GG control. Further investigations will be needed to confirm BMP-2 bioactivity when localised in LAP-GG novel bioink formulations. However, the current results show a promising localisation/release kinetic useful in aiding bone regeneration compare to silicate-free GG [279]. Similar to lysozyme absorption/release kinetics, the nanosilicate-based gel was found to rapidly absorb BSA from the surrounding solution. BSA was found entrapped within the LAP-GG structure releasing a lower amount compared to the silicate-free GG.

This property was harnessed in combination with 3D deposition technology, to load and produce scaffolds for CAM assay. Following a previous study [280] where compounds of interests (ibuprofen, acetaminophen, indomethacin) were studied to diffuse through agarose with similar diffusion coefficient as in water, in this chapter, dyes in agarose fluid gel were found to penetrate LAP-GG with a greater depth than GG printed constructs confirming greater absorption capacity of nanosilicate bioink. The CAM assay [281] was used to investigate integration of the 3D printed scaffolds with the vascularised membrane of the developing chick. Cylindrical bulk scaffolds were printed, and loaded while printing, with VEGF solution in the agarose fluid gel. A fluid gel bed was used for the first time as a functional loading platform, working as a support and drug reservoir during printing. As previously demonstrated [280], drugs embedded into an agarose gel, result to diffuse similarly as when suspended or solubilised in acquaeous environment. Therefore, LAP-GG printing in agarose results particularly attractive as a single-step clinically relevant implant production by printing living cells while loading drugs simultaneously.

The CAM assay showed a greater effect of VEGF-loaded LAP-GG constructs compared to controls. VEGF, similarly to BSA, entrapped in LAP-GG constructs showed a greater angiogenic effect than VEGF-free scaffolds and VEGF-GG constructs. Absorption and localisation of VEGF mediated by Laponite has been previously reported [103] confirming the ability of Laponite gels to stimulate and guide angiogenesis both *in vitro* and *in vivo* after a brief exposure to VEGF solution. Release of VEGF has been investigated exclusively from GG-alginate bioinks [277] and resulted in similar kinetics as BSA release from silicate-free GG *in vitro*. *Ex vivo* results showed a greater effect of LAP-GG+VEGF suggesting greater ability to localise VEGF and providing a chemotactic platform beneficial for vascular infiltration.

6.5 Conclusions

Free-form printing is a promising novel biofabrication technology. Supporting gel matrices should display shear-thinning and self-healing properties to allow nozzle movement and support printed structures. LAP-GG novel nanocomposite bioink offers significant potential in printing fidelity, with tailorable swelling characteristics and enhanced shape retention compared to silicate-free GG. A porous internal structure is ideal to enable cell encapsulation and sustain cell viability and proliferation *in vitro.* Laponite inclusion increased cell-laden bioink functionality, evidenced by elevated ALP expression after 1 day of culture. Absorption/release properties of the LAP-GG blend were dependent on silicate incorporation in the GG matrix, with higher absorption and slower release for lysozyme, and similar absorption but slower release for BSA compound. CAM assays with printed scaffolds, absorbed while printing, with VEGF solubilised in agarose, provided an innovative drug-loading solution aiding biofabrication application. LAP-GG+VEGF samples were found integrated in the chorioallantoic membrane with a significantly greater amount of afferent blood vessels.

However, lack of i) further dynamic mechanical analysis tests, ii) release investigations other than *in vitro,* and iii) *in vivo* investigation of vascular and bone formation, clearly indicate the limitations for LAP-GG constructs for further preclinical development. Moreover, human SSCs printing and functionality need to be investigated to determine if LAP-GG offers an ideal composite material. Nevertheless, functionality of LAP-GG showing higher ALP expression *in vitro* and greater integration *ex vivo*, indicates the successful development of a bioactive construct with a promising application for orthopaedic reparation.

Nevertheless, in a clinical scenario, even though LAP-GG could be utilised as versatile bioink system able to produce large scale constructs in combination with agarose, the use of a fluid gel bath could result in a more complex printing process, supporting a chemical crosslinking (e.g. $CaCl_2$) which can often affects cell viability and functionality. Therefore an efficient and functional bioink is needed aided by a rapid and reliable crosslinking platform that might help to preserve cell viability and able to be easilty translated for clinical application. This technology is illustrated in the following chapter.

Chapter 7 Visible-light curable nanosilicate bioink: an innovative tool for vascular induction and skeletal regeneration

7.1 Introduction

Cell printing is often carried out at the expense of cell viability and functionality [150]. Current bioinks require a method of crosslinking to support 3D structures encapsulated with cells post printing [282]. In recent times, gelatin methacryloyl (GelMA) hydrogels have been widely used as a cell-carrier given its potential to simulate the highly hydrated native 3D cellular microenvironment, support cell adhesion and aid functionality [283]. GelMA is a photopolymerisable macromer [284] initially developed to provide a chemically stable hydrogel with the capacity to retain its physical shape at physiological temperature [285]. This gelatin-based hydrogel has been previously functionalised with chemical groups able to entangle gelatin polymeric chain when expose to external stimuli. Crosslinking approaches such as ionic, thermal and chemical can be harmful for cells encapsulated in the bioink.

One simple solution to address this issue, is to use visible-light to rapidly crosslink printed bioinks. Lim *et al.* [151] have used ruthenium (Ru) and sodium persulfate (SPS) as a novel photoinitiator combinations to crosslink GelMA [284]. This approach minimised oxygen inhibition and allowed printing of high fidelity scaffolds. Cell viability of encapsulated cells was found to be significantly higher in respect to scaffolds crosslinked with UV light. Furthermore, a collagen filler was added to the visible-light crosslinked GelMA to stabilise the bioink while printing, but with no apparent functional benefit. Moreover, functionality as a cell-carrier, drug-delivery system and bioink were not fully evaluated, components that could be tailored according to filler inclusion. The use of GelMA as a bioink is limited by the low viscosity and the narrow biofabrication window afforded by this hydrogel, resulting in poor filament extrusion and shape fidelity over 20-37°C (room temperature to body temperature) [86,151], even at relatively high GelMA concentrations of 10-20 wt%. Encapsulated human bone marrow stromal cells (HBMSCs) targeted for osteogenic differentiation require a permissive hydrogel microenvironment to allow adequate cell function (i.e. cell spreading, cell communication and mechanosensing) [286,287], typically provided by low GelMA concentrations (5-10 wt%). To address issues around printability, multiple GelMA composites have been developed through the blending of various materials including hyaluronic acid [86], gellan gum [275] and collagen [151] relating to their viscosity modifying and/or yield stress modifying capabilities. Nevertheless, none of the developed composite bioinks has targeted bioprinting of soft permissive hydrogels with high shape fidelity in combination with the skeletal-specific requirements of bone formation and blood vessel ingrowth [288].

Nanoclay has been used extensively in the pharmaceutical industry [97,98] and has recently gained interest as a nanofiller for biomaterials for regenerative medicine applications [95]. Specifically, Laponite is a smectite nanomaterial able to generate colloidal-like suspensions when dispersed within an aqueous environment [103]. Dispersions of Laponite contain disc-shaped nanoparticles of 1 nm in thickness and 25 nm in diameter with a positive rim charge and negative surfaces. Clay-based gels have been shown to behave as a functional vehicle for drug retention and delivery with preferential clay-protein interactions [103]. Combinations of Laponite with a wide library of polymers offer an attractive solution for enhancing bioinks printability using Laponite shear-thinning properties.

Previous work [56] has demonstrated that Laponite inclusion within an alginate-methylcellulose bioink network can improve its printability, mechanical stability, limit swelling after crosslinking and preserve cell viability and density. The addition of clay can improve mechanical and physical properties of bioinks, and modulate functionality by clay-protein interaction and entrapment stimulating the cell-laden microenvironment. Gibbs *et al.* [110] have reported on the functionality of Laponite gels containing physiological doses of BMP-2. Harnessing silicate sorptive capacity, BMP-2 activity could be preserved and used following Laponite gel implantation *in vivo*, showing ectopic bone formation with a low dose (40 ng) of BMP-2. Furthermore, the functional impact of clay dispersion on human SSCs has been recently reported [93], identifying more than 4,000 genes and major cellular pathways (e.g. MAPK) influenced as a consequence of cell-clay interaction.[138] Laponite inclusion in GelMA has been previously reported [102,215], but the functional and clinical potential were limited due to the lack of further experimental studies beyond *in vitro* characterisation. Moreover, UV-crosslinking has been previously shown to be disruptive for cell viability and functionality. Pre-clinical application of LAP-GelMA has never been reported before.

This chapter details the use of a nanosilicate (Laponite) to physically modify a GelMA network generating a functional visible-light crosslinking bioink to: i) retain shape fidelity after printing (Figure 7.1 a), ii) encapsulate HBMSCs (Figure 7.1 b), iii) localise compounds of interest (Figure 7.1 c) and, iv) promote drug-aided vasculogenesis *ex vivo* (Figure 7.1 d).

Hypothesis (V):

Laponite (LAP) can be blended with GelMA and visible-light crosslinking technology to synthesize a new bioink with improved printing fidelity. The use of visible-light crosslinking in combination with photoinitiators can allow continuous deposition and crosslinking of LAP-GelMA. Silicate addition can improve functionality of the cell-laden nanocomposite and in combination with drug absorption/release abilities mediated by silicate inclusion, can localised VEGF and stimulate angiogenesis *ex vivo*.

Aims:

- To mix Laponite and GelMA to synthesise and print a novel nanocomposite bioink (LAP-GelMA) with a continuous visible-light curing technology;
- To quantify viability/proliferation and functionality of encapsulated and seeded SSCs;
- To evaluate LAP-GelMA absorption and release of drugs analogues;
- To investigate VEGF-absorbed LAP-GelMA potential for CAM integration and angiogenesis.

Overview of Chapter 7:

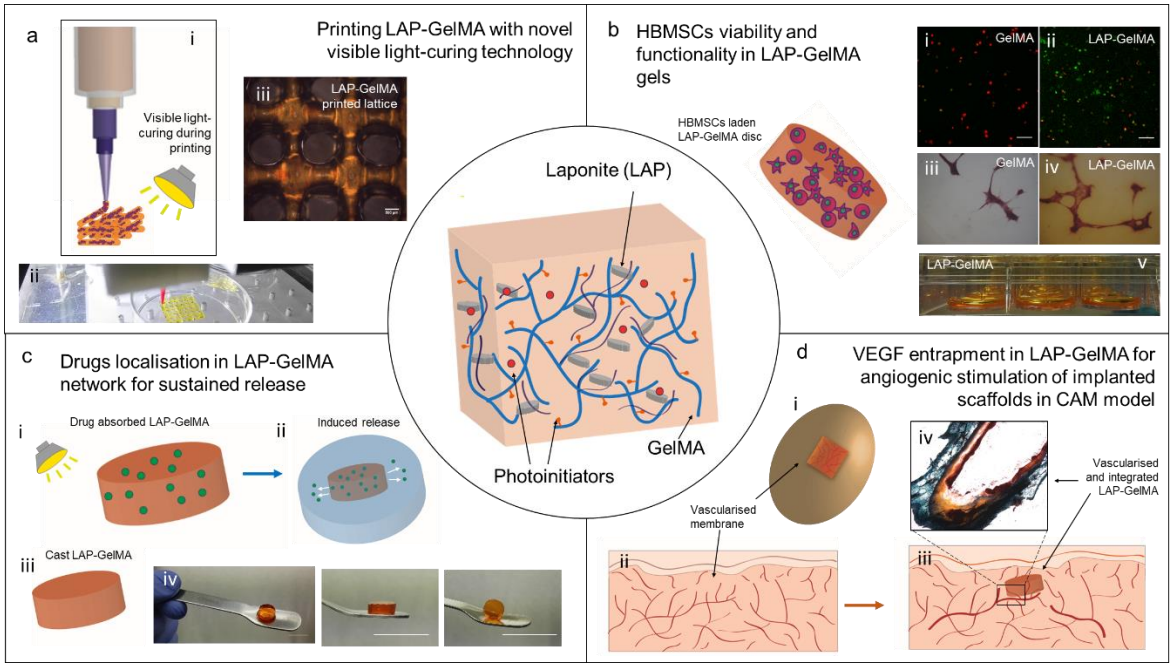

Figure 7.1. Schematic of LAP-GelMA characterisation *in vitro* and *ex vivo*.

Printing LAP-GelMA by light-curing technology (a) during printing (a-i) an aid to improved printability (a-ii) and higher shape fidelity (a-iii). HBMSCs viability (b) can be enhanced (b-i,ii) by LAP inclusion in GelMA network as well as functionality (b-iii,iv) HBMSCs seeded (b-v) on LAP-GelMA. Drugs of interests (c) can be localised in LAP-GelMA gels (c-i) and tailored for release (c-ii). Cast LAP-GelMA (c-iii,iv) can be used as a precise model for drug absorption/release kinetic study. Vascularised membrane (d) of a developing chick embryo (d-i,ii) can be used to assess integration and blood vessels penetration (d-iii,iv) in LAP-GelMA 3D scaffolds. Scale bar: (b-i,ii) 100 µm, (c-iv) 20 mm, 50 mm

7.2 Methods

7.2.1 Laponite

This methodology is detailed in Chapter 2 (2.2.1 page 43)

7.2.2 Gelatin-Methacryloyl

Gelatin-methacryloyl (GelMA) was kindly supplied by Prof Tim Woodfield (University of Otago, Christchurch, New Zealand) and synthesised following a previously employed protocol [151] by collaborators at University of Otago. Briefly, gelatine (porcine skin; 300g bloom strength, Sigma-Aldrich) was dissolved in 1× PBS at 10 % w/v concentration. Methacylic anhydride (0.6 g/ml) was added to the gelatine solution and the reaction allowed to occur for 1 h at 50°C under constant stirring. The solution was centrifuged and dialysed against deionised water to remove any unreacted methacrylic anhydride. The GelMA solution pH was adjusted to 7.4, followed by sterile filtration (0.22 µm filter) and lyophilisation. The degree of modification for methacryloyl substitution was quantified to be 60 % using 1H-proton nuclear magnetic resonance spectroscopy (Bruker Advance 400 MHz).

7.2.3 Laponite-gelatin methacryloyl

Laponite (LAP) suspension was prepared as previously described in the paragraph 2.2.1 (page 43). Briefly, DW was left to stir at 5 G (Figure 7.2 a) and Laponite sterile powder at 1 % w/v concentration was weighed and suspended in DW by slow addition (Figure 7.2 b). A clear suspension (Figure 7.2 c) was obtained after 6 h of continuous shear. Sterile GelMA, in its lyophilised form (Figure 7.2 d) was weighed to 7.5 % w/v and inserted into the Laponite suspension (Figure 7.2 e). Incubation at 37°C was carried out overnight to allow

GelMA complete inclusion in Laponite suspension, obtaining a clear gel precursor suspension (Figure 7.2 f).

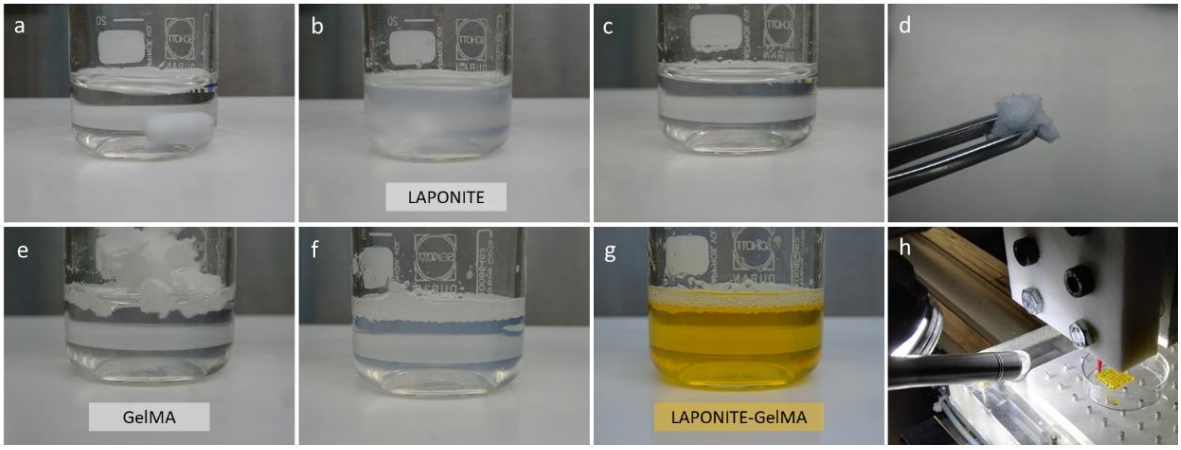

Figure 7.2. Synthesis of Laponite-GelMA bioink.

DW was allowed to stir (a) and Laponite added (b) slowly to allow full dispersion of nanoparticles (c). Gellan gum was then added (d) and allowed to solubilise in heated Laponite suspension, leaving a homogeneous bioink (e) that can be immediately be used in combination with agarose fluid gel for free-form printing (f). LAP-GG gel stored at a temperature below 37°C will harden (g) and gel (h).

Tris (2,2-bipyridyl) dichlororuthenium (II) hexahydrate (Ru) and sodium persulfate (SPS) were used as photoinitiators to trigger the GelMA crosslinking mechanism. Their inclusion in a 1:10 Ru/SPS ratio in LAP-GelMA coloured bioink with a bright orange colour (Figure 7.2 g). After Ru/SPS addition LAP-GelMA bioink was ready to be used for printing applications (Figure 7.2 h).

7.2.4 Fabrication of 3D printed Laponite-GelMA scaffolds

Scaffolds were produced with the in-house built bioprinting system reported in the paragraph 2.4.1 (page 49). Scaffolds of 12 × 12 mm and 10 layer high were fabricated by extrusion of LAP-GelMA bioink at 15 kN using a 250 µm conical nozzle (Fisnar Europe, UK). Scaffolds were printed with a constant velocity of 2.5 mm s^{-1}. The use of conical UV-tapered nozzles allowed the free printing without covering of the nozzle. Continuous irradiation with visible light was carried out while producing scaffolds. A high intensity visible light source (250 mW cm^{-2}) was used to crosslinked scaffolds during printing. A blue light lamp (Thorlabs LED 450 nm array LIU LAMP (LIU450A-SP1)) was used post-printing to

specifically match photoinitiators wavelength and maximise crosslinking efficiency. Further crosslinking of 3D printed scaffolds was allowed by illuminating scaffolds for 5 min post-printing.

7.2.5 Scaffold printability and swelling

Three-dimensional scaffolds were fabricated by layer-by-layer deposition of LAP-GelMA or GelMA as control, via extrusion printing. Printing was carried out using a 410 µm cylindrical nozzle cylindrical in shape (Fisnar Europe, UK). Extruded fibres were deposited with an average force of 14 KN. A layer height 350 µm was used to produce a 20 × 20 mm lattice scaffold. Scaffold printability was evaluated following 10 layer printing and microscopic measurements of fibre shape fidelity after printing. A visible-light source of 250 mW cm^{-2} was used to crosslinked scaffolds during printing. A further 5 min crosslinking with visible-light after printing was carried out. Measurements were carried out on pictures taken in 5 different spots of multiple scaffolds (n=5) using a stereo microscope. Images were analysed with Image J (1.44p, National Institutes of Health, Bethesda, Maryland, USA).

7.2.6 Fabrication of Laponite-GelMA discs

Three-dimensional discs were fabricated as previously described [151]. Briefly, Ru and SPS were used as photoinitiators to trigger the GelMA crosslinking mechanism. Photoinitiators were added at a 1:10 ratio to the LAP-GelMA suspension. A volume of 30 µl was transferred to a silicone mould (Ø 5 mm × 1 mm) layered on a glass slide and subsequently covered with a glass coverslip. Similarly to 7.2.4 (page 196), hydrogel was then irradiated with a blue visible light lamp.

7.2.7 Skeletal stem cells isolation

This methodology is detailed in Chapter 2 (2.1.3 page 41)

7.2.8 Fabrication of SSC-laden discs

HBMSCs were isolated from a single patient (F66) femoral head samples following standard laboratory procedure reported in section 2.1.3 (page 41). HBMSCs were encapsulated within nanocomposite hydrogels at a density of 1×10^6 cells ml^{-1} and positioned within moulds and upon glass slides. Crosslinking by visible light (400-450 nm) for 10 min was carried out using visible light (OmniCure S1500, Excelitas Technologies), with the surfaces of the gels exposed to air. Scaffolds were removed with sterile forces and incubated in full α-MEM media at 37°C and 5 % CO_2 balanced air.

7.2.9 Viability and proliferation of SSCs-laden discs

This methodology is detailed in Chapter 2 (2.5.4 page 57)

7.2.10 Seeding of SSCs on Laponite-GelMA films and functionality

Laponite-GelMA films were produced by a series of centrifugation and crosslinking steps. Briefly, GelMA and LAP-GelMA were pipetted into wells a of 24-well plate and allowed to disperse on the bottom of the well following a series of centrifugation at 300 G for 4 min. Resting at room temperature was then allowed for 1 min and a further centrifugation was carried out at 835 G for 2 min to aid spreading of films of 1 mm in thickness. Samples were subsequently crosslinked with visible light (400-450 nm, OmniCure S1500, Excelitas Technologies) irradiating the films for 5 min from the top and the bottom respectively. HBMSCs isolated from a single patient and reported in section 7.2.9 (page 198) for cell viability investigation, were seeded at an initial density of 0.1×10^6 cell ml^{-1} in each well. Cells were left to attach for 24 h on a rocket shaker at 37°C and 5 % CO_2 balanced air. Media was then replaced with basal and osteogenic media (formulation reported in Chapter 2 (2.1.4 page 42)) at the start of the differentiation experiment. Therefore, 24 h later was considered as day 1 time point. ALP staining was performed following the protocols illustrated in Chapter 2 (2.5.5 page 57).

7.2.11 Drug analogues absorption and release

This methodology is detailed in Chapter 2 (2.6.1 page 58). Discs of gel reported in section 7.2.5 (page 197) were used in this assay.

7.2.12 CAM assay

7.2.12.1 Sample fabrication

Cylindrical-shaped scaffolds were fabricated for CAM implantation. The disc scaffolds produced using the methodology presented in the section 7.2.5 (page 197) resulted in a small volume (only 30 µl) to be implanted in large fertilised eggs. LAP-GelMA and GelMA were loaded in 3 ml slip tip syringes (BD Plastipak, UK) and crosslinked with a visible-light lamp (400-450 nm, OmniCure S1500, Excelitas Technologies) for 10 min. Syringe tips were then removed with a sterile scalpel and 300 µl cylinders extruded from an aperture with the diameter of the 3 ml syringe (8.66 mm). Scaffolds were collected and stored at 4°C overnight for VEGF absorption and CAM implantation. LAP-GelMA (n=15) and GelMA (n=15) scaffolds were absorbed in a 1× PBS solution with a 100 µg ml^{-1} of VEGF (recombinant human VEGF 165, Peptrotech, USA) for 1 h at 4°C and then washed with 1× PBS to remove unbound VEGF. VEGF-free LAP-GelMA (n=15) and GelMA (n=15) scaffolds were kept at 4°C and implanted simultaneously with VEGF-absorbed samples.

7.2.12.2 Implantation, extraction and Chalkley score

This methodology is detailed in Chapter 2 (2.7.2 page 61 and 2.7.3 page 62)

7.2.13 Histology

This methodology and specific staining are reported in Chapter 2 (2.10 page 65 and 2.10.1 page 65)

7.2.14 Statistical analysis

This methodology is detailed in Chapter 2 (2.11 page 66). Statistical analysis is reported in the figure captions.

7.3 Results

7.3.1 Nanosilicate-based light-curable hydrogel synthesis

Nanosilicate-based hydrogels were fabricated by direct mixing of clay and gelatin materials. LAP-GelMA synthesis was optimised to obtain a uniform paste prepared from a nanosilicate suspension of fixed concentration (Figure 7.3).

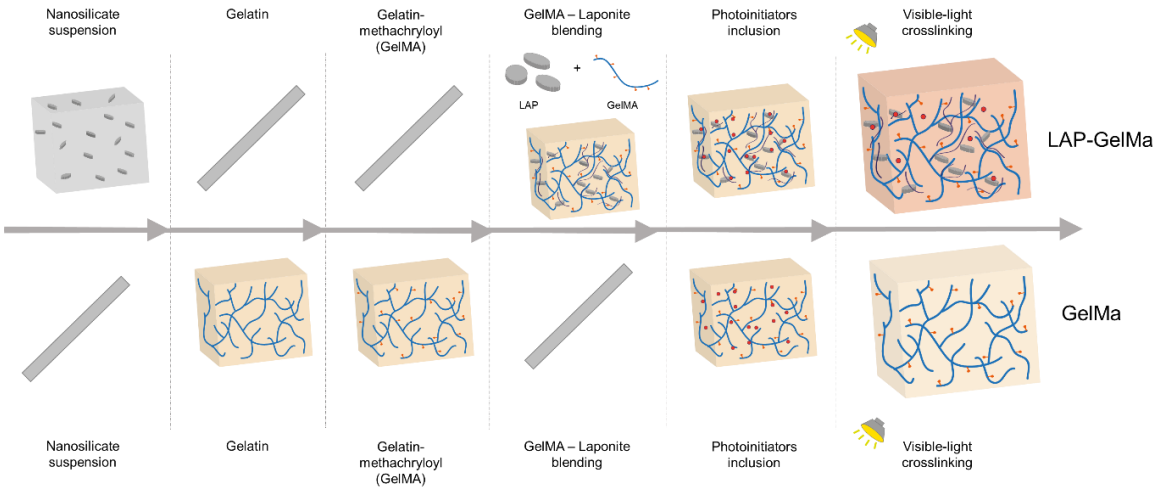

Figure 7.3. Nanocomposite bioinks synthesis.

Nanosilicate (Laponite) can be suspended in deionised water to gelate under constant shear. Gelatin is functionalised with methacryloyl groups which, when exposed to visible light, can form irreversible covalent links. Gelatine methacryloyl (GelMA) precursor can then be dispersed in deionised water or in Laponite suspension. Photoinitiators can be included in the suspensions. GelMA releasing photoinitiators, after crosslinking, result in sample transparency when placed in solution.

The Laponite suspension was mixed on a magnetic stirrer for at least 3 hours to allow complete Laponite nano-discs dispersion. GelMA was added to the suspension and mixed thoroughly. Inclusion of GelMA within the Laponite network was carried out overnight at 37°C. To induce gelation, 1:10 Ru/SPS photoinitiators were added. Silicate-based gels were observed to be bright orange in colour immediately after photoinitiators were added. This characteristic was maintained over a period of 21 days in culture. In contrast, GelMA control samples released excess photoinitiator and were observed to be colourless after 24 h of culture.

7.3.2 Printability of nanocomposite scaffolds is improved by continuous exposure to visible light during printing

Printing was carried out with an extrusion printer (Figure 7.4 a) using LAP-GelMA bioink. Lattice structures (Figure 7.4 b,c) were produced with a constant velocity of 2.4 ± 0.56 mm s^{-1} allowing a continuous production of 3D printed structures (10 in only 30 min). The resulting scaffolds were consistent in their lattice shape (Figure 7.4 d) and were crosslinked immediately after printing (Figure 7.4 e,f) with a blue 405 nm LED lamp.

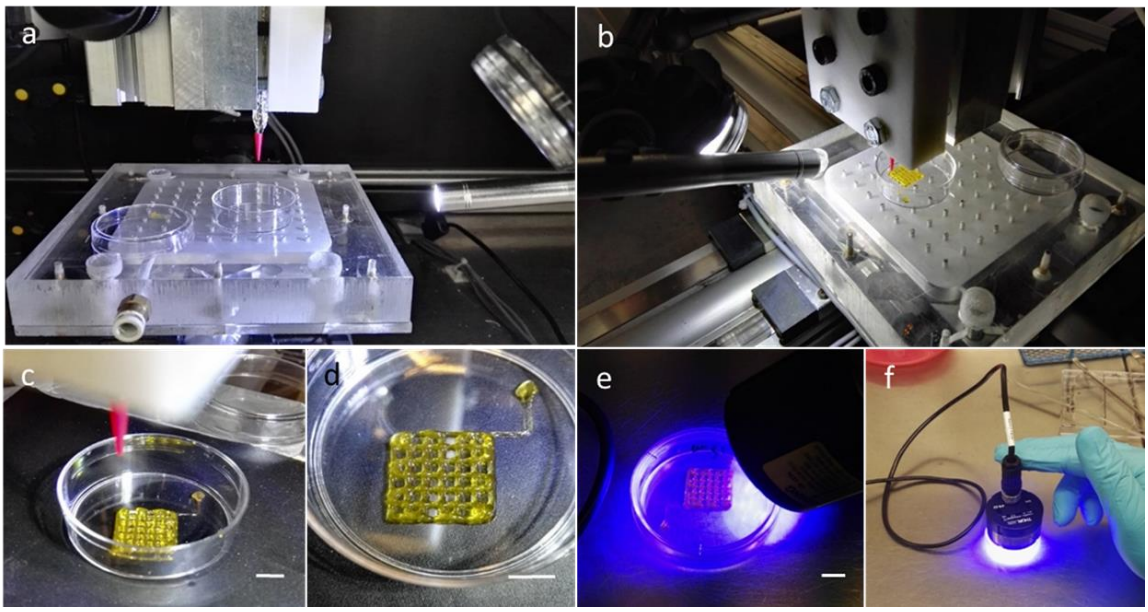

Figure 7.4. Silicate bioink printing optimisation.

In-house built extrusion-based bioprinter (a) was used to deposit LAP-GelMA hydrogels. Visible light (b) was positioned onto a mobile arm to allow crosslinking immediately post printing. Scaffolds printed with a 250 µm conical nozzle (c) resulted in (d) accurately fabricated, but partially stable when printed in air. (e,f) Further aid to crosslinking process was carried out using a 450 nm (blue) LED light. Scale bar: (c-e) 5 mm.

Acellular printing of LAP-GelMA was optimised to obtain the highest shape fidelity results possible. Printing was optimised to fabricate scaffolds with a constant exposure to high intensity visible light (Figure 7.5 a-c). This resulted in a higher precision compared to post-printing crosslinking, ameliorating not only the paste deposition but also the shape fidelity of the final printed structure.

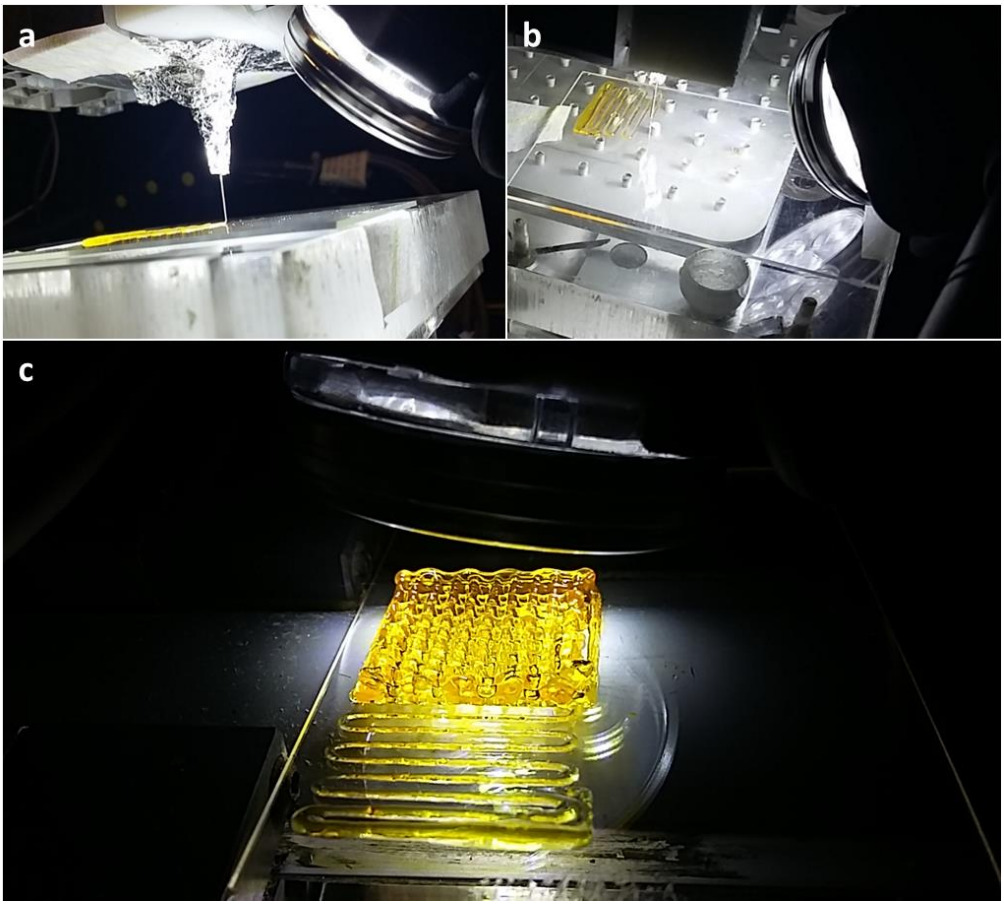

Figure 7.5. LAP-GelMA 3D printing.

LAP-GelMA bioink extruded through a 250 µm cylindrical blunt nozzle. Shielded nozzle (a) to prevent rapid crosslinking during extrusion enabling fine deposition. High intensity light (b) was used to continuously project visible light on the sample during printing. After extrusion (c) further crosslinking was carried out by close proximity of the visible light on the mobile arm to the printed scaffold.

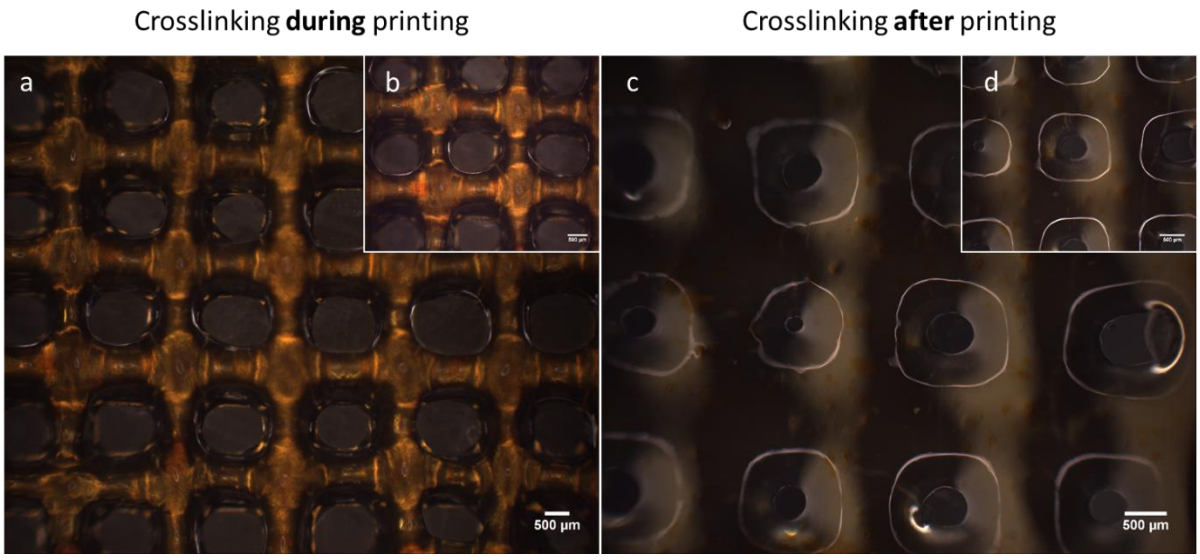

Figure 7.6. LAP-GelMA scaffold physical characterisation.

Using a high intensity visible light source during printing (a, b) compared to post-printing crosslinking lamp (c, d) allowed higher precision in paste deposition, limiting strand collapse and enhancing bioink uniformity and shape fidelity.

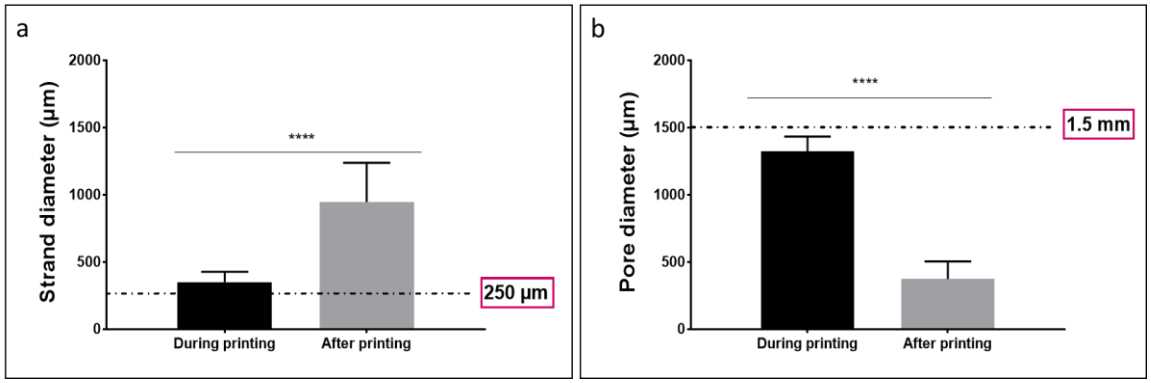

Figure 7.7. Quantitative analysis of LAP-GelMA scaffold printed using visible light crosslinking during printing or immediately post printing.

LAP-GelMA composites printed using visible light crosslinking during extrusion, displayed significantly different measurements in pore (a) and strand (b) diameter. Statistical significance assessed by Unpaired T-test with two-tailed correction. Mean ± S.D. n=10, ****p<0.0001.

Lattice scaffolds were evaluated for shape fidelity after printing. The use of a high intensity light source (250 mW cm^{-2}) active during printing aided the fine deposition of LAP-GelMA (Figure 7.6 a,b) compared to the printing of LAP-GelMA in the absence of light and crosslinked immediately after printing (Figure 7.6 c,d). When exposed to high intensity light during printing, LAP-GelMA was extruded homogenously and deposited in fibres with increased accuracy. The characteristic orange colour was maintained and distributed evenly throughout the entire scaffold. In contrast, LAP-GelMA printed in the absence of a light source flowed non-homogenously and showed aggregated material and photoinitiators within the fibres. Quantitative analysis of printed scaffolds (Figure 7.7 a,b) showed a positive effect on the use of elevated intensity light during printing, producing scaffolds with an average strand diameter of 350.64 ± 76.07 µm, significantly ($p<0.0001$) lower compared to post-printing crosslinked scaffolds with 945.84 ± 291.82 µm strands. The overall structure was compromised by the use of visible light crosslinking after printing displaying collapsed pores of 373.85 ± 130.13 µm. The use of the light crosslinking method during printing generated pores with a significantly larger ($p<0.0001$) diameter (1321.72 ± 120.67 µm) and a lattice structure that could accurately reproduce the desired blueprint.

7.3.3 Nanosilicate-based constructs preserve cell viability, support proliferation and functionality after 21 days culture *in vitro*

HBMSCs were encapsulated in LAP-GelMA bioink for initial assessment of cell viability, survival and proliferation after printing. Confocal images of HBMSCs encapsulated in LAP-GelMA and GelMA hydrogel pastes were collected after cell printing (Figure 7.8 a). HBMSCs displayed a round morphology with no signs of spreading. GelMA bioink was used as a positive control.

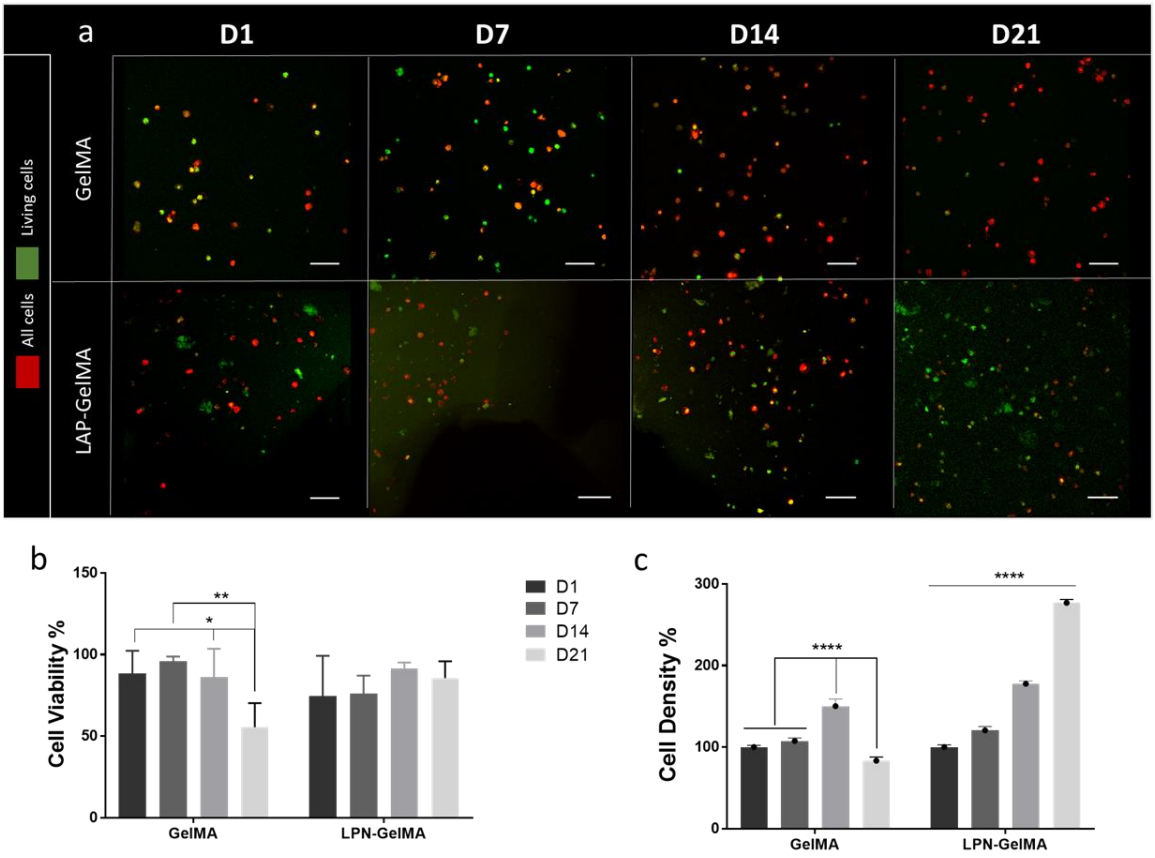

Figure 7.8. Cell viability and proliferation of HBMSCs-laden 3D constructs.

Confocal micrographs (a) illustrate maximum intensity projection of HBMSCs-laden 3D scaffolds cultured for up to 21 days. Encapsulated HBMSCs were stained for mitotically active cells at 1, 7, 14 and 21 days. Cells were pre-labelled with DiD lipid-labelling dye (red) staining all cells prior to encapsulation and printing. Viable cells were stained at select time-points with Calcein AM (green). Dead cells were stained only in red (within population). Cell viability percentages (b) were obtained from difference in the values between viable and total cell fraction. Cell density percentages (c) were calculated from viable cells normalised to volume of interest. Scale bar: 200 µm. Statistical significance assessed by two-way ANOVA followed by Tukey's multiple comparison tests. Mean ± S.D. n=3, *p<0.1, **p<0.01, ****p<0.0001

Cells encapsulated in GelMA (Figure 7.8 b) were viable after 24 h (88.40 ± 13.89 %), increasing after 7 days (95.88 ± 2.90 %) and decreased over time from 14 (86.26 ± 17.22 %) to 21 days (55.54 ± 14.72 %). A significant difference ($p<0.01$) in cell viability was registered at 1 and 21 days compared to 7 days after encapsulation. HBMSCs in LAP-GelMA constructs were viable after 24 h (74.44 ± 24.89 %) and the gels remained stable after 7 days (76.12 ± 10.93 %). Viability peaked after 14 days of culture (91.57 ± 3.62 %) and decreased up to 21 days (85.60 ± 10.27 %). Cell density results (Figure 7.8 c, day 1 set as 100 %) confirmed elevated initial viability for GelMA control after 7 (107.57 ± 3.86 %) days and a significant increase ($p<0.0001$) after 14 days (150.36 ± 8.58 %), decreasing rapidly and significantly ($p<0.0001$) after 21 days of culture (83.36 ± 4.57 %). The reduction in cell density in GelMA constructs indicates that the number of living and total number of cells decreased over time. In contrast, HBMSCs-laden LAP-GelMA scaffolds showed a sustained and significant ($p<0.0001$) increase in cell density from 7 (120.55 ± 4.46 %), 14 (177.74 ± 3.30 %), up to 21 days of culture (276.91 ± 4.28 %). A rapid increase in the density of cells encapsulated in LAP-GelMA indicated sustained HBMSCs proliferation. Even after 21 days of culture when viability of HBMSCs-laden LAP-GelMA was observed to fall, the number of living cells per μm^3 increased.

Functionality of HBMSCs-seeded 2D nanosilicate-based gel films cultivated up to 21 days in basal (Appendix C Figure 7.1) and osteogenic (Appendix C Figure 7.2) conditioned media was investigated by ALP staining. Cells were found to proliferate on LAP-GelMA, GelMA and in control (tissue culture plastic) conditions. HBMSCs were found to preferentially form colonies when seeded onto LAP-GelMA (Appendix C Figure 7.1 and Appendix C Figure 7.2) compared to GelMA and control. As expected, cells were found extensively stained with ALP when conditioned with osteogenic media. HBMSCs cultured on LAP-GelMA in basal media (Figure 7.9 a) displayed, after 1 day, the typical colony morphology of HBMSCs *in vitro* (Figure 7.9 c). HBMSCs seeded on GelMA (Figure 7.9 b) were observed to spread over a larger area compared to LAP-GelMA. After 7 days, HBMSCs were observed to form compact colony aggregates on LAP-GelMA (Figure 7.9 d) compared to day 1 cultures. GelMA films after 7 days (Figure 7.9 e), were noted to have started to degrade, revealing fibrous structures populated by HBMSCs staining positively for ALP. In contrast, control HBMSCs on cell culture plastic (Figure 7.9 f) displayed intense ALP staining in colonies. After 21 days of culture, LAP-GelMA (Figure 7.9 g) integrity was noted to be maintained and to support the proliferation of HBMSCs colonies evidenced by positive ALP staining. On the contrary, GelMA films were found to loose integrity over time (Figure 7.9 h) allowing HBMSCs to attach on tissue culture plastic resulting positively stained for ALP. Control at 21 days (Figure 7.9 i) showed a higher number of cells stained but with a lower intensity of ALP expression.

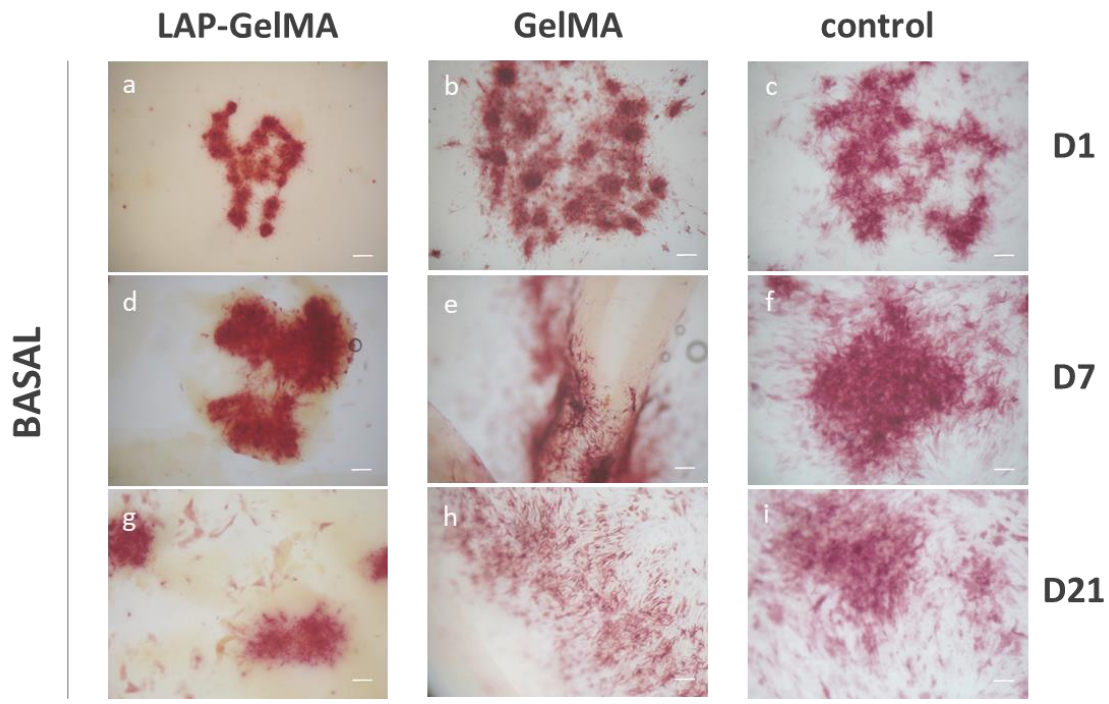

Figure 7.9. Functional study of HBMSCs seeded on 2D LAP-GelMA gels in basal conditioned media.

HBMSCs were seeded onto 2D LAP-GelMA and GelMA films with tissue culture wells as control. ALP staining analysed under basal conditions after 1 (a, b, c), 7 (d, e, f) and 21 (g, h, i) days for LAP-GelMA, GelMA and control respectively. Scale bar: 500 µm.

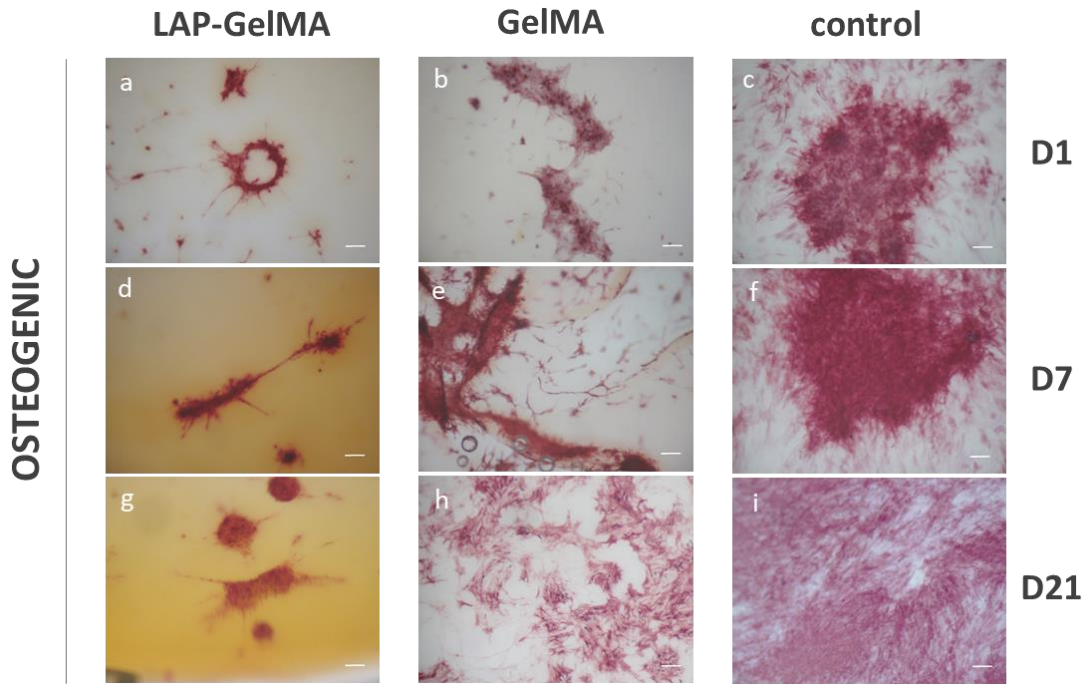

Figure 7.10. Functional study of HBMSCs seeded on 2D LAP-GelMA gels in osteogenic conditioned media.

ALP staining analysed after culture in osteogenic media for 1 (a, b, c), 7 (d, e, f) and 21 (g, h, i) days for cells maintained in LAP-GelMA, GelMA and tissue culture plastic (control) respectively. Scale bar: 500 µm.

HBMSCs conditioned with osteogenic media displayed a distinct phenotype to cells maintained in basal conditions. HBMSCs on LAP-GelMA displayed a discrete number of small circular colonies positive for ALP staining (Figure 7.10 a). Cells on GelMA attached on the film, formed elongated colonies (Figure 7.10 b), and, in contrast, control samples (Figure 7.10 c) displayed large colonies of HBMSCs expressing ALP. After 7 days of culture, HBMSCs on LAP-GelMA (Figure 7.10 d) assembled in small colonies that stained intensely for ALP and appeared elongated on the surface of the gel. Colonies on GelMA (Figure 7.10 e) showed ALP staining. However, GelMA films started to degrade with some HBMSCs attached to the culture plastic well. Cells on plastic control after 7 days (Figure 7.10 f) were found to assemble into colonies with strong ALP expression. After 21 days of culture in osteogenic media, cells on LAP-GelMA showed colonies with fibroblast-like morphology (Figure 7.10 g). HBMSCs on GelMA were found to be predominantly spread across the tissue culture well rather than on the GelMA, that had degraded (Figure 7.10 h). HBMSCs on control plastic surface spread on a large surface, losing colony-forming ability and with a reduced ALP staining intensity (Figure 7.10 i).

7.3.4 Nanocomposite hydrogels show higher drug retention/localisation within the 3D matrix

Drug absorption was investigated to elucidate the absorption mechanism of GelMA with the addition of a nanosilicate component. Three-dimensional discs of 30 µl volume (Figure 7.11 a,b) were fabricated and crosslinked with 1:10 Ru/SPS photoinitiators for 10 min. LAP-GelMA showed a higher retention capacity for the Ru/SPS than GelMA which displayed rapid release of the photoinitiators after a few minutes of incubation. Lysozyme (10 µg ml^{-1}) was absorbed onto LAP-GelMA and GelMA discs. Absorption was monitored after 1, 2, 4, 8 and 24 hours following initial loading (Figure 7.11 c). Results demonstrate that 1 % w/v Laponite inclusion in GelMA did not significantly affect the absorption capacity. After 1h, lysozyme absorbed into LAP-GelMA (0.40 ± 0.51 µg ml^{-1}) and GelMA (1.74 ± 0.29 µg ml^{-1}) discs. LAP-GelMA and GelMA were saturated with lysozyme after 1h and started to release small amounts into the solution up to 24 h (LAP-GelMA: 1.69 ± 0.59 µg ml^{-1}, GelMA: 3.98 ± 0.19 µg ml^{-1}). Collagenase solution (1 mg ml^{-1}) was used to simulate *in vivo* digestion conditions. Results (Figure 7.11 d) show that GelMA released nearly the total absorbed lysozyme after 4 h in the digestion bath (9.889 ± 1.20 µg ml^{-1}), reaching a plateau and a continuous release profile up to 24 hours (9.095 ± 2.347 µg ml^{-1}).

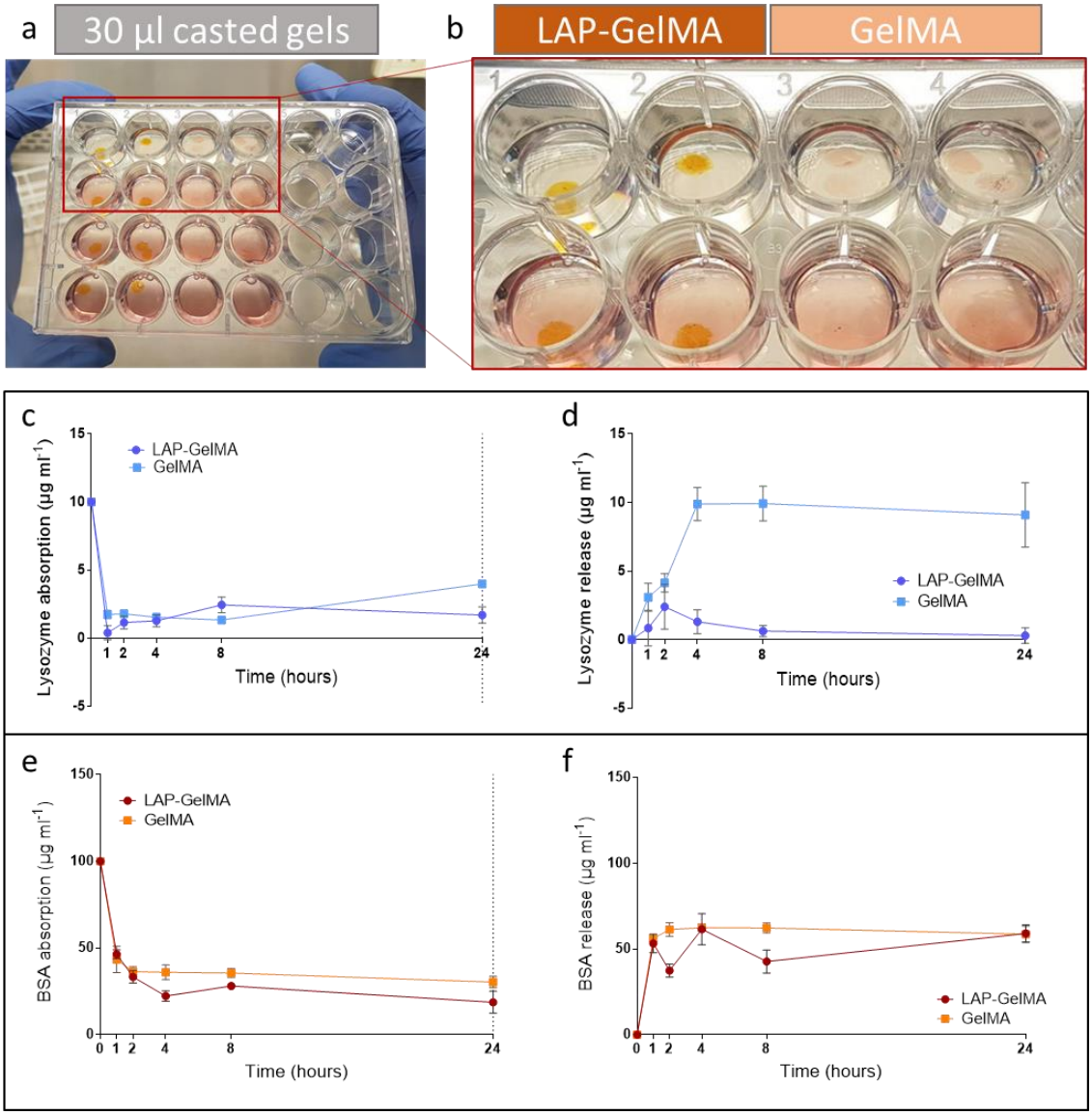

Figure 7.11. Lysozyme and BSA absorption and induced release from nanosilicate composite scaffolds.

30 µl casted gels (a) were fabricated and divided into groups (b) of LAP-GelMA and GelMA scaffolds. LAP-GelMA retained the photoinitiators compared to GelMA silicate-free. Proteins were absorbed onto scaffolds for 24 hours. Collagenase solution (1mg ml^{-1}) was used to simulate *in vivo* conditions of biomaterial degradation. Lysozyme absorption (c) and induced release (d) in LAP-GelMA and GelMA scaffolds show rapid absorption from LAP-GelMA and GelMA with a burst release of lysozyme from GelMA compared to the retained lysozyme in LAP-GelMA. BSA absorption (e) and release (f) from LAP-GelMA and GelMA. BSA resulted absorbed onto LAP-GelMA and GelMA with a similar trend. Release from GelMA was more rapid than LAP-GelMA to reach a similar release profile after 24 h.

LAP-GelMA released a smaller discrete amount after 2 hours (2.39 ± 1.63 µg ml^{-1}) compared to GelMA (4.14 ± 0.67 µg ml^{-1}) and significantly smaller amounts at 4 hours (1.297 ± 0.86 µg ml^{-1}) and up to 24 hours (0296 ± 0.568 µg ml^{-1}) showing drug localisation within the gel. BSA (100 µg ml^{-1}) absorption (Figure 7.11 e) displayed a similar profile to

lysozyme absorption, with an immediate absorption of the BSA in solution (LAP-GelMA: 46.42 ± 2.54 µg ml^{-1}, GelMA: 43.29 ± 7.59 µg ml^{-1}) up to saturation. LAP-GelMA showed higher absorption capacity (22.21 ± 3.01 µg ml^{-1}) than GelMA (35.94 ± 4.25 µg ml^{-1}) at 4 hours up to 24 hours of incubation (LAP-GelMA: 18.631 ± 6.39 µg ml^{-1}, GelMA: 30.30 ± 3.29 µg ml^{-1}).

Collagenase digestion (Figure 7.11 f) induced the rapid release of BSA from GelMA discs after only 2 hours (61.41 ± 3.95 µg ml^{-1}) of digestion. GelMA discs were maintained in collagenase for digestion and induction of BSA release up to 24 hours (58.66 ± 4.681 µg ml^{-1}). LAP-GelMA showed immediate release of BSA after 1 hour (53.25 ± 5.37 µg ml^{-1}) with a lower release after 2 hours (37.439 ± 3.81 µg ml^{-1}). 4 hours after collagenase inclusion, the digested gel started to release BSA (61.55 ± 9.05 µg ml^{-1}) up to 24 hours (59.05 ± 5.058 µg ml^{-1}).

7.3.5 Chicken chorioallantoic membrane model for implantation of LAP-GelMA 3D scaffolds demonstrated high vascularisation and sample integration

The CAM was used to investigate the ability of LAP-GelMA to retain pro-angiogenic factors and to stimulate vasculogenesis in comparison to silicate-free GelMA. Cylindrical scaffolds of LAP-GelMA (Appendix C Figure 7.3) and GelMA were produced and implanted in 10 day old developing chick eggs. LAP-GelMA-VEGF (Figure 7.12 a), GelMA-VEGF (Figure 7.12 b), LAP-GelMA (Figure 7.12 c) and GelMA (Figure 7.12 d) were implanted on to the CAM of a 10 day old developing chicken egg. After 7 days of incubation at 37°C, LAP-GelMA-VEGF (Figure 7.12 e), GelMA-VEGF (Figure 7.12 f), LAP-GelMA (Figure 7.12 g) and GelMA (Figure 7.12 h) resulted in demonstrable integration and vascularisation of the scaffold in situ with the CAM.

Integrated samples were isolated and imaged. LAP-GelMA-VEGF (Figure 7.13 a) showed elevated integration with the CAM vasculature (Figure 7.13 b) penetrating through the 3D construct. GelMA-VEGF (Figure 7.13 c) resulted in integration of the scaffold but demonstrated a lower degree of vascular penetration (Figure 7.13 d). Interestingly, LAP-GelMA VEGF-free (Figure 7.13 e) resulted in integration with chick chorioallantoic membrane with new vasculature covering the construct (Figure 7.13 f). GelMA (Figure 7.13 g) implant resulted in integration with the major vessels wrapped around the sample but penetration was not noted (Figure 7.13 h). Chalkley score (Figure 7.13 i) confirmed

significantly ($p<0.0001$) higher vascular penetration in VEGF-absorbed LAP-GelMA (13.75 ± 2.45) compared to GelMA-VEGF (7.66 ± 1.61), LAP-GelMA (9.66 ± 2.10) and GelMA (5.50 ± 1.56) samples. Addition of VEGF did not produce any significant differences when absorbed onto GelMA scaffolds compared to VEGF-free LAP-GelMA, but showed a non-significant difference ($p<0.05$) compared to VEGF-free GelMA.

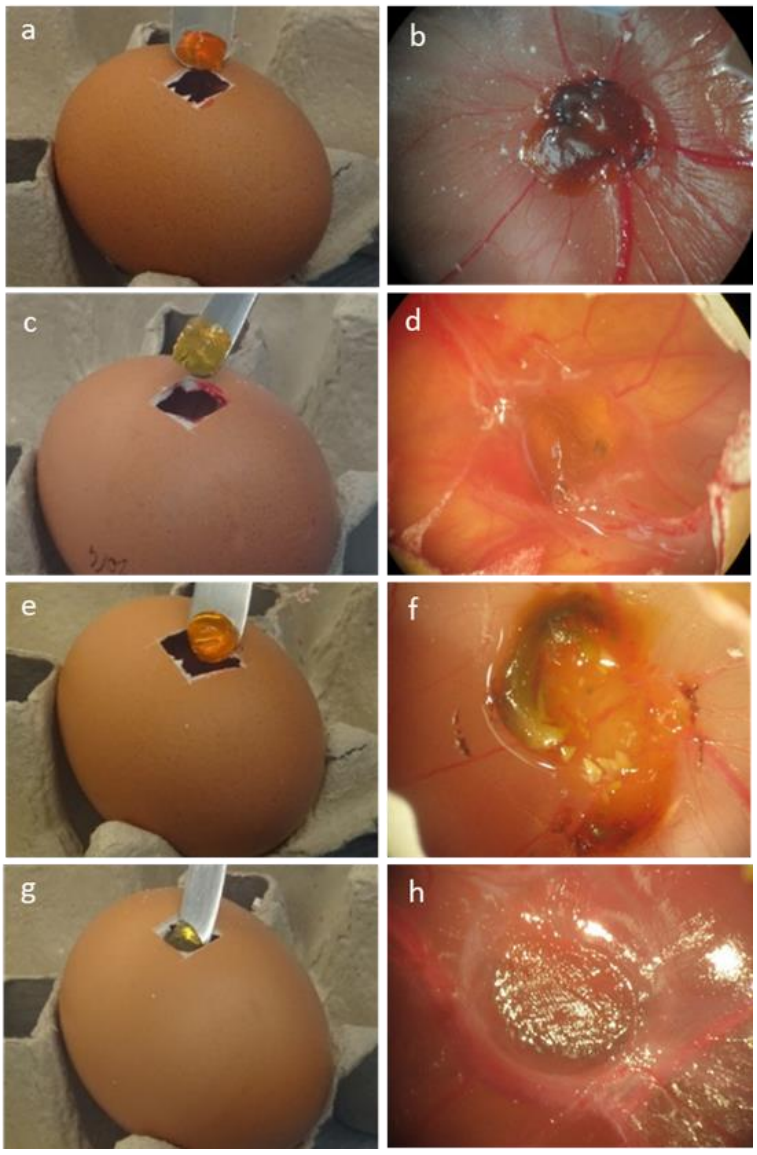

Figure 7.12. Chicken chorioallantoic membrane *ex vivo* model implantation of LAP-GelMA and GelMA 3D scaffolds.

Implantation of 3D scaffold was carried out through a window incision on the outer egg-shell to expose the chorioallantoic membrane. Macrographs of implantation of VEGF-LAP-GelMA, VEGF-GelMA, LAP-GelMA, and GelMA (a-d) confirmed reproducibility of the implantation. In situ macrographs of VEGF-LAP-GelMA, VEGF-GelMA, LAP-GelMA and GelMA (e-h) confirmed integration of all the scaffolds, with enhanced vascularisation in (e) VEGF-LAP-GelMA and (f) VEGF-GelMA as hypothesised.

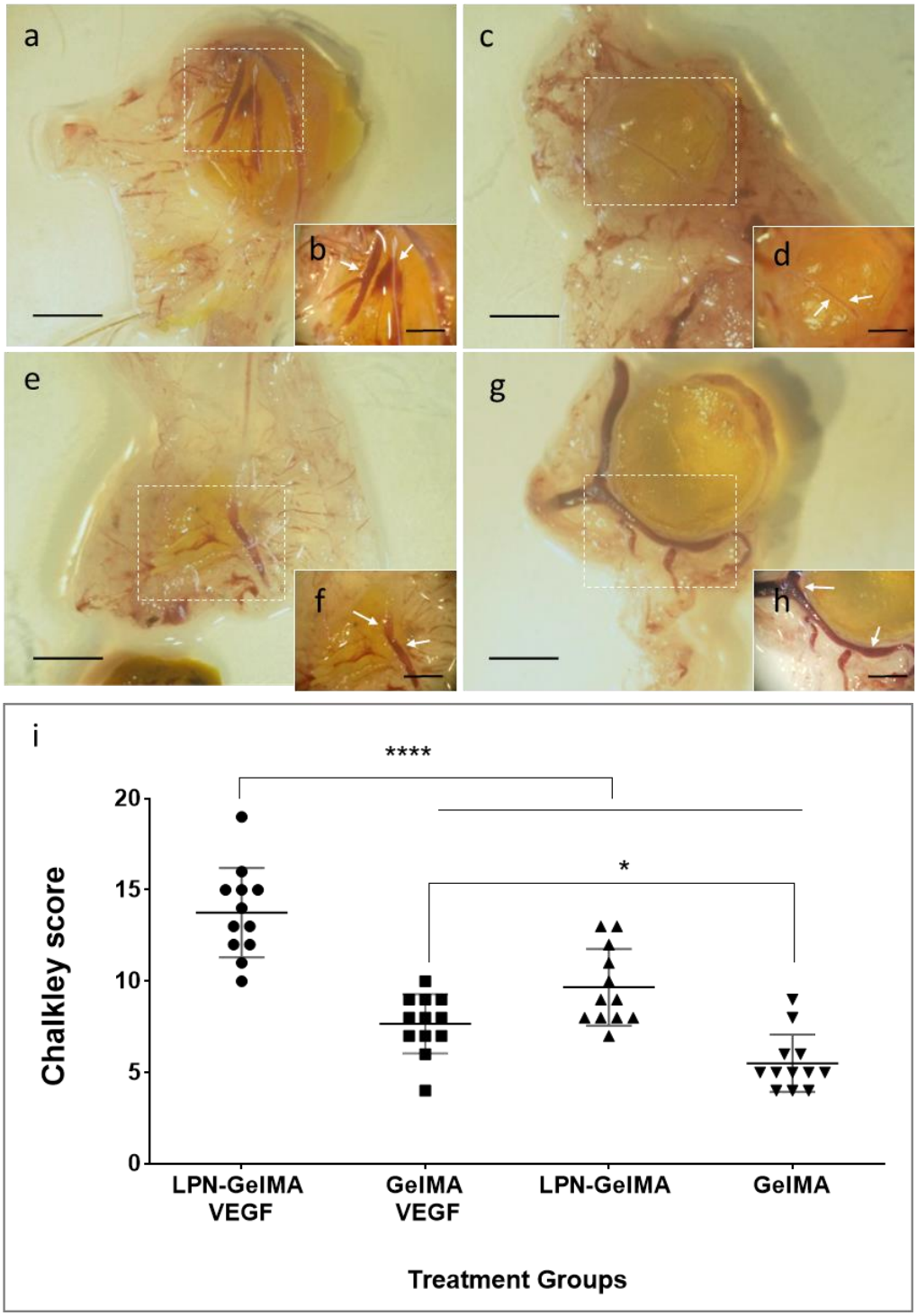

Figure 7.13. CAM scaffolds demonstrated vascular integration.

VEGF-absorbed LAP-GelMA 3D scaffolds (a) show integration with chorioallantoic membrane. Close-up macrographs (b) highlights intricate vasculature surrounding the sample. VEGF-GelMA scaffolds (c) resulted integrated and (d) highly vascularised. LAP-GelMA scaffolds (e) integrated well with surrounding tissue and (f) presented blood vessel penetration. GelMA 3D constructs (g) resulted in poorly penetrated but surrounding vasculature (h) with thick blood vessel circumnavigating the sample. Chalkley score (i) was perfomed with Chalkley grid and counting of afferent and penetrating blood vessels. Statistical significance assessed by one-way ANOVA followed by Tukey's multiple comparison tests. Mean ± S.D. n=12, *p<0.05, ****p<0.0001

Histological analysis (Figure 7.14) revealed that VEGF absorbed LAP-GelMA (Figure 7.14 I a-h) had a significant effect on CAM integration and vessel penetration within the 3D scaffold compared to VEGF absorbed GelMA (Figure 7.14 II a-h). In particular, LAP-GelMA - VEGF showed CAM integration around the sample perimeter (Figure 7.14 I a-f) with vessel adherence and infiltration (Figure 7.14 I g,h). GelMA discs absorbed in VEGF and implanted (Figure 7.14 II a-h) showed CAM integration (Figure 7.14 II a-d) with membrane tissue penetration and close proximity of blood vessels (Figure 7.14 II e-h) but with negligible indications of vessel penetration. LAP-GelMA controls (Figure 7.14 III a-h) showed major vessels proximity to the scaffold (Figure 7.14 III a-d) with clear integration with surrounding CAM and microporous internal structures depicting blood vessels penetration and integration (Figure 7.14 III g,h). GelMA controls (Figure 7.14 IV a-h) presented signs of CAM integration (Figure 7.14 IV a,b) and blood vessels proximal to the implant (Figure 7.14 IV c,d). Partial integration with the chick vascularised membrane was observed but with major separation gaps surrounding GelMA samples (Figure 7.14 IV e,f).

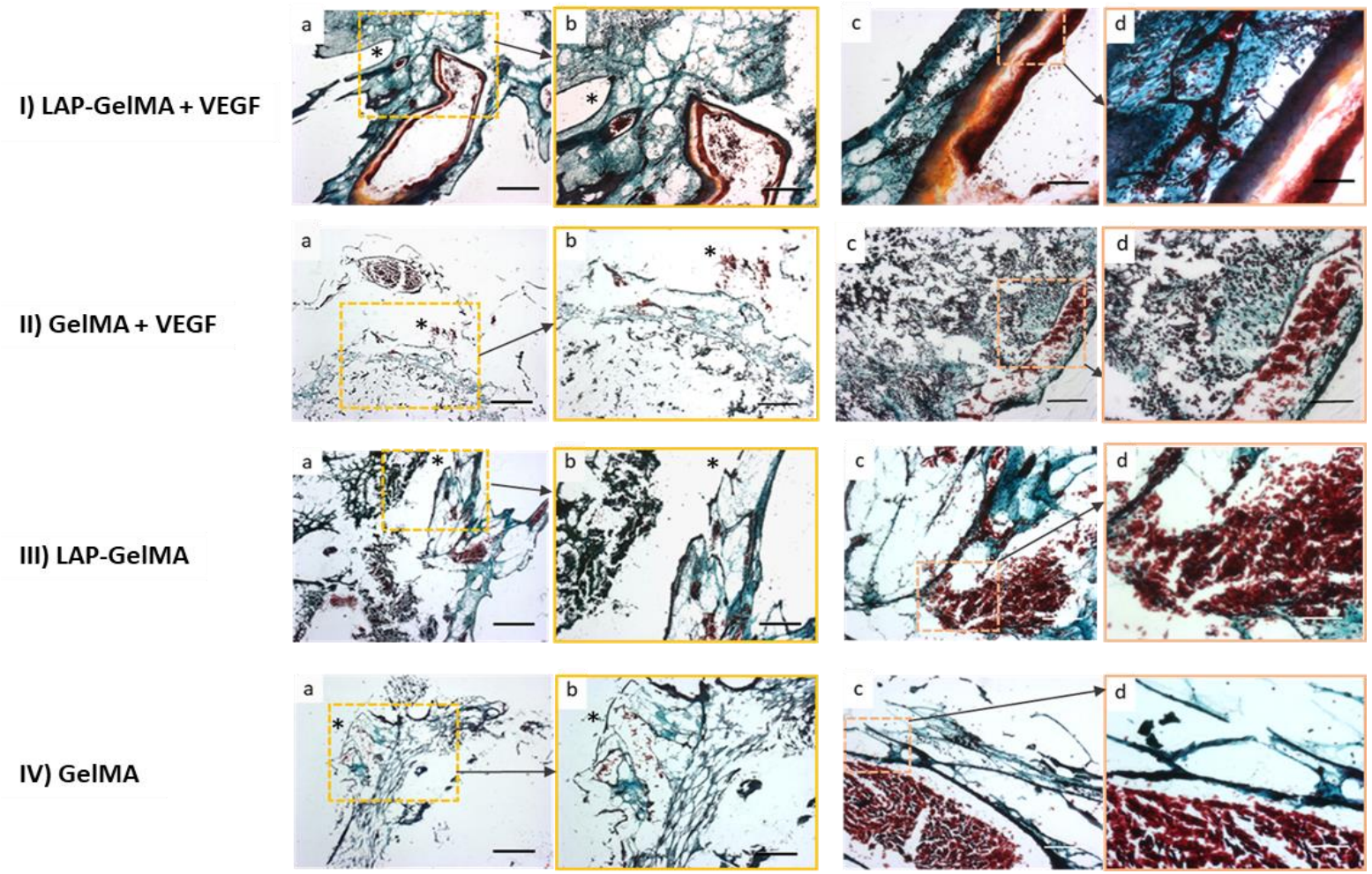

Figure 7.14. Histological analysis of VEGF-absorbed or free LAP-GelMA and GelMA in CAM model. Goldner's Trichrome staining showing erythrocytes in red, collagen in green. haematoxylin staining showing nuclei in black. I) LAP-GelMA scaffolds with VEGF (a,b) resulted in a high integration with the CAM vascularised (*) membrane. Orange photoinitiators were still entrapped within LAP-GelMA outer surface. (c,d) Major blood vessels (*) were found in proximity of the integrated scaffolds edges (dark black). II) GelMA scaffolds with VEGF (a,b) were found in proximity of major vessels (*). (c,d) GelMA scaffold porous structure (black) integrated with the vascularised (*) CAM membrane. III) LAP-GelMA scaffolds (a,b) were found integrated with the membrane (*). (c,d) Major blood vessels (*) were found in the vicinity of the LAP-GelMA scaffolds which was found still loaded with photoinitiators. Blood vessels were found in the outer proximity and even internalised in the scaffolds. IV) GelMA scaffolds (a,b) integrated with small (*) and large vessels closely found on the outside of the scaffolds. Close integration was evident in proximity of the vessels (c,d) and a small portion of the CAM. GelMA scaffolds showed a less compact structure (*) and integrated compared to VEGF absorbed samples. Scale bar: I) II) III) IV) a: 500 µm; I) II) III) IV) b: 250 µm I) II) III) IV) c: 100 µm I) II) III) IV) d: 50 µm

7.4 Discussion

Bioprinting seeks to achieve elevated cell viability and functionality post-printing, with the highest material shape fidelity after deposition [56]. Therefore, highly biocompatible and physically stable bioinks have to be engineered. Gelatin [289] is widely used in medical research as a matrix platform for drug delivery [290] and for tissue engineering [284] applications. However, the majority of approaches and compounds (e.g. glutaraldehyde [291,292]) results are disruptive and non-biocompatible. Chemical modification of gelatin is relatively simple and methacryloyl groups can be added to gelatin macromers to synthesize gelatin methacryloyl (GelMA) [284]. GelMA shows similar biological and physical properties to gelatin, resulting not printable if not in combination with other polymers (e.g. collagen [151], PEG [48], gellan gum [86,274]) but can be further crosslinked by UV irradiation upon inclusion of photoinitiators (e.g. Irgacure). Thus, 3D printing of GelMA hydrogels can be achieved by tailoring both temperature and post-printing light curing [90] approaches. However, UV light application is particularly toxic for encapsulated cells [293] and alterations in temperature can result in significant challenges in the control of fine fibre deposition [86]. To overcome UV dependent damages, Lim *et al.* [151] firstly reported the use of visible-light curable gelatin-based hydrogel networks with limited oxygen inhibition and able to sustain cell viability *in vitro*. However, temperature-dependent extrusion is still required to regulate GelMA deposition.

Laponite, a nanoparticulate material, offers the chance to regulate polymeric material rheological properties acting as a filler even at low concentration [95]. Previous studies on LAP-GelMA composites have shown beneficial integration of nanosilicate particles within GelMA matrices with elevated physical, chemical and biological properties. Xavier *et al.* [102] proved safety and efficacy of LAP-GelMA hydrogel mainly focusing in testing their stability and mechanical properties *in vitro*. Paul *et al.* [107] presented the potential of LAP-GelMA *in vitro* and *in vivo* for bone regeneration. These applications were carried out using UV light crosslinking. The use of a visible light crosslinking method provides the unique advantage of a mild crosslinking technology compared to ionic, chemical and UV crosslinking. Therefore, the visible-light curing system here reported, can be easily evaluated as biologically safe and potentially used constantly during printing application. For the first time it is here reported the accurate combination of Laponite and GelMA to produce a visible-light curable bioink with tailorable mechanical properties and increased shape retention after printing as well as biofunctionality, showing growth factors localisation and vasculogenesis stimulation in an *ex vivo* model.

In this study, nanosilicate incorporation within the GelMA network induced an uncontrolled gelation of the composite, leading to subsequent photoinitiators aggregation and poor gelation. Following a previously employed protocol [102], the inclusion of GelMA within nanosilicate dispersion led to a more homogeneous integration and final gel product. Photoinitiators [151] could be included easily in the mixture and crosslinking appeared similar to pure GelMA gelation. To ensure complete GelMA inclusion and a clear final suspension, LAP-GelMA was incubated overnight at 37°C. The resulting clear solution was then incorporated with 1:10 Ru/SPS photoinitiators. When placed in solution to evaluate gels stability, GelMA discs started swelling as reported before [151] releasing Ru/SPS in solution after 1 h of incubation. Nanosilicate inclusion altered this process, inducing a retention of the photoinitiators with a negligible release into the solution after 24 h of incubation. Given the proven [151] safety use of initiator concentrations between 0.2:2 and 2:20 mM ratio, 1:10 Ru/SPS was employed, resulting in a homogeneous and consistent crosslinking. Initial tests were carried out on several concentrations of LAP-GelMA to determine an optimal print composition. LAP-GelMA with a 1 % w/v Laponite and 7.5 % w/v GelMA was found to be ideal for printing. Printing performed at room temperature resulted in non-precise control of bioink gelation in the syringe barrel leading to extrusion of low resolution lattice structure. LAP-GelMA extruded and immediately cured by the light exposure, allowed deposition in a more accurate fashion compared to the free-flow deposition of LAP-GelMA without immediate curing method. Final constructs resulted significantly improved in their fidelity to the blueprint confirming this novel method as optimal for nanosilicate-based bioink [294].

The biocompatibility of LAP-GelMA was tested by the encapsulation of HBMSCs into discs shaped material compared to GelMA controls. HBMSCs cultured in GelMA discs were viable up to 21 days, with an initial rapid increase in number – as confirmed by cell density analysis – before decreasing in both number and viability by day 21. This phenomenon as shown before for soft gels [218] could be due to cells escaping from the soft GelMA discs and attaching to the cell culture well plate. In contrast, HBMSCs encapsulated in LAP-GelMA were found to preserve their viability and proliferate over time up to 21 days. Cell number did not appear to decrease proving the addition of silicate beneficial for encapsulated cell retention and viability preservation. HBMSCs resulted functional on LAP-GelMA films resulting stained with ALP after 1 day in culture. Similar results were reported by Xavier *et al.* [102] where an upregulation of ALP activity was found in a preosteoblast cell line after only 3 days of culture on LAP-GelMA gels. Interestingly, a nanosilicate dose-dependent ALP expression was illustrated, with higher concentrations of Laponite inducing an increase of ALP activity. In the study here presented, a small fraction in volume of Laponite (only 1 % w/v) induced a change in cell morphology, film integrity and ALP staining intensity over a period of 21 days. In basal and osteogenic conditioning,

HBMSCs on LAP-GelMA films preserved colony behaviour and fibroblastic appearance confirming active and functional cell differentiation *in vitro*. Interestingly, a circle pattern morphology for HBMSCs colonies seeded on LAP-GelMA and conditioned with osteogenic media was observed. This particular behaviour has not been reported before in literature, but was found extensively present in ostegenic conditioned LAP-GelMA samples. Possibly, as reported in literature [295] cells at the centre of the colony might undergo detatchment from the gel as the collagenase used in treating the previously plastic-adherent cells is still active.

The ability of Laponite to localise drugs of interest has been extensively investigated [103,105]. However, the potential of LAP-GelMA for drug delivery has not been reported before. Here, nanocomposite drug-entrapping properties were confirmed with an absorption/release study from LAP-GelMA discs. Lysozyme and BSA were used as model proteins for BMP-2 and VEGF respectively (as illustrated in Chapter 6 discussion). Absorption of drugs was preferred over loading, imitating classical clinical application of collagen sponges absorption with BMP-2 or to preserve short half-life (only 90 minutes [296]) of a potent angiogenic factor such as VEGF. Release was forcibly induced by enzymatic degradation mimicking *in vivo* conditions. Particularly, this study validated the greater absorption/retention capacity of silicate-based gels compared to silicate-free matrices. LAP-GelMA, similarly to GelMA, absorbed the lysozyme in solution (10 µg ml^{-1}) in only 1 hour. However, when release was induced by collagenase inclusion, GelMA released the entire absorbed compound in only 4 hours, suggesting a burst release of the cargo. In contrast, LAP-GelMA reached a negligible peak of release after 2 hours to then confirm the lysozyme retention within its matrix. BSA (100 µg ml^{-1}) absorption followed a trend line similar to lysozyme inclusion, but LAP-GelMA resulted absorbing a superior quantity compared to GelMA alone. Burst release of BSA from GelMA occurred in only 1 hour. LAP-GelMA reached a peak of release at 1 and 4 hours with a profile that confirmed retention of absorbed BSA within the hydrogel network. Results indicate that the absorption mechanism is mostly governed by GelMA swelling behaviour, with LAP-GelMA and GelMA presenting a similar absorption profile over 24 hours. However, Laponite inclusion resulted in limiting the release of lysozyme and BSA because of its strong interaction with the negatively (lysozyme) and positively (BSA) charged compounds.

Further effects for LAP-GelMA drug localisation potential was harnessed in samples loaded with VEGF to test the LAP-GelMA drug-retention hypothesis when implanted in a chicken chorioallantoic membrane model. The CAM model [297] has been widely used as an *ex vivo* assay for angiogenesis studies during early embryo development. As shown before in other chapters (Chapters 4 and 6) the implantation of 3D scaffolds was carried out in CAM model to test the hypothesis of a VEGF-absorbed construct able to induce vasculogenesis

and integrate with the chick membrane. Gels were allowed to absorb VEGF in solution for 2 hours in accordance with LAP-GelMA and GelMA similar absorption trend reported in the BSA absorption results. LAP-GelMA and GelMA with VEGF resulted integrated, as the VEGF-free controls. LAP-GelMA with VEGF resulted significantly integrated with chorioallantoic membrane, with several afferent blood vessels. Blood clots were found in proximity of LAP-GelMA with VEGF and drug-free control, suggesting a strong angiogenic potential. However, clots are to be avoided, therefore, a more careful evaluation of VEGF loading will need to be carried out to control VEGF concentration within the implanted gel. Particularly, LAP-GelMA with VEGF resulted significantly perfused by membrane vessels compared to GelMA – VEGF, indicating stronger retention ability of VEGF within LAP-GelMA polymeric structure. The effects of Laponite addition resulted in the LAP-GelMA control showing extensive inclusion with the chick membrane and blood vessel penetration. GelMA control integrated well with the CAM but negligible vessels were observed to directly penetrate the implant. From the histological analysis with Goldner's Trichrome, LAP-GelMA appeared to display potent angiogenic potential by retaining the majority of VEGF and stimulating extensive penetration of blood vessels and integration with CAM membrane. GelMA implants were surrounded by major vessels, but with limited penetration in the core of the discs due to the burst release of the angiogenic factor which could have dispersed into the surrounding tissue.

7.5 Conclusions

Nanosilicate composite bioinks present the ideal characteristics (such as viscoelastic and cell encapsulating properties) for skeletal biofabrication application. Laponite silicate has been blended with GelMA to create a novel visible-light curing composite formulation, limited in swelling, tuneable in viscoelastic properties, and in the ability to control spatially, bioactive molecule release. The addition of clay significantly improved printability and helped to retain shape fidelity after printing. Visible-light crosslinking improved high viability up to day 21 of culture *in vitro. Ex vivo* CAM model was used to investigate clay composite and silicate-free GelMA ability to stimulate angiogenesis and resulted in the integration with the chick vascularised membrane. VEGF was used as angiogenic factor to aid or increase angiogenic potential of test bioinks. Clay-GelMA scaffolds showed a greater angiogenic response with major blood vessel infiltration and membrane integration compared to controls as confirmed by histological analysis.

Laponite inclusion in GelMA network appeared to have a significant functional effect on angiogenesis. However, further *ex vivo* and *in vivo* evaluations are needed to consider this new blend as a skeletal regenerative platform. The high absorption/retention capacity and the retention of photoinitiators within the LAP-GelMA network is not ideal for the vision of clinical applications. However, significant improved viability, proliferation and functionality suggest that LAP-GelMA can function as an efficient bioink vehicle for the delivery of HBMSCs in three-dimensions. Further investigations will be needed to test safety and the efficacy of HBMSCs-laden LAP-GelMA in an *in vivo* environment.

However, altogether, these results showed the superior potential of Laponite-GelMA composite to sustain viability, proliferation, angiogenic factors localisation demonstrating functional properties for vascular bone repair.

Chapter 8 **General discussion**

8.1 Summary of the main study findings

The loss of bone tissue functionality, as a consequence of injury or disease, results in reduced quality of life at significant socio-economic cost worldwide [16]. Currently, tissue engineering approaches offer a promising solution but remain unable to address the unmet clinical need (e.g. large bone volume, architectural stability) to regenerate bone tissue [298]. Biofabrication is able to engineer tissues such as bone, producing 3D structures in an automated fashion by simultaneous extrusion of biomaterial hydrogels (called bioinks) encapsulating living cells. An ideal bioink should contain a low-polymeric fraction and shear upon pressure regaining its structure upon extrusion.

This PhD study aimed to investigate the use of a nanoclay and composite materials to engineer nanocomposite bioinks with low polymeric density and shear thinning properties to produce viable and functional 3D printed cell-laden constructs to support bone formation both *in vitro* and *in vivo*. Three main formulations of nanocomposites have been investigated in this thesis blending Laponite clay with popular bioinks such as alginate-methylcellulose (**Chapter 3**, **4** and **5**) gellan gum (**Chapter 6**) and GelMA (**Chapter 7**) to improve their printability and functionality.

The initial experiments in **Chapter 3** tested the hypothesis that *Laponite could be used to aid printability of a silicate-free natural bioink to produce viable cell-laden constructs in vitro.* Laponite was blended with alginate and methylcellulose and the viscous properties were tested to identify a printable nanocomposite bioink. The 3 % w/v Laponite, alginate and methylcellulose formulation (3-3-3) proved ideal for printing purposes. Large structures were produced via extrusion-deposition printing, generating self-supportive lattice structures with open pores, after crosslinking with $CaCl_2$ solution. Laponite homogenous inclusion was confirmed and swelling stability investigated over 21 days, demonstrating limited swelling of the 3-3-3 printed scaffolds. Cell-laden scaffolds were viable after 21 days proving that the Laponite-alginate-methylcellulose hydrogel could support cells *in vitro*.

Building on the work in Chapter 3, the studies in **Chapter 4** examined whether *3-3-3 bioink could be used to print SSCs in vitro and stimulate angiogenesis ex vivo by localising VEGF in lattice printed scaffolds.* Unselected and selected (Stro-1^+) populations of SSCs were encapsulated and printed in 3-3-3. Results showed the significant increase in proliferation up to 21 days *in vitro* for unselected and selected SSCs from two different patients. The encapsulation and printing of unselected SSCs from a single donor revealed excellent cell viability over 21 days and a significant difference in proliferation after 7 days. ALP and nodule formation confirmed the functionality of such an approach. Functionality

was further confirmed by micro-CT analysis which showed enhanced mineral deposition *in vitro* after 45 days. *Ex vivo* implantation in the chick chorioallantoic membrane model showed integration of the 10 × 10 mm^2 scaffolds of both acellular (compared to scaffolds of smaller or greater dimensions) and HUVECs-seeded – VEGF-loaded (compared to printed, VEGF-loaded and HUVECs-seeded) scaffolds. These results demonstrated the potential of the 3-3-3 hydrogel to encapsulate and deliver SSCs with bone formation and vasculogenesis observed following HUVECs and VEGF inclusion.

Chapter 5 examined the hypothesis *3-3-3 bioink could be used to 3D print scaffolds which could be loaded with BMP-2 or that included SSCs to aid bone tissue formation in vivo.* BMP-2 was absorbed prior to implantation onto printed and bulk scaffolds. Significant differences in bone volume and density were found after 4 weeks between printed scaffolds compared to bulk alginate gel, with and without BMP-2. Histological analysis confirmed mineralisation and bone tissue formation within the BMP-2-absorbed printed scaffold group compared to drug-free and bulk alginate loaded with BMP-2. A further *in vivo* study aimed to investigate the effect of SSCs-laden 3-3-3 printed compared to the bulk scaffolds implanted in athymic mice. Particularly, bone volume and density was found higher for SSCs-laden 3D printed scaffold group compared to bulk 3-3-3 with SSCs and the two control groups (3D printed and bulk without cells). After 8 weeks, histological analysis confirmed bone formation and vascular infiltration within SSCs-laden 3-3-3 printed scaffolds, suggesting an enhanced effect of SSCs inclusion compared to SSCs-free scaffolds and bulk scaffolds containing cells. The data demonstrated the potential of 3-3-3 printed in combination with BMP-2, to aid mineral deposition *in vivo*, and to be extruded with SSCs fabricating functional constructs evidenced by bone tissue *in vivo*.

In **Chapter 6** a novel technology for cell-printing in mild conditions and large scaffolds fabrication was introduced. A novel nanocomposite (gellan gum – Laponite), in combination with a fluid gel bed, was used to test the **hypothesis** that *Laponite could be used, when blended with GG, to print constructs in an agarose fluid gel bed that showed high shape fidelity, limited swelling, elevated viability in vitro and vascularisation ex vivo.* The addition of nanosilicate in gellan gum (LAP-GG) showed significant differences in swelling behaviour when compared to silicate-free GG. Inclusion of C2C12 cells within the bioink resulted in the fabrication of viable constructs *in vitro* up to 21 days both in LAP-GG and in GG alone. Cells resulted in highly functional in LAP-GG when constructs were cultured in osteogenic conditions with visible nodule formation at 21 days. The drug absorption capacity on nanocomposite gel was harnessed to load VEGF into scaffolds during printing by the dispersion of VEGF into agarose fluid gel bed. LAP-GG and GG were subsequently implanted into the CAM model, where vessels were found to be greatly afferent to LAP-GG loaded with VEGF compared to GG-VEGF and drug-free controls. The novel printing

technology aided by Laponite inclusion, generated viable and functional structures with elevated printing fidelity, aided by the limited swelling behaviour in agarose of the clay-based bioink and with the potential to retain drugs for the localisation and stimulation of angiogenesis *ex vivo.*

Clay functional properties were finally harnessed in **Chapter 7** to test the **hypothesis** that *Laponite and gelatin methacryloyl (GelMA) could be blended and crosslinked with a visible-light, printing acellular strands in mild conditions, sustaining HBMSCs viability, proliferation and functionality, localising drugs of interest and retaining VEGF ex vivo stimulating vasculogenesis and integration in a CAM vascularised membrane.* Inclusion of Laponite in the GelMA network allowed preparation of a novel bioink that could be printed in air, with high shape fidelity, even at a low polymeric content. The use of a continuous crosslinking visible light showed a significant difference in printing fidelity when compared with a lattice printed and crosslinked with visible light at the end of the printing process. HBMSCs included in the blend remained viable up to 21 days *in vitro*. LAP-GelMA displayed a capacity for drug localisation and retention. This property was used to localise VEGF in LAP-GelMA discs and stimulate integration and angiogenesis *ex vivo* in a CAM model. The outcomes demonstrate the advantage of Laponite inclusion in a GelMA bioink, aiding printability, cell and drug retention, cell viability and functionality and stimulating angiogenesis *ex vivo.*

8.2 Relevance of the study findings, limitations and future opportunities

The work here presented indicates that the addition of a clay nanomaterial such as Laponite, can revolutionise bioinks behaviour and functionality *in vitro* and *in vivo* [56]. The inert and hard ceramic or thermoplastic material that is commonly printed for skeletal biofabrication purposes [234,294], is now a functional soft ink [299] that can be loaded with SSCs, aiming for the fabrication of a complex microenvironment resembling the bone tissue. Several bioinks have been produced and illustrated in this thesis, focused on a single application (bone tissue engineering) but with clear advantages and disadvantages that can be employed in specific clinical circumstances. This last feature is pivotal for the ultimate translation of the clay-based biofabrication for the treatment of bone loss and repair.

Laponite-alginate-methylcellulose (3-3-3) blend produced a robust, scalable, reliable bioink for bone printing. The 3-3-3 bioink could be printed with a common air-pressure (**Chapter**

3) or a piston (**Chapter 4** and **5**) driven extrusion printer. High shape fidelity printing was achieved even at a low polymeric content (total of 9 % w/v) resulting an ideal bioink for cell printing and cell-laden implant fabrication [65]. The 3-3-3 bioink could be printed with great fidelity to the blueprint and result highly functional *in vitro*. Scaffolds conditioned with VEGF and HUVECs could stimulate angiogenesis in CAM model. Vascularisation is rarely achieved in bone tissue engineering, and have shown to be crucial for bone tissue growth and repair [160]. Currently, proposed bioink formulations are prepared with an elevated polymeric content (e.g. 13 % [138], 14 % [216] 10-20 % [89], 20 % [300] w/v) resulting in significant constraint for encapsulated cells. Particularly, SSC-laden scaffolds implanted *in vivo* were found to actively produce bone tissue *de novo* with a larger volume than controls. A volume and density as large as the SSC-laden printed scaffolds generated offer the potential for large bone defect repair. However, the complexity of the nanocomposite blend and the unclear mechanism of interaction of Laponite nanodiscs with alginate and methylcellulose remain **limitations** of this bioink system to be resolved. Moreover, clear efficacy of ostegenic and angiogenic 3-3-3 scaffolds have been reported in this thesis, but safety is to be evaluated by further repetition of *in vivo* investigations and by the use of larger animal models as a real pre-clinical assessment.

Compared to the bioinks listed in this thesis, 3-3-3 results highly mechanically stable when printed in air able to generate open porosity in the vertical alignment. Moreover, this bioink system has been fully investigate *in vitro, ex vivo* and *in vivo*, resulting exhaustively characterised with clear advantages in functionality over LAP-GG/agarose and LAP-GelMA systems.

The LAP-GG bioink presented in **Chapter 6** has been developed to print cell-laden structure in an agarose supporting gel. Free-form printing is adding a further supporting structure to preserve shape fidelity of the print and allow crosslinking avoiding morphological distorsion of the final construct. Agarose affords advantages for i) building large structures (as the 3D sleeve) with the soft LAP-GG bioink with the possibility of printing living cells, and ii) loading drugs of interest during printing. Therefore, free-form printing results are advantageous for the possible clinical application towards the fabrication of a larger functional construct for bone repair. A central clinical approach in stimulating bone growth for major defects consists in the rapid absorption or loading of BMP using absorbable collagen sponges (ACS) [301]. However, the short half-life of BMP-2 (only 15 min [230]), can hinder the use in a clinical scenario [110,302]. Therefore, the ability to produce an implantable construct loaded during fabrication with a desired factor is attractive. However, the lack of studies on the physico-chemical properties LAP-GG, the absence of results using SSCs post-printing and the need for further *in vivo* investigation, are **limitations** still to be resolved.

LAP-GG can be extruded in a supportive gel bed. 3-3-3 and LAP-GelMA has never attempted to be extruded in a supporting gel but will result high in viscosity therefore leaving a disadvantage in printing resolution, but generating structure that can be more stable than LAP-GG. Clear advantage of LAP-GG and agarose free-form printing is the possibility to extrude larger structure compared to the other clay-based bioinks. However, this bioink system is still at its infancy, with limited functional investigation and pre-clinical translation, and will require further studies to validate its safety and the efficacy.

A promising bioink platform with exciting biofabrication and clinical applications is the LAP-GelMA bioink reported in **Chapter 7**. Recent advancements in polymer chemistry led to the fabrication of light-activated polymers [303] such as GelMA, that result particularly appealing for the repair of bone tissue in clinical scenario. Laponite addition in a GelMA hydrogel, even at low concentrations (only 1 % w/v) enhanced print shape fidelity and drug localisation. The use of a visible-light crosslinking technology offered the unparalleled opportunity to 3D print implants during crosslinking of the three-dimensional structure. This solution, in combination with Laponite addition, enhanced printability together with cell viability. Light-curing bioinks are popular among the plethora of bioinks currently available, given their optimal crosslinking degree and versatility [86,260,304,305]. However, UV-light is widely used to strengthen scaffolds post printing, typically affecting cell viability [293]. Overcoming this major issue, the LAP-GelMA bioink was found to modulate bone differentiation in SSCs and vasculogenesis in CAM model. The system offers additional opportunities to aid simultaneous osteogenesis and vasculogenesis for bone repair via endochondral ossification, with a clear advantage over standard avascular implants. **Limitation** for the use of the visible-light clay bioink is the sensitivity of the crosslinking system (that can be triggered by the ambient light exposure). Moreover, the low mechanical stability *in vitro* will need to be improved further to sustain *in vivo* implantation and bone formation.

LAP-GelMA results more versatile than the other bioink system here presented given the easy synthesis and functionalisation. This bioink and light-curable printing system can be adapted to print complex structure in a clinical scenario and further improve the mechanical properties in situ or while printing thanks to normal visible light. However, compared to the 3-3-3, LAP-GelMA bioink require further development and characterisation regarding its translation *in vivo.* Moreover, compared to LAP-GG/agarose systems, LAP-GelMA ultimately results limited in printing dimension and GFs loading which can be pivotal in clinical applications for bone regeneration.

The investigation of a plethora of clay-based bioinks for bone regeneration has produced a series of approaches for the production of skeletal tissue *in vitro* and *in vivo*. However, there are some common **limitations** with the use of clay-based bioinks.

i) Laponite has been widely investigated for its **absorption abilities** [306] (e.g. Laponite used as absorbant for large metal ions such as Ni(II) from aqueous solutions [307]). The Laponite nanodiscs positive and negative charges allow the entrapment of different molecules and compounds, and the specific localisation of these in the interlamellar space or at the solution/clay interface [308]. This sorptive capacity, typical for clay materials, has been proposed to catalyse the polymerisation of RNA, facilitate the formation of fatty-acid vesicles and provide protection for nucleic acids otherwise digested by enzymes at the dawn of life on Earth [309]. However, nanoclays are particularly efficient in the uptake and consequent entrapment of small molecules, presenting challenges in for example staining evaluation and gene expression analysis. Localisation of growth factors within an implantable hydrogel network can aid the regenerative processes [310]. However, the temporal release of these factors are essential for bone tissue regeneration as demonstrated by the bone remodelling mechanism where a series of growth factors (e.g. BMPs, fibroblast growth factor 23 (FGF 23), transforming growth factor beta (TGF-β), etc.) play an active role, at specific time points, in the repair process [2]. Laponite gels have been shown to be limited in the release of absorbed compounds after inclusion in aqueous media [103,311]. Nevertheless, the release of active agents from Laponite can be tailored by the addition of polymers [111,126,132] or by the use of loaded Laponite materials as a nanoparticle delivery system [103,311]. In this thesis, several polymers were mixed with Laponite and the delivery efficacy of drugs was tested *in vitro* and assessed *ex vivo*, but not explored *in vivo* and remain areas for further work.

ii) Implants appropriate for the repair of bone tissue need to be **mechanically competent** [13]. 3D printed scaffolds can be fabricated to match critical-size defects in bones. However, biofabrication approaches have yet to produce robust printed mechanically competent scaffolds for the repair of large fractures in load-bearing bones. The approach in this thesis has sought to address this by the inclusion of SSCs as active building blocks for a functional bone repair. It is still unclear whether the addition of SSCs alone in printed scaffolds is beneficial for bone regeneration, although, *in vivo* results presented in chapter 5 (3-3-3), indicate the superior advantage of SSC-laden 3D printed constructs over cell-free implants. Additional studies will be needed to investigate the potential of 3-3-3 scaffolds for the repair of large defects and the ability of the other bioink systems (LAP-GG and LAP-GelMA) to generate mineralised tissue *in vivo*.

iii) Skeletal biofabrication is a growing field that aims to aid clinical repair of damaged or missing bone tissue. Currently, biofabrication is evolving towards a more complex approach

to produce intricate **multi-material scaffolds**. SSC-laden scaffolds were produced and the bone formation potential was mainly evaluated *in vitro*. However, in an *in vivo* scenario the printed implant should provide not only support for the encapsulated cells, but also drive integration across the bone defect. Biofabrication platforms provide the possibility to deposit multiple materials with precision. Particularly, thermoplastic [85] or ceramic [81] materials have proved useful for providing mechanical stability to soft hydrogels. Nanocomposite bioinks (such as 3-3-3) provide enhanced mechanical properties compared to hydrogels with similar polymer content, but still remain far from ideal in terms of mechanical competence required in bone. For the repair of a large bone defects, a further supporting scaffold structure will be needed to sustain the load and retain in place of the printed bioink with SSCs that will deposit new bone tissue bridging the fracture gap.

Future work could include:

(I) Investigation of the use of clays as a reinforcing agent for polymeric materials (e.g. reinforced 3-3-3 lattice) that can be printed as support for multi-layered structures comprising a SSC-laden bioink system (e.g. gellan gum, GelMA, etc.), aiding further functionality to the implant. This would remove the need to print inert thermoplastic materials, and generate an active implant;

(II) Development of novel free-form printing approaches by using Laponite as a fluid gel bed;

(III) Implementation of the use of a visible-light crosslinking system for *in vivo* applications with the printing of cellular components (e.g. SSCs and HUVECs) for bone and vasculature development.

Parallel to the technological advances of biofabrication, bioinks development is moving towards the goal of using tissue-specific and derived ECM hydrogels that can be prepared from the patient's own tissue [312]. As the advancements in the decellularisation of whole-organs develop, new bioink formulations can be prepared to encapsulate stem cells. This can be conceived instead of the current gold standard of total hip arthroplasty Now, approaches could include the use of ECM gels (Chapter 2, 2.2.5 (page 45) , Figure 8.1) generated from the femoral head together with SSCs, fabricated to personal specification with the help of a desktop bioprinter – such an approach is currently under development as part of my EPSRC fellowship from autumn 2018 using bovine demineralised bone matrix (bDBM, reported in Chapter 2 (2.3.4 page 48) and illustrated in

Figure 8.2) and printing of the Laponite-bone ECM-alginate bioink with the aim to generate bone tissue both *in vitro* and *in vivo*.

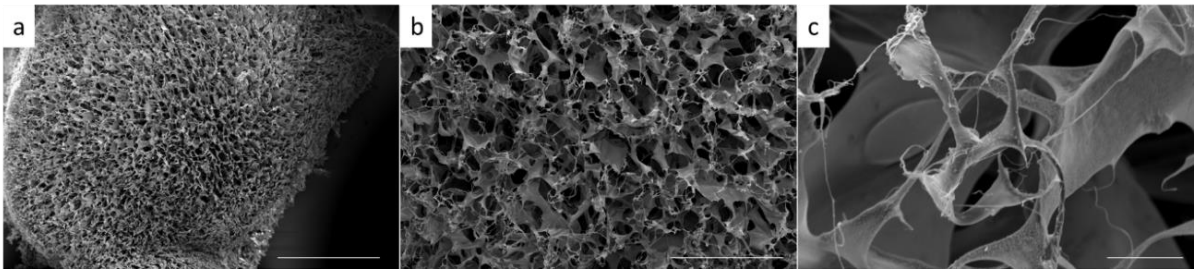

Figure 8.1. SEM of bone ECM.

Bone ECM freeze-dried and images on SEM (FEI Quanta 250) showing macroscopic appearance and resemblance with a trabecular structure (a) with open (b) and interconnected pores (c) throughout the entire bone ECM scaffold. Scale bar: (a) 1 mm, (b) 300 µm (c) 10 µm. Methodology is reported in Chapter 2 (2.4.5.3).

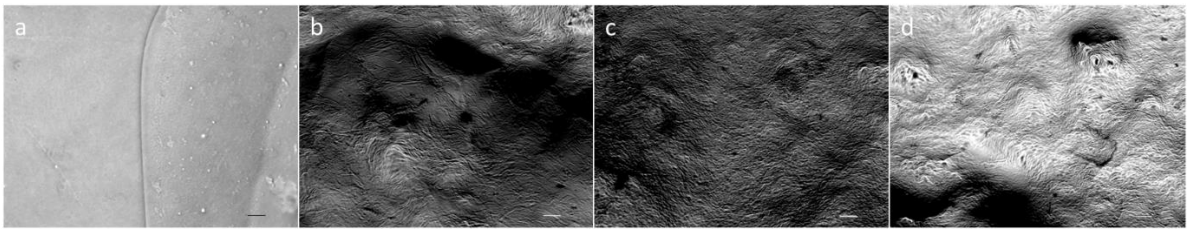

Figure 8.2. Brightfield phase contrast images of bDBM blends.

Bone demineralized bone matrix (bDBM) (a), Laponite 2 % - alginate 1% – bDBM (b), Laponite 2.5 % - alginate 1% – bDBM (c), Laponite 3 % - alginate 1% – bDBM (d) composites. Scale bar: (a-d) 200 µm.

The fabrication of functional but complex tissues and organs, still remains a considerable challenge [33], despite the recent advances in the field [35,165,234]. Clinical translation of the biofabrication rationale, is unlikely to depend only on FDA approved materials (e.g. alginate) blended with the autologous stem cells, but will need to consider the printing of a living bone implants [33]. Particularly, the inclusion of SSCs within printed constructs will potentially generate viable constructs of superior functionality compared to current inert and non-degradable metal implants. However, the ideal source of cells still needs to be identified. Encapsulation in select bioinks will be essential for SSCs viability and functionality before and after implantation. Clay inclusion could be used to aid physical support to the ECM bioink, which would otherwise collapse if not crosslinked post-printing. Thus bioinks prepared from decellularised and demineralised bone tissue (bone ECM) warrant further examination.

8.3 Conclusions

The current studies show, for the first time, Laponite as a functional component of a library of bioinks to generate bone tissue both *in vitro* and *in vivo*. 3-3-3 bioink (Figure 8.3 a) functioned as a robust bioink for SSCs printing and bone formation, showing for the first time *in vivo*, the superior ossification capacity of SSC-laden printed scaffolds compared to bulk controls. The LAP-GG bioink (Figure 8.3 b) showed enhanced printability, viability and functionality than silicate-free GG, with the generation of complex and large three-dimensional structures with the aid of the agarose fluid gel support. LAP-GelMA (Figure 8.3 c), used as bioink for printing or as hydrogel matrix for SSCs encapsulation, demonstrated a therapeutic potential for bone and vascular tissue engineering for the functional results obtained from SSCs differentiation and vascular integration in an *ex vivo* model.

These studies indicate the advantages of clay-based bioinks that are capable of encapsulating and printing SSCs, generating viable constructs for skeletal biofabrication with implications therein for repair of bone defects in an increasing ageing population.

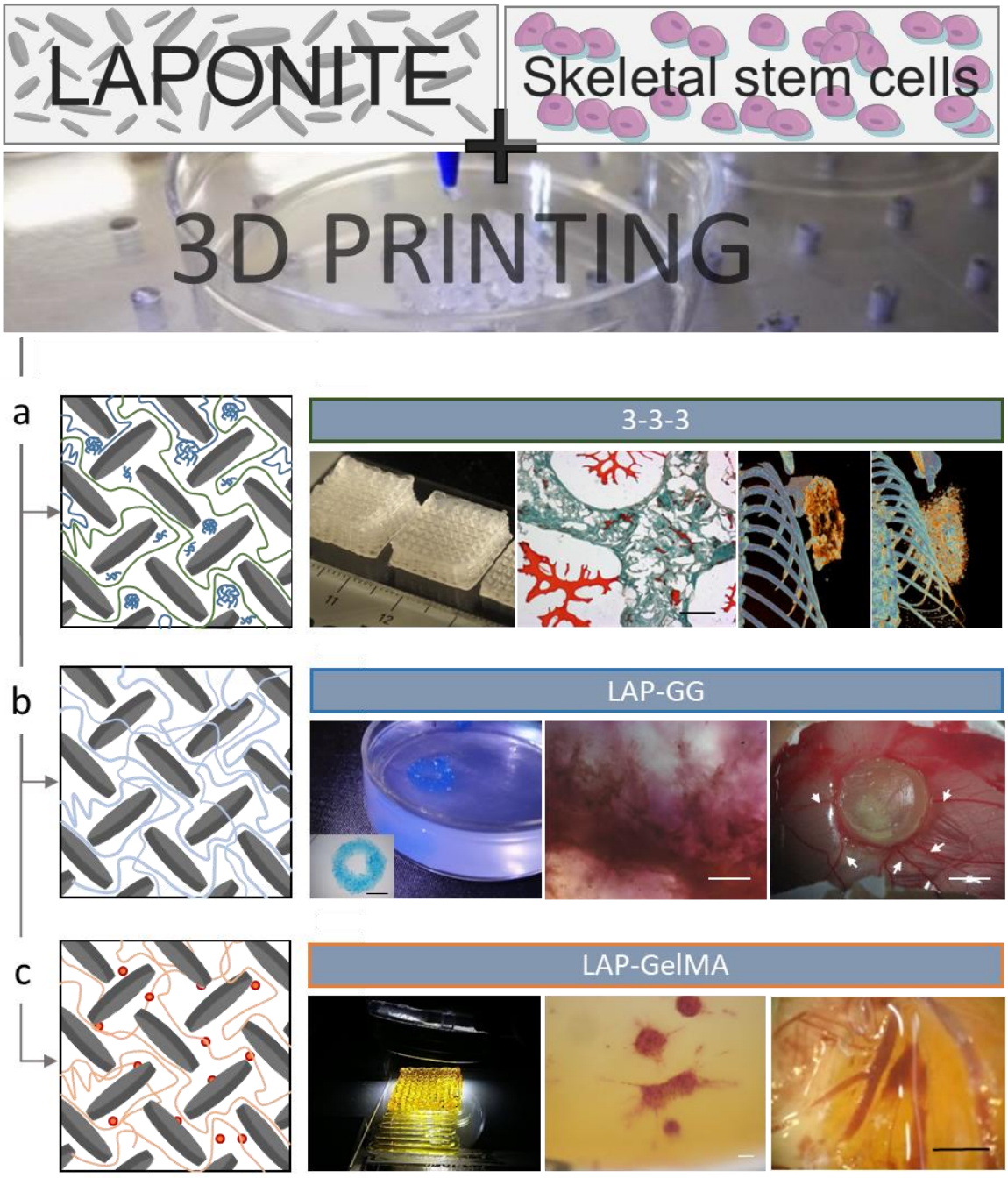

Figure 8.3. Graphical summary of the impact of the thesis.

Laponite and skeletal stem cells have been used to fabricate with a custom-made 3D printer, viable and functional constructs. Several novel bioinks were implemented such as (a) 3-3-3, (b) LAP-GG and (c) LAP-GelMA. Implants fabricated with these bioinks were finally proven viable and functional using SSCs or cell lines *in vitro*, *ex vivo* and for the 3-3-3 even *in vivo.*

Appendix A LabVIEW GUI

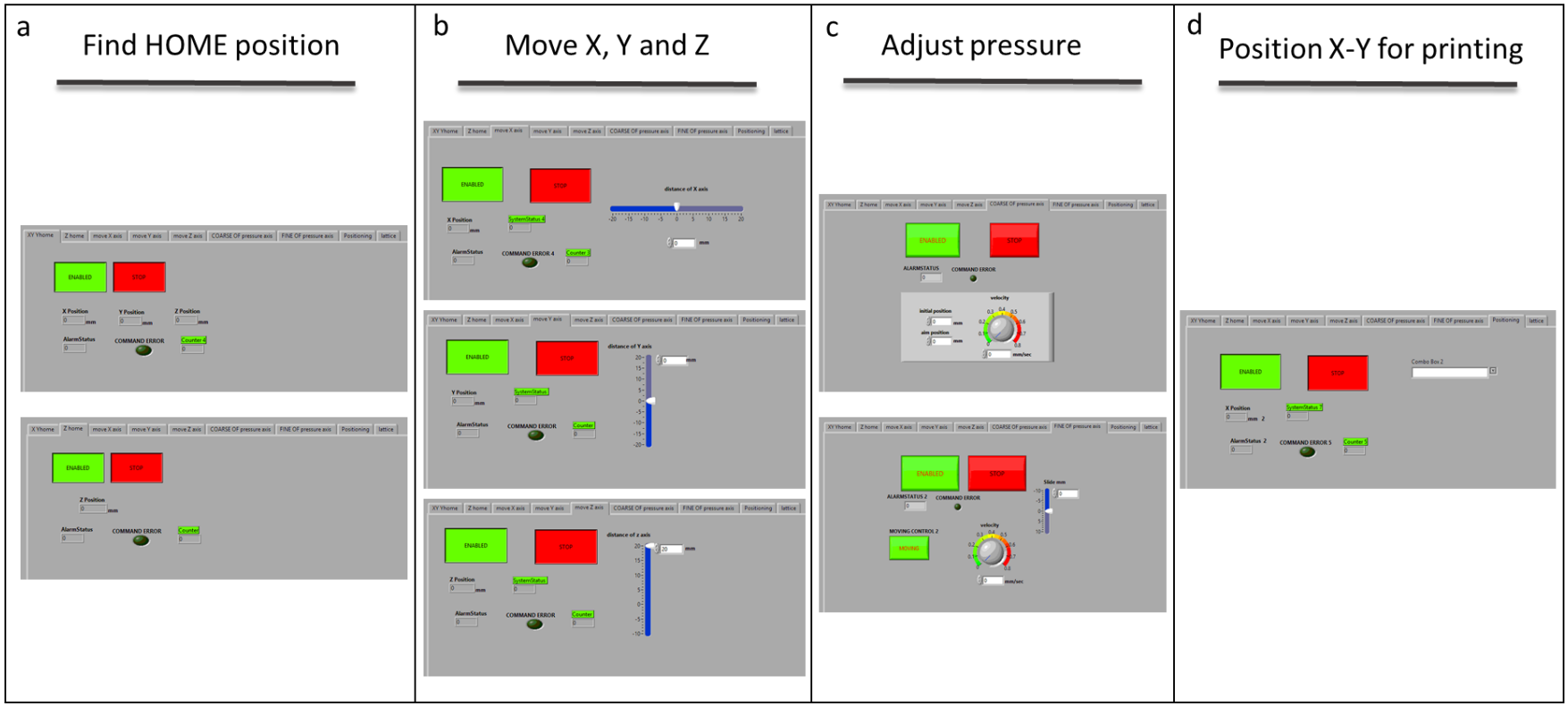

Appendix A Figure 2.1.LabVIEW GUI panel. The panel where the user can provide basic input for the printer is divided into 4 portions. The HOME tabs (a) are used to find X-Y table home position and Z axis starting position. The MOVE tabs (b) are used for moving the printing bed on × and Y positions and move the Z axis to find the optimal settings. The PRESSURE tabs (c) are for the pressure to be adjusted (move forward or retract) with a coarse or fine movement. The POSITIONING tab (d) is for the X-Y table to find a specific location in the space where the user wants to print. Final GUI (lattice) is reported in Figure 2.6.

Appendix B 6K4 AND LABVIEW PROGRAMMING CODE

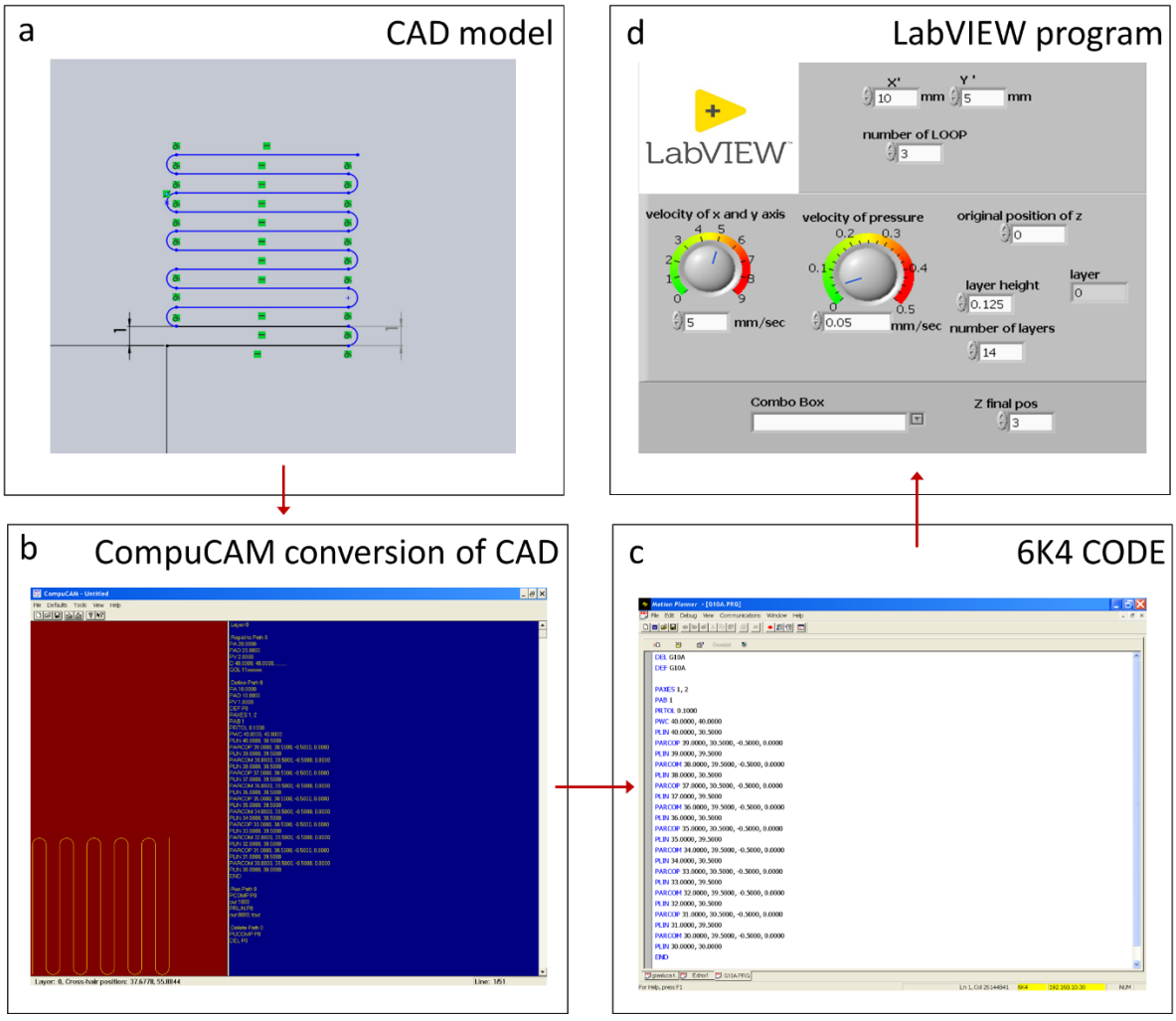

Appendix B Figure 2.2. Printing workflow.

To produce a code that can be translated into a scaffold, a CAD model (a) needs to be design. A single layer of the 3D blueprint is then imported in CompuCAM (b) and translated in 6K4 language which is imported in the Motion Planner (c) control panel. The code is then adjusted and translated to a LabVIEW (d) program that is able to interface with the user by simple commands.

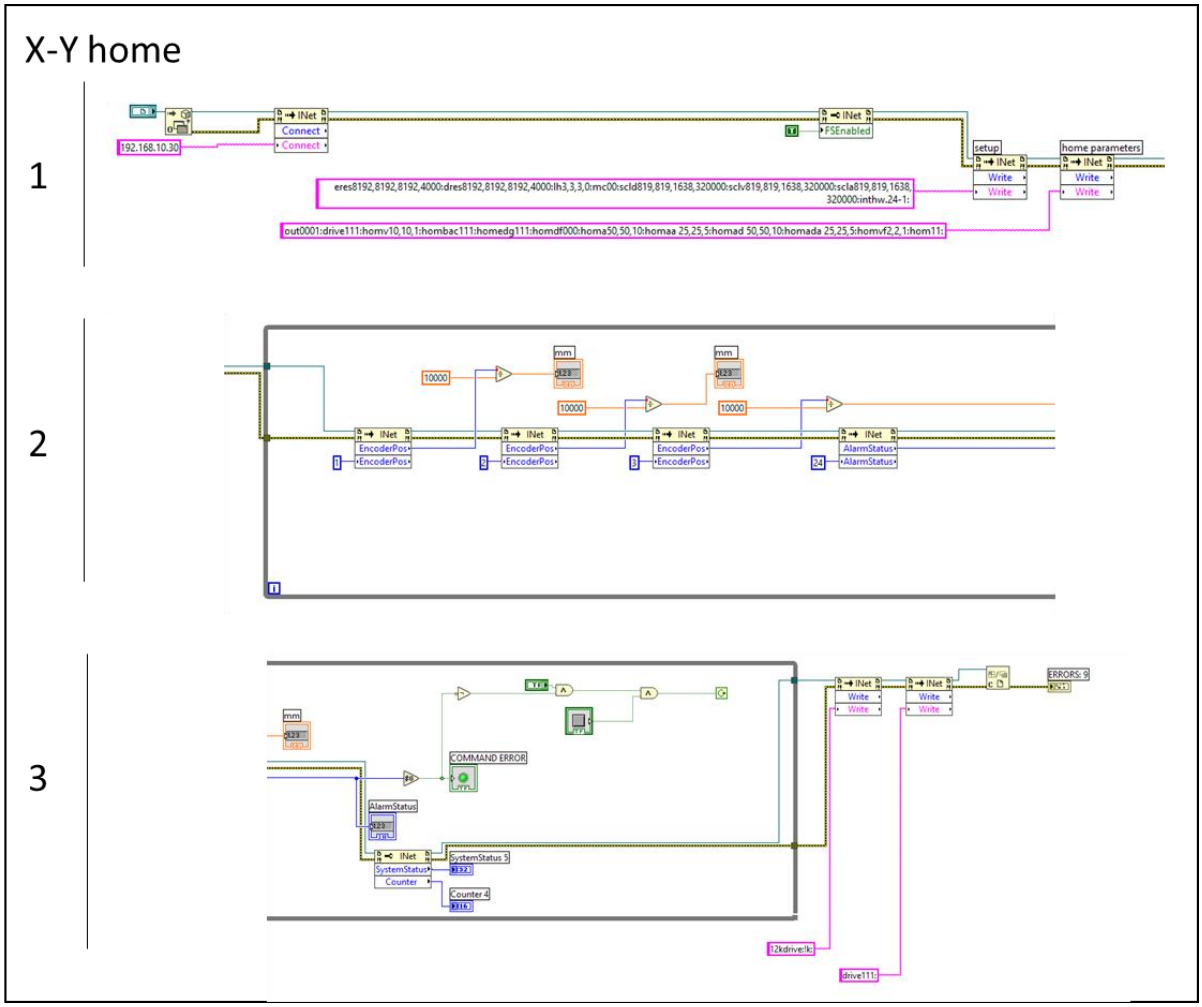

Appendix B Figure 2.3. X-Y home code.

This code stored in the block diagram of the LabVIEW program allows to position the printing bed to its home position before starting printing.

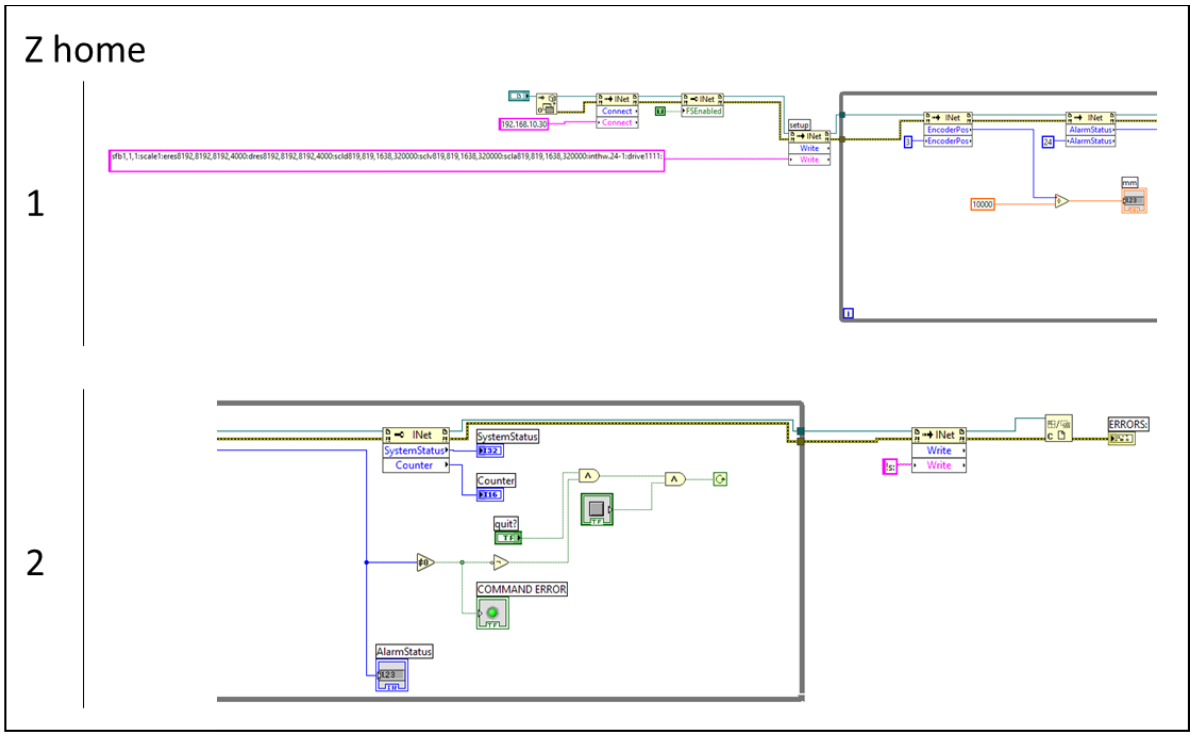

Appendix B Figure 2.4. Z home code.

This code stored in the block diagram of the LabVIEW program guide the Z arm to its home position before printing. This position can be used also to load the syringe in the holder.

Appendix B

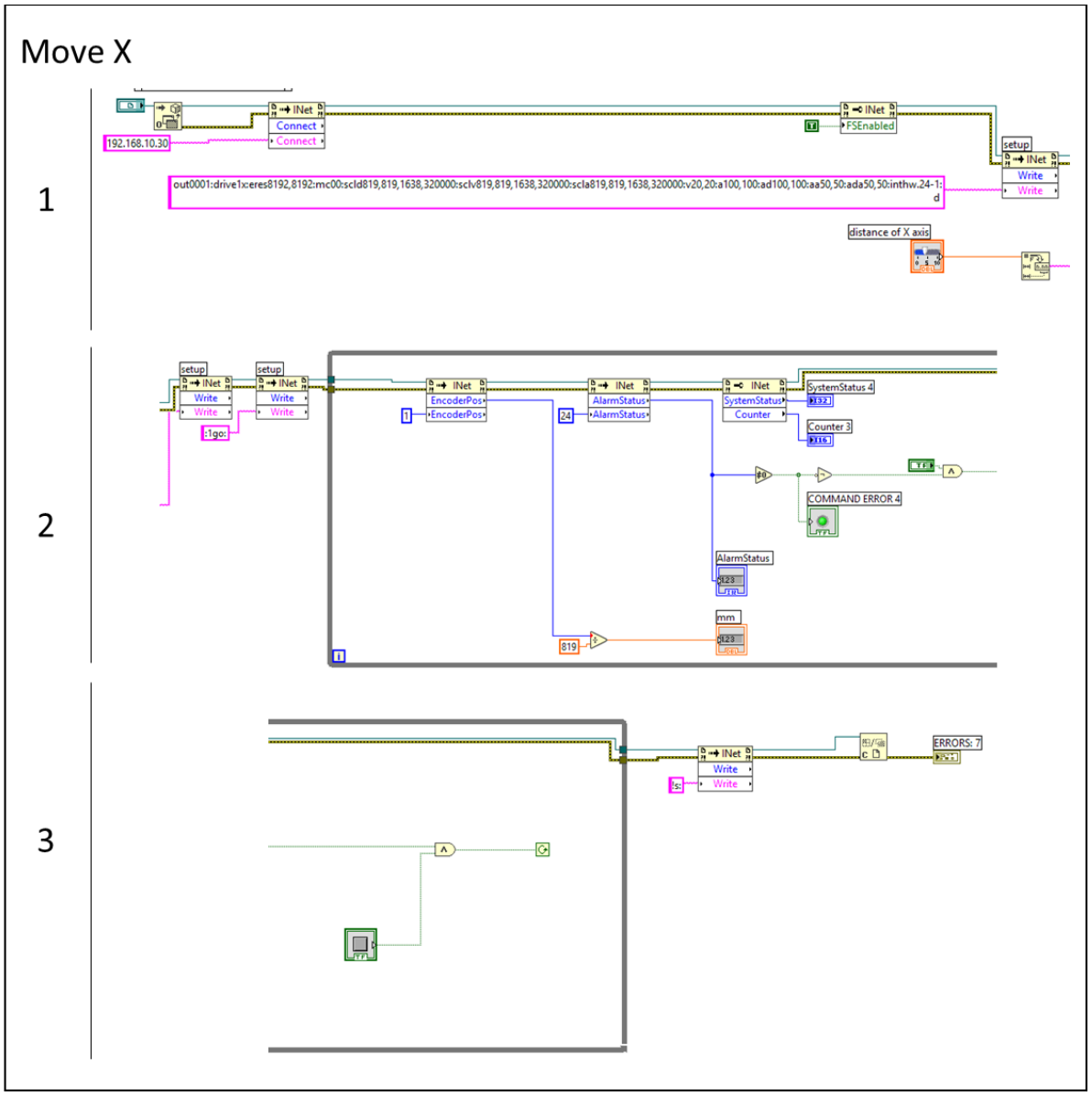

Appendix B Figure 2.5. Move × code.

This code stored in the block diagram of the LabVIEW program is used to move the printing bed along the × axis. The printing platform can be tuned to a positive and negative position to adjust the initial printing position.

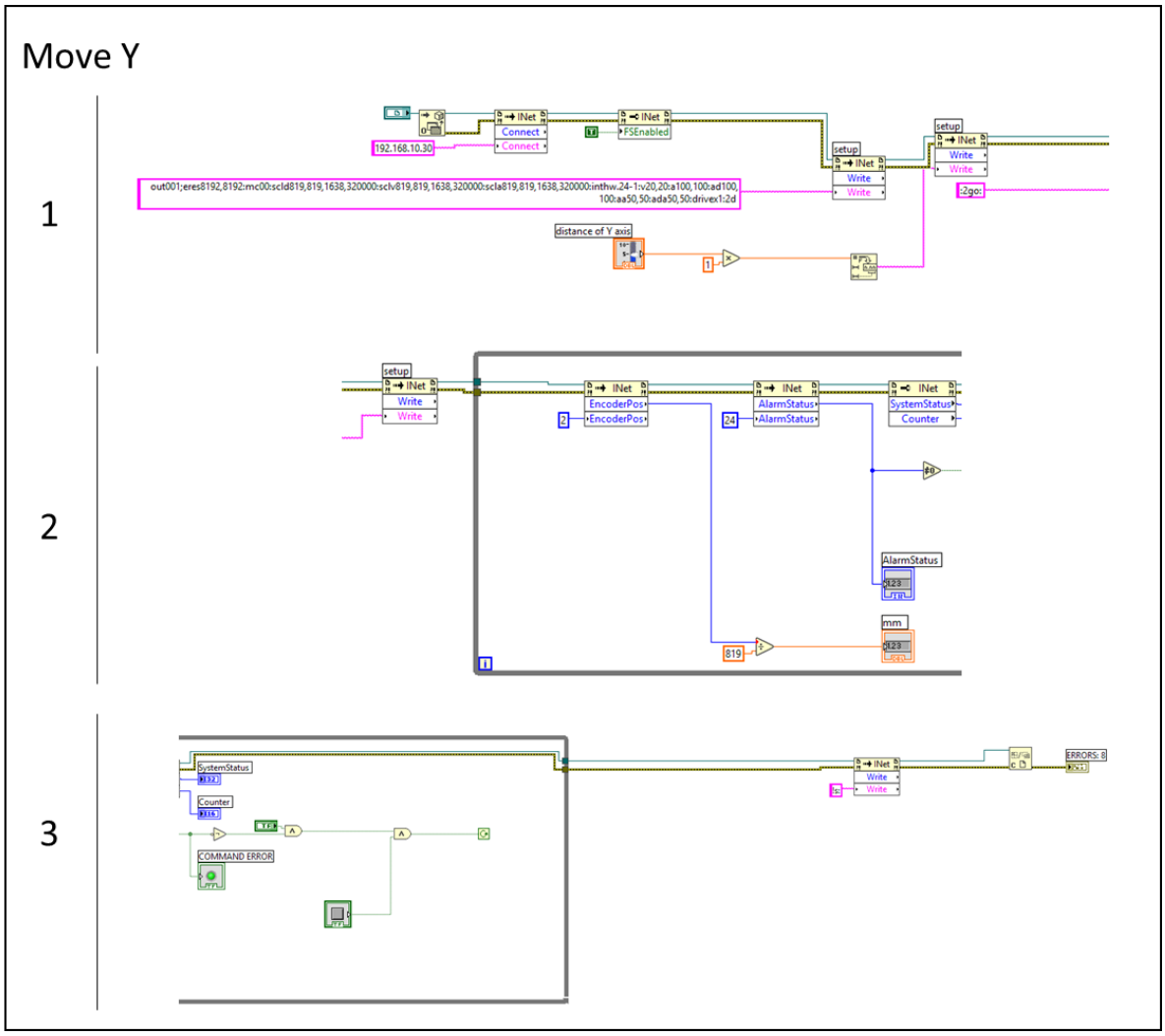

Appendix B Figure 2.6. Move Y code.

This code stored in the block diagram of the LabVIEW program is used to move the printing bed along the Y axis. The printing platform can be adjusted in a positive and negative direction to reach the desired printing position.

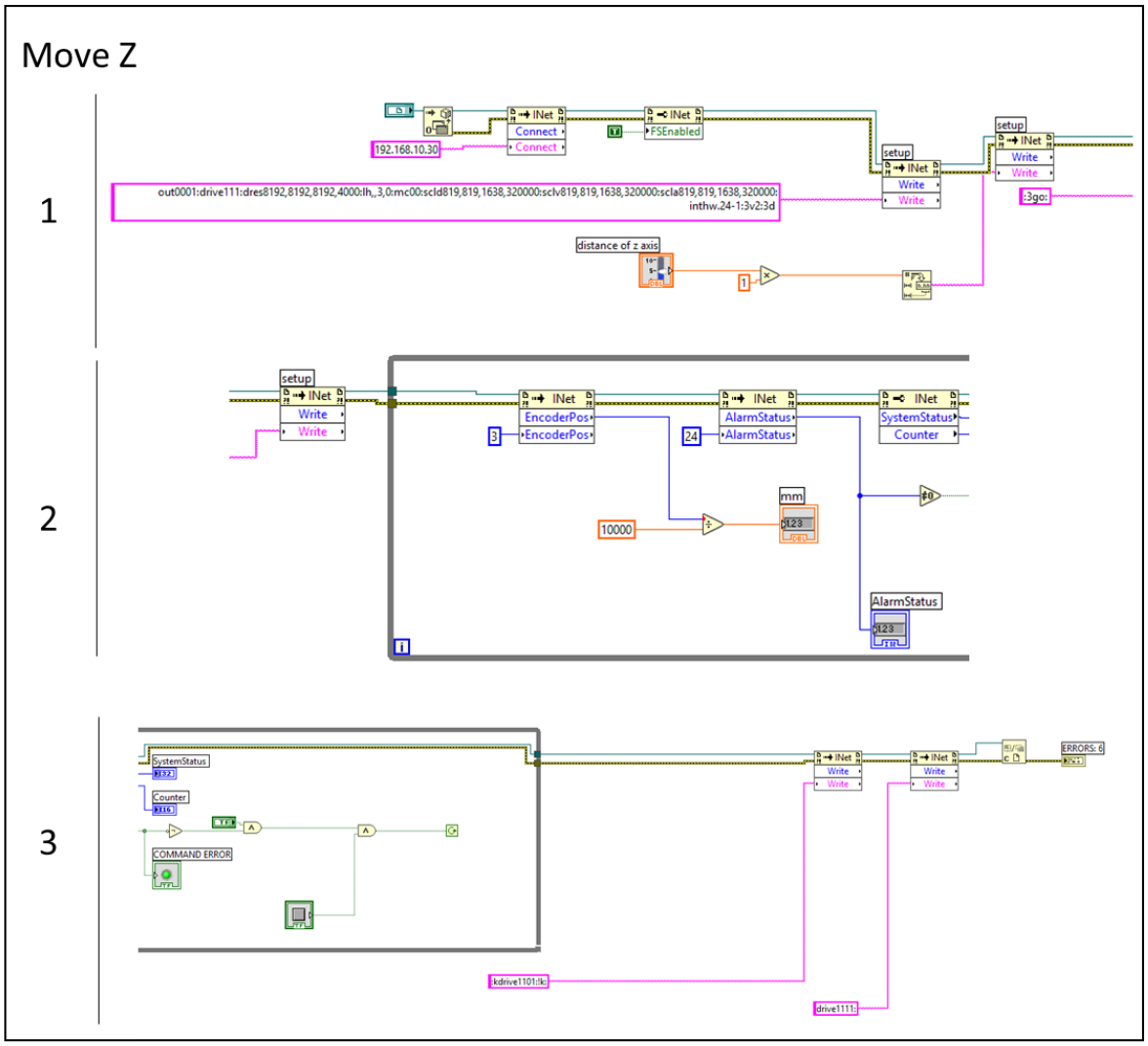

Appendix B Figure 2.7. Move Z code.

This code stored in the block diagram of the LabVIEW program is used to move the extrusion arm along the Z axis. The printing arm is adjust in a positive and negative direction to reach optimal deposition height.

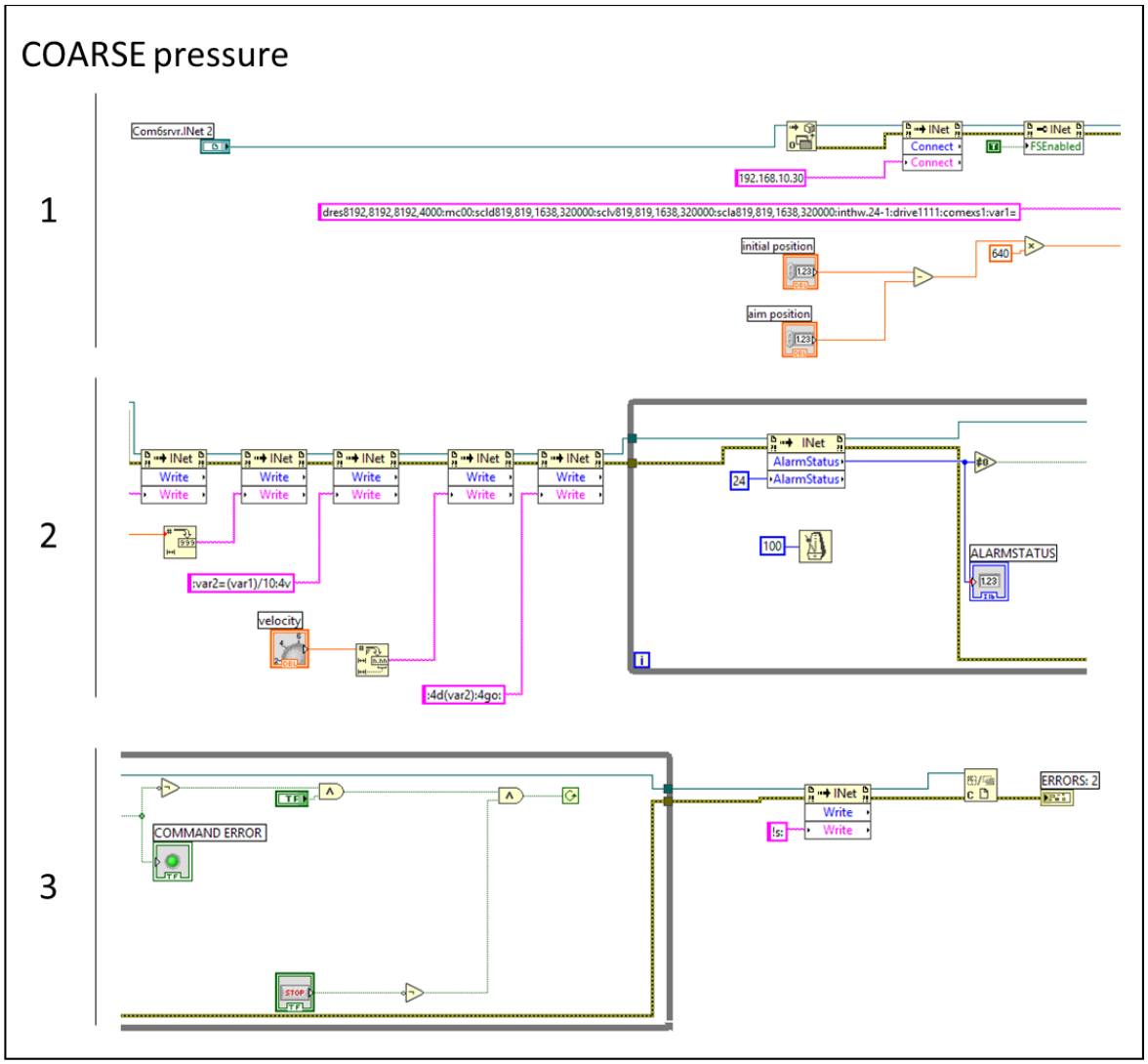

Appendix B Figure 2.8. Coarse pressure code.

This code stored in the block diagram of the LabVIEW program can be used to tuned, with a coarse adjustment of the pressure, the level of bioink extrusion. The pressure can be adjust by the retraction or forward movement of the load stage at a rate of 1-0.1 mm s^{-1}.

Appendix B

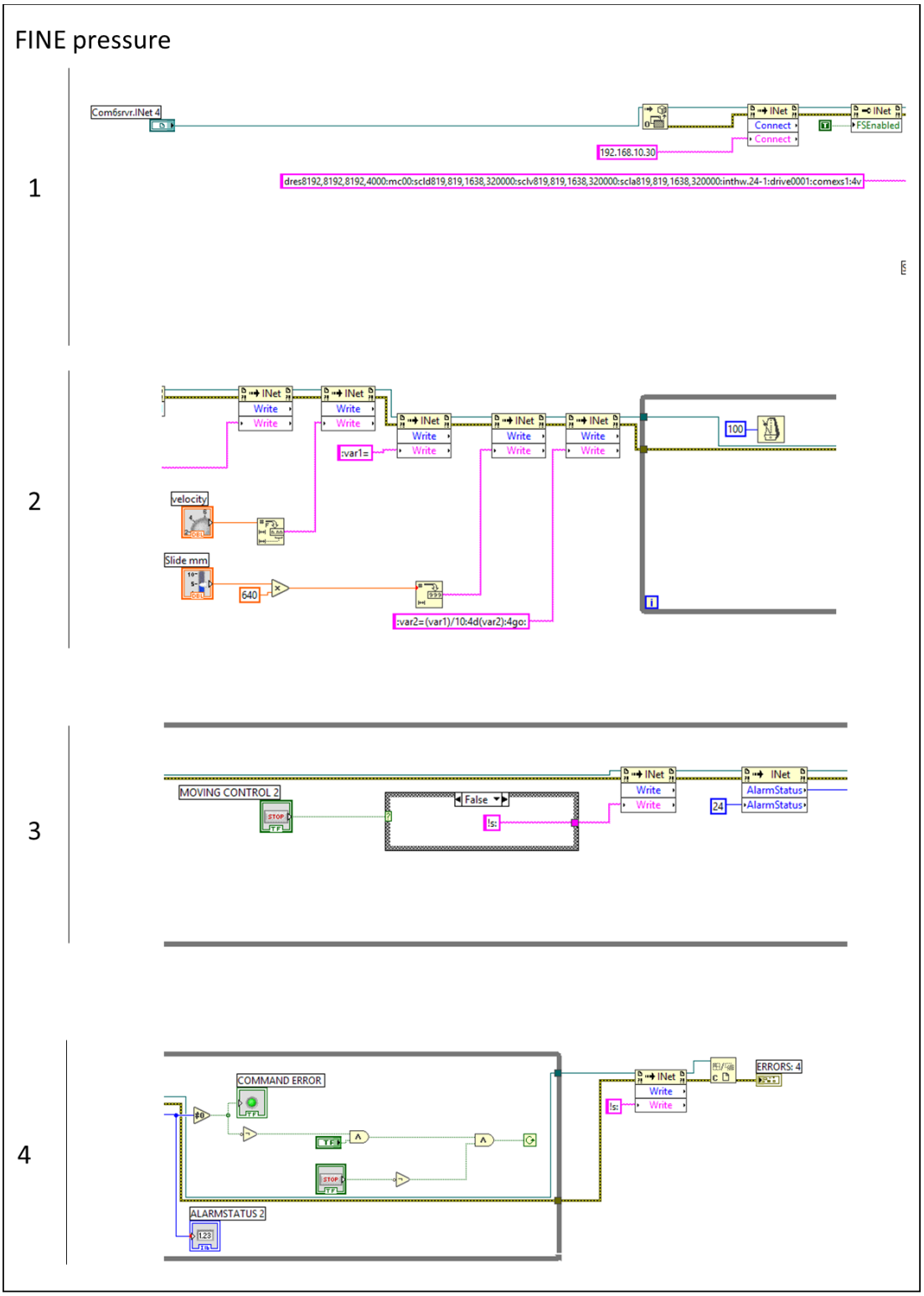

Appendix B Figure 2.9. Fine pressure code.

This code stored in the block diagram of the LabVIEW program can be used to tuned, with a fine adjustment of the pressure, the level of bioink extrusion. The pressure can be adjust by the retraction or forward movement of the load stage at a rate of 0.1-0.001 mm s^{-1}.

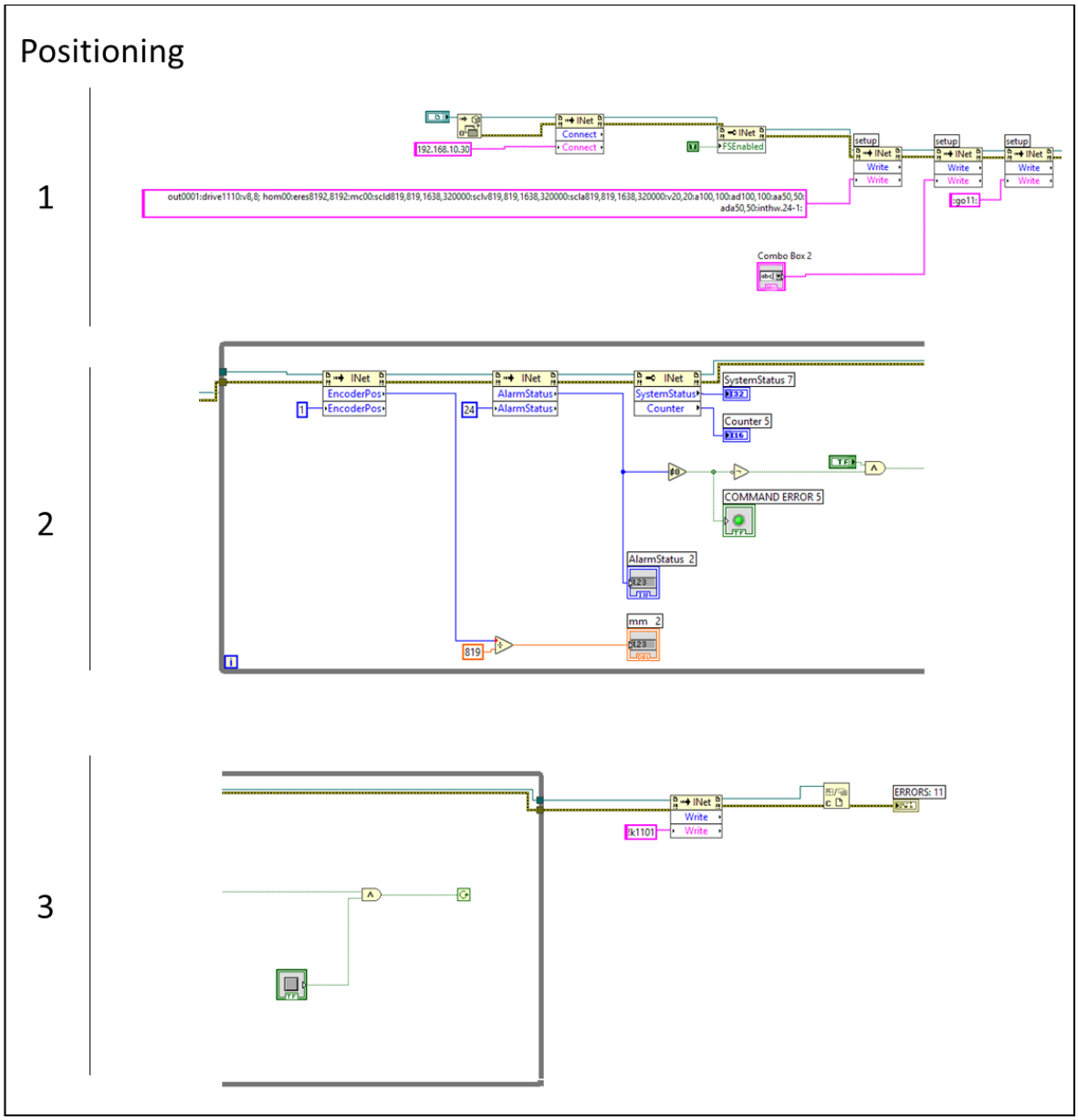

Appendix B Figure 2.10. X-Y printing bed positioning code.

This code stored in the block diagram of the LabVIEW program can be used in case of automatic printing bed positioning is needed. This code is implemented to serve the 6-well printing mode. However, the code reported here is used to print in 6 different positions on the printing bed.

LATTICE (*1 of 2*)

1

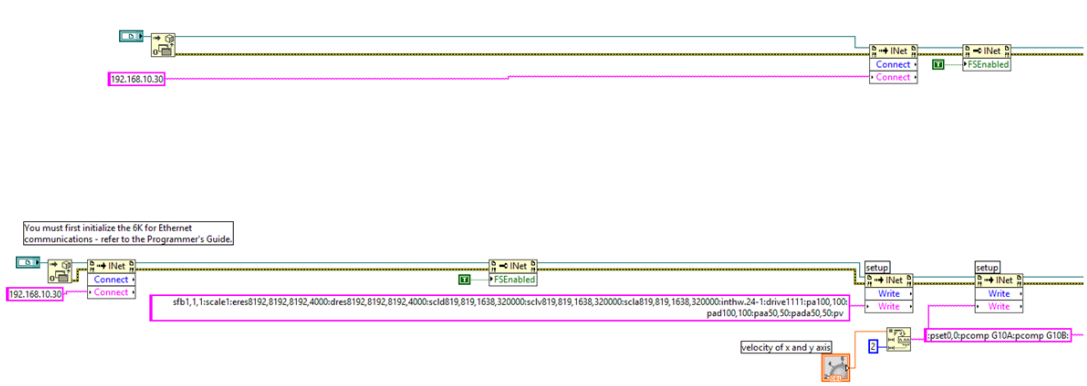

2

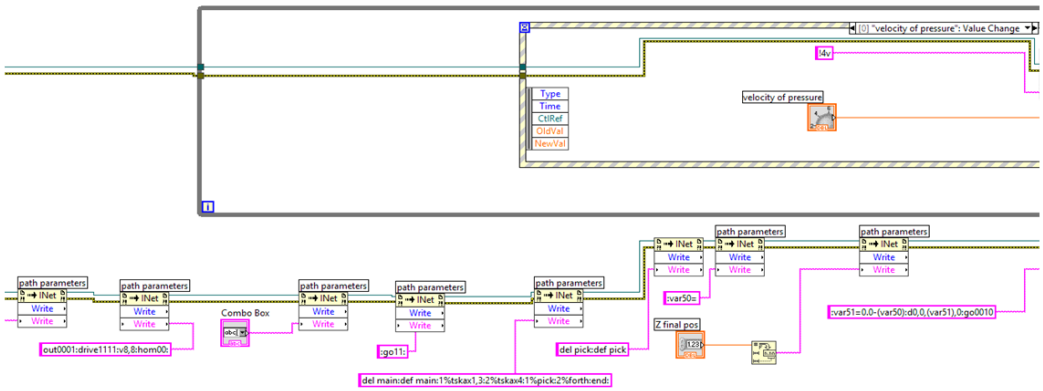

3

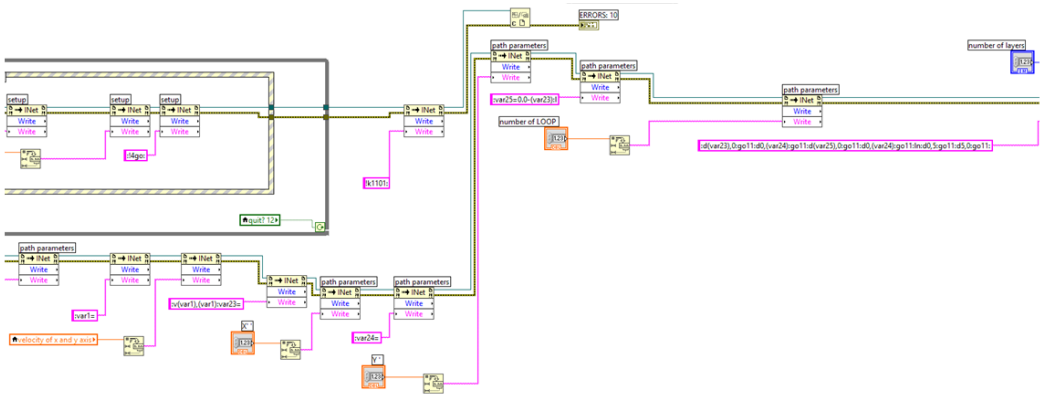

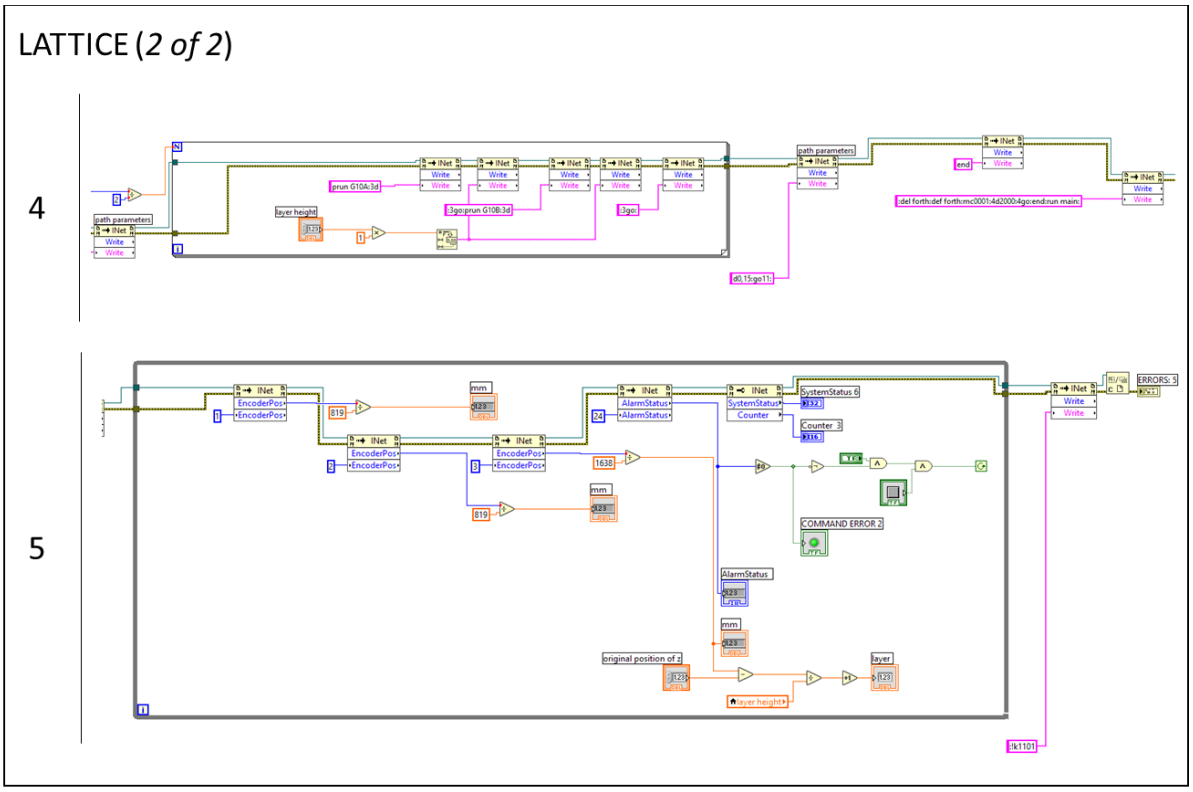

Appendix B Figure 2.11. Lattice printing code.

This code stored in the block diagram of the LabVIEW program ant constitute the main code of the printing program. This block is related to the front panel reported in Figure 2.6. It is used to guide the printer to extrude the bioink at set pressure and velocity of the printing bed, to raise the Z axis of a set gap and to print a specified number of layers.

Appendix C Chapter 3 supplementary data

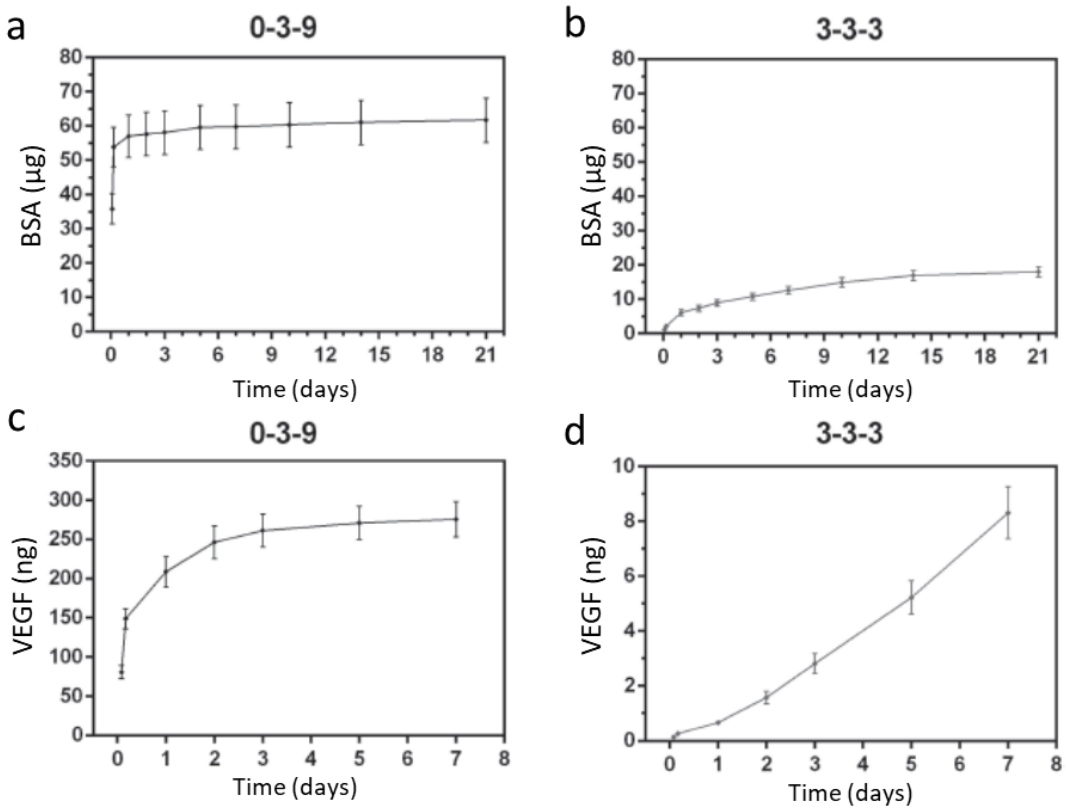

Appendix C Figure 3.1. Release of proteins from 0-3-9 and 3-3-3 printed scaffolds.

Cumulative release curves of BSA from 0-3-9 (a) and 3-3-3 (b). Data suggest, that a significant amount of BSA remained inside the 3-3-3 blend, while BSA was released from 0-3-9 with a burst release kinetic. Cumulative release curves of VEGF from 0-3-9 (c) and 3-3-3 (d). A high initial burst was observed from 0-3-9 scaffolds, while VEGF from 3-3-3 was released in a sustained manner.

Appendix C Chapter 4 supplementary data

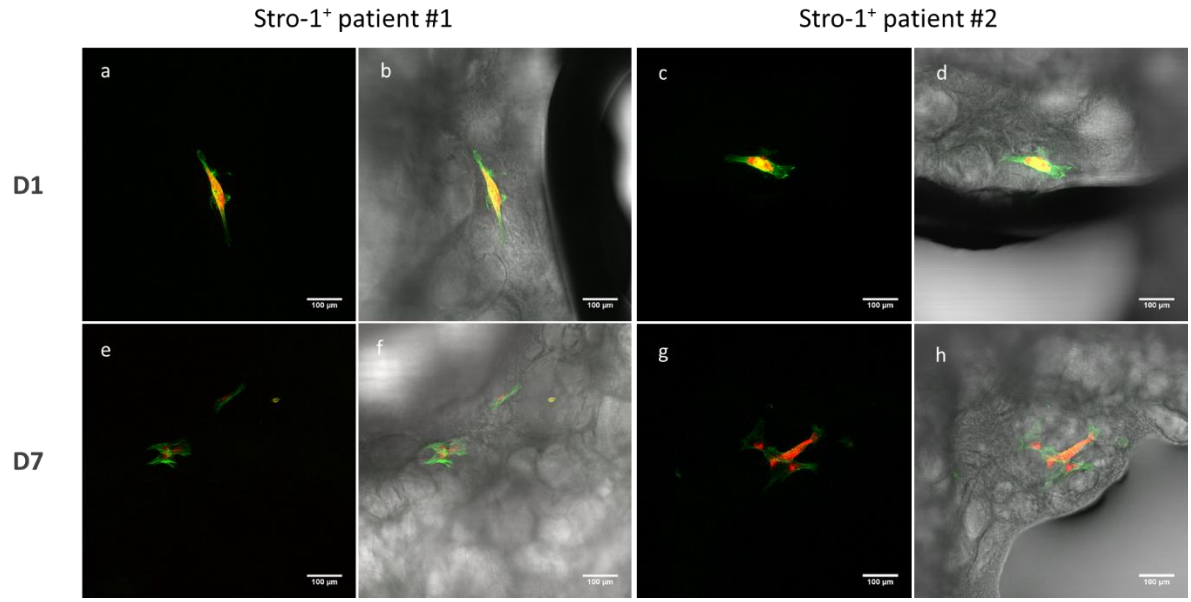

Appendix C Figure 4.1. 3D printed scaffolds seeded with Stro-1+.

Seeding was carried at low density to assess cell attachment. Scaffolds were fixed and imaged with confocal microscope after staining with Alexa fluor 488 (phalloidin) and being pre-stained with Vybrant DiD (red). After 1 day, scaffolds seeded with Stro-1+ from first (a,b) and second (c,d) donor were imaged. Incubated for 7 days, scaffolds seeded with HBMSCs from first (e,f) and second (g,h) donors were assessed for proliferation. Scale bar: (a-h) 100 µm.

Appendix C Chapter 5 supplementary data

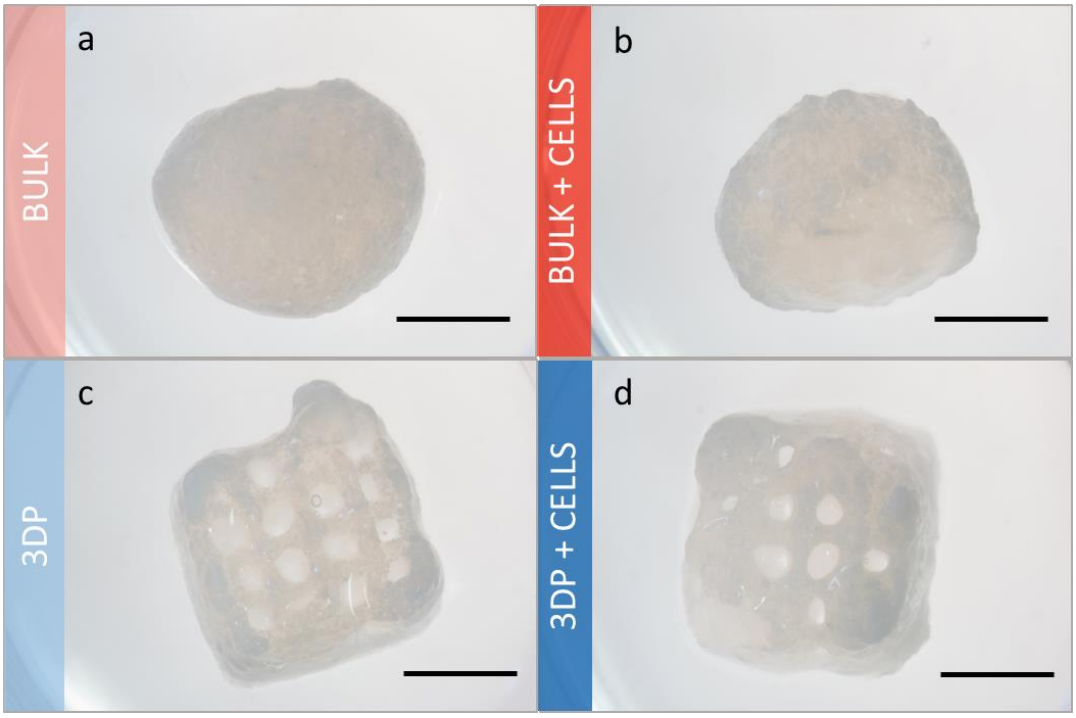

Appendix C Figure 5.1. *In vitro* control of implanted scaffolds cultured for 56 days.

Bulk (a), bulk + HBMSCs (b), 3D printed (c) and 3D printed + HBMSCs (d) macroscopic images of appearance after 56 days of *in vitro* incubation. Scale bar: 5 mm.

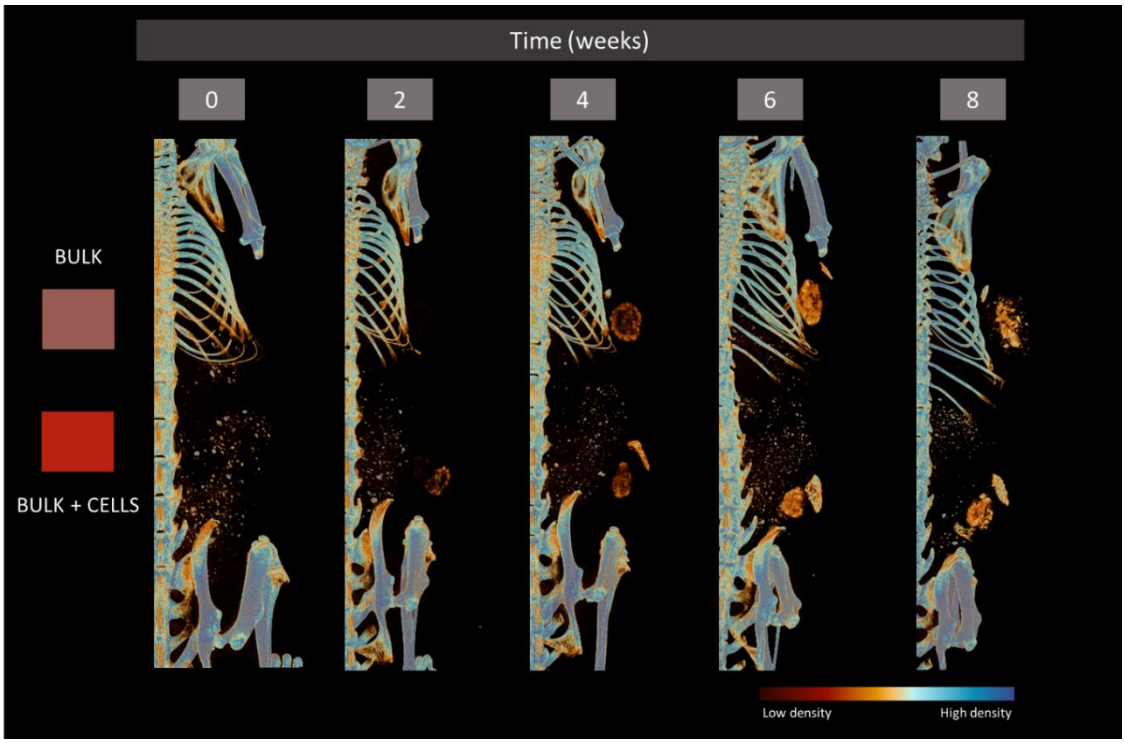

Appendix C Figure 5.2. CT images of *in vivo* implanted scaffolds.

Bulk scaffolds (cranial posterior) and HBMSC-laden bulk scaffolds (caudal posterior) scanned at 0, 2, 4, 6 and 8 weeks after implantation. Bone density scale indicates low density bone as dark red and high-density bone as blue.

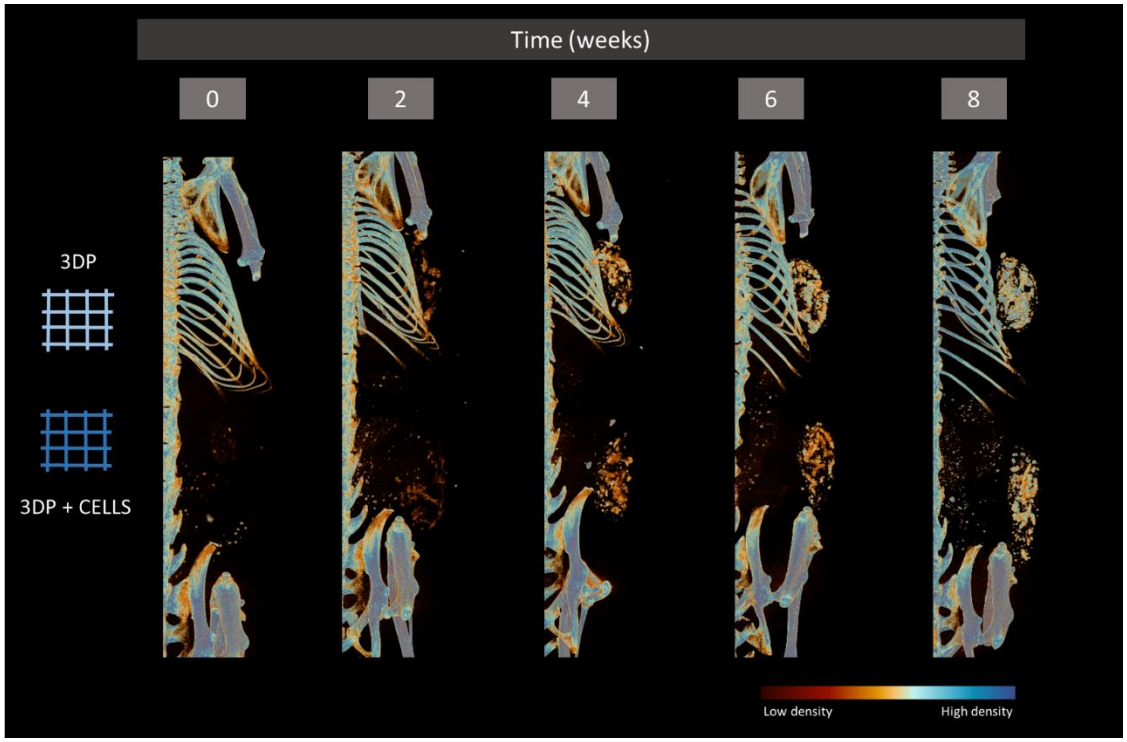

Appendix C Figure 5.3. CT images of *in situ* implanted scaffolds.

3D printed scaffolds (cranial posterior) and HBMSC-laden 3D printed scaffolds (caudal posterior) scanned at 0, 2, 4, 6 and 8 weeks after implantation. Bone density scale indicates low density bone as dark red and high-density bone as blue.

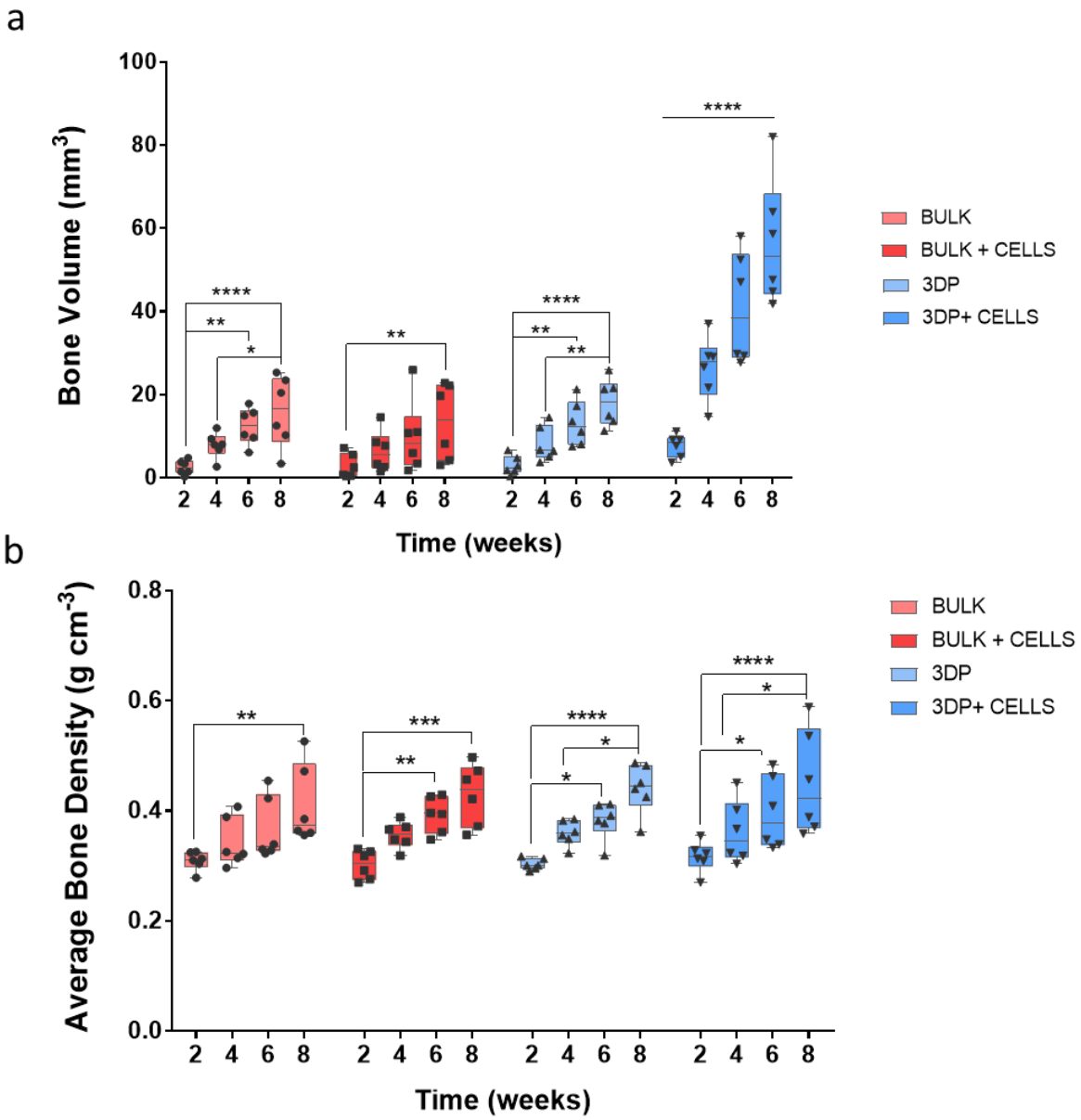

Appendix C Figure 5.4. Quantitative analysis of *in vivo* implanted cell-laden scaffolds.

Bone volume (a) and average bone density (b) of three-dimensional constructs implanted *in vivo* were analysed by treatment conditions, including bulk, bulk with HBMSCs, 3D printed and 3D printed with HBMSCs. Statistical significance assessed by two-way ANOVA followed by Tukey's multiple comparison tests. Mean ± S.D., n=6, *p<0.05, **p<0.01, ***p<0.001, ****p<0.0001.

Appendix C Chapter 6 supplementary data

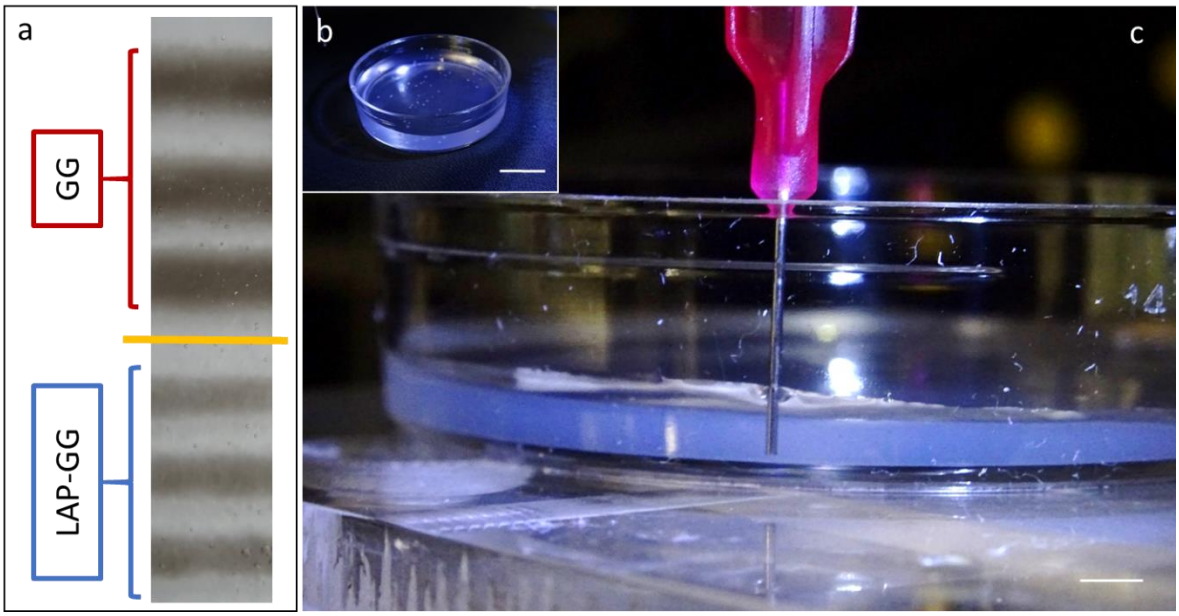

Appendix C Figure 6.1. Printing stability and swelling kinetics in agarose.

GG and LAP-GG stands (a) printed in agarose fluid gel. Agarose gel (b) loaded at 2 mm in thickness. Printing of strand (c) for swelling test. Scale bar: (b) 10 mm, (c) 2 mm.

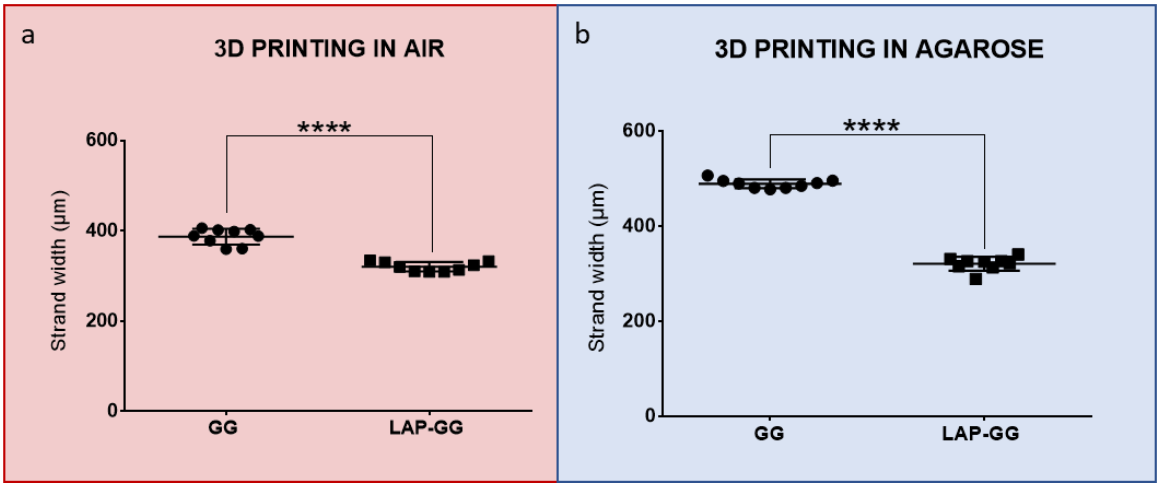

Appendix C Figure 6.2. Comparison of fibre diameter immediately after deposition.

Measurements were carried out on samples printed in air (a) and in agarose (b). Statistical significance assessed by two-way ANOVA followed by Tukey's multiple comparison tests. Mean ± S.D. n=3 *p<0.05, ****p<0.0001.

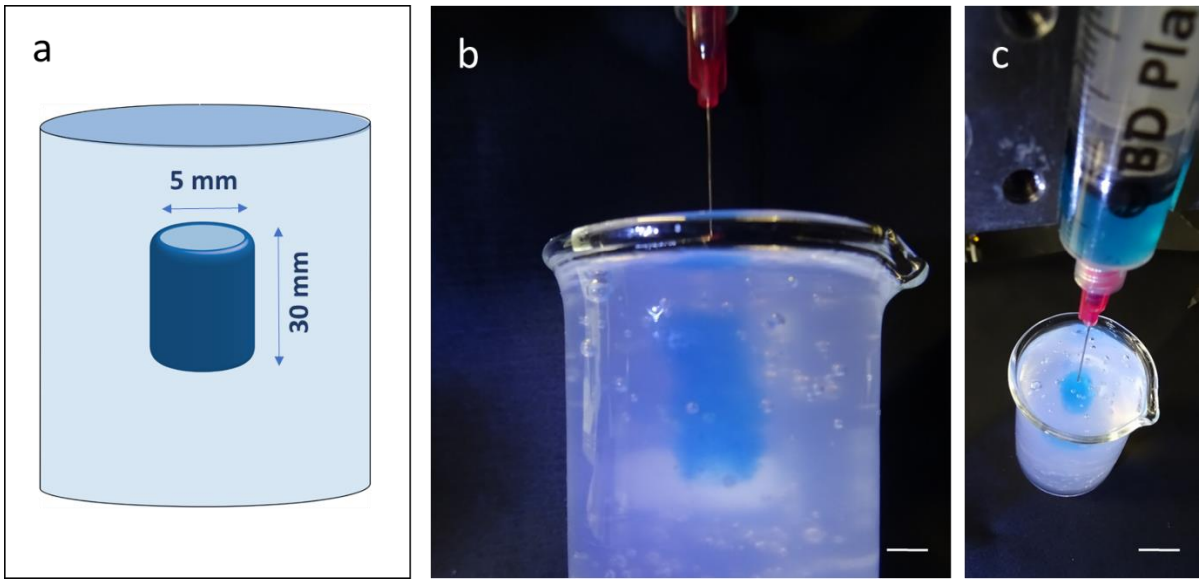

Appendix C Figure 6.3. Printing 3D sleeve for repairing of large bone defects.

A blueprint of a 3D sleeve (a) was generated with an initial height of 30 mm. Extrusion of LAP-GG (blue) in agarose fluid gel (transparent) resulted in the fabrication of a large structure (b,c). Scale bar: (b) 10 mm, (c) 5 mm.

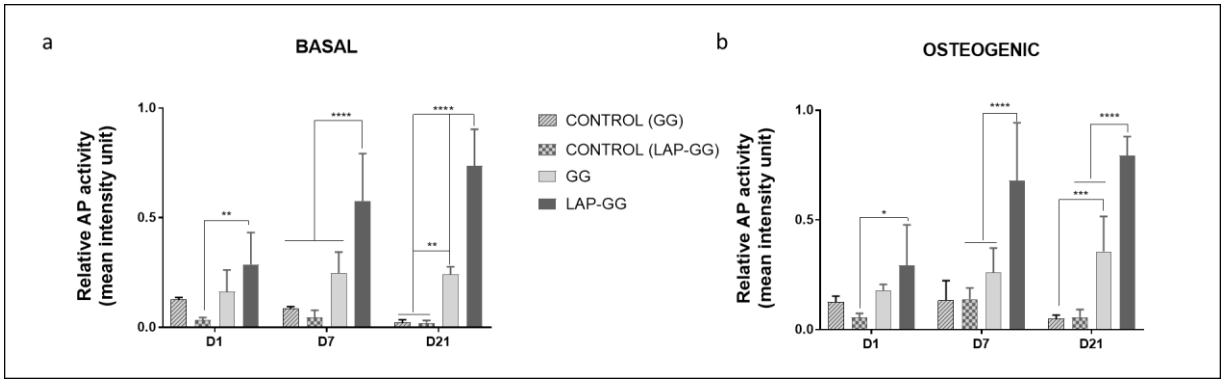

Appendix C Figure 6.4. Quantitative analysis of ALP by mean intensity unit analysis.

Acellular (controls) and cell-laden GG and LAP-GG were stained for ALP and investigate for intensity of ALP expression. Analysis was carried out after 1, 7 and 21 days of culture *in vitro* in basal (a) and osteogenic (b) media. Statistical significance assessed by two-way ANOVA followed by Tukey's multiple comparison tests. Mean ± S.D. n=3, *p<0.05, **p<0.01, ***p<0.001, **** p<0.0001.

Appendix C Chapter 7 supplementary data

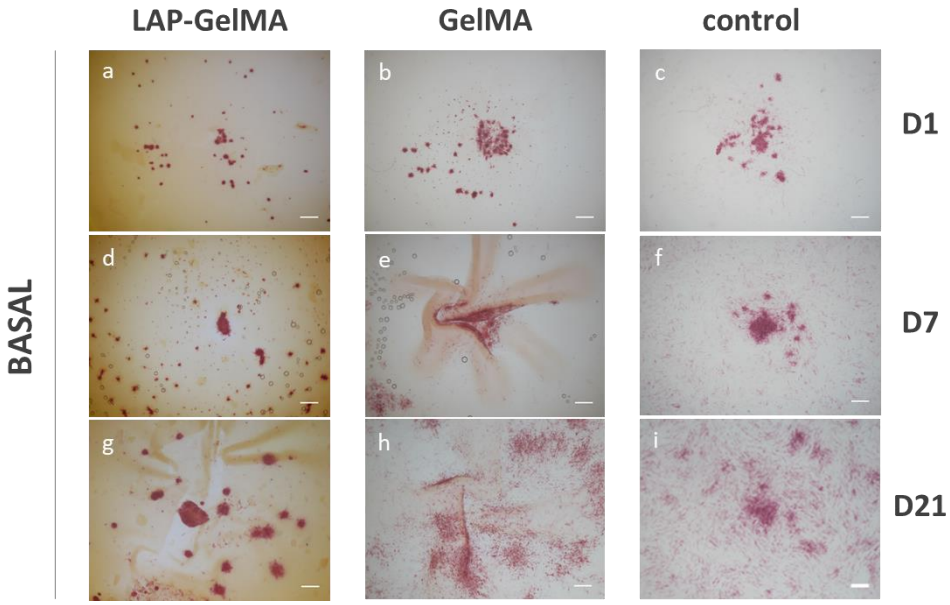

Appendix C Figure 7.1. Functional study of HBMSCs seeded on 2D LAP-GelMA gels in basal conditioned media.

HBMSCs were seeded onto 2D LAP-GelMA and GelMA films with tissue culture wells as control. ALP staining analysed under basal conditions after 1 (a, b, c), 7 (d, e, f) and 21 (g, h, i) days for LAP-GelMA, GelMA and control respectively. Scale bar: 1 mm.

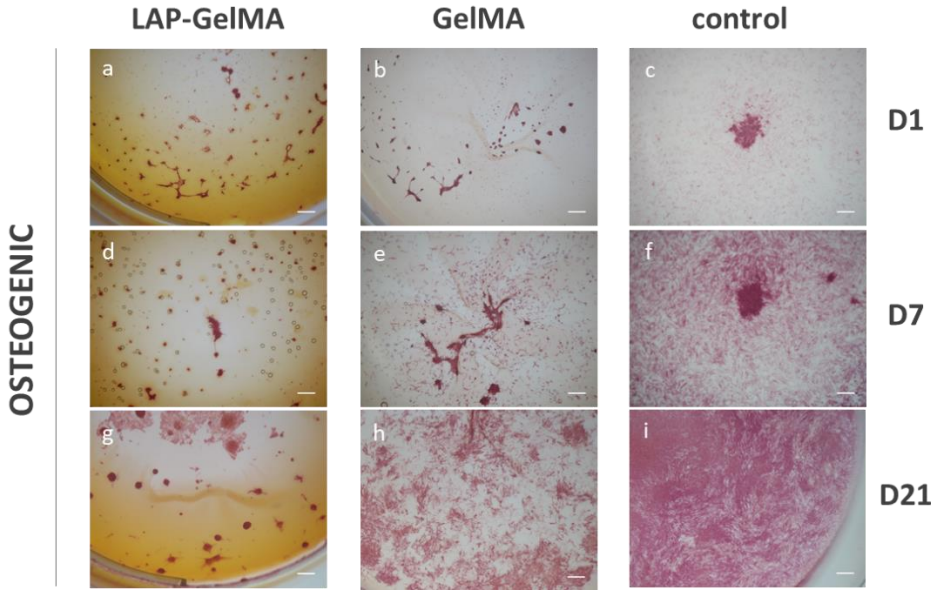

Appendix C Figure 7.2. Functional study of HBMSCs seeded on 2D LAP-GelMA gels in osteogenic conditioned media.

HBMSCs were seeded onto 2D LAP-GelMA and GelMA films with tissue culture wells as control. ALP staining analysed under osteogenic conditions after 1 (a, b, c), 7 (d, e, f) and 21 (g, h, i) days for LAP-GelMA, GelMA and control respectively. Scale bar: 1 mm.

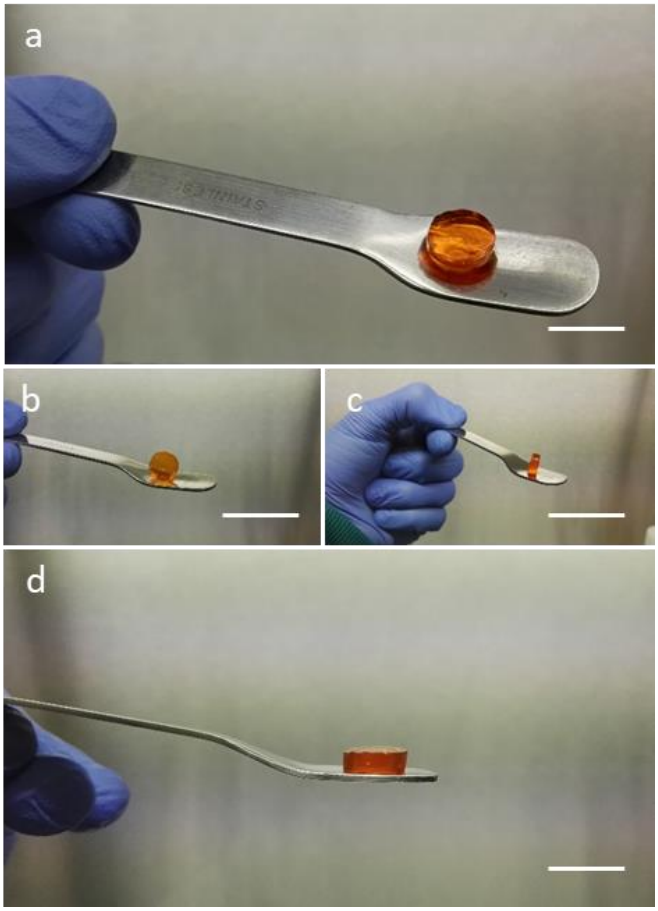

Appendix C Figure 7.3. 3D casted LPN-GelMA prior to CAM implantation.

Casted LAP-GelMA demonstrated high shape fidelity after visible light crosslinking. LAP-GelMA 300 µl disc. (Scale bar: a,d) 20 mm, b,c) 50 mm)

References

[1] Clarke B 2008 Normal Bone Anatomy and Physiology *Clin. J. Am. Soc. Nephrol.* **3** S131–9

[2] Ralston S H 2013 Bone structure and metabolism *Med. (United Kingdom)* **41** 581–5

[3] Weiner S and Wagner H D 1998 The material bone: structure-mechanical function relations. *Annu. Rev. Mater. Sci.* **28** 271–98

[4] Berendsen A D and Olsen B R 2015 Bone development *Bone* **80** 14–8

[5] Bayliss L, Mahoney D J and Monk P 2012 Normal bone physiology, remodelling and its hormonal regulation *Surg.* **30** 47–53

[6] McKibbin B 1978 The biology of fracture healing in long bones. *J. Bone Joint Surg. Br.* **60**–**B** 150–62

[7] Marsell R and Einhorn T A 2011 The biology of fracture healing *Injury* **42** 551–5

[8] Hernlund E, Svedbom A, Ivergård M, Compston J, Cooper C, Stenmark J, McCloskey E V, Jönsson B and Kanis J A 2013 Osteoporosis in the European Union: medical management, epidemiology and economic burden *Arch. Osteoporos.* **8** 136

[9] Mishra R, Bishop T, Valerio I L, Fisher J P and Dean D 2016 The potential impact of bone tissue engineering in the clinic. *Regen. Med.* **11** 571–87

[10] Petite H, Viateau V, Bensaïd W, Meunier A, De Pollak C, Bourguignon M, Oudina K, Sedel L and Guillemin G 2000 Tissue-engineered bone regeneration *Nat. Biotechnol.* **18** 959–63

[11] Damien C J and Parsons J R 1991 Bone graft and bone graft substitutes: A review of current technology and applications *J. Appl. Biomater.* **2** 187–208

[12] Learmonth I D, Young C and Rorabeck C 2007 The operation of the century: total hip replacement *Lancet* **370** 1508–19

[13] Hench L L 1991 Bioceramics: From Concept to Clinic *J. Am. Ceram. Soc.* **74** 1487–510

[14] Ingham E and Fisher J 2000 Biological Reaction to Wear Debris in Total Joint Replacement *Proc Inst Mech Eng H* **73** 21–37

[15] Hutmacher D 2000 Scaffolds in tissue engineering bone and cartilage *Biomaterials* **21** 2529–43

[16] Frohlich M, Grayson W, Wan L, Marolt D, Drobnic M and Vunjak- Novakovic G 2008 Tissue Engineered Bone Grafts: Biological Requirements, Tissue Culture and Clinical Relevance *Curr. Stem Cell Res. Ther.* **3** 254–64

[17] Pittenger M F, Mackay A M, Beck S C, Jaiswal R K, Douglas R, Mosca J D, Moorman M A, Simonetti D W, Craig S and Marshak D R 1999 Multilineage potential of adult human mesenchymal stem cells. *Science* **284** 143–7

[18] Bianco P and Robey P G 2004 Skeletal Stem Cells *Handb. Stem Cells* **2** 415–24

[19] Bianco P, Riminucci M, Gronthos S and Robey P G 2001 Bone marrow stromal stem cells: nature, biology, and potential applications. *Stem Cells* **19** 180–92

[20] Tare R S, Babister J C, Kanczler J and Oreffo R O C 2008 Skeletal stem cells: Phenotype, biology and environmental niches informing tissue regeneration *Mol. Cell. Endocrinol.* **288** 11–21

[21] Oreffo R O C, Cooper C, Mason C and Clements M 2005 Mesenchymal stem cells lineage, plasticity, and skeletal therapeutic potential *Stem Cell Rev.* **1** 169–78

[22] Caplan A I 1991 Mesenchymal stem cells *J. Orthop. Res.* **9** 641–50

[23] da Silva Meirelles L 2006 Mesenchymal stem cells reside in virtually all post-natal organs and tissues *J. Cell Sci.* **119** 2204–13

[24] Tare R S, Kanczler J, Aarvold A, Jones A M H, Dunlop D G and Oreffo R O C 2010 Skeletal stem cells and bone regeneration: Translational strategies from bench to clinic *Proc. Inst. Mech. Eng. Part H J. Eng. Med.* **224** 1455–70

[25] Owen M and Friedenstein A J 1988 Stromal stem cells: marrow-derived osteogenic precursors. *Ciba Found. Symp.* **136** 42–60

[26] Bolland B J R F, Kanczler J M, Ginty P J, Howdle S M, Shakesheff K M, Dunlop D G and Oreffo R O C 2008 The application of human bone marrow stromal cells and poly(dl-lactic acid) as a biological bone graft extender in impaction bone grafting *Biomaterials* **29** 3221–7

[27] Bolland B J R F, Kanczler J M, Dunlop D G and Oreffo R O C 2008 Development of in vivo μCT evaluation of neovascularisation in tissue engineered bone constructs *Bone* **43** 195–202

References

[28] Quarto R, Mastrogiacomo M, Cancedda R, Kutepov S M, Mukhachev V, Lavroukov A, Kon E and Marcacci M 2001 Repair of Large Bone Defects with the Use of Autologous Bone Marrow Stromal Cells *N. Engl. J. Med.* **344** 385–6

[29] Marcacci M, Kon E, Moukhachev V, Lavroukov A, Kutepov S, Quarto R, Mastrogiacomo M and Cancedda R 2007 Stem Cells Associated with Macroporous Bioceramics for Long Bone Repair: 6- to 7-Year Outcome of a Pilot Clinical Study *Tissue Eng.* **13** 947–55

[30] Groll J, Boland T, Blunk T, Burdick J A, Cho D, Paul D, Derby B, Forgacs G, Li Q, Mironov V A and Moroni L 2016 Biofabrication : Reappraising the definition in an evolving field *Biofabrication* **013001** 1–6

[31] Moroni L, Boland T, Burdick J A, De Maria C, Derby B, Forgacs G, Groll J, Li Q, Malda J, Mironov V A, Mota C, Nakamura M, Shu W, Takeuchi S, Woodfield T B F, Xu T, Yoo J J and Vozzi G 2018 Biofabrication: A Guide to Technology and Terminology *Trends Biotechnol.* **36** 384–402

[32] Langer R and Vacanti J P 1993 Tissue Engineering *Science (80-.).* **260** 920–6

[33] Malda J and Groll J 2016 A Step Towards Clinical Translation of Biofabrication *Trends Biotechnol.* **34** 356–7

[34] Levato R, Visser J, Planell J A, Engel E, Malda J and Mateos-Timoneda M A 2014 Biofabrication of tissue constructs by 3D bioprinting of cell-laden microcarriers *Biofabrication* **6** 035020

[35] Kang H-W, Lee S J, Ko I K, Kengla C, Yoo J J and Atala A 2016 A 3D bioprinting system to produce human-scale tissue constructs with structural integrity *Nat. Biotechnol.* **34** 312–9

[36] Klebe R J 1988 Cytoscribing: A method for micropositioning cells and the construction of two- and three-dimensional synthetic tissues *Exp. Cell Res.* **179** 362–73

[37] Giannitelli S M, Accoto D, Trombetta M and Rainer A 2014 Current trends in the design of scaffolds for computer-aided tissue engineering *Acta Biomater.* **10** 580–94

[38] Whang K, Healy K E, Elenz D R, Nam E K, Tsai D C, Thomas C H, Nuber G W, Glorieux F H, Travers R and Sprague S M 1999 Engineering Bone Regeneration with Bioabsorbable Scaffolds with Novel Microarchitecture *Tissue Eng.* **5** 35–51

[39] Xu T, Jin J, Gregory C, Hickman J J and Boland T 2005 Inkjet printing of viable mammalian cells *Biomaterials* **26** 93–9

[40] Odde D J and Renn M J 2000 Laser-guided direct writing of living cells *Biotechnol. Bioeng.* **67** 312–8

[41] Crawford R H, Beaman J J, Cavello C, Jackson J, Weiss L E and Séquin C . 1999 Solid freeform fabrication: A new manufacturing paradigm *IEEE Spectr.* **36**

[42] Vozzi G, Previti a, De Rossi D and Ahluwalia a 2002 Microsyringe-based deposition of two-dimensional and three-dimensional polymer scaffolds with a well-defined geometry for application to tissue engineering. *Tissue Eng.* **8** 1089–98

[43] Wilson W C and Boland T 2003 Cell and organ printing 1: Protein and cell printers *Anat. Rec.* **272A** 491–6

[44] Boland T, Mironov V, Gutowska A, Roth E A and Markwald R R 2003 Cell and organ printing 2: Fusion of cell aggregates in three-dimensional gels *Anat. Rec.* **272A** 497–502

[45] Xu T, Kincaid H, Atala A and Yoo J J 2008 High-Throughput Production of Single-Cell Microparticles Using an Inkjet Printing Technology *J. Manuf. Sci. Eng.* **130** 021017

[46] Xu T, Olson J, Zhao W, Atala A, Zhu J-M and Yoo J J 2008 Characterization of Cell Constructs Generated With Inkjet Printing Technology Using In Vivo Magnetic Resonance Imaging *J. Manuf. Sci. Eng.* **130** 021013

[47] Cui X, Dean D, Ruggeri Z M and Boland T 2010 Cell damage evaluation of thermal inkjet printed chinese hamster ovary cells *Biotechnol. Bioeng.* **106** 963–9

[48] Gao G, Schilling A F, Hubbell K, Yonezawa T, Truong D, Hong Y, Dai G and Cui X 2015 Improved properties of bone and cartilage tissue from 3D inkjet-bioprinted human mesenchymal stem cells by simultaneous deposition and photocrosslinking in PEG-GelMA *Biotechnol. Lett.* **37** 2349–55

[49] Gruene M, Deiwick A, Koch L, Schlie S, Unger C, Hofmann N, Bernemann I, Glasmacher B and Chichkov B 2011 Laser Printing of Stem Cells for Biofabrication of Scaffold-Free Autologous Grafts *Tissue Eng. Part C Methods* **17** 79–87

[50] Chrisey R X and Z Z and W C and Y H and D B 2015 Freeform drop-on-demand laser printing of 3D alginate and cellular constructs *Biofabrication* **7** 45011

[51] Catros S, Guillotin B, Bacáková M, Fricain J C and Guillemot F 2011 Effect of laser

energy, substrate film thickness and bioink viscosity on viability of endothelial cells printed by laser-assisted bioprinting *Appl. Surf. Sci.* **257** 5142–7

[52] Gruene M, Pflaum M, Hess C, Diamantouros S, Schlie S, Deiwick A, Koch L, Wilhelmi M, Jockenhoevel S, Haverich A and Chichkov B 2011 Laser Printing of Three-Dimensional Multicellular Arrays for Studies of Cell–Cell and Cell–Environment Interactions *Tissue Eng. Part C Methods* **17** 973–82

[53] Ma X, Qu X, Zhu W, Li Y-S, Yuan S, Zhang H, Liu J, Wang P, Lai C S E, Zanella F, Feng G-S, Sheikh F, Chien S and Chen S 2016 Deterministically patterned biomimetic human iPSC-derived hepatic model via rapid 3D bioprinting *Proc. Natl. Acad. Sci.* **113** 201524510

[54] Koch L, Gruene M, Unger C and Chichkov B 2013 Laser assisted cell printing. *Curr. Pharm. Biotechnol.* **14** 91–7

[55] Vaezi M and Yang S F 2015 A novel bioactive PEEK/HA composite with controlled 3D interconnected HA network *Int. J. Bioprinting* **1** 66–76

[56] Ahlfeld T, Cidonio G, Kilian D, Duin S, Akkineni A R, Dawson J I, Yang S, Lode A, Oreffo R O C and Gelinsky M 2017 Development of a clay based bioink for 3D cell printing for skeletal application *Biofabrication* **9** 034103

[57] Fedorovich N E, De Wijn J R, Verbout A J, Alblas J and Dhert W J A 2008 Three-Dimensional Fiber Deposition of Cell-Laden, Viable, Patterned Constructs for Bone Tissue Printing *Tissue Eng. Part A* **14** 127–33

[58] Lu X, Lee Y, Yang S, Hao Y, Evans J R G and Parini C G 2009 Fine lattice structures fabricated by extrusion freeforming: Process variables *J. Mater. Process. Technol.* **209** 4654–61

[59] Yang S, Yang H, Chi X, Evans J R G, Thompson I, Cook R J and Robinson P 2008 Rapid prototyping of ceramic lattices for hard tissue scaffolds *Mater. Des.* **29** 1802–9

[60] Gibbs D M, Vaezi M, Yang S and Oreffo R O C 2014 Hope versus hype: what can additive manufacturing realistically offer trauma and orthopedic surgery? *Regen Med* **9** 535–49

[61] Paxton N, Smolan W, Böck T, Melchels F, Groll J and Jungst T 2017 Proposal to assess printability of bioinks for extrusion-based bioprinting and evaluation of rheological properties governing bioprintability *Biofabrication* **9** 044107

[62] Nicodemus G D and Bryant S J 2008 Cell Encapsulation in Biodegradable Hydrogels for Tissue Engineering Applications *Tissue Eng. Part B. Rev.* **14** 149–65

[63] Richtering W and Saunders B R 2014 Gel architectures and their complexity. *Soft Matter* **10** 3695–702

[64] Sawkins M J, Bowen W, Dhadda P, Markides H, Sidney L E, Taylor A J, Rose F R A J, Badylak S F, Shakesheff K M and White L J 2013 Hydrogels derived from demineralized and decellularized bone extracellular matrix *Acta Biomater.* **9** 7865–73

[65] Malda J, Visser J, Melchels F P, Jüngst T, Hennink W E, Dhert W J A, Groll J and Hutmacher D W 2013 25th anniversary article: Engineering hydrogels for biofabrication *Adv. Mater.* **25** 5011–28

[66] Pati F, Shim J H, Lee J S and Cho D W 2013 3D printing of cell-laden constructs for heterogeneous tissue regeneration *Manuf. Lett.* **1** 49–53

[67] Truby R L and Lewis J A 2016 Printing soft matter in three dimensions *Nature* **540** 371–8

[68] Chen H, Malheiro A D B F B, Van Blitterswijk C, Mota C, Wieringa P A and Moroni L 2017 Direct Writing Electrospinning of Scaffolds with Multidimensional Fiber Architecture for Hierarchical Tissue Engineering *ACS Appl. Mater. Interfaces* **9** 38187–200

[69] Schütz K, Placht A-M, Paul B, Brüggemeier B, Gelinsky M and Lode A 2015 Three-dimensional plotting of a cell-laden alginate/ methylcellulose blend: towards biofabrication of tissue engineering constructs with clinically relevant dimensions *J. Tissue Eng. Regen. Med.* **2** 408–17

[70] Fedorovich N E, Kuipers E, Gawlitta D, Dhert W J a. and Alblas J 2011 Scaffold Porosity and Oxygenation of Printed Hydrogel Constructs Affect Functionality of Embedded Osteogenic Progenitors *Tissue Eng. Part A* **17** 2473–86

[71] Weinand C, Gupta R, Huang A Y, Weinberg E, Madisch I, Qudsi R A, Neville C M, Pomerantseva I and Vacanti J P 2007 Comparison of Hydrogels in the In Vivo Formation of Tissue-Engineered Bone Using Mesenchymal Stem Cells and Beta-Tricalcium Phosphate *Tissue Eng.* **13** 757–65

[72] Cubo N, Garcia M, Del Cañizo J F, Velasco D and Jorcano J L 2017 3D bioprinting of functional human skin: Production and in vivo analysis *Biofabrication* **9** 015006

References

[73] Norotte C, Marga F S, Niklason L E and Forgacs G 2009 Scaffold-free vascular tissue engineering using bioprinting *Biomaterials* **30** 5910–7

[74] Taniguchi D, Matsumoto K, Tsuchiya T, Machino R, Takeoka Y, Elgalad A, Gunge K, Takagi K, Taura Y, Hatachi G, Matsuo N, Yamasaki N, Nakayama K and Nagayasu T 2018 Scaffold-free trachea regeneration by tissue engineering with bio-3D printing† *Interact. Cardiovasc. Thorac. Surg.* **26** 745–52

[75] Wu Z, Su X, Xu Y, Kong B, Sun W and Mi S 2016 Bioprinting three-dimensional cell-laden tissue constructs with controllable degradation *Sci. Rep.* **6** 24474

[76] Freeman F E and Kelly D J 2017 Tuning alginate bioink stiffness and composition for controlled growth factor delivery and to spatially direct MSC Fate within bioprinted tissues *Sci. Rep.* **7** 1–12

[77] Chang R, Nam J and Sun W 2008 Effects of Dispensing Pressure and Nozzle Diameter on Cell Survival from Solid Freeform Fabrication–Based Direct Cell Writing *Tissue Eng. Part A* **14** 41–8

[78] Sarkar K, Xue Y and Sant S 2017 Host Response to Synthetic Versus Natural Biomaterials BT - The Immune Response to Implanted Materials and Devices: The Impact of the Immune System on the Success of an Implant ed B Corradetti (Cham: Springer International Publishing) pp 81–105

[79] Kolesky D B, Homan K A, Skylar-Scott M A and Lewis J A 2016 Three-dimensional bioprinting of thick vascularized tissues *Proc. Natl. Acad. Sci.* **113** 3179–84

[80] Ribeiro A, Blokzijl M M, Levato R, Visser C W, Castilho M, Hennink W E, Vermonden T and Malda J 2017 Assessing bioink shape fidelity to aid material development in 3D bioprinting *Biofabrication* **10** 014102

[81] Ahlfeld T, Doberenz F, Kilian D, Vater C, Korn P, Lauer G, Lode A and Gelinsky M 2018 Bioprinting of mineralized constructs utilizing multichannel plotting of a self-setting calcium phosphate cement and a cell-laden bioink *Biofabrication* **10** 045002

[82] Schuurman W, Khristov V, Pot M W, van Weeren P R, Dhert W J a and Malda J 2011 Bioprinting of hybrid tissue constructs with tailorable mechanical properties. *Biofabrication* **3** 021001

[83] Shim J H, Lee J S, Kim J Y and Cho D W 2012 Bioprinting of a mechanically enhanced three-dimensional dual cell-laden construct for osteochondral tissue engineering using a multi-head tissue/organ building system *J. Micromechanics Microengineering* **22** 085014

[84] Lee H, Ahn S, Bonassar L J and Kim G 2013 Cell(MC3T3-E1)-Printed Poly(ϵ -caprolactone)/Alginate Hybrid Scaffolds for Tissue Regeneration *Macromol. Rapid Commun.* **34** 142–9

[85] Shim J-H, Jang K-M, Hahn S K, Park J Y, Jung H, Oh K, Park K M, Yeom J, Park S H, Kim S W, Wang J H, Kim K and Cho D-W 2016 Three-dimensional bioprinting of multilayered constructs containing human mesenchymal stromal cells for osteochondral tissue regeneration in the rabbit knee joint *Biofabrication* **8** 014102

[86] Schuurman W, Levett P A, Pot M W, van Weeren P R, Dhert W J A, Hutmacher D W, Melchels F P W, Klein T J and Malda J 2013 Gelatin-methacrylamide hydrogels as potential biomaterials for fabrication of tissue-engineered cartilage constructs *Macromol. Biosci.* **13** 551–61

[87] Ferreira J, Gloria A, Cometa S, Coelho J F J and Domingos M 2017 Effect of in vitro enzymatic degradation on 3D printed poly(ε-caprolactone) scaffolds: morphological, chemical and mechanical properties *J. Appl. Biomater. Funct. Mater.* **15** 0–0

[88] Pati F, Jang J, Ha D H, Won Kim S, Rhie J W, Shim J H, Kim D H and Cho D W 2014 Printing three-dimensional tissue analogues with decellularized extracellular matrix bioink *Nat. Commun.* **5** 1–11

[89] Rutz A L, Hyland K E, Jakus A E, Burghardt W R and Shah R N 2015 A multimaterial bioink method for 3D printing tunable, cell-compatible hydrogels *Adv. Mater.* **27** 1607–14

[90] Billiet T, Gevaert E, De Schryver T, Cornelissen M and Dubruel P 2014 The 3D printing of gelatin methacrylamide cell-laden tissue-engineered constructs with high cell viability *Biomaterials* **35** 49–62

[91] Kong H J, Smith M K and Mooney D J 2003 Designing alginate hydrogels to maintain viability of immobilized cells *Biomaterials* **24** 4023–9

[92] Nguyen D, Hägg D A, Forsman A, Ekholm J, Nimkingratana P, Brantsing C, Kalogeropoulos T, Zaunz S, Concaro S, Brittberg M, Lindahl A, Gatenholm P, Enejder A and Simonsson S 2017 Cartilage Tissue Engineering by the 3D Bioprinting of iPS Cells in a Nanocellulose/Alginate Bioink *Sci. Rep.* **7** 658

[93] Carrow J K, Cross L M, Reese R W, Jaiswal M K, Gregory C A, Kaunas R, Singh I and Gaharwar A K 2018 Widespread changes in transcriptome profile of human mesenchymal stem cells induced by two-dimensional nanosilicates *Proc. Natl.*

Acad. Sci. 201716164

[94] Pujiang Shi, Yang-Hee Kim, Mohamed Mousa, Roxanna Ramnarine Sanchez R O O and J I D 2018 Self-assembling nanoclay diffusion gels for bioactive osteogenic micro-environments *Adv. Healthc. Mater.* **Accepted M** 1–11

[95] Dawson J I and Oreffo R O C 2013 Clay: New opportunities for tissue regeneration and biomaterial design *Adv. Mater.* **25** 4069–86

[96] Carretero M I 2002 Clay minerals and their beneficial effects upon human health. A review *Appl. Clay Sci.* **21** 155–63

[97] Carretero M I and Pozo M 2009 Clay and non-clay minerals in the pharmaceutical industry. Part I. Excipients and medical applications *Appl. Clay Sci.* **46** 73–80

[98] Carretero M I and Pozo M 2010 Clay and non-clay minerals in the pharmaceutical and cosmetic industries Part II. Active ingredients *Appl. Clay Sci.* **47** 171–81

[99] Sposito G, Skipper N T, Sutton R, Park S -h., Soper A K and Greathouse J A 1999 Surface geochemistry of the clay minerals *Proc. Natl. Acad. Sci.* **96** 3358–64

[100] Mehrali M, Thakur A, Pennisi C P, Talebian S, Arpanaei A, Nikkhah M and Dolatshahi-Pirouz A 2017 Nanoreinforced Hydrogels for Tissue Engineering: Biomaterials that are Compatible with Load-Bearing and Electroactive Tissues *Adv. Mater.* **29**

[101] Ruiz-Hitzky E, Aranda P, Darder M and Rytwo G 2010 Hybrid materials based on clays for environmental and biomedical applications *J. Mater. Chem.* **20** 9306–21

[102] Xavier J R, Thakur T, Desai P, Jaiswal M K, Sears N, Cosgriff-Hernandez E, Kaunas R and Gaharwar A K 2015 Bioactive nanoengineered hydrogels for bone tissue engineering: A growth-factor-free approach *ACS Nano* **9** 3109–18

[103] Dawson J I, Kanczler J M, Yang X B, Attard G S and Oreffo R O C 2011 Clay gels for the delivery of regenerative microenvironments *Adv. Mater.* **23** 3304–8

[104] Gibaud T, Barentin C, Taberlet N and Manneville S 2009 Shear-induced fragmentation of laponite suspensions *Soft Matter* **5** 3026

[105] Aguzzi C, Cerezo P, Viseras C and Caramella C 2007 Use of clays as drug delivery systems: Possibilities and limitations *Appl. Clay Sci.* **36** 22–36

[106] Cross L M, Shah K, Palani S, Peak C W and Gaharwar A K 2017 Gradient nanocomposite hydrogels for interface tissue engineering *Nanomedicine*

Nanotechnology, Biol. Med. 1–10

[107] Paul A, Manoharan V, Krafft D, Assmann A, Uquillas J A, Shin S R, Hasan A, Hussain M A, Memic A, Gaharwar A K and Khademhosseini A 2016 Nanoengineered biomimetic hydrogels for guiding human stem cell osteogenesis in three dimensional microenvironments *J. Mater. Chem. B* **4** 3544–54

[108] Gaharwar A K, Mihaila S M, Swami A, Patel A, Sant S, Reis R L, Marques A P, Gomes M E and Khademhosseini A 2013 Bioactive silicate nanoplatelets for osteogenic differentiation of human mesenchymal stem cells *Adv. Mater.* **25** 3329–36

[109] Viseras C, Aguzzi C, Cerezo P and Bedmar M C 2008 Biopolymer–clay nanocomposites for controlled drug delivery *Mater. Sci. Technol.* **24** 1020–6

[110] Gibbs D M R, Black C R M, Hulsart-Billstrom G, Shi P, Scarpa E, Oreffo R O C and Dawson J I 2016 Bone induction at physiological doses of BMP through localization by clay nanoparticle gels *Biomaterials* **99** 16–23

[111] Becher T B, Mendonça M C P, de Farias M A, Portugal R V., de Jesus M B and Ornelas C 2018 Soft Nanohydrogels Based on Laponite Nanodiscs: A Versatile Drug Delivery Platform for Theranostics and Drug Cocktails *ACS Appl. Mater. Interfaces* **10** 21891–900

[112] Campbell T A and Ivanova O S 2013 3D printing of multifunctional nanocomposites *Nano Today* **8** 119–20

[113] Pacelli S, Paolicelli P, Moretti G, Petralito S, Di Giacomo S, Vitalone A and Casadei M A 2015 Gellan gum methacrylate and laponite as an innovative nanocomposite hydrogel for biomedical applications *Eur. Polym. J.* **77** 114–23

[114] Labanda J, Sabate J and Llorens J 2007 Rheology changes of Laponite aqueous dispersions due to the addition of sodium polyacrylates of different molecular weights *Colloids Surfaces A Physicochem. Eng. Asp.* **1**–**3** 8–15

[115] Dávila J L and d'Ávila M A 2017 Laponite as a rheology modifier of alginate solutions: Physical gelation and aging evolution *Carbohydr. Polym.* **157** 1–8

[116] Pozzo D C and Walker L M 2004 Reversible shear gelation of polymer-clay dispersions *Colloids Surfaces A Physicochem. Eng. Asp.* **240** 187–98

[117] Sydney Gladman A, Matsumoto E A, Nuzzo R G, Mahadevan L and Lewis J A 2016 Biomimetic 4D printing *Nat. Mater.* **15** 413–8

[118] Hong S, Sycks D, Chan H F ai, Lin S, Lopez G P, Guilak F, Leong K W and Zhao X 2015 3D Printing of Highly Stretchable and Tough Hydrogels into Complex, Cellularized Structures *Adv. Mater.* **27** 4034

[119] Sharifi S, Blanquer S B G, Van Kooten T G and Grijpma D W 2012 Biodegradable nanocomposite hydrogel structures with enhanced mechanical properties prepared by photo-crosslinking solutions of poly(trimethylene carbonate)-poly(ethylene glycol)-poly(trimethylene carbonate) macromonomers and nanoclay particles *Acta Biomater.* **8** 4233–43

[120] Li T, Liu Z L, Xiao M, Yang Z Z, Peng M Z, Li C Di, Zhou X J and Wang J W 2018 Impact of bone marrow mesenchymal stem cell immunomodulation on the osteogenic effects of laponite *Stem Cell Res. Ther.* **9** 100

[121] Jin Y, Compaan A, Chai W and Huang Y 2017 Functional Nanoclay Suspension for Printing-Then-Solidification of Liquid Materials *ACS Appl. Mater. Interfaces* **9** 20057–66

[122] Jin Y, Liu C, Chai W, Compaan A M and Huang Y 2017 Self-Supporting Nanoclay as Internal Scaffold Material for Direct Printing of Soft Hydrogel Composite Structures in Air *ACS Appl. Mater. Interfaces* acsami.7b03613

[123] Gaharwar A K, Rivera C P, Wu C J and Schmidt G 2011 Transparent, elastomeric and tough hydrogels from poly(ethylene glycol) and silicate nanoparticles *Acta Biomater.* **7** 4139–48

[124] Gaharwar A K, Dammu S a., Canter J M, Wu C J and Schmidt G 2011 Highly extensible, tough, and elastomeric nanocomposite hydrogels from poly(ethylene glycol) and hydroxyapatite nanoparticles *Biomacromolecules* **12** 1641–50

[125] Gaharwar A K, Schexnailder P J, Kline B P and Schmidt G 2011 Assessment of using Laponite cross-linked poly(ethylene oxide) for controlled cell adhesion and mineralization *Acta Biomater.* **7** 568–77

[126] Wang G, Maciel D, Wu Y, Rodrigues J, Shi X, Yuan Y, Liu C, Tomas H and Li Y 2014 Amphiphilic Polymer-Mediated Formation of Laponite-Based Nanohybrids with Robust Stability and pH Sensitivity for Anticancer Drug Delivery. *ACS Appl. Mater. Interfaces* **6** 16687–95

[127] Rodriguez M J, Dixon T A, Cohen E, Huang W, Omenetto F G and Kaplan D L 2018 3D freeform printing of silk fibroin *Acta Biomater.* **71** 379–87

[128] Kiaee G, Mostafalu P, Samandari M and Sonkusale S 2018 A pH-Mediated

Electronic Wound Dressing for Controlled Drug Delivery *Adv. Healthc. Mater.* **1800396** 1800396

[129] Gaharwar A K, Mukundan S, Karaca E, Dolatshahi-Pirouz A, Patel A, Rangarajan K, Mihaila S M, Iviglia G, Zhang H and Khademhosseini A 2014 Nanoclay-Enriched Poly(ε-caprolactone) Electrospun Scaffolds for Osteogenic Differentiation of Human Mesenchymal Stem Cells *Tissue Eng. Part A* **20** 2088–101

[130] Nair B P, Sindhu M and Nair P D 2016 Polycaprolactone-laponite composite scaffold releasing strontium ranelate for bone tissue engineering applications. *Colloids Surf. B. Biointerfaces* **143** 423–30

[131] Gaharwar A K, Schexnailder P J, Jin Q, Wu C J and Schmidt G 2010 Addition of chitosan to silicate cross-linked PEO for tuning osteoblast cell adhesion and mineralization *ACS Appl. Mater. Interfaces* **2** 3119–27

[132] Zhou B, Wu B, Wang J, Qian Q, Wang J, Xu H, Yang S, Feng P, Chen W, Li Y, Jiang J and Han B 2018 Drug-mediation formation of nanohybrids for sequential therapeutic delivery in cancer cells *Colloids Surfaces B Biointerfaces* **163** 284–90

[133] Haraguchi K, Takehisa T and Ebato M 2006 Control of cell cultivation and cell sheet detachment on the surface of polymer/clay nanocomposite hydrogels *Biomacromolecules* **7** 3267–75

[134] Zhai X, Ma Y, Hou C, Gao F, Zhang Y, Ruan C, Pan H, Lu W W and Liu W 2017 3D-Printed High Strength Bioactive Supramolecular Polymer/Clay Nanocomposite Hydrogel Scaffold for Bone Regeneration *ACS Biomater. Sci. Eng.* **3** 1109–18

[135] Li Y, Maciel D, Tomás H, Rodrigues J, Ma H and Shi X 2011 pH sensitive Laponite/alginate hybrid hydrogels: swelling behaviour and release mechanism *Soft Matter* **7** 6231

[136] Goncalves M, Figueira P, Maciel D, Rodrigues J, Shi X, Tom??s H and Li Y 2014 Antitumor efficacy of doxorubicin-loaded laponite/alginate hybrid hydrogels *Macromol. Biosci.* **14** 110–20

[137] Gaharwar A K, Avery R K, Assmann A, Paul A, McKinley G H, Khademhosseini A and Olsen B D 2014 Shear-Thinning Nanocomposite Hydrogels for the Treatment of Hemorrhage *ACS Nano* **8** 9833–42

[138] Chimene D, Peak C W, Gentry J L, Carrow J K, Cross L M, Mondragon E, Cardoso G B, Kaunas R and Gaharwar A K 2018 Nanoengineered Ionic–Covalent Entanglement (NICE) Bioinks for 3D Bioprinting *ACS Appl. Mater. Interfaces* **10**

9957–68

[139] Wilson S A, Cross L M, Peak C W and Gaharwar A K 2017 Shear-Thinning and Thermo-Reversible Nanoengineered Inks for 3D Bioprinting *ACS Appl. Mater. Interfaces* **9** 43449–58

[140] Zhao Y, Li Y, Mao S, Sun W and Yao R 2015 The influence of printing parameters on cell survival rate and printability in microextrusion-based 3D cell printing technology *Biofabrication* **7** 045002

[141] Kesti M, Fisch P, Pensalfini M, Mazza E and Zenobi-Wong M 2016 Guidelines for standardization of bioprinting: a systematic study of process parameters and their effect on bioprinted structures *BioNanoMaterials* **17**

[142] Kang K H, Hockaday L a and Butcher J T 2013 Quantitative optimization of solid freeform deposition of aqueous hydrogels. *Biofabrication* **5** 035001

[143] Nair K, Gandhi M, Khalil S, Yan K C, Marcolongo M, Barbee K and Sun W 2009 Characterization of cell viability during bioprinting processes *Biotechnol. J.* **4** 1168–77

[144] Blaeser A, Duarte Campos D F, Puster U, Richtering W, Stevens M M and Fischer H 2016 Controlling Shear Stress in 3D Bioprinting is a Key Factor to Balance Printing Resolution and Stem Cell Integrity *Adv. Healthc. Mater.* **5** 326–33

[145] LI M, TIAN X, KOZINSKI J A, CHEN X and HWANG D K 2015 Modeling Mechanical Cell Damage in the Bioprinting Process Employing a Conical Needle *J. Mech. Med. Biol.* **15** 1550073

[146] Snyder J, Rin Son A, Hamid Q, Wang C, Lui Y and Sun W 2015 Mesenchymal stem cell printing and process regulated cell properties *Biofabrication* **7** 044106

[147] Ouyang L, Yao R, Zhao Y and Sun W 2016 Effect of bioink properties on printability and cell viability for 3D bioplotting of embryonic stem cells *Biofabrication*

[148] Hölzl K, Lin S, Tytgat L, Van Vlierberghe S, Gu L and Ovsianikov A 2016 Bioink properties before, during and after 3D bioprinting. *Biofabrication* **8** 032002

[149] Liu W, Heinrich M A, Zhou Y, Akpek A, Hu N, Liu X, Guan X, Zhong Z, Jin X, Khademhosseini A and Zhang Y S 2017 Extrusion Bioprinting of Shear-Thinning Gelatin Methacryloyl Bioinks *Adv. Healthc. Mater.* **1601451** 1601451

[150] Aguado B A, Mulyasasmita W, Su J, Lampe K J and Heilshorn S C 2012 Improving Viability of Stem Cells During Syringe Needle Flow Through the Design of Hydrogel

Cell Carriers *Tissue Eng. Part A* **18** 806–15

[151] Lim K S, Schon B S, Mekhileri N V., Brown G C J, Chia C M, Prabakar S, Hooper G J and Woodfield T B F 2016 New Visible-Light Photoinitiating System for Improved Print Fidelity in Gelatin-Based Bioinks *ACS Biomater. Sci. Eng.* **2** 1752–62

[152] Loebel C, Rodell C B, Chen M H and Burdick J A 2017 Shear-thinning and self-healing hydrogels as injectable therapeutics and for 3D-printing *Nat. Protoc.* **12** 1521–41

[153] Bhattacharjee T, Zehnder S M, Rowe K G, Jain S, Nixon R M, Sawyer W G and Angelini T E 2015 Writing in the granular gel medium *Sci. Adv.* **1** e1500655–e1500655

[154] Faulkner-Jones A, Fyfe C, Cornelissen D-J, Gardner J, King J, Courtney A and Shu W 2015 Bioprinting of human pluripotent stem cells and their directed differentiation into hepatocyte-like cells for the generation of mini-livers in 3D. *Biofabrication* **7** 044102

[155] Hirsch T, Rothoeft T, Teig N, Bauer J W, Pellegrini G, De Rosa L, Scaglione D, Reichelt J, Klausegger A, Kneisz D, Romano O, Secone Seconetti A, Contin R, Enzo E, Jurman I, Carulli S, Jacobsen F, Luecke T, Lehnhardt M, Fischer M, Kueckelhaus M, Quaglino D, Morgante M, Bicciato S, Bondanza S and De Luca M 2017 Regeneration of the entire human epidermis using transgenic stem cells *Nature* **551** 327–32

[156] Bianco P 2015 Stem cells and bone: a historical perspective. *Bone* **70** 2–9

[157] Bianco P and Robey P G 2001 Stem cells in tissue engineering. *Nature* **414** 118–21

[158] Engler A J, Sen S, Sweeney H L and Discher D E 2006 Matrix Elasticity Directs Stem Cell Lineage Specification *Cell* **126** 677–89

[159] Riddle R C, Taylor A F, Genetos D C, Donahue H J and Ryan C 2006 MAP kinase and calcium signaling mediate fluid flow-induced human mesenchymal stem cell proliferation **17033** 776–84

[160] Kanczler J M and Oreffo R O C 2008 Osteogenesis and angiogenesis: The potential for engineering bone *Eur. Cells Mater.* **15** 100–14

[161] Kolesky D B, Truby R L, Gladman A S, Busbee T A, Homan K A and Lewis J A

2014 3D bioprinting of vascularized, heterogeneous cell-laden tissue constructs *Adv. Mater.* **26** 3124–30

[162] Mekhileri N V., Lim K S, Brown G C J, Mutreja I, Schon B S, Hooper G J and Woodfield T B F 2018 Automated 3D bioassembly of micro-tissues for biofabrication of hybrid tissue engineered constructs *Biofabrication* **10** 024103

[163] Fedorovich N E, Schuurman W, Wijnberg H M, Prins H-J, van Weeren P R, Malda J, Alblas J and Dhert W J A 2012 Biofabrication of Osteochondral Tissue Equivalents by Printing Topologically Defined, Cell-Laden Hydrogel Scaffolds *Tissue Eng. Part C Methods* **18** 33–44

[164] Zhu W, Qu X, Zhu J, Ma X, Patel S, Liu J, Wang P, Lai C S E, Gou M, Xu Y, Zhang K and Chen S 2017 Direct 3D bioprinting of prevascularized tissue constructs with complex microarchitecture *Biomaterials* **124** 106–15

[165] Daly A C, Pitacco P, Nulty J, Cunniffe G M and Kelly D J 2018 3D printed microchannel networks to direct vascularisation during endochondral bone repair *Biomaterials* **162** 34–46

[166] Oreffo R O, Virdi A S and Triffitt J T 1997 Modulation of osteogenesis and adipogenesis by human serum in human bone marrow cultures. *Eur. J. Cell Biol.* **74** 251–61

[167] Tare R S, Mitchell P D, Kanczler J and Oreffo R O C 2012 Isolation, Differentiation, and Characterisation of Skeletal Stem Cells from Human Bone Marrow In Vitro and In Vivo *Bone Research Protocols* ed M H Helfrich and S H Ralston (Totowa, NJ: Humana Press) pp 83–99

[168] Vaezi M, Black C, Gibbs D, Oreffo R, Brady M, Moshrefi-Torbati M and Yang S 2016 Characterization of New PEEK/HA Composites with 3D HA Network Fabricated by Extrusion Freeforming *Molecules* **21** 687

[169] Yang H Y, Thompson I, Yang S F, Chi X P, Evans J R G and Cook R J 2008 Dissolution characteristics of extrusion freeformed hydroxyapatite- tricalcium phosphate scaffolds *J. Mater. Sci. Mater. Med.* **19** 3345–53

[170] Kawamoto T and Shimizu M 2000 A method for preparing 2- to 50-micron-thick fresh-frozen sections of large samples and undecalcified hard tissues. *Histochem. Cell Biol.* **113** 331–9

[171] Schumacher M, Deisinger U, Detsch R and Ziegler G 2010 Indirect rapid prototyping of biphasic calcium phosphate scaffolds as bone substitutes: influence

of phase composition, macroporosity and pore geometry on mechanical properties *J. Mater. Sci. Mater. Med.* **21** 3119–27

[172] Castilho M, Moseke C, Ewald A, Gbureck U, Groll J, Pires I, Te\s smar J and Vorndran E 2014 Direct 3D powder printing of biphasic calcium phosphate scaffolds for substitution of complex bone defects *Biofabrication* **6** 015006

[173] Williams J M, Adewunmi A, Schek R M, Flanagan C L, Krebsbach P H, Feinberg S E, Hollister S J and Das S 2005 Bone tissue engineering using polycaprolactone scaffolds fabricated via selective laser sintering *Biomaterials* **26** 4817–27

[174] Lode A, Krujatz F, Brüggemeier S, Quade M, Schütz K, Knaack S, Weber J, Bley T and Gelinsky M 2015 Green bioprinting: Fabrication of photosynthetic algae-laden hydrogel scaffolds for biotechnological and medical applications *Eng. Life Sci.* **15** 177–83

[175] Pfister A, Landers R, Laib A, Hübner U, Schmelzeisen R and Mülhaupt R 2004 Biofunctional rapid prototyping for tissue-engineering applications: 3D bioplotting versus 3D printing *J. Polym. Sci. Part A Polym. Chem.* **42** 624–38

[176] Jungst T, Smolan W, Schacht K, Scheibel T and Groll J 2016 Strategies and Molecular Design Criteria for 3D Printable Hydrogels *Chem. Rev.* **116** 1496–539

[177] Gaetani R, Doevendans P A, Metz C H G, Alblas J, Messina E, Giacomello A and Sluijter J P G 2012 Cardiac tissue engineering using tissue printing technology and human cardiac progenitor cells *Biomaterials* **33** 1782–90

[178] Lozano R, Stevens L, Thompson B C, Gilmore K J, Gorkin III R, Stewart E M, in het Panhuis M, Romero-Ortega M and Wallace G G 2015 3D printing of layered brain-like structures using peptide modified gellan gum substrates *Biomaterials* **67** 264–73

[179] Fan R, Piou M, Darling E, Cormier D, Sun J and Wan J 2016 Bio-printing cell-laden Matrigel–agarose constructs *J. Biomater. Appl.* **31** 684–92

[180] Dawson J I, Kanczler J, Tare R, Kassem M and Oreffo R O C 2014 Concise Review: Bridging the Gap: Bone Regeneration Using Skeletal Stem Cell-Based Strategies-Where Are We Now? *Stem Cells* **32** 35–44

[181] Ding X, Gao J, Wang Z, Awada H and Wang Y 2016 A shear-thinning hydrogel that extends in vivo bioactivity of FGF2 *Biomaterials* **111** 80–9

[182] Su D, Jiang L, Chen X, Dong J and Shao Z 2016 Enhancing the Gelation and

Bioactivity of Injectable Silk Fibroin Hydrogel with Laponite Nanoplatelets *ACS Appl. Mater. Interfaces* **8** 9619–28

[183] Ghadiri M, Chrzanowski W, Lee W H, Fathi A, Dehghani F and Rohanizadeh R 2013 Physico-chemical, mechanical and cytotoxicity characterizations of Laponite®/alginate nanocomposite *Appl. Clay Sci.* **85** 64–73

[184] Haraguchi K, Farnworth R, Ohbayashi A and Takehisa T 2003 Compositional Effects on Mechanical Properties of Nanocomposite Hydrogels Composed of Poly(N , N -dimethylacrylamide) and Clay *Macromolecules* **36** 5732–41

[185] Valencia G A, Lourenco R V, Bittante A M Q B and do Amaral Sobral P J 2016 Physical and morphological properties of nanocomposite films based on gelatin and Laponite *Appl. Clay Sci.* **124**–**125** 260–6

[186] Hoppe A, Güldal N S and Boccaccini A R 2011 A review of the biological response to ionic dissolution products from bioactive glasses and glass-ceramics *Biomaterials* **32** 2757–74

[187] Wang J, Lin L, Cheng Q and Jiang L 2012 A strong bio-inspired layered PNIPAM-clay nanocomposite hydrogel *Angew. Chemie - Int. Ed.* **51** 4676–80

[188] Wang Q, Mynar J L, Yoshida M, Lee E, Lee M, Okuro K, Kinbara K and Aida T 2010 High-water-content mouldable hydrogels by mixing clay and a dendritic molecular binder *Nature* **463** 339–43

[189] Luo Y, Lode A and Gelinsky M 2013 Direct Plotting of Three-Dimensional Hollow Fiber Scaffolds Based on Concentrated Alginate Pastes for Tissue Engineering *Adv. Healthc. Mater.* **2** 777–83

[190] Sarker B, Singh R, Silva R, Roether J A, Kaschta J, Detsch R, Schubert D W, Cicha I and Boccaccini A R 2014 Evaluation of Fibroblasts Adhesion and Proliferation on Alginate-Gelatin Crosslinked Hydrogel ed M Yamamoto *PLoS One* **9** e107952

[191] Xavier M, Rosendahl P, Herbig M, Kräter M, Spencer D, Bornhäuser M, Oreffo R O C, Morgan H, Guck J and Otto O 2016 Mechanical phenotyping of primary human skeletal stem cells in heterogeneous populations by real-time deformability cytometry. *Integr. Biol. (Camb).* 10–2

[192] Tate M C, Shear D A, Hoffman S W, Stein D G and LaPlaca M C 2001 Biocompatibility of methylcellulose-based constructs designed for intracerebral gelation following experimental traumatic brain injury *Biomaterials* **22** 1113–23

[193] Nasatto P L, Pignon F, Silveira J L M, Duarte M E R, Noseda M D and Rinaudo M 2015 Methylcellulose, a cellulose derivative with original physical properties and extended applications *Polymers (Basel).* **7** 777–803

[194] Böcker W, Yin Z, Drosse I, Haasters F, Rossmann O, Wierer M, Popov C, Locher M, Mutschler W, Docheva D and Schieker M 2008 Introducing a single-cell-derived human mesenchymal stem cell line expressing hTERT after lentiviral gene transfer *J. Cell. Mol. Med.* **12** 1347–59

[195] Knaack S, Lode A, Hoyer B, Rösen-Wolff A, Gabrielyan A, Roeder I and Gelinsky M 2014 Heparin modification of a biomimetic bone matrix for controlled release of VEGF *J. Biomed. Mater. Res. - Part A* **102** 3500–11

[196] Murphy S V and Atala A 2014 3D bioprinting of tissues and organs. *Nat. Biotechnol.* **32** 773–85

[197] Chang R, Nam J and Sun W 2008 Effects of Dispensing Pressure and Nozzle Diameter on Cell Survival from Solid Freeform Fabrication–Based Direct Cell Writing *Tissue Eng. Part A* **14** 41–8

[198] Akkineni A, Ahlfeld T, Funk A, Waske A, Lode A and Gelinsky M 2016 Highly Concentrated Alginate-Gellan Gum Composites for 3D Plotting of Complex Tissue Engineering Scaffolds *Polymers (Basel).* **8** 1–16

[199] Luo Y, Lode A, Sonntag F, Nies B and Gelinsky M 2013 Well-ordered biphasic calcium phosphate–alginate scaffolds fabricated by multi-channel 3D plotting under mild conditions *J. Mater. Chem. B* **1** 4088

[200] Tabriz A G, Hermida M A, Leslie N R and Shu W 2015 Three-dimensional bioprinting of complex cell laden alginate hydrogel structures *Biofabrication* **7** 045012

[201] Bernhardt A, Wehrl M, Paul B, Hochmuth T, Schumacher M, Schütz K and Gelinsky M 2015 Improved Sterilization of Sensitive Biomaterials with Supercritical Carbon Dioxide at Low Temperature *PLoS One* **10** e0129205

[202] Ruzicka B, Zulian L and Ruocco G 2004 Routes to gelation in a clay suspension *Phys. Rev. Lett.* **93** 1–4

[203] Zhao L Z, Zhou C H, Wang J, Tong D S, Yu W H and Wang H 2015 Recent advances in clay mineral-containing nanocomposite hydrogels *Soft Matter* **11** 9229–46

[204] Lagaron J M and Fendler a. 2009 High Water Barrier Nanobiocomposites of Methyl Cellulose and Chitosan for Film and Coating Applications *J. Plast. Film Sheeting* **25** 47–59

[205] Lee K Y and Mooney D J 2012 Alginate: properties and biomedical applications *Prog. Polym. Sci.* **37** 106–26

[206] O'Brien F J 2011 Biomaterials & scaffolds for tissue engineering *Mater. Today* **14** 88–95

[207] Sarker B, Rompf J, Silva R, Lang N, Detsch R, Kaschta J, Fabry B and Boccaccini A R 2015 Alginate-based hydrogels with improved adhesive properties for cell encapsulation *Int. J. Biol. Macromol.* **78** 72–8

[208] Mason B N, Califano J P and Reinhart-King C A 2012 Matrix Stiffness: A Regulator of Cellular Behavior and Tissue Formation *Engineering Biomaterials for Regenerative Medicine* ed S K Bhatia (Springer New York) pp 19–37

[209] Ding X, Gao J, Wang Z, Awada H and Wang Y 2016 A shear-thinning hydrogel that extends in vivo bioactivity of FGF2 *Biomaterials* **111** 80–9

[210] Zhao Y, Li F, Carvajal M T and Harris M T 2009 Interactions between bovine serum albumin and alginate: An evaluation of alginate as protein carrier ed J Hartley and K McWilliam *J. Colloid Interface Sci.* **332** 345–53

[211] Li Q, Hou T, Zhao J and Xu J 2011 Vascular Endothelial Growth Factor Release from Alginate Microspheres Under Simulated Physiological Compressive Loading and the Effect on Human Vascular Endothelial Cells *Tissue Eng. Part A* **17** 1777–85

[212] Phan H T M, Bartelt-Hunt S, Rodenhausen K B, Schubert M and Bartz J C 2015 Investigation of Bovine Serum Albumin (BSA) Attachment onto Self-Assembled Monolayers (SAMs) Using Combinatorial Quartz Crystal Microbalance with Dissipation (QCM-D) and Spectroscopic Ellipsometry (SE) ed D Hinderberger *PLoS One* **10** e0141282

[213] Claaßen C, Sewald L, Tovar G and Borchers K 2017 Controlled Release of Vascular Endothelial Growth Factor from Heparin-Functionalized Gelatin Type A and Albumin Hydrogels *Gels* **3** 35

[214] Ruzicka B and Zaccarelli E 2011 A fresh look at the Laponite phase diagram *Soft Matter* **7** 1268–86

[215] Sheikhi A, Afewerki S, Oklu R, Gaharwar A K and Khademhosseini A 2018 Effect of ionic strength on shear-thinning nanoclay–polymer composite hydrogels *Biomater. Sci.* **6** 2073–83

[216] Peak C W, Stein J, Gold K A and Gaharwar A K 2018 Nanoengineered Colloidal Inks for 3D Bioprinting *Langmuir* **34** 917–25

[217] Detela G, Bain O W, Kim H W, Williams D J, Mason C, Mathur A and Wall I B 2018 Donor Variability in Growth Kinetics of Healthy hMSCs Using Manual Processing: Considerations for Manufacture of Cell Therapies *Biotechnol. J.* **13** 1–10

[218] Cavo M, Caria M, Pulsoni I, Beltrame F, Fato M and Scaglione S 2018 A new cell-laden 3D Alginate-Matrigel hydrogel resembles human breast cancer cell malignant morphology, spread and invasion capability observed “in vivo” *Sci. Rep.* **8** 1–12

[219] Lim K S, Levato R, Costa P F, Castilho M D, Alcala-Orozco C R, Dorenmalen K M A van, Melchels F P W, Gawlitta D, Hooper G J, Malda J and Woodfield T B F 2018 Bio-resin for high resolution lithography-based biofabrication of complex cell-laden constructs *Biofabrication* **10** 34101

[220] Jaiswal N, Haynesworth S E, Caplan A I and Bruder S P 1997 Osteogenic differentiation of purified, culture-expanded human mesenchymal stem cells in vitro *J. Cell. Biochem.* **64** 295–312

[221] Malaval L, Modrowski D, Gupta A K and Aubin J E 1994 Cellular expression of bone- related proteins during in vitro osteogenesis in rat bone marrow stromal cell cultures *J. Cell. Physiol.* **158** 555–72

[222] Olderøy M O, Xie M, Andreassen J P, Strand B L, Zhang Z and Sikorski P 2012 Viscoelastic properties of mineralized alginate hydrogel beads *J. Mater. Sci. Mater. Med.* **23** 1619–27

[223] Xiao X, Wang W, Liu D, Zhang H, Gao P, Geng L, Yuan Y, Lu J and Wang Z 2015 The promotion of angiogenesis induced by three-dimensional porous beta-tricalcium phosphate scaffold with different interconnection sizes via activation of PI3K/Akt pathways *Sci. Rep.* **5** 9409

[224] Mehdizadeh H, Sumo S, Bayrak E S, Brey E M and Cinar A 2013 Three-dimensional modeling of angiogenesis in porous biomaterial scaffolds *Biomaterials* **34** 2875–87

[225] Bates D O 2010 Vascular endothelial growth factors and vascular permeability *Cardiovasc. Res.* **87** 262–71

[226] Bai Y, Bai L, Zhou J, Chen H and Zhang L 2018 Sequential delivery of VEGF, FGF-2 and PDGF from the polymeric system enhance HUVECs angiogenesis in vitro and CAM angiogenesis *Cell. Immunol.* **323** 19–32

[227] Armesilla A L, Lorenzo E, DelArco P G, MartinezMartinez S, Alfranca A and Redondo J M 1999 Vascular endothelial growth factor activates nuclear factor of activated T cells in human endothelial cells: a role for tissue factor gene expression *Mol. Cell. Biol.* **19** 2032

[228] Holmes A M, Charlton A, Derby B, Ewart L, Scott A and Shu W 2017 Rising to the challenge: Applying biofabrication approaches for better drug and chemical product development *Biofabrication* **9** 1–20

[229] Scott M A, Levi B, Askarinam A, Nguyen A, Rackohn T, Ting K, Soo C and James A W 2012 Brief Review of Models of Ectopic Bone Formation *Stem Cells Dev.* **21** 655–67

[230] Yamamoto M, Takahashi Y and Tabata Y 2003 Controlled release by biodegradable hydrogels enhances the ectopic bone formation of bone morphogenetic protein *Biomaterials* **24** 4375–83

[231] Iordachescu A, Amin H D, Rankin S M, Williams R L, Yapp C, Bannerman A, Pacureanu A, Addison O, Hulley P A and Grover L M 2017 An In Vitro Model for the Development of Mature Bone Containing an Osteocyte Network *Adv. Biosyst.* **1700156** 1700156

[232] Friess W, Uludag H, Foskett S, Biron R and Sargeant C 1999 Characterization of absorbable collagen sponges as recombinant human bone morphogenetic protein-2 carriers *Int. J. Pharm.* **185** 51–60

[233] Sicari B M, Rubin J P, Dearth C L, Wolf M T, Ambrosio F, Boninger M, Turner N J, Weber D J, Simpson T W, Wyse A, Brown E H P, Dziki J L, Fisher L E, Brown S and Badylak S F 2014 An Acellular Biologic Scaffold Promotes Skeletal Muscle Formation in Mice and Humans with Volumetric Muscle Loss *Sci. Transl. Med.* **6** 234ra58-234ra58

[234] Jakus A E, Rutz A L, Jordan S W, Kannan A, Mitchell S M, Yun C, Koube K D, Yoo S C, Whiteley H E, Richter C-P, Galiano R D, Hsu W K, Stock S R, Hsu E L and Shah R N 2016 Hyperelastic “bone”: A highly versatile, growth factor–free, osteoregenerative, scalable, and surgically friendly biomaterial *Sci. Transl. Med.* **8** 358ra127-358ra127

[235] Dawson J I and Oreffo R O C 2008 Bridging the regeneration gap: Stem cells, biomaterials and clinical translation in bone tissue engineering *Arch. Biochem. Biophys.* **473** 124–31

[236] Vozzi G and Ahluwalia A 2007 Microfabrication for tissue engineering: rethinking the cells-on-a scaffold approach *J. Mater. Chem.* **17** 1248

[237] Daly A C, Cunniffe G M, Sathy B N, Jeon O, Alsberg E and Kelly D J 2016 3D Bioprinting of Developmentally Inspired Templates for Whole Bone Organ Engineering *Adv. Healthc. Mater.* **5** 2353–62

[238] Loozen L D, Wegman F, Öner F C, Dhert W J A and Alblas J 2013 Porous bioprinted constructs in BMP-2 non-viral gene therapy for bone tissue engineering *J. Mater. Chem. B* **1** 6619

[239] Otto I A, Breugem C C, Malda J and Bredenoord A L 2016 Ethical considerations in the translation of regenerative biofabrication technologies into clinic and society *Biofabrication* **8** 042001

[240] Uludag H, D'Augusta D, Palmer R, Timony G and Wozney J 1999 Characterization of rhBMP-2 pharmacokinetics implanted with biomaterial carriers in the rat ectopic model *J. Biomed. Mater. Res.* **46** 193–202

[241] Winkler T, Sass F A, Duda G N and Schmidt-Bleek K 2018 A review of biomaterials in bone defect healing, remaining shortcomings and future opportunities for bone tissue engineering *Bone Joint Res.* **7** 232–43

[242] Sun J and Tan H 2013 Alginate-based biomaterials for regenerative medicine applications *Materials (Basel).* **6** 1285–309

[243] Levy G and Rao B K 1972 Enhanced intestinal absorption of riboflavin from sodium alginate solution in man *J. Pharm. Sci.* **61** 279–80

[244] Cao Y, Shen X, Chen Y, Guo J, Chen Q and Jiang X 2005 pH-induced self-assembly and capsules of sodium alginate *Biomacromolecules* **6** 2189–96

[245] Abbah S A, Liu J, Lam R W M, Goh J C H and Wong H K 2012 In vivo bioactivity of rhBMP-2 delivered with novel polyelectrolyte complexation shells assembled on an alginate microbead core template *J. Control. Release* **162** 364–72

[246] Toscano L, Montero G, Stoytcheva M, Cervantes L and Gochev V 2014 Comparison of the performances of four hydrophilic polymers as supports for lipase immobilisation *Biotechnol. Biotechnol. Equip.* **28** 52–60

[247] Gibbs D M, Vaezi M, Yang S and Oreffo R O 2014 Hope versus hype: what can additive manufacturing realistically offer trauma and orthopedic surgery? *Regen. Med.* **9** 535–49

[248] Rolfe B, Mooney J, Zhang B, Jahnke S, Le S-J, Chau Y-Q, Huang Q, Wang H, Campbell G and Campbell J 2011 The Fibrotic Response to Implanted Biomaterials: Implications for Tissue Engineering *Regen. Med. Tissue Eng. - Cells Biomater.*

[249] Black C R M, Goriainov V, Gibbs D, Kanczler J, Tare R S and Oreffo R O C 2015 Bone Tissue Engineering *Curr. Mol. Biol. Reports* **1** 132–40

[250] Ikehara S, Pahwa R N, Fernandes G, Hansen C T and Good R a 1984 Functional T cells in athymic nude mice. *Proc. Natl. Acad. Sci. U. S. A.* **81** 886–8

[251] Szadvari I, Krizanova O and Babula P 2016 Athymic Nude Mice as an Experimental Model for Cancer Treatment *Physiol. Res* **65** 441–53

[252] Park J S and Park K H 2016 Light enhanced bone regeneration in an athymic nude mouse implanted with mesenchymal stem cells embedded in PLGA microspheres *Biomater. Res.* **20** 1–8

[253] Miers L, DeNardo S J, Lamborn K and DeNardo G L 2005 Implantation of different malignant human cell lines in an athymic mouse does not alter success and growth rates of either xenograft. *Cancer Biother. Radiopharm.* **20** 614–9

[254] Michael S, Sorg H, Peck C T, Koch L, Deiwick A, Chichkov B, Vogt P M and Reimers K 2013 Tissue Engineered Skin Substitutes Created by Laser-Assisted Bioprinting Form Skin-Like Structures in the Dorsal Skin Fold Chamber in Mice ed A T Slominski *PLoS One* **8** e57741

[255] Guilak F, Alexopoulos L G, Upton M L, Youn I, Choi J B, Cao L, Setton L A and Haider M A 2006 The pericellular matrix as a transducer of biomechanical and biochemical signals in articular cartilage *Ann. N. Y. Acad. Sci.* **1068** 498–512

[256] Cushing M C and Anseth K S 2007 Hydrogel cell cultures *Science (80-.).* **316** 1133–4

[257] Slaughter B V., Khurshid S S, Fisher O Z, Khademhosseini A and Peppas N A 2009 Hydrogels in Regenerative Medicine *Adv. Mater.* **21** 3307–29

[258] Hinton T J, Hudson A, Pusch K, Lee A and Feinberg A W 2016 3D Printing PDMS Elastomer in a Hydrophilic Support Bath via Freeform Reversible Embedding *ACS*

Biomater. Sci. Eng. **2** 1781–6

[259] Moxon S R, Cooke M E, Cox S C, Snow M, Jeys L, Jones S W, Smith A M and Grover L M 2017 Suspended Manufacture of Biological Structures *Adv. Mater.* **29** 1605594

[260] Highley C B, Rodell C B and Burdick J a. 2015 Direct 3D Printing of Shear-Thinning Hydrogels into Self-Healing Hydrogels *Adv. Mater.* **27** 5075–9

[261] Kim B S, Kim H, Gao G, Jang J and Cho D-W 2017 Decellularized extracellular matrix: a step towards the next generation source for bioink manufacturing *Biofabrication* **9** 034104

[262] Jin Y, Chai W and Huang Y 2017 Printability study of hydrogel solution extrusion in nanoclay yield-stress bath during printing-then-gelation biofabrication *Mater. Sci. Eng. C* **80** 313–25

[263] Hinton T J, Jallerat Q, Palchesko R N, Park J H, Grodzicki M S, Shue H, Ramadan M H, Hudson A R and Feinberg A W 2015 Three-dimensional printing of complex biological structures by freeform reversible embedding of suspended hydrogels *Sci. Adv.* **1** 1–10

[264] Grasdalen H and Smidsrød O 1987 Gelation of gellan gum *Carbohydr. Polym.* **7** 371–93

[265] Jansson P-E, Lindberg B and Sandford P A 1983 Structural studies of gellan gum, an extracellular polysaccharide elaborated by Pseudomonas elodea *Carbohydr. Res.* **124** 135–9

[266] Douglas T E L, Krawczyk G, Pamula E, Declercq H A, Schaubroeck D, Bucko M M, Balcaen L, Van Der Voort P, Bliznuk V, van den Vreken N M F, Dash M, Detsch R, Boccaccini A R, Vanhaecke F, Cornelissen M and Dubruel P 2016 Generation of composites for bone tissue-engineering applications consisting of gellan gum hydrogels mineralized with calcium and magnesium phosphate phases by enzymatic means *J. Tissue Eng. Regen. Med.* **10** 938–54

[267] Oliveira J T, Martins L, Picciochi R, Malafaya P B, Sousa R A, Neves N M, Mano J F and Reis R L 2010 Gellan gum: A new biomaterial for cartilage tissue engineering applications *J. Biomed. Mater. Res. - Part A* **93** 852–63

[268] Osmałek T, Froelich A and Tasarek S 2014 Application of gellan gum in pharmacy and medicine *Int. J. Pharm.* **466** 328–40

[269] Pidcock G C and In Het Panhuis M 2012 Extrusion printing of flexible electrically conducting carbon nanotube networks *Adv. Funct. Mater.* **22** 4790–800

[270] Shoichet M S, Li R H, White M L and Winn S R 1996 Stability of hydrogels used in cell encapsulation: An in vitro comparison of alginate and agarose *Biotechnol. Bioeng.* **50** 374–81

[271] Topuz F, Nadernezhad A, Caliskan O S, Menceloglu Y Z and Koc B 2018 Nanosilicate embedded agarose hydrogels with improved bioactivity *Carbohydr. Polym.* **201** 105–12

[272] Miyoshi E 1996 Rheological and thermal studies of gel-sol transition in gellan gum aqueous solutions *Carbohydr. Polym.* **30** 109–19

[273] Shi L, Carstensen H, Hölzl K, Lunzer M, Li H, Hilborn J, Ovsianikov A and Ossipov D A 2017 Dynamic Coordination Chemistry Enables Free Directional Printing of Biopolymer Hydrogel *Chem. Mater.* **29** 5816–23

[274] Mouser V H M, Melchels F P W, Visser J, Dhert W J A, Gawlitta D and Malda J 2016 Yield stress determines bioprintability of hydrogels based on gelatin-methacryloyl and gellan gum for cartilage bioprinting *Biofabrication* **8** 1–13

[275] Visser J, Peters B, Burger T J, Boomstra J, Dhert W J a, Melchels F P W and Malda J 2013 Biofabrication of multi-material anatomically shaped tissue constructs. *Biofabrication* **5** 035007

[276] Ferris C J, Gilmore K J, Beirne S, McCallum D, Wallace G G and in het Panhuis M 2013 Bio-ink for on-demand printing of living cells *Biomater. Sci.* **1** 224–30

[277] Akkineni A R, Ahlfeld T, Lode A and Gelinsky M 2016 A versatile method for combining different biopolymers in a core/shell fashion by 3D plotting to achieve mechanically robust constructs *Biofabrication* **8** 045001

[278] Alom N, Peto H, Kirkham G R, Shakesheff K M and White L J 2017 Bone extracellular matrix hydrogel enhances osteogenic differentiation of C2C12 myoblasts and mouse primary calvarial cells *J. Biomed. Mater. Res. Part B Appl. Biomater.* 1–9

[279] López-Cebral R, Civantos A, Ramos V, Seijo B, López-Lacomba J L, Sanz-Casado J V and Sanchez A 2017 Gellan gum based physical hydrogels incorporating highly valuable endogen molecules and associating BMP-2 as bone formation platforms *Carbohydr. Polym.* **167** 345–55

[280] Upadrashta S M, Häglund B O and Sundelöf L - O 1993 Diffusion and concentration profiles of drugs in gels *J. Pharm. Sci.* **82** 1094–8

[281] Moreno-Jiménez I, Hulsart-Billstrom G, Lanham S A, Janeczek A A, Kontouli N, Kanczler J M, Evans N D and Oreffo R O 2016 The chorioallantoic membrane (CAM) assay for the study of human bone regeneration: a refinement animal model for tissue engineering *Sci. Rep.* **6** 32168

[282] Murphy S V., Skardal A and Atala A 2013 Evaluation of hydrogels for bio-printing applications *J. Biomed. Mater. Res. - Part A* **101 A** 272–84

[283] Yue K, Trujillo-de Santiago G, Alvarez M M, Tamayol A, Annabi N and Khademhosseini A 2015 Synthesis, properties, and biomedical applications of gelatin methacryloyl (GelMA) hydrogels *Biomaterials* **73** 254–71

[284] Nichol J W, Koshy S T, Bae H, Hwang C M, Yamanlar S and Khademhosseini A 2010 Cell-laden microengineered gelatin methacrylate hydrogels *Biomaterials* **31** 5536–44

[285] Van Den Bulcke A I, Bogdanov B, De Rooze N, Schacht E H, Cornelissen M and Berghmans H 2000 Structural and rheological properties of methacrylamide modified gelatin hydrogels *Biomacromolecules* **1** 31–8

[286] Zhao X, Liu S, Yildirimer L, Zhao H, Ding R, Wang H, Cui W and Weitz D 2016 Injectable Stem Cell-Laden Photocrosslinkable Microspheres Fabricated Using Microfluidics for Rapid Generation of Osteogenic Tissue Constructs *Adv. Funct. Mater.* **26** 2809–19

[287] Khetan S, Guvendiren M, Legant W R, Cohen D M, Chen C S and Burdick J A 2013 Degradation-mediated cellular traction directs stem cell fate in covalently crosslinked three-dimensional hydrogels *Nat. Mater.* **12** 458–65

[288] Nguyen L H, Annabi N, Nikkhah M, Bae H, Binan L, Park S, Kang Y, Yang Y and Khademhosseini A 2012 Vascularized Bone Tissue Engineering: Approaches for Potential Improvement *Tissue Eng. Part B Rev.* **18** 363–82

[289] Yang G, Xiao Z, Long H, Ma K, Zhang J, Ren X and Zhang J 2018 Assessment of the characteristics and biocompatibility of gelatin sponge scaffolds prepared by various crosslinking methods *Sci. Rep.* **8** 1–13

[290] Kim Y H and Tabata Y 2017 Enhancement of wound closure by modifying dual release patterns of stromal-derived cell factor-1 and a macrophage recruitment agent from gelatin hydrogels *J. Tissue Eng. Regen. Med.* **11** 2999–3013

[291] Guo C, Zhou L and Lv J 2013 Effects of expandable graphite and modified ammonium polyphosphate on the flame-retardant and mechanical properties of wood flour-polypropylene composites *Polym. Polym. Compos.* **21** 449–56

[292] Poursamar S A, Lehner A N, Azami M, Ebrahimi-Barough S, Samadikuchaksaraei A and Antunes A P M 2016 The effects of crosslinkers on physical, mechanical, and cytotoxic properties of gelatin sponge prepared via in-situ gas foaming method as a tissue engineering scaffold *Mater. Sci. Eng. C* **63** 1–9

[293] Sinha R P and Häder D-P 2002 UV-induced DNA damage and repair: a review *Photochem. Photobiol. Sci.* **1** 225–36

[294] Kumar A, Mandal S, Barui S, Vasireddi R, Gbureck U, Gelinsky M and Basu B 2016 Low temperature additive manufacturing of three dimensional scaffolds for bone-tissue engineering applications: Processing related challenges and property assessment *Mater. Sci. Eng. R Reports* **103** 1–39

[295] Amit M and Itskovitz-Eldor J 2012 Morphology of Human Embryonic and Induced Pluripotent Stem Cell Colonies Cultured with Feeders *Atlas of Human Pluripotent Stem Cells* (Totowa, NJ: Humana Press) pp 15–39

[296] Kleinheinz J, Jung S, Wermker K, Fischer C and Joos U 2010 Release kinetics of VEGF165 from a collagen matrix and structural matrix changes in a circulation model *Head Face Med* **6** 17

[297] Auerbach R, Lewis R, Shinners B, Kubai L and Akhtar N 2003 Angiogenesis assays: A critical overview *Clin. Chem.* **49** 32–40

[298] Derby B 2012 Printing and prototyping of tissues and scaffolds *Science (80-.).* **338** 921–6

[299] Lewis J A 2006 Direct ink writing of 3D functional materials *Adv. Funct. Mater.* **16** 2193–204

[300] Fedorovich N E, Swennen I, Girones J, Moroni L, Van Blitterswijk C A, Schacht E, Alblas J and Dhert W J A 2009 Evaluation of photocrosslinked lutrol hydrogel for tissue printing applications *Biomacromolecules* **10** 1689–96

[301] Geiger M, Li R H and Friess W 2003 Collagen sponges for bone regeneration with rhBMP-2 *Adv. Drug Deliv. Rev.* **55** 1613–29

[302] Smith E L, Kanczler J M, Gothard D, Roberts C A, Wells J A, White L J, Qutachi O, Sawkins M J, Peto H, Rashidi H, Rojo L, Stevens M M, El Haj A J, Rose F R A J,

Shakesheff K M and Oreffo R O C 2014 Evaluation of skeletal tissue repair, Part 1: Assessment of novel growth-factor-releasing hydrogels in an ex vivo chick femur defect model *Acta Biomater.* **10** 4186–96

[303] Nguyen M K, McMillan A, Huynh C T, Schapira D S and Alsberg E 2017 Photocrosslinkable, biodegradable hydrogels with controlled cell adhesivity for prolonged siRNA delivery to hMSCs to enhance their osteogenic differentiation *J. Mater. Chem. B* **5** 485–95

[304] Mouser V H M, Abbadessa A, Levato R, Hennink W E, Dhert W J A, Gawlitta D, Vermonden T and Malda J Development of a thermosensitive HAMA-containing bio-ink for the fabrication of composite cartilage repair constructs *Manuscr. Prep.*

[305] de Ruijter M, Ribeiro A, Dokter I, Castilho M and Malda J 2018 Simultaneous Micropatterning of Fibrous Meshes and Bioinks for the Fabrication of Living Tissue Constructs *Adv. Healthc. Mater.* **1800418** 1800418

[306] Thompson D W and Butterworth J T 1992 The Nature of Laponite and Its Aqueous Dispersions pH Titration of Laponite Dispersions Analysis of Laponite Dispersion Media and Measurements *J. Colloid Interface Sci.* **15** 236–43

[307] Cao X, Yan B, Huang Y, Zhang Y, Li L, Qiu J and Lyu X 2018 Use of laponite as adsorbents for Ni(II) removal from aqueous solution *Environ. Prog. Sustain. Energy* **37** 942–50

[308] López Arbeloa F, Herrán Martinez J M, López Arbeloa T and López Arbeloa I 1998 The hydrophobic effect on the adsorption of rhodamines in aqueous suspensions of smectites. the rhodamine 3B/Laponite B system *Langmuir* **14** 4566–73

[309] Yang D, Peng S, Hartman M R, Gupton-Campolongo T, Rice E J, Chang A K, Gu Z, Lu G Q M and Luo D 2013 Enhanced transcription and translation in clay hydrogel and implications for early life evolution. *Sci. Rep.* **3** 3165

[310] Kim S W, Bae Y H and Okano T 1992 Hydrogels: swelling, drug loading, and release. *Pharm. Res.* **9** 283–90

[311] Wang S, Wu Y, Guo R, Huang Y, Wen S, Shen M, Wang J and Shi X 2013 Laponite Nanodisks as an Efficient Platform for Doxorubicin Delivery to Cancer Cells *Langmuir* **29** 5030–6

[312] Crapo P M, Gilbert T W and Badylak S F 2011 An overview of tissue and whole organ decellularization processes *Biomaterials* **32** 3233–43